Microstructural Development and Mechanical Property Manipulation of Co-Cr-Mo Biomedical Implant Material Through Processing and Nitrogen Alloying

Wade Lewis Karlsen
B.S., University of Washington, 1993

A dissertation submitted to the faculty of the
Oregon Graduate Institute of Science and Technology
in partial fulfillment of the
requirements for the degree
Doctor of Philosophy
in
Materials Science and Engineering

December, 1997

The dissertation "Microstructural Development and Mechanical Property Manipulation of Co-Cr-Mo Biomedical Implant Material Through Processing and Nitrogen Alloying" by Wade Karlsen has been examined and approved by the following Examination Committee:

Dr. David Atteridge, Advisor
Professor

Dr. Jack Devletian
Professor

Dr. Milt Scholl
Professor

Dr. John Simmons
Dept. of Energy—Albany Research Center

Dr. Sanjay Shendye
PCC Structurals, Inc.

Dedicated to my many family and friends whose enjoyable
distractions added to the challenge of completing this work.

ACKNOWLEDGEMENTS

I wish to express my gratitude to all those whose help and encouragement assisted me in completing this work. I would like to especially thank:

Dr. D. Atteridge (OGI), my dissertation committee advisor, for his guidance and criticism during this investigation,

Dr. J. Simmons (DOE), for his participation in and many contributions to the project, and for serving on my dissertation committee.

Dr. S. Shendye (PCC), Dr. J. Devletion (OGI), and Dr. M. Scholl (OGI) for their participation serving on my dissertation committee.

The Department of Energy's Albany Research Center, Albany Oregon, for their significant contribution of equipment use and analysis services, as well as for producing the high-nitrogen melts.

PED Manufacturing, Ltd., Oregon City, Oregon, and Precision Castparts Corporation, Portland, Oregon for their financial support of the project, and for their contribution of cast F75 materials, and their respective participating members for their discussions and feedback.

The Oregon Metals Initiative funding organization for their matching funds to support the project.

Deloro Stellite, Belleville, Ontario, Canada, for their contribution of Stellite 21.

Jim Gardner of PED Manufacturing, Ltd. for his participation in beginning the project and exploring the initial directions of the work.

Larry Sink of Precision Castparts Corp. for his encouragement of my ideas since before graduate school, and subsequently in later stages of the project.

Finally, I would like to thank the Oregon Graduate Institute's Materials Science & Engineering department's technical staff for their assistance and advice in sample preparation, analysis, and testing, and the office staff for their assistance in procuring funding and supplies, and general smoothing of the office details of the project.

TABLE OF CONTENTS

LIST OF FIGURES

LIST OF TABLES

ABSTRACT

Microstructural Development and Mechanical Property Manipulation
of
Co-Cr-Mo Biomedical Implant Material Through Processing and Nitrogen Alloying

Wade Karlsen, B.S.
Supervising professor: Dr. David Atteridge

There has been an on-going effort to improve the mechanical performance of the ASTM F75 Co-Cr-Mo biomedical implant alloy. However, efforts have been thwarted by the alloy's dependence upon carbon and carbide structures for strengthening, which are associated with lower incipient melting temperatures, and lower ductilities.

In this study, the microstructural development of investment cast F75 subjected to hot-isostatic pressing, solutionization, and aging at various temperatures and times was investigated. Both conventional dendritic and fine-grained castings were explored. Subsequently, the microstructural development of nitrogen-high pressure melted (N-HPM) Stellite 21 material in the as-cast, solution treated, thermomechanically processed, and further heat treated forms was analyzed. Ingots with nitrogen contents ranging from 0.1wt% to 1.2wt% were examined.

Microstructural characterization following the various processing steps included identification of nitride/carbide populations, assessment of their morphology and distribution, and quantification of the grain structure. Room temperature tensile mechanical properties were measured for many of the conditions, demonstrating how the nitrogen content and the microstructures developed through the process alterations affected the final properties.

The findings indicate that a fine, equiaxed grain structure increases the yield strength at low second phase contents, and that as the second phase content increases, it

also increases the yield strength. Additionally, at low second phase contents a finer grain size improves ductility, but as the second phase content increases, the ductility is adversely affected. Additions of nitrogen increased the second phase content.

Nitrogen alloying also changed the morphology of the second phase content from a $Cr_{23}C_6$-type, to a Cr_2N-type, with an apparent elevation of the incipient melting temperature to above 1260°C (2300°F). As an interstitial, the nitrogen increased the ductility of the alloy. Finally, alloying with nitrogen did not negatively impact the localized corrosion resistance in 0.9% NaCl solution, or the abrasive wear resistance properties, retaining the suitability of the alloy for biomedical applications.

1. INTRODUCTION

Co-Cr-Mo alloys are widely used as surgical implant materials [1], largely due to their proven corrosion and wear resistance, and biocompatibility [2, 3]. They are especially popular in the resurgent application of metal-on-metal hip implants [4, 5]. As younger, more active patients are being fitted with biomedical implants, there is a constant drive towards improving their performance in an attempt to reduce the instances of premature failure. A more detailed look at the biomedical aspects of this material can be found in **Appendix A**.

Many authors have published work regarding the effects of processing of the material on the microstructure, or on the effects of processing on the properties, but often the relationships between the processing, consequent microstructure, and resultant properties are not clearly related. Therefore, the ultimate goal of this project was to evaluate the effect of nitrogen on the mechanical properties of the Co-Cr-Mo alloy through an evaluation of effects of the processing steps on the properties of Co-Cr-Mo, but from a microstructural perspective.

There are two different approaches typically used to shape the components of a total joint replacement; these are forging and casting (usually investment casting). As stated in the ASM Metals Handbook [6], "The cobalt-chromium alloys are used for surgical implants in both the cast and wrought forms, which are typified, respectively, by Haynes Stellite 21 (H.S. 21), . . . and Stellite-25 . . . ". In a previous chapter, the ASM Metals Handbook [3] also pointed out that biomedical Co-Cr-Mo alloys are specified in a cast version (ASTM F75 [7]), *and* a wrought version (ASTM F799 [8]).

The most significant differences between the two processing methods are that forging generally results in better mechanical properties, but investment casting is less expensive. For example, Devine and Wulff [9] found that the measured tensile and fatigue strengths of wrought and heat treated cobalt-chromium-molybdenum-carbon alloys such as H.S.21 were more than twice those of cast alloys of the same composition. This difference between forging and casting is generally attributed to the greater chemical and structural homogeneity, as well as to the finer grain size and distribution of secondary phases of the forged product. The same study found that the crevice corrosion resistance of forged material in isotonic salt solution was also greater than that of the cast counterpart.

The ASM Metals Handbook [3] comments that *thermomechanical treating* and annealing of the *cast* material will result in improvement of the mechanical properties. It also states that "Higher-strength, fine-grain, cobalt-chromium-molybdenum devices have been made by *forging of nitrogen-strengthened bar stock*."

Other methods of strengthening the prosthetics have led to using powder metallurgy to reduce grain size. Luckey et. al. [10] found that the Co-Cr-Mo alloy properties could be improved by hot isostatically pressing Co-Cr-Mo powders to achieve a grain size that was significantly smaller than that of the investment cast version.

Wang, Gustavson, and Dumbleton report [11] that a dispersion strengthened Vitallium alloy made by gas atomization exhibited excellent room temperature fatigue strength (621MPa (90ksi) at 10^7 cycles). However, the process required alloy powder with a small amount of dispersed oxides and nitrides to first be produced by a carefully controlled gas atomization process. The atomized powder was then consolidated by extrusion. The extruded bar was further hot rolled, swaged and forged into implants, and then sintered at 1300°C (2370°F).

As summarized in the previous paragraphs, many processing options are available to enhance the properties of the Co-Cr-Mo alloy, with a variety of effects on the microstructure and on the properties. This project chose to apply solutionization and aging heat treatments to conventional and fine-grained cast versions of the non-nitrogen material to look at the second phase and grain size effects on the properties. Nitrogen alloying was done by the nitrogen-high pressure melting process, and then those materials were subsequently hot-rolled and subjected to solutionization treatments. By considering the nitrogen alloyed materials together with the investment cast materials, the microstructures were correlated with the properties to determine the effects of nitrogen alloying.

2. BACKGROUND

2.1 Metallurgy of the Co-Cr-Mo system

As a group, the cobalt-based alloys may be generally described as wear resistant, corrosion resistant, and strong, even at high temperatures. Many of the properties of the alloys arise from the basic nature of cobalt, the solid-solution-strengthening effects of chromium and molybdenum, as well as interstitial carbon, and the formation of second phase particles [12]. Thus, these topics will each be taken up in turn.

2.1.1 Elemental Cobalt Considerations:

Cobalt is a tough silver-gray magnetic metal that resembles iron and nickel in appearance and in some properties. Elemental cobalt is intriguing in itself because it is a metallically bonded substance, with high ductility, and undergoes a martensitic crystallographic phase change, as well as formation of stacking faults, and twins.

Cobalt exists in two phases. It maintains a Mg-type [13] hexagonal close-packed (HCP) structure from room temperature up to the allotropic transformation temperature of about 400°C (750°F) [14], and exhibits a Cu-type [13] face-centered cubic (FCC) structure up to its melting point of 1493°C (2719°F) [15]. However, mixtures of the two can generally coexist at room temperature [16]. Additionally, the FCC structure can be entirely retained at room temperature [16]. The lattice parameter of the HCP is 2.5071Å in the **a** and **b** directions, and 4.0695Å in the **c** direction, and that of the FCC is 3.537Å [13].

The HCP form of Co is stacked along the [0001] direction as two different plane types, commonly known as **A** and **B**, in the sequence **ABAB**. Three atom planes exist in the FCC cobalt. They are stacked in an **ABCABC** sequence along the <111> direction. If a stacking fault forms on every other plane of the FCC structure, the HCP crystal structure is obtained. It is well known that this is one mechanism whereby the cobalt phase transformation occurs [17].

Plastic deformation of a crystal lattice occurs by the movement of dislocations through the crystal structure in two ways: by *slipping*, or by *displacing*. The cobalt structure can experience slip in both types of crystals, and undergoes displacement by twinning, or by a martensitic shear transformation from FCC to HCP. Slip is addressed first, beginning with a description of the preferred slip systems.

Deformation by Slip:

Twelve slip systems are present in cobalt's FCC structure. The slip is generally in the <110> directions on the close-packed {111} octahedral planes. In HCP systems, the basal (0001) planes are identical to the (111) planes of the FCC systems, and are also the close-packed planes. This slip plane would support slip in the <1120> directions. However, whether or not glide occurs preferentially along the basal plane has been shown [18] to be related to the **c/a** ratio of the cell. For elements demonstrating high **c/a** (1.886, 1.856), the basal plane was preferred, but for low **c/a** (1.586, 1.590) this was not the case. Cobalt has a **c/a** ratio of 1.623, which lies between the ranges. Magnesium has a **c/a** of 1.624 and has been shown to prefer the basal plane, but that may not be the case for hexagonal cobalt. The next HCP slip system that has been shown to support preferred slip is the {1010} prism planes in the <1120> close-packed directions. Thus, in the HCP cobalt lattice slip will occur in one of these two systems. Considering this fact, even assuming that both slip systems have equal chance of being used (allowing cross-slip), the HCP Co still has less opportunity for deformation than the FCC cobalt that has 12 possible slip systems.

Stacking Faults:

Since cobalt has a low stacking fault energy (SFE), it can have quite a large spacing between the partial dislocations, leading to stacking faults that are on the order of 12 atom spacings [18]. Decreases in SFE result in wider partial dislocation separation, more planar dislocation structures, and reduced cross-slip.[19]. The stacking fault width is inversely proportional to SFE and the stress for nucleation of deformation twins proportional to SFE. Thus, a lower SFE would increase the tendency for both features. [20].

Alloying additions to cobalt markedly affect its stacking fault energy. The effect of alloying additions can often be predicted by examination of their effect on the temperature of the HCP-to-FCC phase transformation in pure Co. For example, Ni and

Fe are very important because, although they do not have a very potent effect on the basis of each percentage added, their solubility in Co is quite high, so that the overall effect is significant. On the other hand, Nb has a potent effect, but the solubility is low so that little can be dissolved in the FCC matrix, and hence this effect cannot be fully utilized. The BCC elements, such as Mo and W, lower the stacking fault energy, favoring extensive separation of the partial dislocations. Adding Ni or Fe stabilizes the FCC structure, and decreases the separation between partial dislocations [21].

Zhuang and Langer [22] showed that adding Ni to a Co-Cr-Mo alloy dramatically increased its fatigue properties. They concluded that this was due to an increase in stacking fault energy provided by the Ni. Similarly, interstitial carbon has been shown to stabilize the FCC matrix [23], which would suggest a similar increase in SFE. However, the effects of interstitial nitrogen on the SFE is not known.

Twinning:

Deformation or mechanical twinning is a mode of plastic deformation. For cobalt, a twin increases the length of the HCP crystal in a direction parallel to the basal plane, thus allowing it to keep up with the displacement of the FCC grains as the material is further loaded. Twinning is important in hexagonal metals and in metals of low symmetry, but in FCC metals the critical resolved shear stress for *slip* is normally *smaller* than that to twin. As a result, a FCC metal usually begins its deformation by slip. The work hardening resulting from this slip deformation increases the flow stress, and only after the latter reaches the twinning stress does twinning begin. In the low stacking fault energy FCC alloys where the dissociation of the dislocations into widely extended partial dislocations should have a strong effect on work hardening, twinning is significant. In the low stacking fault energy FCC metals, such as cobalt, it is possible to consider deformation twinning and slip as competitive forms of plastic deformation [18].

Martensitic Transformation:

The difference between martensitic reactions and twinning lies in the fact that, although they are both displacive deformations, the martensitic deformation leads to a change in crystal structure.

Elemental cobalt martensitically, reversibly, transforms from high temperature FCC to low temperature HCP. Reported transformation temperatures range from 429 to 450°C (804-842°F) on heating, A_s, and from 398 to 419°C (748-786°F)on cooling, M_s

[14]. For pure cobalt, the amount of martensitic HCP that forms is independent of the quench rate, but does depend upon the grain size, thermal and mechanical history and impurities [14]. The dependence on grain size is displayed by the fact that heat treatment at 475 to 550°C (887-1022°F) suppresses the transition to HCP on quenching, but after treatment at 600°C (1110°F) *some* transformation takes place on quenching. After treatment at a high temperature it is not possible to suppress the transformation by quenching. The cubic Co can also undergo a complete strain-induced transformation to hexagonal Co by cold working at room temperatures [16].

There are two types of martensitic transformations, athermal and isothermal transformation. Whereas isothermal holding between M_s and M_f normally halts the reaction and impedes further transformation, Ray and Smith [14] observed a continued isothermal transformation when holding for one hour at temperatures between M_s and M_f.

Robertson [23] has looked closely at the effect that carbon plays on the martensitic transformation in cobalt alloys near the F75 composition.

In his work, Robertson showed that for a solutionized F75 alloy with ~0.02 wt% carbon, the amount of HCP formed after 1 hour at 600°C was around 15 to 20%, but that at 900°C it approached 100%. For F75 with <0.01 wt% carbon a similar but more pronounced trend was observed, but for F75 with 0.25 wt% carbon, Robertson observed a dramatic reduction in HCP formation, with 1 hour at 900°C only leading to about 20% transformation. This reduction in the quantity of transformation was attributed to the FCC stabilizing effect of carbon in the matrix.[23]

Plastic deformation of the as-cast Co-Cr-Mo alloy at room temperature has been shown to result in partial transformation of the FCC matrix into the thermodynamically stable HCP phase. X-ray examination by Robertson on samples deformed in compression found that the volume fraction of the HCP phase increased rapidly with the amount of deformation, indicating that the strain induced FCC to HCP transformation also occurs readily in *alloyed* cobalt, even at room temperature [23].

2.1.2 Solid Solution Strengthening

When homogeneous mixtures of two or more kinds of atoms occur in the solid state, they are known as solid solutions. They can be one of two distinct types: a *substitutional* solid solution in which solute atoms enter the crystal to take positions normally occupied by solvent atoms, or an *interstitial* solid solution where solute atoms enter interstices *between* the solvent atoms. Extensive interstitial solid solutions occur only if the solute atom has an apparent diameter smaller than 0.59 that of the solvent, so important interstitial solute atoms are carbon, nitrogen, oxygen, and hydrogen. Four basic factors influence the extent of ***substitutional*** solution formation: 1.) the diameters of the elements should differ by less than 15 percent to reduce internal strains, 2.) the relative positions of the two elements in the electromotive series should be close to encourage metallic (over ionic) bonding, 3.) the pure metals should have the same valence, and 4.) they should crystallize in the same lattice form [18].

Solute atoms strain the matrix. For substitutional atoms, if the solute atom is larger than the solvent, then the lattice expands around it, and if the solute atom is smaller, the lattice contracts. In the case of interstitial atoms, the solute atom is larger than the space it is positioned in, pushing apart the solvent atoms. Thus, the free energy of the crystal is reduced if solute atoms and dislocations are able to counteract one another's' stress field (produced by the lattice strain) [18].

Source [21] examined the relationship of the difference in atom size between Co and solute atoms, and the maximum solubility, to obtain an indication of the magnitude of the solid solution strengthening effect to be expected. That text indicates that Cr, W, Ta, Nb and Mo are potentially effective. Consideration of their solubility in the ternary alloys of 30% Cr, suggest that W and Mo are the most effective, demonstrating one reason why Mo and Cr are alloying elements of F75.

2.1.3 Second Phase Materials

Carbides:

In his thesis, Kilner states that "the carbides found in the cobalt alloys are the most important second phase compound from the standpoint of their overall effect upon the physical properties of the alloys, and the frequency with which they are found in the alloys". [24]

In cobalt-base alloys, a number of different carbides can form, depending sensitively upon the chemical composition of the alloys. Because of the high Cr content of cobalt alloys, M_7C_3 and M_3C_2 are seldom found, or if present, will decompose upon heating. The element Cr favors the formation of $M_{23}C_6$ type carbides. The exact composition of the $M_{23}C_6$ carbide depends upon the specific alloy [21], but for F75 the M is typically Cr rich, with other metallic species (such as Mo) substituting for chromium to a limited extent [24]. The addition of Zr, Ti, Nb, and Ta would favor the formation of M_7C_3 and MC (such as TaC) type carbides. Elemental Co forms no carbides, but examination of the Co-Cr-C phase diagram shows that $M_{23}C_6$ will be the stable carbide for the carbon and Cr contents usually encountered in Co-base alloys (e.g., 0.2-1.0% C, 10-30% Cr) [21].

Taking each carbide in turn, the MC carbide is an FCC carbide found mainly in the newer cobalt alloys, and is one of the major strengtheners in these alloys. The strong carbide formers such as Ta, Nb, Zr, and Ti tend to form the MC carbides, at temperatures close to the melting point of the alloys. This type of carbide is extremely stable, especially in the cobalt alloys, and has been found to undergo degeneration to other carbides such as $M_{23}C_6$ only to a very limited extent [24].

The M_6C carbides, or $\boldsymbol{\varepsilon}$ carbides, actually include a wide range of similar carbides with formulae ranging from M_3C to $M_{12}C$. They are again cubic in crystal structure, with lattice parameters in the range 10.89Å to 11.244Å in Mo-Co-C alloys. This type of carbide has a tendency to form in alloys which contain appreciable amounts of Mo and/or W. The M_6C carbides are the second most stable class of carbide found in superalloys. Clemow and Daniell report [25] that in a Co-Cr-Mo alloy solution treated at 1165°C (2130°F) for 64 hours, the $M_{23}C_6$ carbides partially transformed to M_6C by substitution of carbon for molybdenum. From a crystallographic point of view, the M_6C carbide has a close similarity in position of the metal atoms to the intermetallic $\boldsymbol{\mu}$ phase, and the two can coexist [24].

M_7C_3 is a chromium rich carbide which forms at low Cr:C ratios, but it has a tendency to decompose to $M_{23}C_6$ upon aging. It has a complex hexagonal structure, with a=13.9Å and c=4.5Å. It can also incorporate other metallic species such as Fe into the structure, but with little change in lattice parameters. Much interest has centered upon this carbide in recent years as a constituent of directionally solidified Co-Cr-C pseudo-binary alloys, in which the carbide phase is present as elongated fibers [24].

$M_{23}C_6$ is the dominant carbide in alloys with more than 5% chromium, including F75. As such, it will be considered in greater detail than the previous carbides. The presence of this carbide can be due to several reasons. It can be present as a constituent of a eutectic in cast alloys, it can result from the decomposition of other carbides such as M_7C_3 or MC, and it precipitates profusely in the matrix of cobalt alloys at temperatures in the range 650 to 1100°C (1200-2010°F). Kilner et. al. [26] state that heat treatment of the F75 alloy near 1235°C (2255°F) results in $M_{23}C_6$ becoming the only interdendritic phase, refuting Clemow and Daniell's statement that M_6C forms at this temperature. $M_{23}C_6$ shows a relationship to the intermetallic $\boldsymbol{\sigma}$ phase analogous to that between M_6C and $\boldsymbol{\mu}$ phase, and the two phases are commonly found together [24]. The form of $M_{23}C_6$ precipitation is important; it can precipitate as films, globules, platelets, lamellae, and cells. However, it usually forms at grain boundaries [27]. In the Co-Cr-Mo alloy, the $M_{23}C_6$ generally takes on the form $Cr_{23}C_6$.

Carbide structures are fixed mainly by the small size of the carbon atom, which can readily fit into interstitial positions. Consequently, most of the transition metal carbides like $Cr_{23}C_6$ tend to have close-packed metal atoms with carbon atoms in the interstices. The metal-carbon bonding in this structure is intermediate between covalent and metallic [28]. The covalent portion of this bonding leads to the high bond energy between the atoms, and thus its brittle, hard nature. This carbide exerts a beneficial effect upon the strength of cobalt alloys, but as reported by the ASM handbook [12], it can produce deleterious effects on the ductility of the alloy up to 870°C (1600°F) if allowed to precipitate in an uncontrolled fashion in service.

Intermetallic Compounds:

Consideration must be given to the possibility of the formation of the topologically close-packed (TCP) phases such as σ and Laves in the cobalt alloys. The presence of phases such as σ are predicted from the appropriate phase diagrams, such as that of the Co-Cr-Ni and Co-Cr-Mo systems [21].

The occurrence of TCP phases is predicted by first correcting the alloy composition for the presence of carbides, and then the remaining composition is used to calculate the electron hole number, N_v. One source indicates that the critical value of N_v for Co alloys is about 2.7, above which TCP phases will be prone to form. As a comparison, the N_v for Ni alloys is about 2.5 [21].

The TCP type of intermetallic compounds are generally considered to be deleterious when present in the microstructure, although attempts have been made to exploit them as strengtheners [24]. Besides the σ phase already mentioned, this class of compounds includes μ, R, π, and Laves phases. Their effect upon the properties of the alloys can be considered two fold: they precipitate in a plate like morphology which can initiate cracks by decohesion with the matrix, and by their formation they remove important amounts of alloying elements from their role in the matrix composition. According to Kilner [24], in cobalt alloys these elements have been observed to precipitate in both plate-like, and blocky forms.

Sigma phase (σ) is a very common intermetallic compound among the transition metals, and occurs in stainless steels and nickel base superalloys as well as in cobalt alloys. It appears as irregularly shaped globules, often elongated, and forms after extended exposure between 540 and 980°C (1000-1800°F) [27], and is structurally similar to the $M_{23}C_6$ carbide. The σ phase is often observed to nucleate on $M_{23}C_6$ particles, and it has been observed that decarburization of σ prone structures can lead to formation of σ on $M_{23}C_6$ sites. The σ phase is found in systems involving the transition elements, and appears to be stabilized in some cases by the presence of Si. With Al additions in the Co-Cr system, a de-stabilizing effect is seen [24].

The binary mu (μ) phases in the cobalt alloy systems are Co_7W_6 and Co_7Mo_6. Additionally, in the ternary Co-Mo-Cr system μ phase is present as a ternary compound. The phase actually exists over a range of compositions centered close to the stoichiometric formula, such as Co_7W_6, $(Fe,Co)_7(Mo,W)_6$ [27]. It is not as great a concern as σ phase in most cobalt alloy compositions, because the W or Mo contents are generally low enough to prevent its formation. The existence of μ is limited in the ternary Co-Mo-Cr system to compositions in excess of 80 wt% Mo at 1200°C (2190°F). Generally observed in alloys with high levels of Mo or W, it appears as coarse, irregular Widmanstatten platelets, forming at high temperatures [27].

R phase is classified as a ternary intermetallic compound in that it exists only in ternary alloys, and nowhere touches the bounding binaries. It exists in both the Co-Cr-Mo and Co-Cr-W systems. R is a complex hexagonal phase with a typical composition of 43 wt% Co, 41 wt% Mo, and 16 wt% Cr [24].

Laves phase includes a large group of intermetallic compounds of the general formula AB_2. It usually appears as irregularly shaped globules, often elongated, or as platelets after extended high-temperature exposure [27]. The existence of the Laves phase correlates with the ratio of the diameters of the atomic species, with $D_a/D_b=1.225$. It is most common in Fe-base and Co-base superalloys [27]; however, Si can stabilize Laves in systems that would not otherwise contain this phase, including in the Co-W and Co-Mo systems [24].

As alluded to in the above descriptions, the metallurgy of Co-Cr-Mo is very dependent upon the temperature and composition of the alloy. Besides the binary equilibrium phase diagrams found in reference [29] and the 1200°C (2190°F) isothermal ternary found in the paper by S. Rideout et. al. [30], there are various experimentally determined quasiternary and pseudo ternary diagrams which target alloys similar to F75. Kilner shows a quasiternary diagram of Co-Cr+Mo-C at 1200°C (2190°F) in his thesis [24]. The pseudo-ternaries by Clemow and Daniell [25] for Co-Cr+5%Mo-C show that for a composition near that of F75, as the temperature is increased, a region of liquid in the phase diagram begins to develop at high (>3%) carbon contents. This is considered the source of *incipient melting* in the Co-Cr-Mo alloy system, as observed by many authors.

2.1.4 Incipient Melting

When Co-Cr-Mo alloys are held at extremely high temperatures, especially in the 1300°C (2370°F) regime at which the sintering of porous coatings occurs [31], star-shaped second phase particles form upon quenching. These have been speculated [25] and later proved [24] to be due to incipient melting. Incipient melting is the term given to localized melting of constituents at a temperature below the expected melting point of the material.

In the F75 alloy, incipient melting was observed at the grain-boundaries and in the interdendritic material [25]. According to Kilner [24], the interdendritic material in as-cast F75 appears to be a residual quaternary near-eutectic which can be related to the existing Co-Cr-C phase diagram. In this alloy it appears to consist of a mixture of $M_{23}C_6$, M_7C_3, σ phase, and an FCC Co-rich phase [26]. To be produced, large quantities of Mo would have to segregate. Devine and Wulff reported microprobe scan results on cast H.S.21, after annealing at 1200°C (2190°F) for 4 hours, showing regions of segregation up to 20wt% (10at%) Mo and 35wt% Cr [9]. The interdendritic material is relatively stable in composition and extent when heat treatment takes place at temperatures above the eutectic melting temperature. Consequently it may establish a local equilibrium with the Co matrix. According to Kilner, the characteristic serrations which appear at the higher temperatures and higher quench rates are a solidification phenomenon, namely the formation of a cellular interface between liquid and solid [24]. Incipient melting and subsequent resolidification of this near-eutectic mixture accounts for observations of this behavior above 1235°C (2255°F) [26]. The exact incipient melting temperature in Co-Cr-Mo alloys is not known.

The reason that an exact incipient melting temperature (IMT) isn't available for Co-Cr-Mo alloys is that the IMT is dependent upon the carbon content. As introduced above, this is demonstrated in the pseudoternary phase diagrams constructed by Clemow and Daniell. These diagrams show that with increasing carbon wt%, the Co-Cr-Mo composition moves towards the liquid field. Thus, with more carbon, there is more opportunity for the formation of the quaternary eutectic composition that begins to melt at lower temperatures.

As Hassan Farhangi points out in his thesis [32], incipient melting is a concern because it can significantly affect the properties of porous coated implant materials. To attain good porous surface bonding, the sintering operation is carried out at 1300°C (2370 °F), close to the melting point of the implant, for periods of 1 to 3 hours. This sintering temperature is well in excess of the melting point of the interdendritic eutectic mixture in the as-cast microstructure. Hassan found that this results in the incipient melting of the interdendritic precipitates and penetration of the liquid phase into not only the grain boundaries, but also the bead-substrate and the bead-bead neck regions. Upon subsequent cooling to room temperature, the liquid phase solidifies and long grain boundary networks form. The result of the presence of this phase is that corrosion fatigue cracks initiate at sites of incipiently melted regions, adjacent to the top of bead-substrate interface regions, which is undesirable.

The metallurgy of Co-Cr-Mo is very important to its performance in total joint components. Also significant is the processing of the material, and how the alloy responds to the different processes. These processes not only include the aforementioned HIPing and porous coating, but perhaps of greater significance, the fabricating and heat treating. For that reason, each of these processes will be examined more closely in the following section.

2.2 Processing of the Co-Cr-Mo Material

Several different processing techniques were summarized in the Introduction. However, implants are typically investment cast, and then possibly subjected to one or more post-casting processes that could include hot isostatic pressing (HIPing), porous bead coating, and heat treatment. Alternatively, the implants are also commonly fabricated through hot forging. Each of these processes has significant effects on the microstructure of the Co-Cr-Mo alloy.

2.2.1 Casting Solidification

Many of the structural features that ultimately control product properties are set during solidification. This includes solute distribution, dendrite formation, micro-segregation, and interdendritic carbides. Additionally, many casting defects, such as gas porosity and shrinkage are solidification phenomena [33].

On a macro scale, most metals solidify as a gradual thickening envelope of solid metal. There are relative rates of freezing at internal and external angles and on plain surfaces, and directional solidification toward the heavier section. Dendritic freezing is generally observed, with refinement dependent upon the temperature of the metal and the cooling rate [34]. The cast structure may have as many as three distinct zones. Each of these regions can exhibit different chemistry, with the outer edge being almost pure solvent, and the center being high in solute atoms. Solidification occurs on a micro scale in two stages: nucleation, and growth, and it is important to control both of these processes.

Nucleation occurs when a stable solid particle forms from within the molten liquid, and can be either homogeneous or heterogeneous. Homogeneous nucleation is very difficult to obtain because it requires high cleanliness in the liquid to prevent heterogeneous nucleation, as well as a large degree of supercooling to provide the necessary driving force to form an entirely new, spherical surface at the solid/liquid interface. Heterogeneous nucleation occurs on existing surfaces, such as the mold wall or solid impurity particles, requiring less surface energy and thus less supercooling for its formation. The more nucleation events during solidification, the finer the resulting grain-structure will be.

Growth occurs as the heat of fusion is continually extracted from the liquid material. The direction, rate, and type of growth can be controlled by the way in which heat is extracted, and can produce substantial variation in the resulting structure and properties. Directional growth, in which the solidification interface sweeps continuously through the material in a confined direction, can be used to ensure the production of a sound casting [33]. Faster rates of cooling generally produce products with finer grain size and superior mechanical properties; for example, the rapid cooling in metal-die-casting generally produces higher-strength products than that of sand casting. Various types of sands can also produce different cooling rates, and sands with a high moisture content extract heat faster than sands with a low moisture content.

Co-Cr-Mo alloys, like most other alloys, exhibit dendritic growth. One common result of the dendritic growth in an alloy is that due to the non-uniform solute distribution, microsegregation, or coring, can occur. The original dendrite arms freeze as relatively pure metal, so the liquid surrounding these arms is, accordingly, enriched in solutes [18]. Besides the segregation of intentionally added solute atoms, the liquids that are frozen to form industrial alloys may contain impurity elements from the ores from which the basic metals were obtained, from the refractory brick linings of furnaces used in melting or refining, and from the gases in the furnace atmospheres. These can react to form compounds (oxides, silicates, sulfides, etc.) [18].

Another effect that can occur in a dendritically solidified alloy, is that dendrite arms can fragment at the junction between a branch and its stem and then be transported to the interior bulk liquid where they may survive and grow into equiaxed crystals. This fragmentation can occur through re-melting of the dendrite stem, or through fracture due to mold vibration, mold rotation, and electromagnetic or mechanical stirring [35]. If controlled, this is another method whereby finer grains can be achieved in a casting.

Traditional Co-Cr-Mo Solidification:

The typical as-cast microstructure of Co-Cr-Mo consists of large grains with extensive dendritic coring, with interdendritic and grain boundary carbides, as well as casting porosity [32]. In the F75 alloys, the interdendritic material has been identified as a mixture of a cobalt rich FCC phase, σ phase, M_7C_3, and $M_{23}C_6$ carbides with a near eutectic composition [24]. Clemow and Daniell [25] reported that Cr is the primary segregating element over Mo, with 19% Cr existing in the dendrites and 35% in the interdendritic region. Mo was found to be 4% in the dendrites and 6% in the interdendritic region. However, Zhuang and Langer [36] measured about 9 wt% Mo in the dendrites and 4.5 wt% in the interdendritic regions, and for Cr 32 wt% in the dendrites and 27 wt% in the interdendritic regions. Robertson [23] found that carbides form close to, and along the grain boundaries in addition to the interdendritic carbide islands, resulting in a microstructure consisting of approximately 12% to 15% carbides in the continuous Co-rich matrix. Zhuang and Langer [36] state that the outer layer microstructure of an F75 casting displays the directional growth of dendrites, and an inhomogeneous distribution of interdendritic carbide precipitates. A more coarse dendrite structure with random growth directions and a more homogeneous distribution of carbides is present in the center part of the casting.

Fine-grained Co-Cr-Mo Solidification:

The above microstructure is for a traditional air cooled sand mold casting. Zhuang and Langer [36] used a metallic water cooled mold to obtain a fast cooling rate. The result was a microstructure of equiaxed grains with the carbides forming a continuous network along the grain boundaries. The grain size of the center part of the casting was larger than in the outer region, and a thin layer of directionally grown dendrites were at the surface of the casting. They made the following comparisons between a rapid cooled and a slow cooled F75 microstructure: (a) slow cooled grain size (in grains/mm) is 2.6 and fast cooled is 16.0, (b) in slowly cooled, most of the carbides are precipitated in the interdendritic regions and an inhomogeneous distribution of interdendritic carbides is observed; almost no grain boundary carbides are observed; in the fast cooled castings, most of the carbides are precipitated at grain boundaries, (c) in the slowly cooled cast alloy the principle elements exhibit segregation because of the presence of coarse dendritic structure; in fast-cooled cast alloy the element segregation in the equiaxed grains is not observed. The results reported by Zhuang and Langer show a YS of 523 and 578MPa (76 and 84ksi) for slow and fast cooled respectively, and an UTS of 739 and 954MPa (107 and 138ksi), respectively.

The above discussions demonstrate the importance of taking into consideration the casting process variables and solidification kinetics. They also show how the F75 alloy and its properties are affected by these variables. As mentioned, casting of the prosthetic is only the beginning. There are several post-casting operations which can have a marked effect on the microstructure and properties of the product. These include HIPing, porous bead coating, and most importantly, heat treating.

2.2.2 Hot Isostatic Pressing

Hot isostatic pressing (HIPing) is often used to close up the microporosity resulting from microshrinkage or gas porosity in Co-Cr-Mo alloys. In the HIPing process the alloy is heated at a temperature near or above the solution temperature of the alloy while undergoing isostatic compression on the order of 100-170 MPa (15-25 ksi) [37]. The temperature used leads to partial solutionization of the interdendritic and grain boundary carbides. However, traditional HIPing equipment has required a slow cool after the process before the parts can be recovered. In the F75 alloy, this leads to a heavy precipitation of carbides at the grain boundaries. This can lead to higher strength, but lower ductility, and is a condition which usually requires subsequent heat treatment to rectify [38]. In their early study, Hodge and Lee found that HIPing of a Stellite 21 alloy at 1230°C (2250°F) and 10 MPa (15ksi) may have increased the YS and the UTS by 14 MPa (2 ksi), but reduced the ductility by 3 %. However, Vander Sande et. al. [37] noted in a later study that HIPing a cast H.S. 21 alloy at 1200°C (2190°F) and 10 MPa (15ksi) for 4 hours resulted in slightly less average YS but slightly increased average UTS and ductility. They did not specify the cooling rate however.

2.2.3 High Temperature Sintering

The porous sintered-bead coating process is a recent development that is intended to facilitate bone ingrowth. The process of sintering beads to a substrate necessitates thermal exposures at about 1300°C (2370°F), which is well above the carbide eutectic temperature [31]. As described next, this temperature can cause regions of solute segregation to begin to melt, and, according to Farhangi [32], the vacancy migration and segregation associated with this temperature leads to the nucleation of pores in the matrix, and a consequent reduction in properties.

Kilner [24] found that the high temperature used in the porous bead coating leads to incipient melting at the grain boundaries if the carbon content in the base metal is above about 0.17 wt%. If the part is then rapidly quenched, the material is retained and leads to a severe reduction in static mechanical properties of the part. The material *can* be slightly diffused if the part is cooled at a rate in the range of 2°C/minute (3.6° F/minute) down to about 1220°C (2230°F), and then quenched.

Farhangi [32] observed that fatigue crack initiation occurs at the sintered-bead-substrate interface regions in both saline and air environments. In saline solution, corrosion fatigue cracks initiated at sites of microporosity or incipiently melted regions adjacent to the top of bead-substrate interface regions. Slip band fatigue cracks, initiated in air, were also found to originate near the root of the coating-substrate interface regions.

To alleviate the problems associated with porous coating F75, Georgette and Davidson [39] HIPed as-porous coated structures. They found that the HIPing of sintered materials improved both fatigue and tensile properties relative to the "as sintered" condition. However, the fatigue strength was still slightly lower than that of the "as-cast" condition.

2.2.4 Heat Treating

Heat treating Co-Cr-Mo greatly affects the carbide dispersion, distribution of solute atoms, and the martensite reaction. Traditional heat treatments include two major processes: solutionization, and subsequent aging. Both the precipitation of second phases and the transformation of martensite plates are nucleation and growth processes, but the solutionization of the carbides and other phases is primarily a diffusion process. The initial step in most heat treatments is homogenization and solutionization, and is taken up first.

Homogenization and Solutionization Treatment:

Background:

In homogenization a suitable alloy is heated to a temperature at which diffusion takes place, to even out solute concentration gradients existing as solidification artifacts (such as dendrites). In solutionization, an alloy is heated to a temperature at which a second phase (usually present in small quantities) dissolves in the more abundant phase. The metal is held at this temperature until an acceptably homogeneous solid solution is attained, and then it is quenched to a lower temperature to create a supersaturated condition [18]. The time required to achieve a homogeneous solution is dependent upon the rates of diffusion of the components, but homogenization generally occurs more readily than full solutionization. Fleming [34] states that solution temperature, time, and segregate spacing (dendrite arm spacing) are important variables determining the effectiveness of a solution treatment. These factors are all related to the diffusion of the atoms in the alloy.

There are two basic types of diffusion: substitutional diffusion, and interstitial diffusion. Through the years, a number of mechanisms have been proposed to explain the movement of substitutional atoms in a crystal lattice, involving either the motion of a single atom at a time, or the cooperative movement of two of more atoms. As examples of the former, we have diffusion by the vacancy. The vacancy mechanism is generally conceded to be the correct mechanism for substitutional diffusion in FCC metals such as Co. Hexagonal metals are not as clearly defined, and it should be mentioned that, due to the asymmetry of the hexagonal lattice, the rate of diffusion is not the same in all directions through the lattice. Diffusion in the basal plane occurs at a different rate from diffusion in a direction perpendicular to the basal plane. If a vacancy mechanism is assumed for hexagonal metals, this implies that the jump rate of an atom into vacancies lying in the same basal plane as itself will differ from the rate at which it jumps into vacancies lying in the basal planes directly above or directly below it [18].

Interstitial diffusion is much simpler than substitutional diffusion in that the interstitial solute atoms merely jump from one interstitial site into a neighboring one. Because they are typically in dilute quantities, their movement is not contingent upon lattice vacancies, an so thus interstitial diffusion is generally several orders of magnitude faster than that of substitutional atoms.

The diffusion rate is primarily a function of the ability of the atoms to diffuse (the diffusivity), and of the concentration gradient of these atoms (Fick's first law). The concentration gradient is a function of composition and distance between populations (such as the dendrite arm spacing). For that reason, as the solutionizing time progresses, there is a gradual decrease in the rate of dissolution due to a reduction in the driving force (the gradient). The rate of diffusion is also an increasing function of temperature, which is why solutionization generally occurs at a high temperature.

However, atom movements in solids are not restricted to the interiors of crystals. It is a well-known fact that diffusion processes also occur on the surfaces of metallic specimens and along the boundaries between crystals. At very high temperatures, diffusion through the lattice tends to overpower the grain boundary component, but at low temperatures diffusion at the boundaries becomes more and more important in determining the total, or apparent, diffusivity [18].

Clemow and Daniell [25] report that the bulk diffusivity for solute elements in an F75 alloy at about 1200°C (2190°F) is $D_{bulk}=2.2\times10^{-10}$ cm^2/sec. Individually, the diffusivity of the substitutional atoms is $D_{Co}=2.2\times10^{-10}$ cm^2/sec, $D_{Cr}=2.5\times10^{-10}$ cm^2/sec, and $D_{Mo}=1.7\times10^{-10}$ cm^2/sec. The diffusivity of interstitial carbon is much more rapid, at $D_C=2.4\times10^{-7}$ cm^2/sec.

It was mentioned that vacancies are considered the primary mechanism for diffusion in alloys. One of the consequences of this is the resulting formation of porosity during solutionization. The Kirkendall effect demonstrates that the rate at which the two types of atoms of a binary solution diffuse is not the same. Thus, as a result of the vacancy current that accompanies the unequal mass flow in a diffusion couple, voids form. This formation of voids is influenced by several factors. It is generally believed that voids are heterogeneously nucleated on impurity particles. The tensile stress that exists in the region of the specimen where the voids form is also recognized as a contributing factor in the development of voids. If this tensile stress is counteracted by an isostatic compressive stress placed on the sample during the diffusion anneal, the voids can be prevented from forming [18]. This latter statement is in agreement with Fleming, but he also states [34] that homogenization results in some reduction of microporosity in most alloys, with the pores that remain tending to spheroidize and *ripen*.

Solutionization in Co-Cr-Mo:

Solutionization has long been the primary heat treatment applied to Co-Cr-Mo prosthetic components. Researchers have chosen a variety of temperatures and times for this heat treatment, and their results are summarized here.

In a historical background included in a paper by Clemow and Daniell [25], several solutionization parameters were reported. According to Clemow and Daniell, in 1955 J. W. Wheeton et. al. reported that holding a 0.29% C Co-Cr-Mo alloy at 1230°C (2245°F) for 72 hours resulted in complete carbide dissolution. In the same year as Wheeton et. al., F. J. Clauss et. al. observed that holding a 0.2-0.3% C Co-Cr-Mo alloy at 1230°C (2245°F) for 24 hours resulted in complete carbide dissolution, formation of porosity, and grain boundary melting. The same study by Clauss et. al. showed that holding for the same length of time, but at 1190°C (2175°F), led to complete or incomplete solutionization of the carbides, depending upon the carbon content. Then in 1969, S. Ahier reported in his Ph. D. thesis that complete carbide dissolution occurred in a 0.25% C Co-Cr-Mo alloy at 1250°C (2280°F) after 72 hours. However, S. Thorley claimed, in 1974, that holding Co-Cr-Mo alloys with 0.30-0.35% C for 4 hours at temperatures from 1240 to 1280°C (2265 to 2335°F) resulted in incomplete carbide dissolution, plus melting and porosity formation. The same study reportedly stated that holding at 1220°C (2230°F) for 4 hours resulted in incomplete solutionization of carbides, and formation of porosity. Lastly, in 1976, Wulff et. al. reported that holding a 0.3% C Co-Cr-Mo alloy at 1230°C (2245°F) for only 4 hours led to complete dissolution, but incomplete dissolution of the carbides resulted after holding at 1180°C (2155°F) for the same length of time. It is important to note that in all of the above studies, 1.8 to 3.75% Ni was present in the alloys. The alloy used by Clause also had 2.0% Fe, and Wheeton's alloy had 0.7% B. Otherwise, the alloys were similar to the F75 composition. These were all reported in the summary by Clemow and Daniell.

Clemow and Daniell [25] reported in 1979 that holding F75 alloys of 0.24-0.28% C for 1/4 hour at 1230°C (2245°F) resulted in $M_{23}C_6$ transforming to M_6C. Holding at 1210°C (2210°F) for 0 to 1 hour dissolved the $M_{23}C_6$, leaving the more stable M_6C to dissolve later. Full dissolution at 1210°C (2210°F) was reported after holding for 64 hours. When alloys of the same group were held at 1165°C (2130°F) for 64 hours, $M_{23}C_6$ transformed to M_6C, but no dissolution took place. In fact, further precipitation was reported around existing carbides. The mechanism theorized for the transformation of the $M_{23}C_6$ to M_6C was the substitution of carbon by the strong carbide forming element Mo. In cases in which the samples were heated at 200-300°C/minute (390-570°F/minute) instead of 100°C/minute (212°F/minute), the $M_{23}C_6$ transformed to σ due to the rapid depletion of carbon atoms in the compound.

In 1982, Kilner et. al. [26] found that holding a 0.27% C F75 alloy for short times at under 1235°C (2255°F) resulted in $M_{23}C_6$ as the only interdendritic phase. Holding the alloy at this temperature for long times led to complete dissolution of the $M_{23}C_6$ phase.

He also rejected Clemow and Daniell's statement that, in this regime, the $M_{23}C_6$ first transformed to M_6C before dissolving.

David Levine [31] reported that holding a 0.3% C F75 alloy at 1065°C (1950°F) for 2 hours resulted in dissolution of particles at grain boundaries, but the formation of σ in carbon depleted zones. His work was reported in 1988.

Considering the above solutionization conditions together with the work by Levine demonstrates that, for F75 Co-Cr-Mo alloy, solutionization occurs with differing success roughly from >1065°C (1950°F), up to its incipient melting temperature. Kilner et. al. [26] reported that for F75 alloys of typical carbon content (0.27%), incipient melting begins at 1235±5°C (2255±9°F). Since the rate of dissolution increases with elevated temperature, it would be reasonable to solutionize Co-Cr-Mo at the highest temperature that is adequately below the incipient melting temperature.

Aging Treatment:

In the Co-Cr-Mo alloy, aging consists of precipitation of $M_{23}C_6$ in different morphologies, and in different regions of the microstructure. However, within the aging temperature range several other phenomena occur congruently with the carbide precipitation. Source [27] states that in cobalt based super alloys, σ forms at temperatures from about 540°C, up to 980°C (970 to 1760°F). At aging temperatures, the FCC cobalt matrix also transforms to HCP. Some authors claim that intragranular precipitation will only occur in HCP grains.

In 1976, J. B. Vander Sande, J. R. Coke, and J. Wulff [37] performed a TEM analysis of a heat treated 0.3% C H.S.21 Co-Cr-Mo alloy with 2.2% Ni. They found that aging at 650°C (1200°F) resulted in time dependent reactions. At 5 hours, a high density of FCC stacking faults was observed, along with a presence of HCP. After 20 hours, a small amount of precipitation of $M_{23}C_6$ was identified, and extremely dense stacking fault formation was observed. Finally, at 50 hours the microstructure consisted of 90% martensitic HCP, and profuse precipitation of $M_{23}C_6$. The precipitates were described as roughly hexagonal, plate-like structures aligned with the basal planes of the HCP regions.

Krishna Rajan [17] performed a similar analysis in 1982 for a 0.15% C, forged H.S.21 alloy which, following solutionization, was aged at 750°C (1380°F) for different lengths of time. After 2 hours, extensive stacking faults were observed in the FCC phase. Then, at 10 hours, heavily faulted HCP bands were identified with carbide nucleation within the HCP phase only. After 20 hours at this temperature, a second HCP phase (HCP_2), having a low fault density, was observed to be growing into both the first HCP phase, and the original FCC phase. Abundant carbide nucleation was also observed in this second HCP in both a blocky morphology, and a lamellae or fibrous type of cellular precipitation. At times greater than 20 hours, continued HCP_2 growth and coarsening of carbides was reported.

In his paper, Levine [31] stated that at 1065°C (1950°F), not only did particles at the grain boundary dissolve, but $M_{23}C_6$ precipitated within the grains.

In his doctoral thesis work, Steven R. Robertson [23] analyzed the effects of several different aging treatments done on F75 alloys with different C compositions. His very-low-carbon (VLC) alloy contained <0.01%C, his low-carbon (LC) alloy contained ~0.02%C, and his high-carbon (HC) alloy had 0.25%C. Precipitation in the VLC and LC alloys occurred in the HCP phase, and at the HCP/FCC interface. The precipitate shapes varied from cuboids to rods, with the growth direction believed to be $<1120>_{HCP}$ or $<110>_{FCC}$ with a habit plane of $(0001)_{HCP}$. Rod shaped precipitation was reported in the LC alloy, and appeared to nucleate at the HCP/FCC interface and grow perpendicularly into the HCP phase in a $<0002>_{HCP}$ direction. Precipitation in the HC alloy was found to occur in both FCC and HCP regions, with the particles typically taking on a rhombic morphology. Robertson theorized that the reason for the preferential carbide precipitation in the HCP phase lay in the greater solubility of Cr in the HCP phase than in the FCC phase, leading to a greater driving force for precipitation in this phase.

Robertson's work found that aging a solutionized VLC alloy at 900°C (1620°F) resulted in fine, profuse precipitation near residual interdendritic carbides, as well as some grain boundary carbide precipitation near similar residual carbides. Some of the fine precipitation was observed extending along specific directions into the grains themselves. Solutionized LC material that was subsequently aged at 700°C (1290°F) showed little response after 1 hour, but after 8 hours, Widmanstatten type plates were reported to extend in from the grain boundaries. An increase in the aging time at this temperature resulted in an increase in grain boundary precipitation. When a similar LC alloy was aged at 800°C (1470°F), 1 hour resulted in possible grain boundary precipitation, but 8 hours led to fine precipitation heterogeneously dispersed across the entire grain in parallel rows. Some Widmanstatten type plates occurring near the grain boundaries. An increase in temperature to 900°C (1620°F) resulted in profuse fine precipitation across entire grains after just one hour.

When Robertson aged a VLC alloy at 1000°C (1830°F) for an hour, the precipitates were coarse, and took on several morphologies. These included needle or rod shaped, spheroidized, and cuboid carbides. Together with the above paragraphs, this illustrates that the aging of Co-Cr-Mo depends greatly on the temperatures and lengths of time used, and that the possible morphologies of the carbides are wide-ranging and difficult to separate.

The most important feature of solutionizing and aging Co-Cr-Mo is the affect of the process on the mechanical properties of the alloy. Robertson found that the maximum precipitation occurred at 900°C (1620°F), but the maximum yield strength occurred at 800°C (1470°F). **Table 2-1** shows the mechanical properties resulting from the heat treat processes tried by different researchers. The results can be generalized by the statement that solutionizing of the interdendritic carbides brings down the yield strength, but increases the ductility of the alloy. Subsequent aging leads to the precipitation of carbides, which tend to increase the yield strength, but which reduce the ductility at a rapid rate. Researchers are often able to increase the strength dramatically by aging, but the material becomes too brittle to be acceptable.

2.2.5 Hot Working

The alternative method to casting biomedical implants, is hot-forging them. There have been several studies involving hot-working of Co-Cr-Mo alloys. Typically, the hot-forged alloys have a lower carbon content than the cast version, and often have increased Ni contents. These adjustments facilitate easier working of the alloy: the increased Ni to improve the ductility through an increased stacking fault energy, and the reduced carbon content to lower its interstitial hardening effect.

The most important considerations in hot-working of alloys are the temperature at which the working occurs, and the rate at which the material is deformed. **Table 2-2** summarizes various hot-working parameters for Co-Cr-Mo materials, as recorded in various studies. This data indicates that hot-working done by preheating at 1220°C (2230 °F), then hot-rolling at or below 1200°C (2190°F) is most desirable. The temperature of 900°C (1650°F) is reported to be the lower range of hot-workability. Although Carpenter Technology Corp. claims [44] that greater ductility during hot-working of their Co-Cr-Mo-N alloy can be obtained by not solutionizing first, J-P Immarigeon et. al. [45] found that pre-solutionization avoided carbide stringers and eliminated banding during forging. Immarigeon et. al. also found that pre-solutionizing and then reheating to a lower hot-working temperature could produce carbides that pinned the grain-boundaries after hot-working reduced the grain size.

Table 2-1: Mechanical properties of Co-Cr-Mo in various heat treated conditions

Condition	YS-MPa (ksi)	UTS-MPa (ksi)	%El.	%R.A.
1. As-cast HS21-various foundries[37]	430-690 (62-100)	660-900 (96-131)	4.5-11.3	-
2. Cast + 1230°C (2250°F)/1 hour [37]	450-690 (65-100)	690-1100 (100-160)	8-21	-
3. (2.) + 650°C (1200°F)/20hrs [37]	510-710 (74-103)	750-1150 (109-167)	8-17	-
4. Cast + HIP@1200°C (2190°F)/4hrs [37]	380-600 (55-87)	680-930 (99-135)	8-12	-
5. (4.) + heat treatment (3.) [37]	470-720 (68-104)	620-1100 (90-160)	12-16	
6. As-cast F75-Robertson [23]	379 (55)	765 (111)	7	5.5
7. (6.) + "solutionization" [23]	434 (63)	738 (107)	14	9.1
8. As-cast F75-Cox [40]	552 (80)	786 (114)	7.6	9.9
9. (8.) + 1230°C (2250°F)/72 hrs [40]	387 (56)	614 (89)	10.2	12.2
10. (9.) + 700°C (1290°F)/72 hrs [40]	540 (78)	664 (96)	3	3
11. As-cast 0.3%C F75 [31]	558 (81)	855 (124)	6	8
12. (11.) + solution anneal [31]	545 (79)	896 (126)	12	13
13. (11.) + Levine's Thermal Cycle A [31]	469 (68)	710 (103)	9	11
14. (11.) + Levine's Thermal Cycle B [31]	450 (71)	634 (92)	4	6
15. (11.) + Levine's Thermal Cycle C [31]	414 (60)	606 (88)	12	11
16. (11.) + Thermal Cycle C + Aging [31]	552 (80)	738 (107)	3	3
17. As-cast 0.24%C F75 [31]	503 (73)	827 (120)	8	10
18. (17.) + solution anneal [31]	517 (75)	862 (125)	15	14
19. (17.) + Levine's Thermal Cycle A [31]	427 (62)	724 (105)	14	15
20. (17.) + Levine's Thermal Cycle B [31]	359 (52)	614 (89)	16	13
21. (17.) + Levine's Thermal Cycle C [31]	400 (58)	641 (93)	13	15
22. (17.) + Thermal Cycle C + Aging [31]	427 (62)	524 (76)	2	3
23. As-cast Co-Cr-Mo [38]	547 (79)	650 (94)	5	7
24. (23.)+HIP+1230°C (2250°F)/2 hrs[38]	484 (70)	761 (110)	17	17

As noted earlier, hot-working generally results in improved mechanical properties all around. Hodge and Lee [38] list a YS and UTS of 614 MPa (89 ksi) and 1194MPa (173ksi) respectively for a wrought Stellite 21. The same alloy exhibited an elongation and reduction in area of 30% and 25% respectively. In the work of Vander Sande et. al., a 0.15%C alloy worked at 1150°C (2100°F) demonstrated a YS of 740MPa (107ksi), an UTS of 1240MPa (180ksi) and 10% elongation [37].

Table 2-2: Effective hot-working parameters from literature for various alloys

Material	Preheat Temp.	Reduction	Temp. Range	Strain Rate	Source
Austenitic S.S.	1000°C (1830°F)	5 steps of 10%	1000°C (1830°F) 800°C (1470°F)	hot-rolled	[41]
Co-Ni-Cr-Mo	1200-1250°C (2190-2280°F)	at least 50%	1200°C (2190°F) 800°C (1470°F)	0.01-10.0/sec	[42]
Co-Cr-Ni-Mo	1150°C (2100°F)	14-20 forge cycles	1100°C (2010°F) 900°C (1650°F)	Air-hammer	[43]
Co-Cr-Mo-N	above 1093°C (2000°F) for 1 hr	at least 50%	1260°C (2300°F) 1050°C (1920°F)	20/sec	[44]
Co-Cr-Mo	isothermal	12-80%	1150°C (2100°F) 1100°C (2010°F)	10^{-4}-10^{-1}/sec	[45]
Co-Cr-Mo	isothermal	at least 50%	1150°C (2100°F) 900°C (1650°F)	5.0/sec	[46]
Co-Cr-Mo	isothermal	up to 70%	1200°C (2190°F) 900°C (1650°F)	<100/sec	[47]

2.3 Nitrogen-High Pressure Melting

2.3.1 Background

Work by researchers at the U.S. Bureau of Mines have shown that great gains in the tensile and fatigue strength of austenitic stainless steels can be obtained through high nitrogen additions, achieved by melting the alloy in a high pressure nitrogen atmosphere [48]. There are several similarities between the Fe-Cr and the Co-Cr systems which make the ferrous system a useful basis for comparison when considering the diffusion of an interstitial solute like nitrogen in the cobalt system [49]. Both alloy systems have an FCC structure, with similar lattice parameters (0.357 to 0.360 nm, or 3.57 to 3.60 Å), and the major alloy addition for both systems is chromium, which affects the solubility and mobility of carbon and nitrogen atoms [50]. Thus, it is postulated that significant property improvements could be achieved by nitrogen additions to the Co-Cr-Mo system in the same manner, and that the nitrogen would behave in the cobalt system in a manner similar to that observed in the ferrous system.

2.3.2 Nitrogen in Co-Cr-Mo

As an alloying element for use in biological applications, the major known pathological effects of nitrogen in the human body are nitrogen narcosis and Caisson disease (the bends), both of which are the effects of partial pressures of nitrogen well in excess of one atmosphere in the bloodstream [50]. Additionally, the ASTM F75 specification for a biomedical quality Co-Cr-Mo alloy does not specify a limit for nitrogen in the alloy. This makes nitrogen an acceptable choice as an alloying element.

Kilner et. al. [50, 51] also proposed beneficial effects of nitrogen additions to Co-Cr-Mo, but in their work they relied upon solid state diffusion at atmospheric pressure. As Rawers et. al. state in their article [52] regarding Fe-Cr alloys, ion implantation or atomic diffusion from the surface using controlled gas mixtures restricts the nitrogen enhancement to near the surface. Nitrogen concentrations in similar Fe alloys can be substantially increased by N-HPM. Undoubtedly, high pressure melting would be expected to achieve greater concentrations of nitrogen, as well as more even distribution throughout a Co-Cr alloy.

Nitrogen and Co-Cr-Mo Metallurgy:

The work of Blossey and Pehlke [53] found that at 1600°C (2910°F) and 1 atm nitrogen, the solubility of nitrogen in *pure* liquid cobalt is 0.0047wt%. They found that the addition of Cr increases the nitrogen solubility. In the *solid* state work of Kilner et. al. [49], the maximum nitrogen in solid solution at 1200°C (2190°F) was found to be 0.35wt%, and their alloy contained about 25-30wt% Cr.

For both the work on Fe-based alloys [48, 54, 55], and work on Co-based alloys [53], it was found that Sievert's Law applied to the nitrogen addition. Sievert's Law predicts that the total nitrogen concentration in a solid or liquid (at equilibrium) should be proportional to the square root of the nitrogen gas pressure. However, above the solubility limit, deviation from Sievert's Law could occur, due to the formation of second phases. In fact, Rawers et. al. [41] found that the interstitial concentration of nitrogen began *decreasing* with increasing total concentration due to the formation of the second phases. It has also been noted [48] that the FCC crystal structure has a high solubility for interstitials, but that C and N compete for these interstitial sites. Kilner et. al. [50] also determined that the C content of the alloy affected the N behavior in Co-Cr, and calculated a nitrogen diffusivity, D_N, for 0.07% C of 14×10^{-8}cm^2/sec and for 0.22% C of 7×10^{-8}cm^2/sec for an ASTM F75 alloy.

Above the nitrogen solubility limit, Kilner et. al. found that large second phase particles of Cr_2N, and $Cr_2(CN)$ were formed. Looking at the phases present in N-HPM stainless steels, both Cr_2N and CrN are mentioned in various experiments [41, 48, 52]. It is also noted [48] that Si additions may lead to preferential precipitation of Si_3N_4, which may reduce the nitrogen available for use in other roles. The same source also states that the CrN has the greatest thermodynamic stability of the chromium nitrides described.

This is further explained in the observations made by Rawers et. al. [41] on type 304 and 316 stainless steels melted under 200MPa (30ksi) of nitrogen. In their work, the primary CrN was retained at all heat treat temperatures, but eutectic CrN dissolved above 1034°C (1893°F). On the other hand, Cr_2N dissociated below 1000°C (1832°F). This appears contrary to work quoted by Kilner and done by Jack [56], who claims that in Fe-Cr alloys, CrN is more stable than Cr_2N at temperatures below 575°C (1067°F), and is precipitated for any Cr content, and that at 865°C (1589°F), CrN will precipitate in alloys with less than 14wt% Cr. Thus, Cr_2N would be favored at high temperatures and high chromium contents. Perhaps the nitrogen concentration is what makes the real difference.

Morphologically speaking, in the solid state work of Kilner et. al. [50], the Cr_2N was observed to exist in the Co-Cr-Mo alloy primarily as a grain boundary precipitate in nitrided tensile bars, and as large, blocky precipitates in nitrided TEM sized disks. Nitrided TEM samples that were aged at 400°C (752°F) resulted in CrN precipitates that were fine, but which appeared to have nucleated near the surface of the sample. In the N-HPM stainless steel work [41], it was found that 1.09wt% N formed eutectic CrN dendrites and a Cr_2N false pearlite which disappeared after heat treating at 1000°C (1832° F), but that 2.01-2.22wt% N only contained the eutectic CrN dendrites, which required heat treating at 1100°C (2012°F) to remove. Then, for 3.93wt% N, the eutectic CrN dendrites were still present, but primary, equiaxed CrN dendrites were also present. Heat treating of this alloy at 1100°C (2012°F) again removed the pearlite, but the primary dendrites of CrN remained undissociated up to the melting temperature. Aging of all of these solutionized alloys at 500°C (913°F) resulted in the formation of Cr_2N false pearlite. Thus, the stoichiometry of the nitrides produced in the alloy may be a function of nitrogen content, and the distribution of the resulting second phase may be a function of the nitrogenation technique. The grain boundary precipitates observed by Kilner et. al. may be due to the preferential use of grain boundaries as diffusion channels for the nitrogen, whereas the intragranular precipitation observed in the HPM stainless steels may be a function of the liquid-state diffusion of nitrogen allowing for greater distribution throughout the material.

Nitrogen and Co-Cr-Mo Properties:

Turning to the effects of the nitrogen on the properties of the materials, the effects observed by Kilner et. al. [51] for nitriding of ASTM F75 Co-Cr-Mo are first considered. They state that interstitial nitrogen additions to low carbon alloys (0.14wt% carbon) increased the yield strength while maintaining good ductility, but that no beneficial effect was apparent for materials tested in fatigue. However, the poor fatigue properties were blamed on casting defects, and in a high carbon alloy, on carbide solutionization during the nitriding treatment. The tensile properties of specimens with >0.35wt% nitrogen were found to have acceptable yield strength, but the ductility was reduced. This was related to the presence of Cr_2N and $Cr_2(CN)$ precipitation along the grain boundaries. Thus, it is evident that some gains in tensile properties can be realized through interstitial nitrogen strengthening, but since the work done by Kilner et. al. relied upon solid state diffusion, the full potential of nitrogen strengthening has not been well represented. Looking at the actual data generated by the experiments of Kilner et. al. shows that there is no strong link between the nitrogen content of the specimens, and the subsequent properties obtained. This is likely a function of the poor distribution across the specimen section that is obtained by solid state nitriding. Grain boundary diffusion of nitrogen atoms could very likely result in preferential grain boundary precipitation, and simply HIPing the cast specimens could result in a reduction of the casting defects that led to premature fatigue failure. It has been stated [41] that nitrogen is twice as strong as carbon as an interstitial solid solution strengthener, and controlled precipitation of nitrides may also be utilized. The potential effects of higher nitrogen additions to Co-Cr-Mo, can be explored by referring to the work done on stainless steels.

J. Aghazadeh-Mohandesi and R. Priestner [57] made nitrogen additions to stainless steel by solid-state nitriding, similar to Kilner et. al. They found that surface hardness, strength, and fatigue endurance were usefully increased by nitriding, but that the strengthening was wholly attributed to nitrogen in solid solution. They found that greater tensile and fatigue strengthening were directly achieved by greater nitrogen case depth, which was in turn optimized by *not* forming second phase particles. If this were related to the work done by Kilner et. al. on Co-Cr-Mo, it would demonstrate that more complete diffusion is desirable.

Rawers et. al. [41, 53] showed quite clearly in their work that the tensile mechanical properties were proportional to the interstitial nitrogen concentration, but neither the presence of either of the chromium nitride phases nor the quantity of the nitride precipitates had an effect on the tensile properties. On the other hand, hardness, wear, and elastic modulus were all related to the *total* nitrogen concentration and increased in proportion to the quantity of nitride phase present [41]. However, it has been shown [41, 48] that although the high nitrogen can lead to high tensile strengths, the as-cast form of the alloy is quite brittle. It has further been shown [41] that hot-working the as-cast material will break up the CrN dendrite networks and dissolve other nitrides, and achieve enhanced ductility.

Lastly, for biomedical implant applications, the corrosion resistance of the nitrogen alloys should be considered. In 1990, it was stated [48] that nitrogen forms a passive oxide film that improves the corrosion resistance of nitrogen alloyed steels. However, in 1992, Rawers et. al. [41] stated that the formation of chromium nitrides decreases the matrix chromium concentration, thus reducing corrosion protection. Thus, the effect of the nitrogen on the corrosion resistance of a Co-Cr-Mo alloy may be negative if too much of the chromium is used in nitrides, but on the other hand, this may not be a problem with chromium contents of 25-30wt%.

3. EXPERIMENTAL PROCEDURES

The experiments in this study fall into several processing regimes: investment casting, nitrogen-high pressure melting (N-HPM), hot-rolling, and heat treatment. The analysis of the effects of these processes on the materials involved total nitrogen measurement, hardness testing, tensile testing, pitting potential testing, abrasive wear testing, and microstructural characterization. The microstructural characterization included x-ray diffraction, scanning electron microscopy, transmission electron microscopy, light microscopy, and image analysis.

3.1 Initial Materials

The materials involved in this study were two types of similar cobalt-chromium-molybdenum (Co-Cr- Mo) alloys that are commonly used in biomedical implant applications; Stellite 21 and ASTM F75. Both types contained 27-30 wt% Cr, 5-7 wt% Mo, and 0.2-0.25 wt% C. Stellite 21 can also contain up to 3 wt% iron (Fe), as opposed to the maximum of 0.75 wt% Fe in the ASTM F75 alloy. The ASTM F75 material came from two investment casting shops in Portland, Oregon. The Stellite 21 alloy was donated by Delro Stellite Incorporated of Belleville, Ontario, Canada.

3.1.1 Investment Cast Materials

The ASTM F75 alloy was supplied in the form of 1.3 or 1.9 cm (1/2 or 3/4 in) diameter round bars 10 to 30 cm (4 to 12 in) in length, and as actual biomedical hip implant castings. These parts were investment cast either conventionally, or through a proprietary grain-refining process. The conventional method resulted in the heavily cored dendritic structure traditionally expected in these materials. The fine-grained process resulted in an equiaxed grain structure with eutectic material segregating at the grain boundaries, as described by Zuang and Langer in their study [36].

The chemical compositions of these materials were determined by spark emission mass spectroscopy, and are listed in **Table 3-1**.

Table 3-1: Chemical composition of the starting materials in weight percent (wt%)

	Co	Cr	Mo	Fe	Ni	Mn	Si	C
F75 A	bal.	27.6	5.6	0.22	0.1	0.34	0.79	0.21
F75 B	bal.	28.2	6.3	0.33	0.2	0.35	0.84	0.24
Stellite 21	bal.	28.1	5.7	1.6	1.5	0.4	0.8	0.25

3.1.2 Nitrogen-High Pressure Melted Materials

The initial Stellite 21 materials were first cut into pieces and induction remelted in a non-oxygen atmosphere to form cylindrical ingots. These ingots were then induction melted in 1-1.5 kg (2.2-3.3 lb) heats under nitrogen gas pressures ranging from 1.4 to 50 atmospheres (atm). To provide a base-line, a melt was also done under 10 atm of argon gas. The melting was done in a furnace at the Department of Energy's Albany Research Center (DOE-ARC), in Albany, Oregon. The identification of the melts as used throughout this report are shown in **Table 3-2**. A schematic of the N-HPM furnace is shown in **Figure 3-1**.

The material was exposed to the induction field to achieve melting, then held for 15 to 30 minutes as a liquid to allow nitrogen to diffuse into the molten material. Induction eddy currents contributed stirring to the melt in order to encourage uniform nitrogen alloying throughout the material. The high-pressure induction furnace was capable of withdrawing the ingot during solidification, to minimize any solidification

Table 3-2: Identification system for N-HPM Stellite 21 materials

Process	Nominal N (wt%)	Identification
Melted under 10 atm of Ar gas	0.1	10 atm Ar
Melted under 1.4 atm of N_2 gas	0.2	1.4 atm
Melted under 4 atm of N_2 gas	0.3	4 atm
Melted under 16 atm of N_2 gas	0.4	16 atm A
Melted under 16 atm of N_2 gas for long time	0.5	16 atm B
Melted under 50 atm of N_2 gas	0.9	50 atm

pipe formation. The material was then maintained under the high-pressure atmosphere while solidification proceeded. The final castings were approximately 5.7 cm (2.25 in) in diameter, and ranged from 3.8 to 6.4 cm (1.5 to 2.5 in) height.

The chemical composition of these heats was determined by spark emission mass spectroscopy using an ASTM F75 calibration, and the carbon content was determined using LECO Carbon/Sulfur analysis. The results are recorded in **Table 3-1**.

Sectioning of ingots

The ingots were sectioned as shown in **Figure 3-2**, and the material utilized as labeled. The middle 3 cm (1 in) thick section was taken for hot-rolling in order to allow adequate material for subsequent experiments, but at the expense of any microstructural information at the center of the ingot. However, through analysis of the surrounding volume, adequate interpretation was possible.

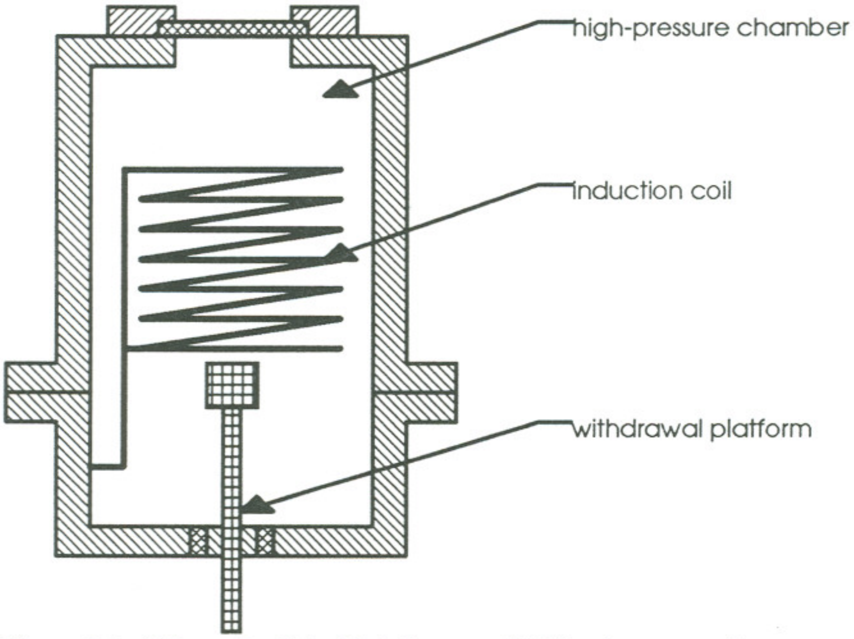

Figure 3-1: Schematic of the High-Pressure Melting furnace at the Department of Energy's Albany Research Center

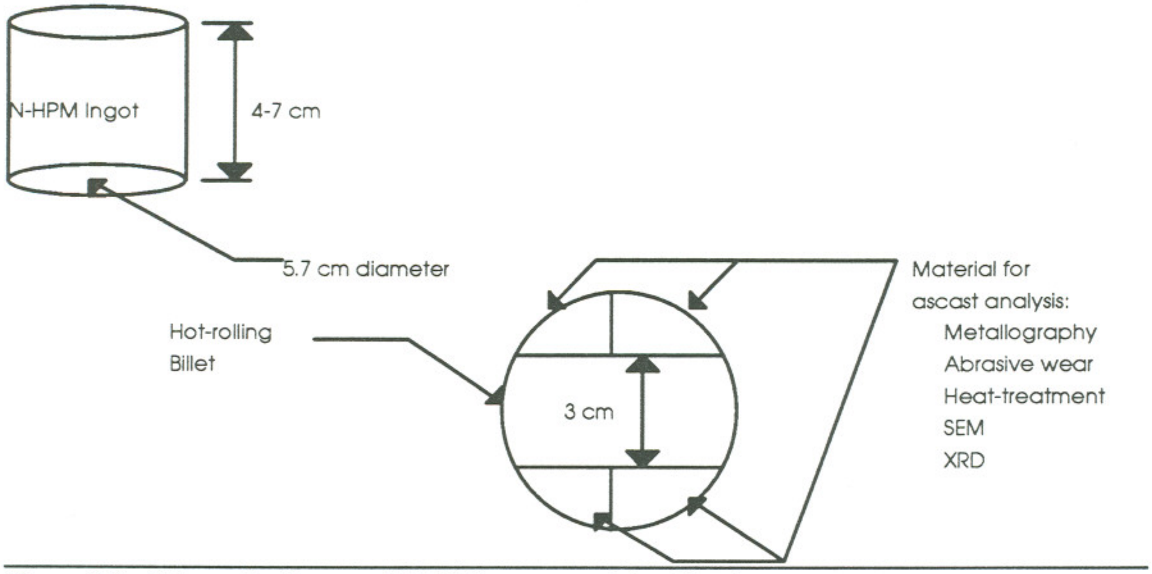

Figure 3-2: Schematic of as cast N-HPM ingot materials utilization

Nitrogen Analysis

Total nitrogen content of samples taken from the materials at different stages in processing was measured by inert carrier gas fusion using a LECO Nitrogen-Oxygen-Determinator, model TC 436 at the DOE-ARC.

Matrix nitrogen content of selected samples was determined by Kjeldahl analysis, in which the matrix was dissolved in 1:1 HCl in methanol solution. The resulting solution was then processed to measure the nitrogen content of it, assuming all of the nitrogen came from the metal matrix. This method also dissolves Cr_2N, however.

The samples were taken from bulk materials with a Micromech Micro-Matic slicer/dicer high-speed saw equipped with a thin (0.5 mm or 0.02 in) blade and liquid coolant. This allowed small samples to be made without excessive heating.

3.2 Thermal and Mechanical Processing

Solutionization, annealing, and aging treatments on both the investment cast F75 and the N-HPM Stellite 21 materials were carried out in a Lucifer refractory brick lined electric muffle furnace. With maximum temperature capabilities of 1260°C (2300°F), the furnace was digitally controlled within ± 5°C (10°F) of the programmed temperature. The volume of the furnace was about 60 liters (2 ft^3).

3.2.1 Solutionization Treatments of Cast Materials

Investment Cast F75 Coupons

To determine the solutionization behavior of the as-cast F75 material over time, 0.7-1 cm (0.3-0.4 in) thick slices were cut from cast round bar, heat treated at various temperatures and times, and then quenched in room temperature water. **Table 3-3** shows the materials and the solutionization heat treatments that they underwent.

Table 3-3: Solutionization heat treatments of cast F75 materials

Material	Temperature	Atmosphere	Times (hours)
Conventionally Cast F75A*	815°C (1500°F)	Quartz capsule/Ar gas	4
Conventionally Cast F75A	1199°C (2190°F)	Quartz capsule/Ar gas	2, 4, 8, 16, 32
Conventionally Cast F75A	1220°C (2220°F)	Quartz capsule/Ar gas	1, 2, 4, 8, 16
Fine-grained F75B	1220°C (2220°F)	Air	1, 2, 4, 8, 16
Fine-grained F75B	1190°C (2175°F)	Air	1, 2, 4, 8, 16

* This sample was intended as a "preheat" sample r.e. J. Cohen, R. M. Rose and J. Wulff, *J. Biomedical Mater. Res.* **12** (1978), pg. 935

Fine-grained Investment Cast F75 Test bars

To determine the effects of various HIP and solutionization treatments on the mechanical properties of the fine-grained, cast F75 material, actual cast prostheses were heat treated according to the conditions shown in **Table 3-4**, then the lower 9 cm (3.5 in) were machined into round tensile bars and tested to failure.

Cast N-HPM Materials

Effect of Furnace Atmosphere on the Nitrogen Content

To determine acceptable procedures for solution annealing of the high-nitrogen materials, experiments were conducted to determine the effects of atmosphere used during the thermal treatment on the final nitrogen contents of the samples.

Samples from the 50 atm melt with a cross-section of about 0.75 cm (0.3 in) were heat treated in three different atmospheres: air, argon, and nitrogen. The argon and nitrogen environments consisted of the gas being continuously introduced into the back of the furnace at a rate of about 400 liters per hour (*l*h), or 15 cfh, and being allowed to leak out through any cracks in the furnace, around the door, etc. The samples were held for 16 hours at 1220°C (2220°F) to allow the captured nitrogen every opportunity to diffuse out.

Table 3-4: HIPing and solutionization schedule for fine-grained cast F75

Sample ID	HIP Temperature	Cooling Rate	Solution Temp./Time	Cooling Rate
1185R	1185°C (2165°F)	Rapid	None	None
1185/1190R	1185°C (2165°F)	Conventional	1190°C (2175°F)/4hrs	Rapid
1185/1190	1185°C (2165°F)	Conventional	1190°C (2175°F)/4hrs	Conventional
1185/1220R	1185°C (2165°F)	Conventional	1220°C (2220°F)/4hrs	Rapid
1220/1190R	1220°C (2225°F)	Conventional	1190°C (2175°F)/4hrs	Rapid
1220/1190	1220°C (2225°F)	Conventional	1190°C (2175°F)/4hrs	Conventional
1220/1220R	1220°C (2225°F)	Conventional	1220°C (2220°F)/4hrs	Rapid
1220/1220	1220°C (2225°F)	Conventional	1220°C (2220°F)/4hrs	Conventional
1185	1185°C (2165°F)	Conventional	None	None
1220	1220°C (2225°F)	Conventional	None	None
1220R/1220R	1220°C (2225°F)	Rapid	1220°C (2220°F)/4hrs	Rapid

The heat treated samples were wet ground to remove any oxide layer, and then small pieces were cut for determination of bulk nitrogen content through LECO analysis. **Table 3-5** shows the results of that experiment, and shows that perhaps heat treating in air or in stainless steel foil would be best.

Solutionization of as-cast N-HPM material

To determine the solutionization behavior of the as-cast material over time, 0.7 cm (0.3 in) thick slices were cut from a section as was depicted in **Figure 3-2**, and then heat treated at 1220°C (2220°F) for various times. The heat treatments took place in air for times of 1, 2, 4, 8, and 16 hours, and were followed by quenching in room temperature water.

Table 3-5: Nitrogen content of 50 atm ingot after 1220°C (2220°F) heat treatments

Sample	Total Nitrogen
Cast 50 atm ingot (top) (bottom)	1.34 wt % 0.83 wt %
16 hours in air	1.02wt%
16 hours in N_2	0.81wt%
4 hrs in Ar(avg.)	0.83wt%
8 hrs in Ar(avg.)	0.74wt%
16 hrs in Ar	0.42wt%

3.2.2 Aging of Investment Cast F75 Materials

Conventionally Cast Material

Aging experiments were first performed on the conventionally cast F75 A material according to the schedule shown in **Table 3-6**. The conditions were arranged in a factorial analysis matrix to allow observation of the effects of multiple variables without the large number of specimens that would be required for a traditional matrix. Specimens consisted of 1.3 cm (1/2 in) diameter round bars 10 cm (4 in) in length for tensile testing, with 0.7 cm (1/4 in) thick slices of the bars for metallography. The materials were cast and then HIPed at 1185°C (2165°F) for 4 hours and conventionally cooled. Three solutionization temperatures were chosen to create a range of solutionized second phase material at a constant time of 8 hours, allowing evaluation of the effect of solutionization on the subsequent aging steps. The solutionization was followed by a water quench. The aging temperatures were chosen based on cited ranges of stacking fault formation (martensitically transformed FCC to HCP) and carbide precipitation, both which take place in approximately the same temperature ranges. The times were chosen to evaluate the phase transformation rates.

Table 3-6: Factorial matrix for aging of conventionally cast F75

Test #	Solutionization Temperature	Aging Temperature	Aging Time	Cooling Rate
A/1070/700/3	1070°C (1960°F)	700°C (1290°F)	3 hours	air
A/1070/900/6	1070°C (1960°F)	900°C (1650°F)	6 hours	oil
A/1070/1050/12	1070°C (1960°F)	1050°C (1920°F)	12 hours	brine
A/1190/700/6	1190°C (2175°F)	700°C (1290°F)	6 hours	brine
A/1190/900/12	1190°C (2175°F)	900°C (1650°F)	12 hours	air
A/1190/1050/3	1190°C (2175°F)	1050°C (1920°F)	3 hours	oil
A/1220/700/12	1220°C (2220°F)	700°C (1290°F)	12 hours	oil
A/1220/900/3	1220°C (2220°F)	900°C (1650°F)	3 hours	brine
A/1220/1050/6	1220°C (2220°F)	1050°C (1920°F)	6 hours	air

Fine-grained Cast Material

Aging was subsequently performed on fine-grained cast F75 B according to **Table 3-7**. Before aging, round bars 2 cm (3/4 in) in diameter and 30 cm (12 in) long were first solutionized at 1190°C (2175°F) for 16 hours in an argon atmosphere, and then water quenched. They were then cut into three pieces and recorded as coming from the top, middle, or bottom (T, M, B respectively). The aging was done in sets of two bars taken at random from the set of solutionized bars, as numbered in **Table 3-7**. The aging took place in stainless steel foil and was followed by air cooling.

Table 3-7: Aging schedule for fine-grained cast F75

Test #	Sample location	Aging temperature	Aging time, hrs
B/650/2	B, T	650°C (1200°F)	2
B/650/4	M, B	650°C (1200°F)	4
B/650/8	M, T	650°C (1200°F)	8
B/650/16	M, B	650°C (1200°F)	16
B/700/2	M, T	700°C (1290°F)	2
B/700/4	B, T	700°C (1290°F)	4
B/700/8	B, T	700°C (1290°F)	8
B/700/16	M, B	700°C (1290°F)	16
B/750/2	M, T	750°C (1380°F)	2
B/750/4	M, B	750°C (1380°F)	4
B/750/8	M, T	750°C (1380°F)	8
B/750/16	M, B	750°C (1380°F)	16
B/750/32	T, B	750°C (1380°F)	32

B=bottom, M=middle, T=top

3.2.3 Hot-Rolling of N-HPM Materials

Hot-Rolling Temperature Determination

Superalloys such as the Co-Cr-Mo alloy are quite sensitive to hot-working, and care is needed to successfully deform them. In order to determine the appropriate parameters for hot-rolling of the N-HPMed ingots, tests were performed on round investment cast bars of ASTM F75 according to the test matrix in **Table 3-8.**

Table 3-8: Exploratory hot-working parameters for F75 material

Rolling Temperature	Deformation		
1000°C (1830°F)	20%	40%	20% x 2
1100°C (2010°F)	20%	40%	20% x 2
1200°C (2190°F)	20%	40%	20% x 2

Following hot-rolling, the samples were water quenched, and then examined for signs of cracking or other defects. Additionally, metallography of the resultant microstructure was used to determine what degree of dynamic recrystallization had occurred, and whether uniform deformation had been achieved without formation of internal defects such as cracks. A complete description of this study can be found in **Appendix B**. Ultimately, repeated deformations of 20% at a temperature of 1100°C (2010°F) were found to lead to an acceptable microstructure.

Hot-Rolling Procedure

Because the N-HPM material contained large quantities of second phase material such as nitrides, the ingots were solutionized for 16 hours at 1220°C (2220°F) before hot-rolling. With interstitial solid solution strengthening by nitrogen expected, the reduction per pass was limited to 8 to 15%. **Figure 3-3** shows an example of the hot-rolling schedule that was followed at the DOE-ARC for the reduction of each ingot.

The 3 cm (1 in) thick billets were preheated for one hour at 1100°C (2010°F), then rolled according to the schedule. The plate was reheated at 1100°C (2010°F) for 10 minutes between passes, and following the final pass, the plate was reheated for 15 minutes and then water quenched. In some cases, the final plate was reheated to 1100°C (2010°F) for 15 minutes and then flattened under a hydraulic press, which effectively quenched it without allowing distortion. The final plate thickness was about 4 mm.

Annealing of Hot-rolled Plates

Leaving hot-rolled material in a condition of potentially high residual stress may have led to widely scattered mechanical property results, as well as to machining difficulties. The effects of the hot-working on the N-HPM plates could also have disguised the strengthening effects of the interstitial nitrogen. Thus, annealing of the material was considered desirable. A brief annealing study conducted on ASTM F75 bars that had experienced five 20% reduction passes concluded that short times even at 1100° C (2010°F) were sufficient to soften the hot-worked material, but that 1200°C (2190°F) countered potential precipitation as well as contributed further softening. Details of this study are in **Appendix B**.

Hot Rolling Schedule for N-HPM Ingots

All rolling to be done at 2010°F (1100°C).
Initial preheat of 1 hour.
10 minute reheat between passes.

10 atm Argon ingot

Initial thickness:	0.97 inches
Initial height:	2.41 inches
Initial width:	2.13 inches

Roll settings:

Pass #	Roll Separation (inches)	Actual % deformation
1	0.92	5.2
2	0.82	10.9
3	0.73	11.0
4	0.65	11.0
5	0.57	12.3
6	0.50	12.3
7	0.43	14.0
8	0.36	16.3
9	0.30	16.7
10	0.25	16.7
11	0.21	16.0
12	0.18	14.3
13	0.155	13.9
14*	0.135	12.9

*Optional based on surface finish of prior passes

Figure 3-3: Sample of schedule for hot rolling of N-HPM ingots at DOE-ARC

Following hot-working, the high-nitrogen plates were annealed at 1200°C (2190°F) for 15 minutes in air. They were then quenched between two flat, heavy, metal plates to achieve rapid heat extraction while minimizing distortion potential. The annealed plates were then each cut into at least 15 test bar blanks measuring 1.5 cm (0.6 in) wide and ~8 cm (~3 in) long. A few of these served as test bar material for the as-annealed material, and the remaining bars were further heat treated. **Figure 3-4** shows how the rolled materials were utilized to maximize the extractable information.

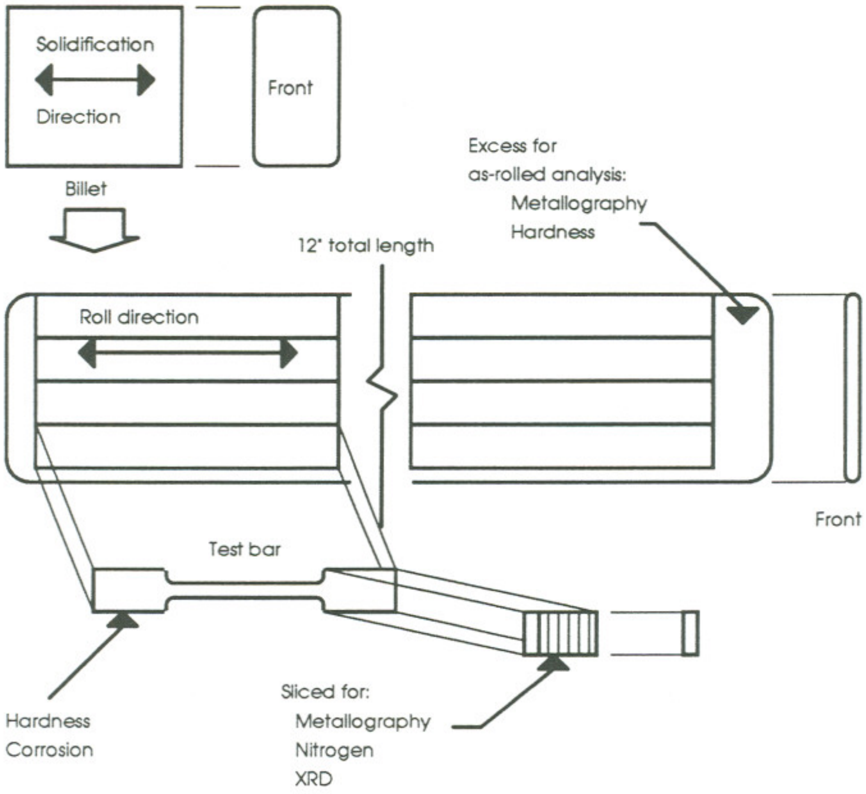

Figure 3-4: Schematic of wrought N-HPM materials utilization

3.2.4 Solutionization of Wrought and Annealed N-HPM Materials

To characterize the thermal response of the second phase material present in the wrought and annealed N-HPM plate material, several solutionization experiments were executed. In the first set, 1 cm x 1 cm (1/2 in x 1/2 in) samples of plate material about 3 mm (1/8 in) thick were heat treated in stainless steel foil bags under the conditions shown in **Table 3-9**, and then quenched in room temperature water.

The second set consisted of heat treating test bar blanks in stainless steel foil bags under the conditions shown in **Table 3-10**, and then quenching them in room temperature water. Two to three bars were heat treated for each condition. The heat treated bars were machined into flat test bars, tensile tested, and then subsequent microstructural characterization was performed.

Table 3-9: Solutionization matrix for wrought/annealed N-HPM specimens

Melt ID	1220°C (2220°F) 1 hour	1220°C (2220°F) 4 hours	1240°C (2260°F) 1 hour	1240°C (2260°F) 4 hours	1260°C (2300°F) 1 hour	1260°C (2300°F) 4 hours
10 atm	X		X		X	
1.4 atm	X		X		X	
4 atm	X	X	X	X	X	X
16 atm A	X	X	X	X	X	X
16 atm B	X	X	X	X	X	X
50 atm	X	X	X	X	X	X

Table 3-10: Solutionization matrix for wrought/annealed N-HPM test bar blanks

Melt ID	1220°C (2220°F) 1 hour	1220°C (2220°F) 4 hours	1260°C (2300°F) 4 hours	1260°C (2300°F) 8 hour	1260°C (2300°F) 16 hour
10 atm	X	X			
1.4 atm	X	X			
4 atm			X		
16 atm A				X	
16 atm B			X	X	X
50 atm				X	X

3.3 Microstructural Characterization

A combination of optical and electron microscopy as well as x-ray diffraction was used in order to evaluate the results of the various processing steps, as well as the nitrogen additions, on the microstructure of the materials. The optical microscopy involved general observations as well as image analysis of grain size and second phase distribution of metallographically prepared specimens.

3.3.1 Optical Microscopy

Metallographic Preparation

Samples for metallographic examination were generally mounted in either a thermosetting polymer using a LECO mounting press, or in a cold-mount resin using a positive pressure chamber to minimize bubble formation. They were then wet ground using SiC papers of 120, 240, 400, and 600 grit sizes. Dry grinding on 800 grit paper was then followed by polishing with 1µm diamond paste on nylon cloth, using an oil-based diamond extender. Final polishing utilized a colloidal silica on a cotton cloth equipped autopolisher.

Chemical Etching and Matrix Dissolution

The etchant most commonly used on the metallographic specimens was an aqueous solution of 10% ammonium persulfate that was used electrolytically at 6V. This solution attacked the grain boundaries and outlined second phase material, so was used especially prior to grain size measurement. Etching for longer times generally resulted in solute gradients such as found in dendrites, being revealed.

Occasionally, Murakami's solution of 10g $K_3Fe(CN)_6$, 10g KOH, and 100 ml of distilled water was used as a swab etchant in order to darken second phase material such as $Cr_{23}C_6$. This was generally done to enable more accurate image analysis measurement of area fractions of second phases.

For careful dissolution of the cobalt matrix, a solution of 10% HCl in methanol was used electrolytically at voltages of 3 to 6 volts. This enabled dissolution of the matrix in order to extract second phase material for subsequent x-ray diffraction analysis. It was, however, quite slow, requiring many hours to dissolve a few milligrams of matrix material.

For aggressive dissolution of the matrix material, a solution of 10% bromine in methanol was used. This etchant enabled deep dissolution of the matrix material without affecting the second phase compounds, thus allowing three dimensional viewing of the second phase in the SEM. This solution was also used to isolate second phase material for subsequent x-ray diffraction analysis. It should be noted, however, that this solution is highly volatile, and that bromine is quite harmful to the body. As with other chemicals, handling of bromine must be very conscientious, and always take place in a safe, vented hood.

Examinations

Macro sections of the top, bottom and longitudinal sections of the as-cast N-HPM ingots were observed at magnifications of 10x using a Nikon stereoscope under direct reflected light. Black and white Polaroid micrographs were taken directly from the microscope at the same magnification.

All other prepared metallographic specimens were examined at magnifications from 50 to 400X using a Nikon Epiphot inverted metallograph. Samples were examined with normal bright-field illumination, polarized light, and differential interference contrast (DIC) using a Nomarski crystal. Black and white Polaroid micrographs were taken directly from the microscope.

Microstructural Quantification

Second Phase Content Measurements

The amount of second phase material present in a given microstructural condition was quantitatively measured using a LECO Model 2001 image analysis unit connected to the Nikon Epiphot metallograph. The metallography specimen was first etched to enable the second phase material to be discerned more easily. An image was then pulled into the image analysis unit through a CCD camera, digitally sharpened, and then the second phase material was highlighted by gray scale thresholding. The area fraction of this highlighted material was then computed by the software. At least ten randomly selected fields were used for each analysis and the results averaged to obtain the final numbers.

Grain Size Measurement

The measurement of the average grain size of a given microstructural condition was also quantitatively measured using the LECO image analyzer and Nikon metallograph. The metallography specimen was first etched to reveal the grain boundaries. An image was then pulled into the image analyzer through the CCD camera, digitally sharpened, and then five lines of a known length were drawn on the image. The number of grain boundary intersections were then counted for each line. These were summed for five fields for each analysis. The average grain size number and mean intercept distance were then calculated in accordance with ASTM E 112.

In the particular case of some of the rolled, N-HPM materials, the grain boundaries did not etch clearly. In those cases, the specimens were aged at 950°C (1740° F) for 1/2 hour and then water quenched. This decorated the grain boundaries with precipitates, and, following polishing, the etching more easily distinguished them.

Dendrite Arm Spacing Measurements

The measurement of average dendrite arm spacing was done in a manner similar to the grain size measurement. The sample was first etched to reveal the dendritic structure, then pulled into the image analyzer through the CCD camera, digitally sharpened, and then several lines of known length were drawn on the image parallel to the spine of the primary dendrite. The number of dendrite arm axes crossing the line were then counted for each one. These were summed for five fields for each analysis, and the average arm spacing calculated from the data.

3.3.2 X-ray Diffraction Analysis of Second Phase Material

One method used for identification of compounds in the materials was X-ray diffraction (XRD). Specimens were analyzed at the DOE-ARC using Ni filtered Cu-K_α radiation and accepted XRD analysis procedures. Particles were extracted from the materials by dissolving the matrix in either the bromine solution or electrolytically via the HCl solution. The residues were filtered onto a glass micro-fiber filter and washed with methanol. These residues were then treated as powder diffraction samples, and analyzed accordingly.

3.3.3 Scanning Electron Microscopy (SEM)

Examination of the second phase morphology within the matrix was done on metallographic specimens which had been deep-etched with bromine solution to remove the matrix while maintaining second phase positioning. A Zeiss digital scanning electron microscope (DSM960) was used in the observations, with beam capabilities of up to 30 KeV.

Energy dispersive x-ray spectroscopy (EDS) microanalysis applied to the processed materials was used to evaluate elemental constituent distribution in conjunction with the Zeiss SEM. This included elemental mapping for such elements as Co, Cr, Mo, Fe, Ni, C, O, and N.

3.3.4 Transmission Electron Microscopy (TEM)

Initial TEM disks were prepared in two ways. In the first case, 3 mm diameter cylinders were first extracted from the material by electric discharge machining (EDM). Slices 0.25 mm (0.010 in) thick were then cut using a high-speed cut-off saw equipped with a liquid cooled 0.5 mm (0.02 in) thick bonded Al_2O_3 abrasive blade. In the second case, thin slices were cut in the same manner from *whole* pieces, and then the 3 mm disks were punched out with a carbide tipped press. Slices were wax mounted on aluminum blocks and then ground to <150mm (0.007 in) in thickness using wet grinding on SiC papers, finishing with 800 grit finish on each side of the disks. The disks were subsequently thinned to perforation by a Fischione twin-jet unit. A solution of 10% perchloric acid in methanol was used at 40 to 50 volts and -30°C (-22°F).

The TEM analyses were conducted using a Hitachi H800 200 KeV analytical electron microscope. The H800 has capabilities for EDS analysis, imaging in standard bright and dark field TEM modes, obtaining selected area electron diffraction patterns, secondary electron imaging, and STEM.

3.4 Hardness and Mechanical Testing

3.4.1 Rockwell Hardness Testing

As an indication of the mechanical performance of the materials in the various processing conditions, Rockwell hardness on the C scale was measured. This was most preferable for evaluating pieces too small for tensile testing. Any scale or rough surface was first ground off before testing of the material was attempted. Each sample was tested in at least 5 to 10 regions, and the measurements were averaged for the final numbers.

3.4.2 Instron Tensile Testing

Hot-rolled and heat treated tensile blanks measuring 1.5 cm (0.6 in) wide by ~7 cm (3 in) long were tensile tested to determine the effects of nitrogen alloying on the mechanical performance of the material. The blanks were first ground to a 600 grit finish to achieve uniform, parallel faces. These bars were then machined into flat plate test bars meeting ASTM E4 specification for sub-sized test bars, with gauge regions measuring 6.4 mm (0.25 in) wide by 25.4 mm (1.0 in) long.

The prepared test bars were tested with an Instron model 2150 controlled servo-hydraulic machine of 0.09 MN (20 kip) capacity. The bars were tested in tension with a cross head speed of 0.064 mm/sec (0.0025 in/sec) and a 0.045 MN (10 kip) load cell. The load and cross-head displacement were recorded through computerized data acquisition sampling at 1 Hz. The engineering yield stress and ultimate tensile stress was calculated from this data based on the initial minimum cross-section of the test bar, and the elongation and reduction in area was calculated from initial and final measurements.

3.5 Corrosion Testing

As an estimate of any changes in the localized corrosion resistance of the Stellite 21 material due to alloying with nitrogen, critical pitting potential (CPP) and critical crevice temperature (CCT) tests were done by the DOE-ARC on samples of the wrought and annealed material (**Figure 3-4**).

The tests were conducted in a "flat cell", a 200 ml electrochemical reaction vessel designed to allow an externally affixed flat piece of metal to be exposed to the electrolytic solution. 1800 ml of solution at 30°C (86°F) was constantly circulated between the flat cell and a 2-liter heated reservoir. For the critical crevice temperature tests, the crevice was created by the sample being pressed against the opening in the flat cell (Teflon ring). For the critical potential tests, the flat cell was modified to provide a flow of 0.06 ml/min of pure water at the crevice, to eliminate any crevice effects during the testing. The electrolyte was 3.5% NaCl, prepared from reagent grade NaCl and high purity water.

For critical pitting potential testing the solution was heated to 30°C (86°F), the protective water flow was initiated at the edge (circumference) of the sample, the electrolyte circulation was started, and the sample surface was cathodically reduced by applying a potential of -1.1v (SCE) for 60 sec. The open circuit potential was then monitored for 30 min, and a potentiodynamic scan was conducted from -0.9v to +1.6v (or until the current density exceeded 2 *m*Amps/cm^2) and then was reversed back to -0.9v.

For the critical crevice temperature testing, the test solution was initially cooled to 10°C (50°F), continuously circulated, and the sample surface reduced by applying a potential of -1.1v for 60 sec. The open circuit potential was monitored for 30 min, and the specimen surface was conditioned at +0.4v for 10 min, and then, at +0.4v, a thermodynamic scan was conducted at a rate of 1°C/min (1.8°F/min) from 10°C to 96°C (50°F to 205°F) and back to 9°C (48°C) (or until the current density exceeded 2 *m*A/cm^2, which it never did for any of the samples tested).

3.6 Abrasive Wear Testing

As an estimate of any changes in the wear resistance of the Stellite 21 material due to alloying with nitrogen, pin-on-drum abrasion tests were performed by the DOE-ARC. Details of the test procedure are found in References [69] and [70]. Wear pins measuring 6.4 mm (0.25 in) diameter by at least 38 mm (1.5 in) long were electron discharge machined (EDM) out of the as-cast N-HPM ingot material (**Figure 3-2**), parallel to the solidification direction of the ingot.

In this study 150 grit garnet (100μm particle size; hardness 13.1 GPa; fracture toughness 1.1 MPa√m), and 600 grit SiC (17μm nominal particle size; hardness 24.0 GPa; fracture toughness 2.5 MPa√m) were used to abrade the various materials. Commercially available abrasive cloth was cut to size and then glued to the drum. The pin was pressed against the cloth/drum and rotated at a peripheral speed of $5.65\text{x}10^{-3}$m/s (17 rpm), while the drum rotated at a speed of $4.5\text{x}10^{-2}$m/s (1.7 rpm). The wear path was 1.6 m (63 in) per drum revolution.

The pins run on the 150 grit garnet were done so in both top and bottom orientations, to determine any effects that may be present due to microstructural differences in the top versus bottom regions of the cast ingots. In the test, the pin was pressed against the drum with a force of 66.7 N. This corresponds to a 2.11 MPa pressure on the pin surface. For those samples abraded on SiC, only the bottom orientation was tested, and the normal force was reduce to 41.8 N. The surface pressure on the pin in this case was 1.32 MPa. After a break-in cycle of four revolutions, wear data was collected for 8 revolutions on the garnet and the SiC. Three sets of tests were performed on the samples abraded on SiC and the garnet.

The mass loss of the individual wear tests were averaged with standard deviations calculated, from which the specific wear rate was calculated using the following equation:

$$\dot{W}_s = \frac{\Delta m}{\rho L F_N}$$

where $\dot{W}_s$ was the specific wear rate (mm^3/N-m); ρ was the density of the test material (mg/mm^3); L was the total sliding distance (m); and F_N was the normal force on the pin (N).

4. RESULTS and ANALYSIS

4.1 Investment Cast F75

4.1.1 Conventionally Cast Materials

The conventionally cast materials were examined in the as-cast form, as well as the solution heat treated and aged conditions.

As-cast material

Microstructure

The typical as-cast microstructure of the conventionally cast materials is illustrated in **Figure 4-1**. In the low magnification micrograph, the coarse grain size and dendritic structure is evident. The results of measuring the dendrite arm spacing in two typical cast hip-stems of F75 B are shown in **Table 4-1**. At higher magnification, the heavy population of interdendritic material is more evident. Measurements of the amount of second phase material in the two conventionally cast hip-stems are also shown in **Table 4-1**. It is apparent that the dendrite arm spacing and the second phase content were not uniform along the casting length, and that generally both increased as the section size increased in the component.

Elemental Distribution

SEM/EDX analysis was performed on polished, conventionally cast F75 A material. Because the measurements were made with an electron beam of 10KeV, the lighter elements may be over represented and heavier elements may be under represented in the resulting spectra. But, the LINK software used by the EDX instrument is capable

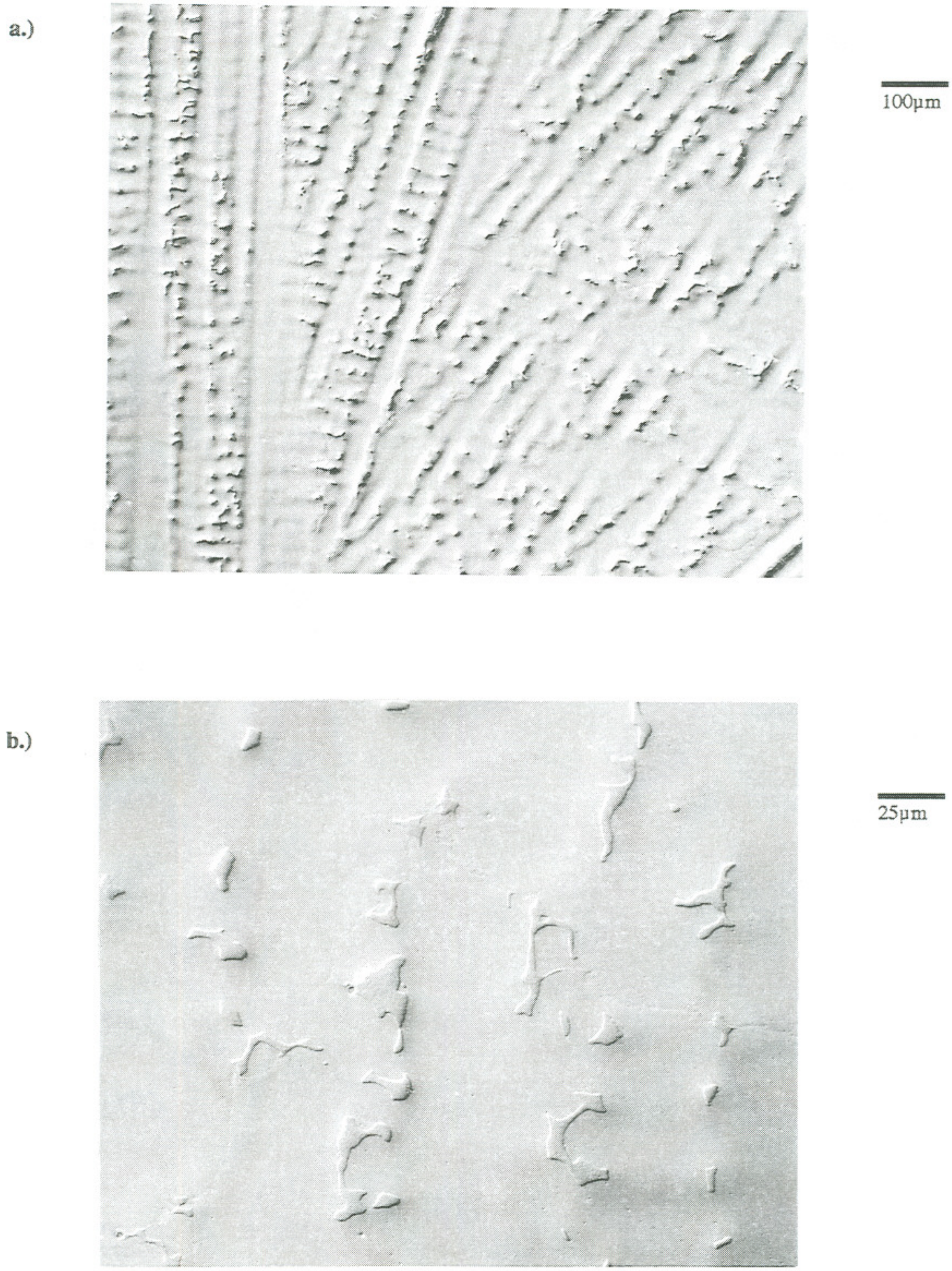

Figure 4-1: Microstructure of conventional as-cast specimen of F75 B a.) showing the coarse dendrite structure; 100x, unetched, b.) showing interdendritic second phase structure; 400x, unetched.

of taking this into consideration to semi-quantitatively calculate the composition represented by the spectra. The as-cast microstructure shows interdendritic segregation whose EDX results fell in the composition ranges of either:

Co: 42.2-44.2%, Cr : 28.1-31.6%, Mo: 21.0-22.3%, and Si: 1.2-1.3%

or

Al: 41.2-54.3%, O: 5.2-19.9%, Co: 11.2-17%, and Cr: 6.7-12.0

or

Si: 35.3-46.7%, O: 28.1-33.8%, Co: 2.1-9.5%, and Cr: 0.9-7.6%

Those high in Cr and Mo were most likely carbides, and those high in Al and Si were most likely oxides. In some cases, oxides and carbides may have coexisted, as shown in **Figure 4-2**. It should be kept in mind that these values include some influence from the matrix, which showed a bulk composition of 64.1% Co, 26.7% Cr, 6.9% Mo, and 0.9 Si. It is also noted that the EDX spectra for the bulk composition of the material showed about 1.3 wt% more Mo and about 1 wt% less Cr than the more accurate mass spectroscopy measurement. However, this is likely due to the fact that semi-quantitation is only done for elements selected, and not necessarily for all elements that are really present. Additionally, it should be taken into consideration that the semi-quantitation technique is a standardless technique, and thus could have some variation. The results seem to indicate materials that are either rich in the metallic elements Co, Cr, and Mo, or that are rich in the oxide-type elements Al and Si. The composition gradients within the cluster of particles of **Figure 4-2** indicate that there may be a coexistence of metallic carbide segregation with some oxide inclusions in the interdendritic material.

Table 4-1: Quantification of microstructural features in conventionally cast hip-stems of F75 B

Region of measurement	Secondary arm spacing (μm)	Second phase vol%
Stem #B/C/1-distal end	18±2.0	4.6±1.2
Stem #B/C/1-mid-section	38±1.9	7.4±0.6
Stem #B/C/1-proximal end	49±6.3	10.1±0.8
Stem #B/C/2-distal end	22±1.4	6.3±0.6
Stem #B/C/2-mid-section	44±1.4	8.1±0.6
Stem #B/C/2-proximal end	57±7.5	9.2±0.8

Effects of solutionization on conventionally cast material

Second phase distribution

The resulting solutionization over time at 1199°C (2190°F) for the conventionally cast F75 A material is shown in **Figure 4-3**, with the micrograph in **Figure 4-4** showing the microstructure after 32 hours of solutionization. It is evident from these figures that at 1199°C (2190°F) the interdendritic phase *did* dissolve, but not completely, and that cooling in water prevented any obvious re-precipitation of other phases. It should be noted that the porosity observed in **Figure 4-4** may have contributed to a slight inflation of the measured second phase quantity. However, this porosity was only significant in the 16 and 32 hour specimens. It was possibly due to Kirkendall voiding, in which the vacancy diffusion mechanism for diffusion of the second phase elements resulted in vacancy segregation at prior second phase sites following dissolution of the second phase into the matrix. **Figure 4-5** shows the solutionization behavior at 1220°C (2220°F). This shows that complete dissolution *did* occur, and within 16 hours. The data for both experiments follow a classical Arrhenius relation for dissolution, with 4 hours being the length of time after which very little subsequent solutionization took place.

Elemental Distribution

In order to determine the distribution and segregation of elements following solutionization, SEM/EDX analysis was performed on polished F75 A material solutionized for 16 and 32 hours. The results of semi-quantitative calculation of the chemistry of the interdendritic phase resulted in a range of:

Co: 32.8-54.4%, Cr: 35.7-54.4%, Mo: 2.9-12.6%, Si: 0.3-3.5%

If this is compared to the composition of the carbides of the as-cast material, it is observed that solutionization resulted in a reduction of the Mo content in the second phase, effectively resulting in enrichment in Cr (although there was an overall reduction in second phase content.)

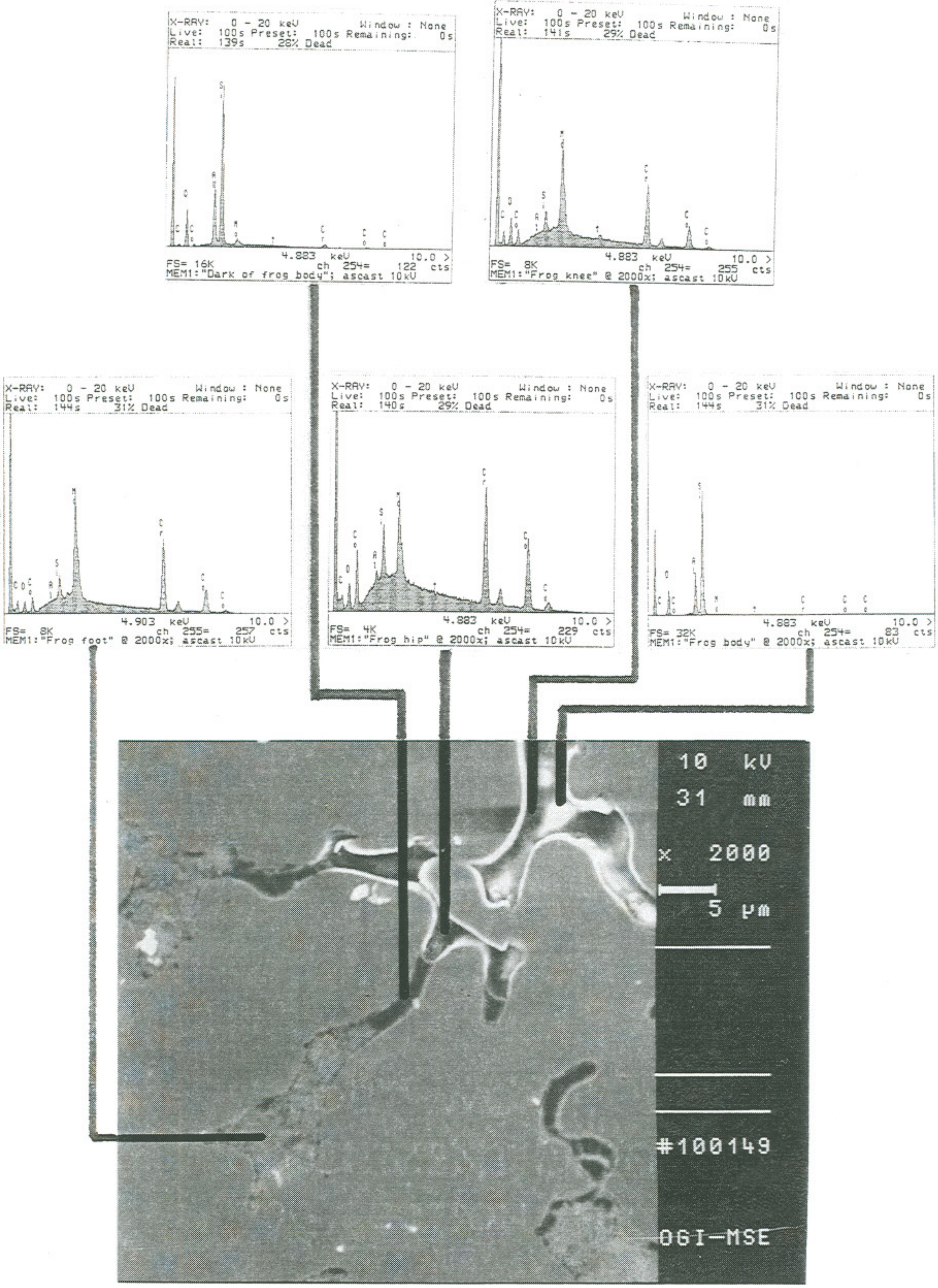

Figure 4-2: Secondary electron image and corresponding EDX spectra of conventionally cast F75 A, demonstrating the compositional gradients that exist within the second phase material;

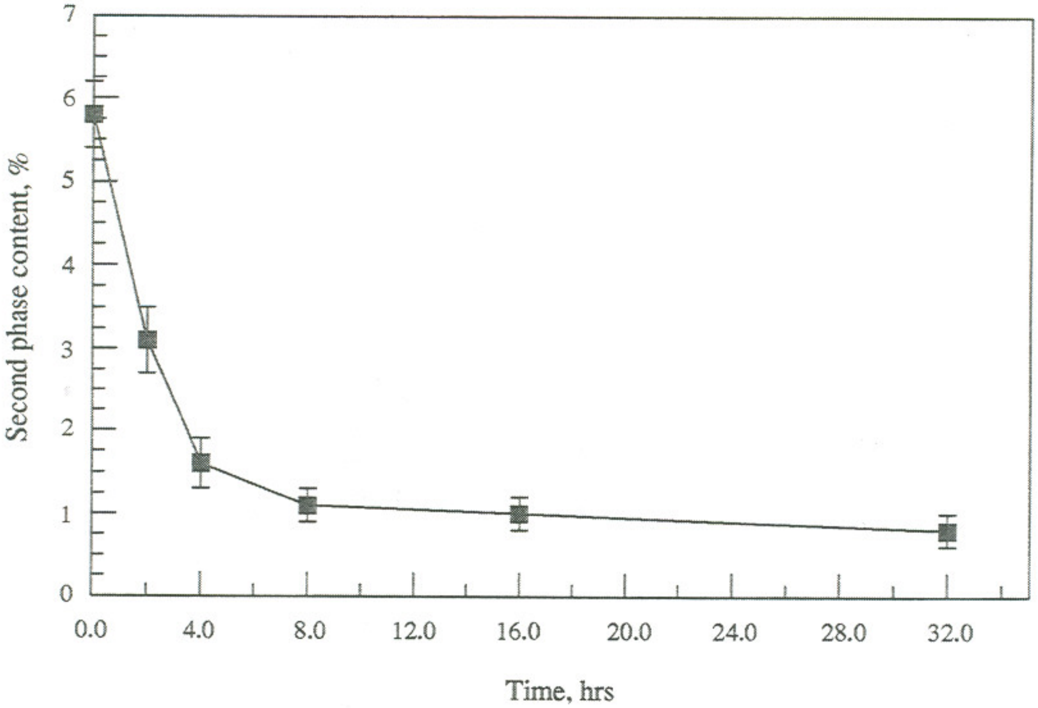

Figure 4-3: Solutionization behavior of conventionally cast F75 A material at 1199°C (2190°F)

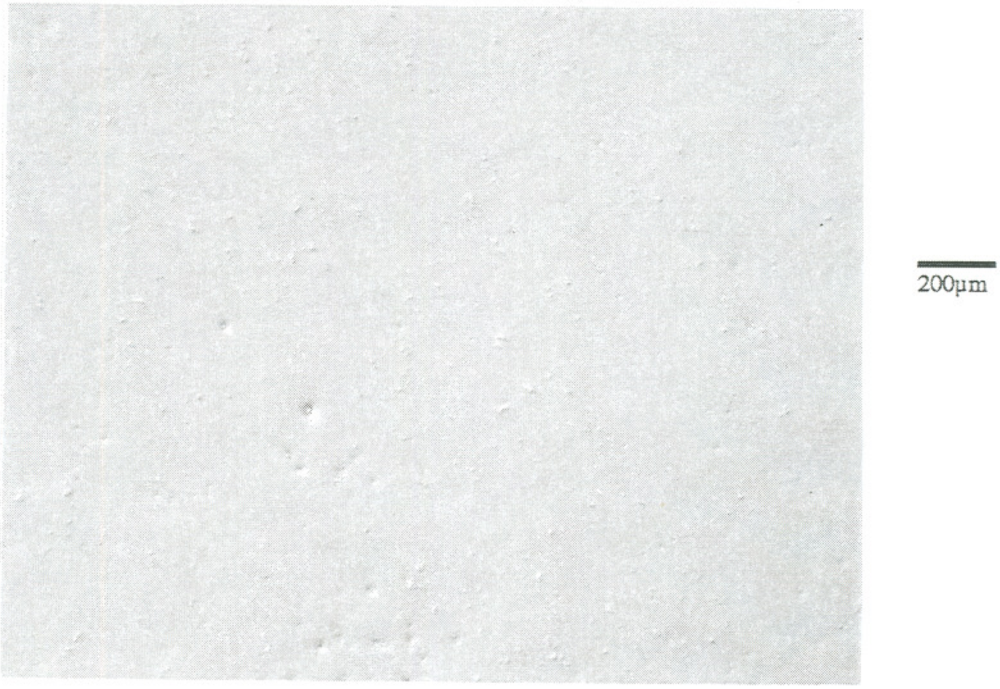

Figure 4-4: Microstructure of F75 A material after solutionizing for 32 hours at 1190°C (2175°F); 50x, unetched. Note possible Kirkendall voiding.

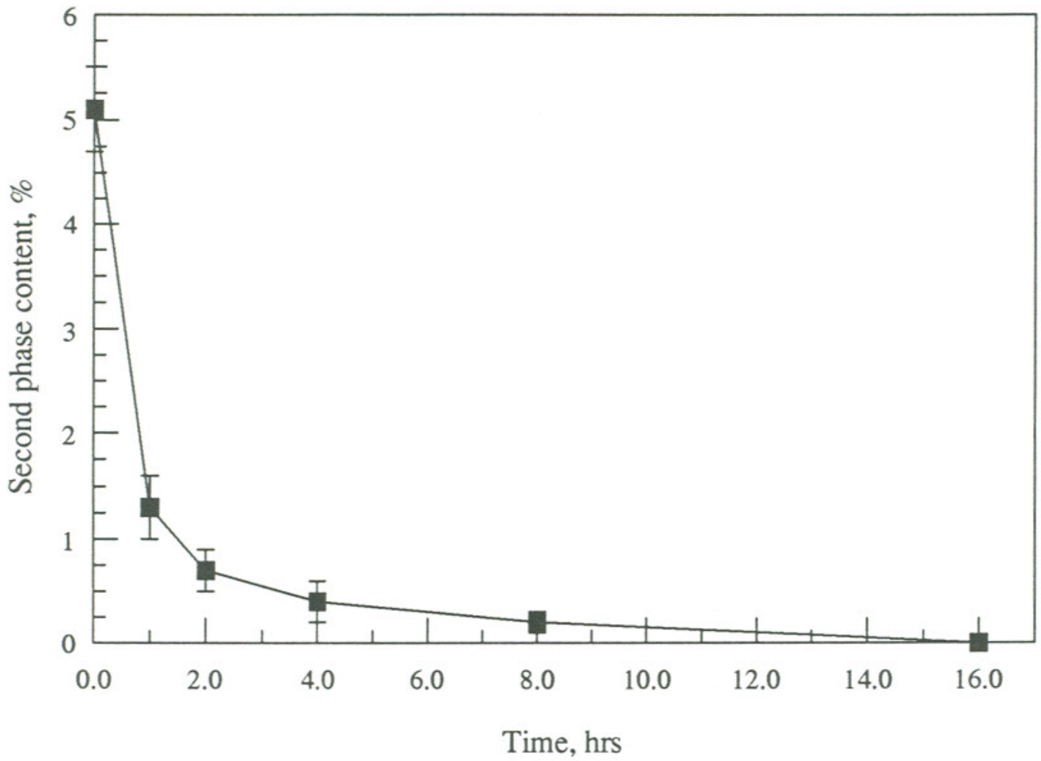

Figure 4-5: Solutionization behavior of conventionally cast F75 A material at 1220°C (2220°F), showing more rapid and complete response (compare x-axis to previous figure).

Effects of aging on conventionally cast materials

Microstructure

Aging of the conventionally cast specimens over such a wide range of temperature and time also resulted in a wide range of precipitate morphologies. They were classified as grain boundary precipitates; lenticular precipitates; transgranular strings of precipitates; fine, stipple of precipitates; and pearlitic precipitates. Additionally, the presence of residual interdendritic islands is noted. Representative microstructures demonstrating the various precipitate morphologies are shown in **Figures 4-6** through **4-10**. The distribution of these morphologies in the various heat treated specimens is summarized in **Table 4-2**.

Figure 4-6: Conventionally cast F75 A, HIPed, and then soaked at 1070°C (1960°F) for 8 hours. Shows some pearlitic precipitation, as well as lenticular, and grain boundary precipitates. Unetched, 400x

Figure 4-7: Conventionally cast F75 A, HIPed, soaked at 1070°C (1960°F) for 8 hours, and then aged for 6 hours at 900°C (1650°F). Shows grain boundary precipitation, as well as some discontinuous transgranular precipitates. Unetched, 400x

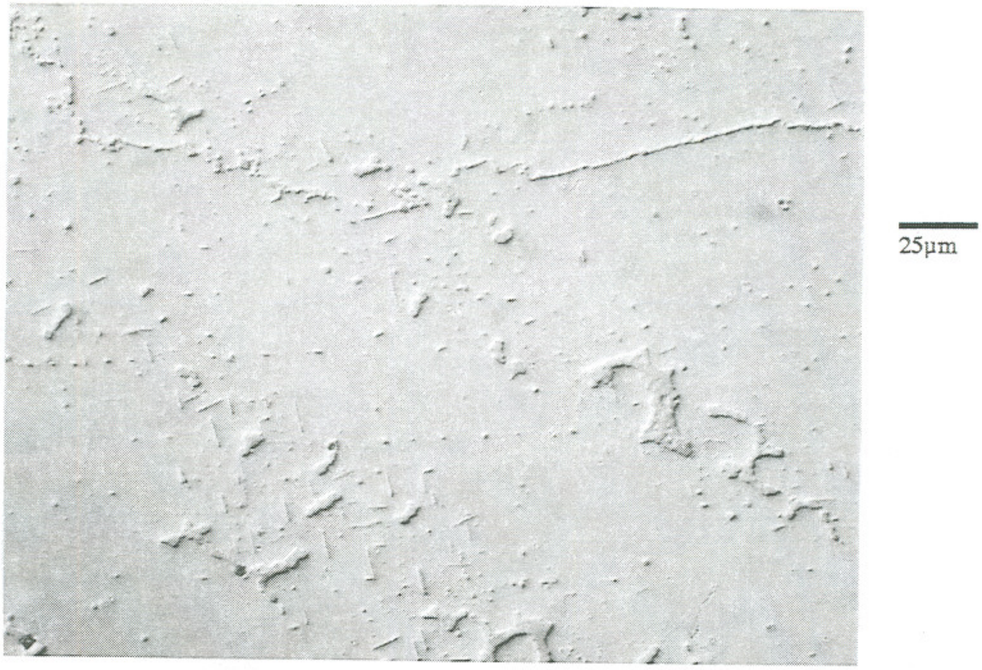

Figure 4-8: **Conventionally cast F75 A, HIPed, soaked at 1070°C (1960°F) for 8 hours, and then aged for 12 hours at 1050°C (1920°F). Shows lenticular precipitation, as well as some grain boundary precipitates. Unetched, 400x**

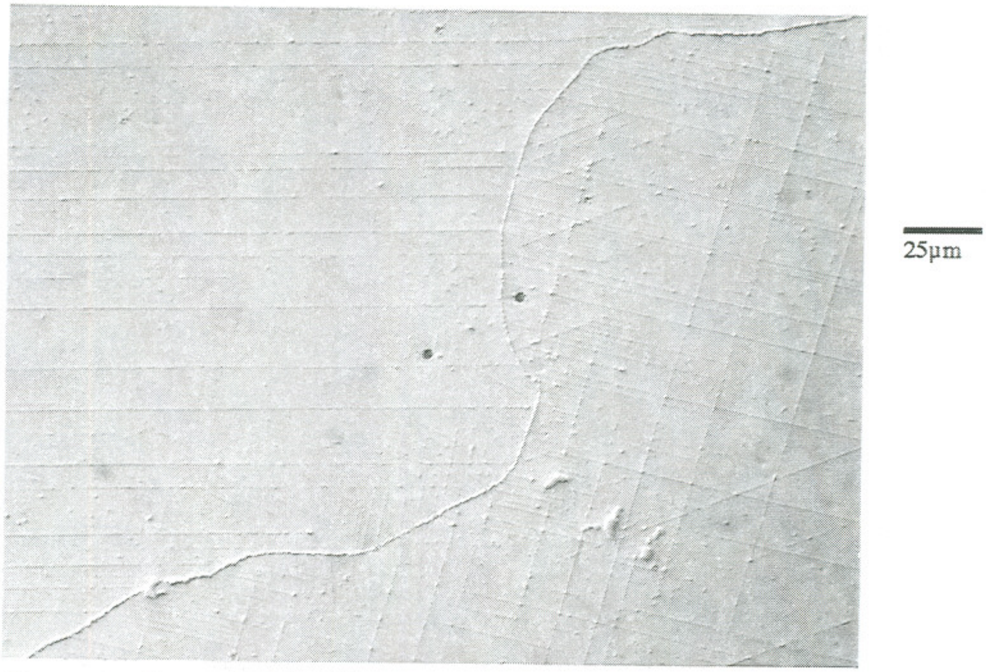

Figure 4-9: **Conventionally cast F75 A, HIPed, soaked at 1190°C (2175°F) for 8 hours, and then aged for 3 hours at 1050°C (1920°F). Shows precipitation in transgranular strings, as well as some grain boundary precipitates. Unetched, 400x**

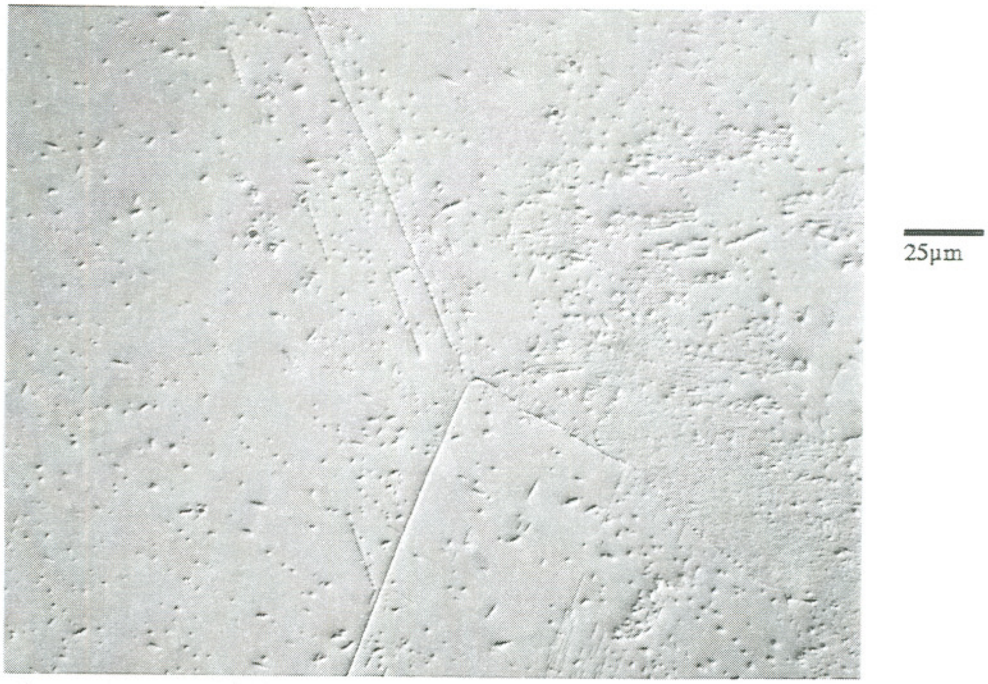

Figure 4-10: Conventionally cast F75 A, HIPed, soaked at 1220°C (2220°F) for 8 hours, and then aged for 6 hours at 1050°C (1920°F). Shows both fine stipple, and pearlitic morphologies, as well as some grain boundary precipitates. Unetched, 400x

Table 4-2: Summary of microstructural features in conventionally cast and then aged F75 A samples

Sample	Interdendritic Islands	Grain boundary	Lenticular	Transgranular Strings	Stipple	Pearlitic
HIPed	Med-high amount	Irregular- Coarse to none	None	None	None	None
1220	None	None	None	None	None	None
1190	Sparse, small	None	None	None	None	None
1070	Almost as much as as-HIPed, but more spread out	Similar to HIPed, but surrounded by other types	Some	Sporadic and discontinuous	Moderate	Quite a bit; near interdendritic islands
A/1070/ 700/3	Similar to 1070	Similar to 1070	More than in 1070	Discontinuous, but well defined	Moderate, but similar to Transgranular strings	A small amount
A/1070/ 900/6	Same as 1070, but less other particles attached	Like 1070, but with less of the other morphologies	Present	Semi-continuous, but not well defined	Sparse	Very little
A/1070/ 1050/12	Present, but not as much as in 1 and 2	Well defined; fairly uniform	Most common morphology	None	Moderately sparse	None
A/1190/ 700/6	Same as in 1190	None or very little	None	Resolved only in some highly polished grains	None	None
A/1190/ 900/12	Same as in 1190	Thin, continuous, well defined	None	None	None	None
A/1190/ 1050/3	Very little	Similar to #5, but more continuous	Very little	Very abundant; continuous, with nodes at intersections	Moderate	None
A/1220/ 700/12	None; only pores	None	None	Very faint	None	None
A/1220/ 900/3	None	Heavy, very coarse	None	None	None	None
A/1220/ 1050/6	None	Continuous, well defined, uniform	Some	Discontinuous and irregular	Very heavy	Quite a bit, generally near grain boundaries

TEM Examination

Examination of the materials in various conditions was made in the TEM. In the as-cast specimen, the second phase was largely identified as $Cr_{23}C_6$ type, although Cr_7C_3 was also identified. In the 4 and 16 hour solutionized specimens, $Cr_{23}C_6$ was found exclusively (**Figure 4-11**). Diffraction patterns of the carbides within the matrix displayed a definite orientation relationship of the type $<111>_{carbide}//<111>_{FCC}$, or $<111>_{carbide}//<0001>_{HCP}$, as is typical of this material. In addition to the carbides, TEM analysis revealed the presence of stacking faults, generally associated with the carbides.

The majority of the TEM work took place on selected aged materials. **Figure 4-12** includes a diffraction pattern showing the clear cube-cube orientation relationship typically observed. The facetted precipitates were identified as $Cr_{23}C_6$ in a FCC Co matrix. Similar cube-cube orientation relations were observed for the precipitates in all of the samples. As shown in **Figure 4-13**, the well-oriented precipitation on a TEM scale varied from very fine carbides in group A/1190/700/6, to the comparatively coarse precipitation of group A/1220/900/3.

The group A/1070/700/3 specimen showed many regions of facetted precipitates. As shown in **Figure 4-14**, group A/1220/700/12 specimens displayed very fine, facetted precipitates, like those in group A/1070/700/6, but group A/1220/900/3 specimens showed reagions of heavy segregation leading to a pearlitic morphology. The sample only held at 1070°C (1960°F) for 8 hours displayed variety of the carbide morphologies present in the alloy. There were clusters of facetted precipitates ranging in size, but generally larger than those observed in the other samples.

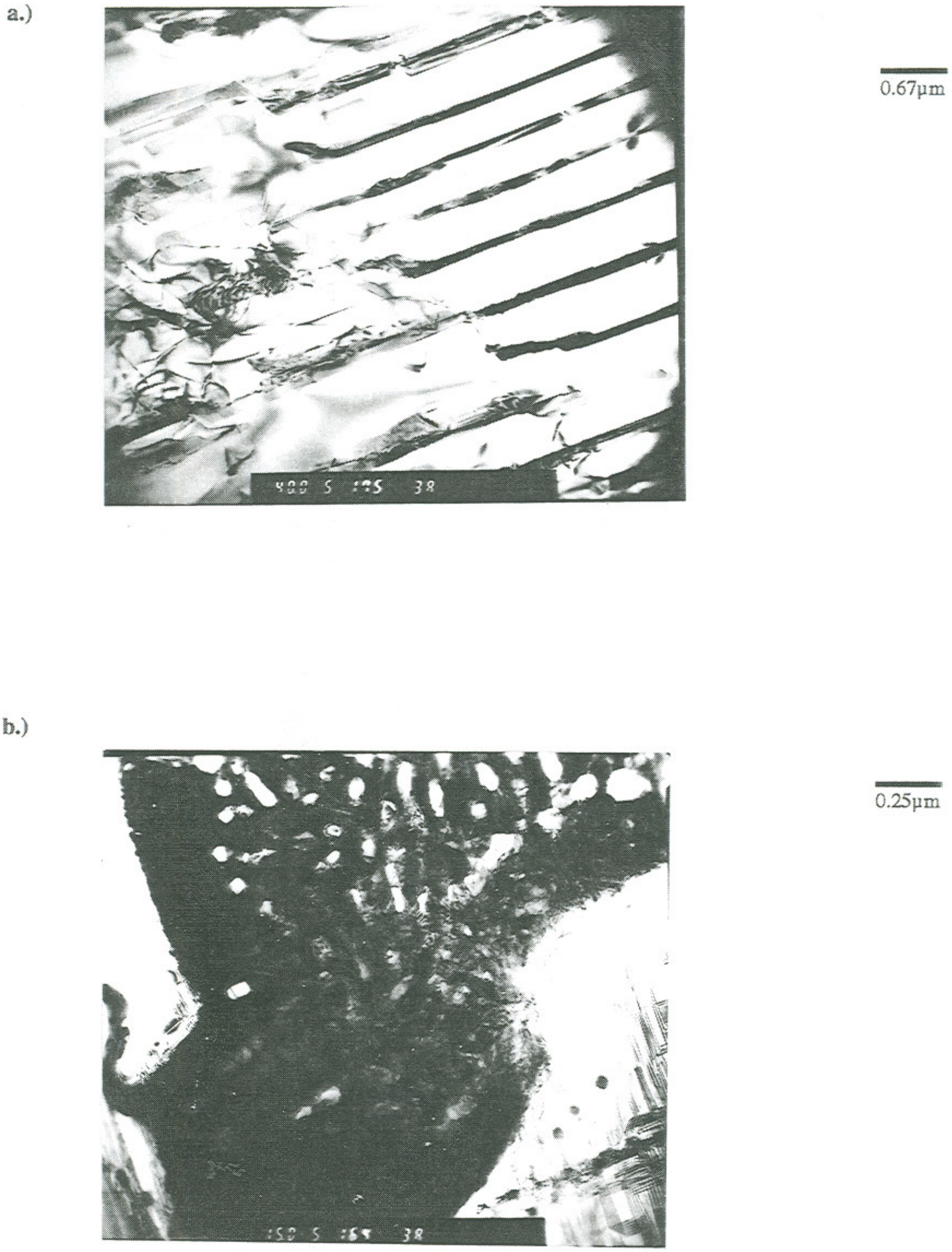

Figure 4-11: BF TEM images of conventionally cast F75 A, partially solutionized. a) Acicular $Cr_{23}C_6$, 40kX, and b.) residual $Cr_{23}C_6$ interdendritic island, 15kX.

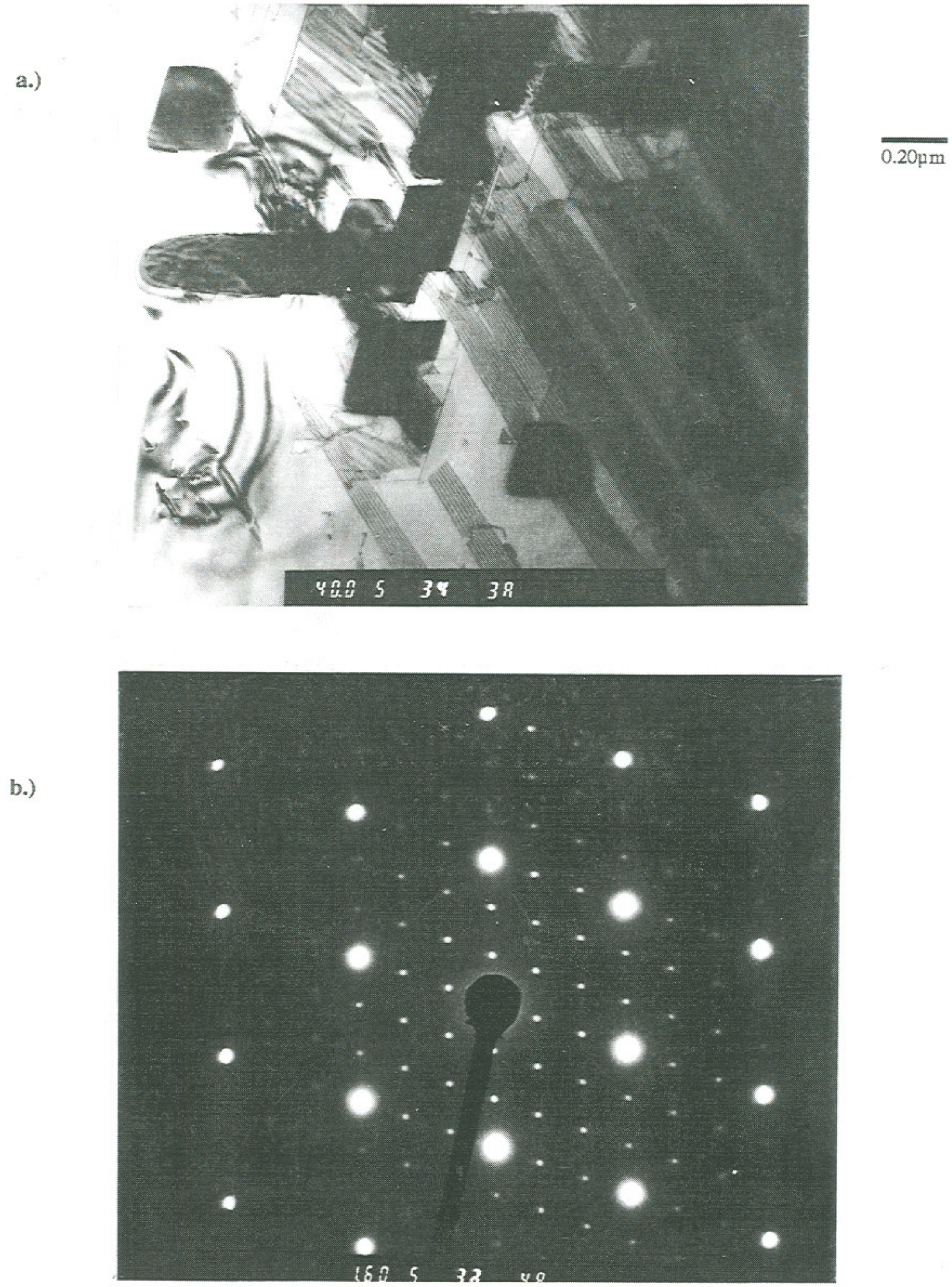

Figure 4-12: a.) BF TEM image of precipitates in sample A/1220/900/3, 40kX, 200keV, and b.) the corresponding SAD pattern showing a clear cube/cube orientation relationship for the precipitates and matrix. All other aged specimens showed similar relationships for the precipitates, only varying in size.

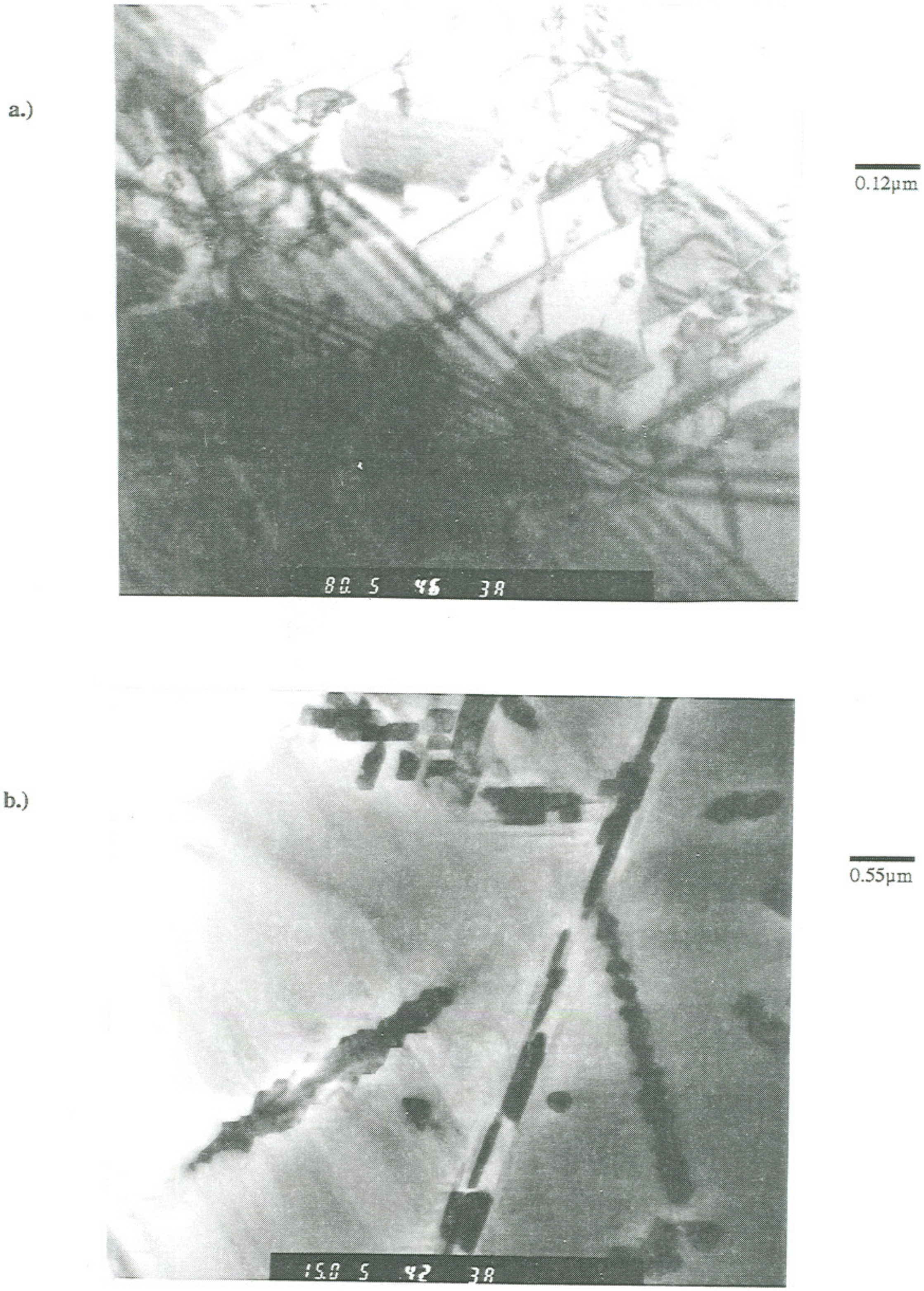

Figure 4-13: BF TEM images of precipitates in a.) sample A/1190/700/6, 80kX, 200keV, and b.) sample A/1220/900/3, 15kX, 200keV, demonstrating how the precipitates varying in size between processing conditions.
]

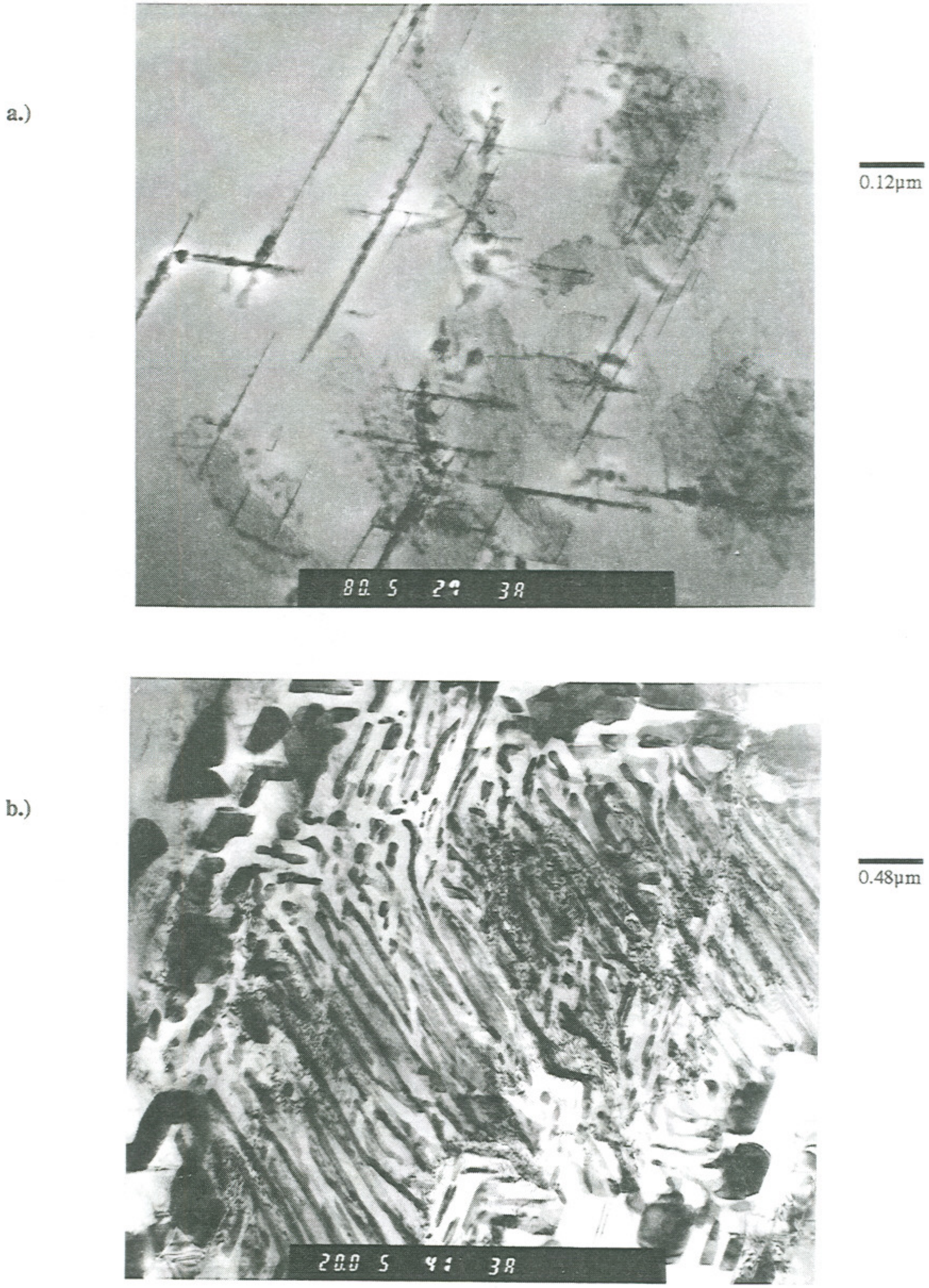

Figure 4-14: BF TEM images of precipitates in a.) sample A/1220/700/12, 80kX, 200keV, and b.) sample A/1220/900/3, 20kX, 200keV demonstrating the difference in morphologies and quantities observed between the processing conditions on a fine scale.

Mechanical Properties

The results of tensile testing round bar specimens of the conventionally cast and aged F75 A are shown in **Table 4-3.** The results with a standard deviation are an average of three test bars, but the others represent testing of only one bar. It is immediately evident from these results that most of the heat treat conditions resulted in a high yield strength, but in a dramatic loss of ductility. Group A/1190/700/6 was an exception, resulting in high ductility but little change in yield strength, and group A/1220/700/12 resulted in a desirable balance of properties that has comparable ductility, but 13% higher yield strength than the as-cast condition.

Table 4-3: Mechanical properties of conventionally cast and aged F75 alloy

Sample	Yield Strength; MPa (ksi)	Ultimate Tensile Strength; MPa (ksi)	Elongation; %	Reduction in Area; %
as-cast	523±3 (75.8±0.5)	775±23 (112.3±3.3)	10.3±1.9	10.7±2.8
1220	508±10 (73.6±1.5)	780±13 (113.1±1.9)	17.2±2.1	19.7±2.3
1190	513 (74.3)	820 (118.8)	18.0	16.5
1070	493 (71.4)	717 (103.9)	4.5	7.0
A/1070/ 700/3	557±31 (80.7±4.5)	714±23 (103.5±3.3)	3.2±1.5	5.0±2.8
A/1070/ 900/6	525±13 (76.1±1.9)	706±17 (102.3±2.4)	2.3±0.2	3.7±0.5
A/1070/ 1050/12	514±3 (74.5±0.5)	714±22 (103.5±3.2)	3.2±0.6	6.2±1.7
A/1190/ 700/6	536±5 (77.7±0.7)	805±1 (116.7±0.1)	13.5±1.5	16.5±3.1
A/1190/ 900/12	608±21 (88.1±3.0)	751±17 (108.9±2.5)	1.7±0.2	1.2±0.2
A/1190/ 1050/3	583±4 (84.5±0.6)	652±22 (94.5±3.2)	0.8±0.2	1.0±0.4
A/1220/ 700/12	591±15 (85.7±2.2)	803±13 (116.4±1.9)	9.3±1.3	10.8±1.8
A/1220/ 900/3	646±3 (93.6±0.4)	800±19 (116.0±2.7)	1.5±0	1.5±0.8
A/1220/ 1050/6	566±21 (82.1±3.1)	665±33 (96.4±4.8)	2.5±1.8	2.8±2.6

4.1.2 Fine-grained Cast Materials

The fine-grained cast materials were also examined in the as-cast form and the solution heat treated and aged conditions.

As-cast material

Microstructure

The results of measuring the grain size and second phase content in two typical fine-grained cast hip-stems of F75 B are shown in **Table 4-4**. **Figure 4-15** shows the typical microstructure resulting from the fine-grained casting process. The equiaxed grains were finer than in conventional castings, but the second phase content was distributed heavily along the grain boundaries. These results indicate a trend towards increasing grain size from bottom to top in the casting. They show a fairly uniform, high average second phase content along the length, until a possible drop in content near the top (as observed in stem #B1). Quantification of an F75 B round bar 1.9 cm (3/4 in) in diameter and 30 cm (12 in) in length at 5 cm (2 in) intervals, further displayed this tendency, as shown in **Figures 4-16** and **4-17**.

Table 4-4: Microstructural features in fine-grained cast hip-stems of F75

Region of measurement	Average grain diameter (μm)	ASTM grain number	Second phase vol%
Stem #B/FG/1-distal end	57±2	5.0	10.7±0.9
Stem #B/FG/1-mid-section	95±13	3.5	10.3±0.8
Stem #B/FG/1-proximal end	120±10	2.8	6.9±0.8
Stem #B/FG/2-distal end	50±3	5.4	10.1±0.6
Stem #B/FG/2-mid-section	72±8	4.3	9.8±1.1
Stem #B/FG/2-proximal end	111±11	3.1	9.4±0.8

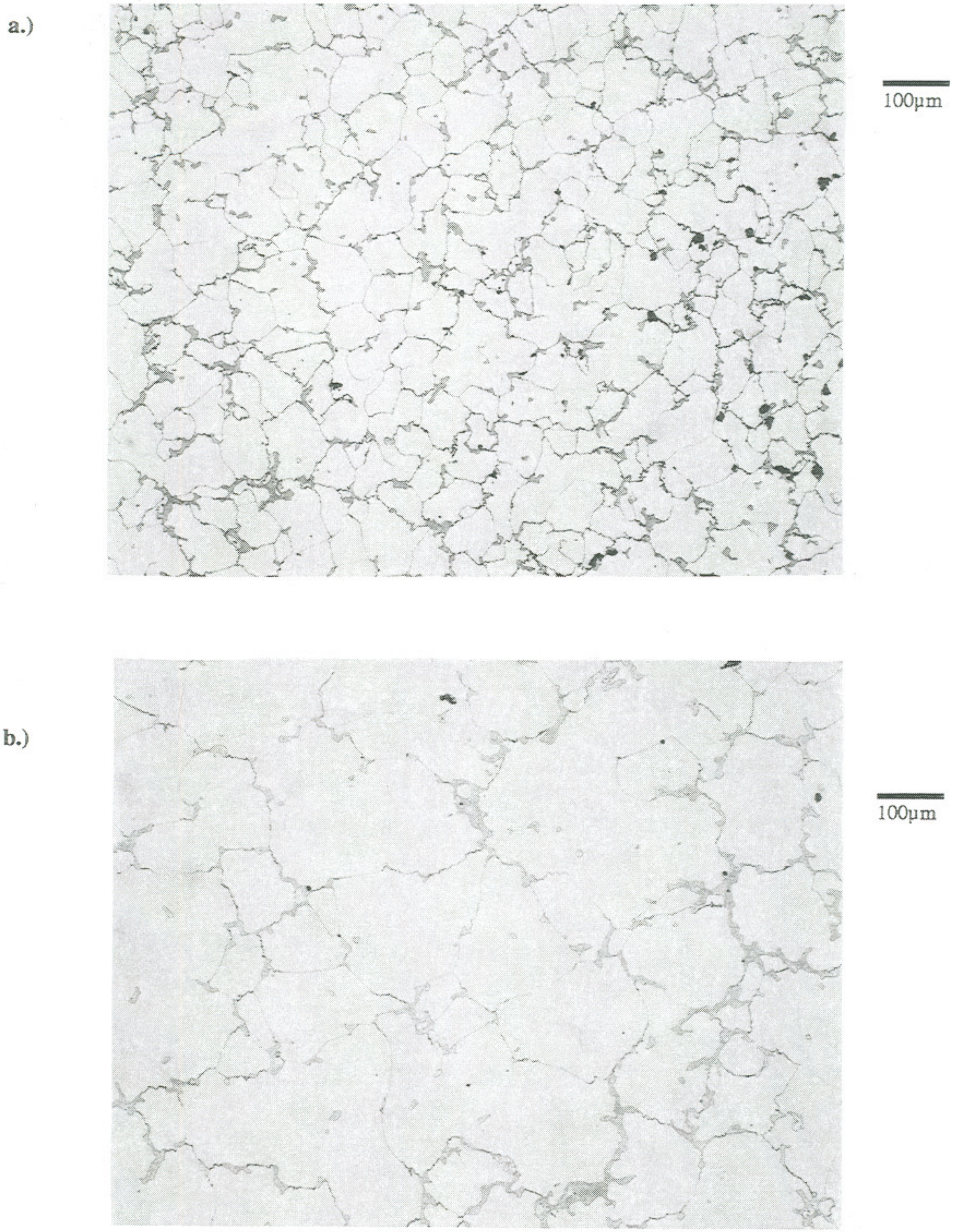

Figure 4-15: As-cast microstructure of fine-grained F75 B material from stem #B/FG/1 a.) distal portion, and b.) proximal portion; electrolytically etched in 10% ammonium persulfate solution, 100x.

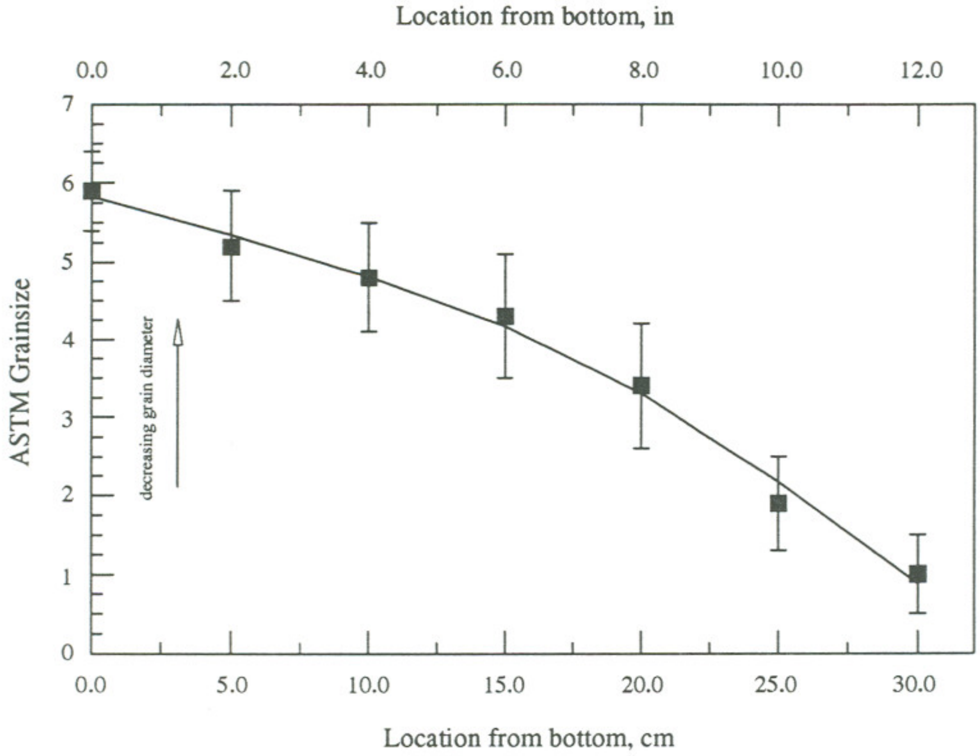

Figure 4-16: Grain size distribution along length of as-cast fine-grained bar of F75 B material

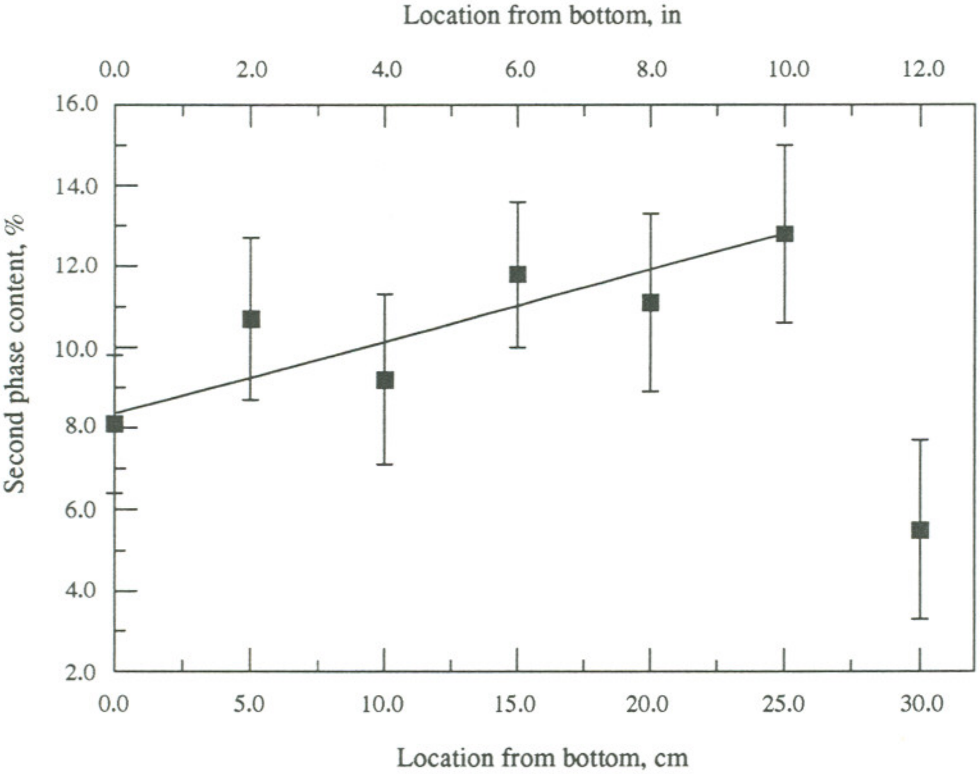

Figure 4-17: Second phase distribution along the length of as-cast fine-grained bar of F75 B material

Elemental Distribution

Semi-quantitative SEM/EDX analysis on a polished sample of the fine-grained material in the as-cast condition yielded an average composition of 33 wt% Co, 36 wt% Cr, 28 wt% Mo, and 1.4 wt% Si for the second phase material. For the conventionally cast version of this same alloy, the second phase material showed an average composition of 62 wt% Co, 20 wt% Cr, 16 wt% Mo and 1.4 wt% Si. The fine-grained second phase composition is higher in Cr, and in Mo than that measured for the conventionally cast second phase material, but shows the same type of dual segregation of Mo and Cr. However, the Cr segregation of the conventionally cast material was lower than the bulk composition. This was observed by Zhuang and Langer in their study [36] of slow cooled cast Co-Cr-Mo, but they did not show the high Mo segregation.

Figures 4-18 and **4-19** are SEM images and corresponding EDX maps for Co, Cr, and Mo segregation in second phase material of a fine-grained specimen. The sample had been HIPed at 1220°C (2225°F) for 4 hours and then slow-cooled (1220). The images indicate heterogeneous segregation of the Cr and Mo within the second phase material, with very little Co in it. This confirms the segregation of Mo, but also shows that the exact point of measurement in the second phase material could yield different results, which could explain the wide range of compositions described previously.

<u>Effect of solutionization on fine-grained material</u>

Solutionized coupons

Microstructure

The results of solutionization over time at 1190°C (2175°F) and 1220°C (2220°F) on the second phase content of the fine-grained F75 B material are shown in **Figure 4-20**. The graph in **Figure 4-21** illustrates the effect the thermal treatment had on the grain size of these samples. These figures show that solutionization occurred over time, with the lower temperature yielding less dissolution than the higher temperature for equal times. Also, grain-growth occurred non-uniformly within the specimens held for long times at the higher temperature. The specimens held at the lower temperature did not display significant grain growth. As shown in **Figure 4-22**, regions of grain growth were often associated with regions displaying more complete solutionization.

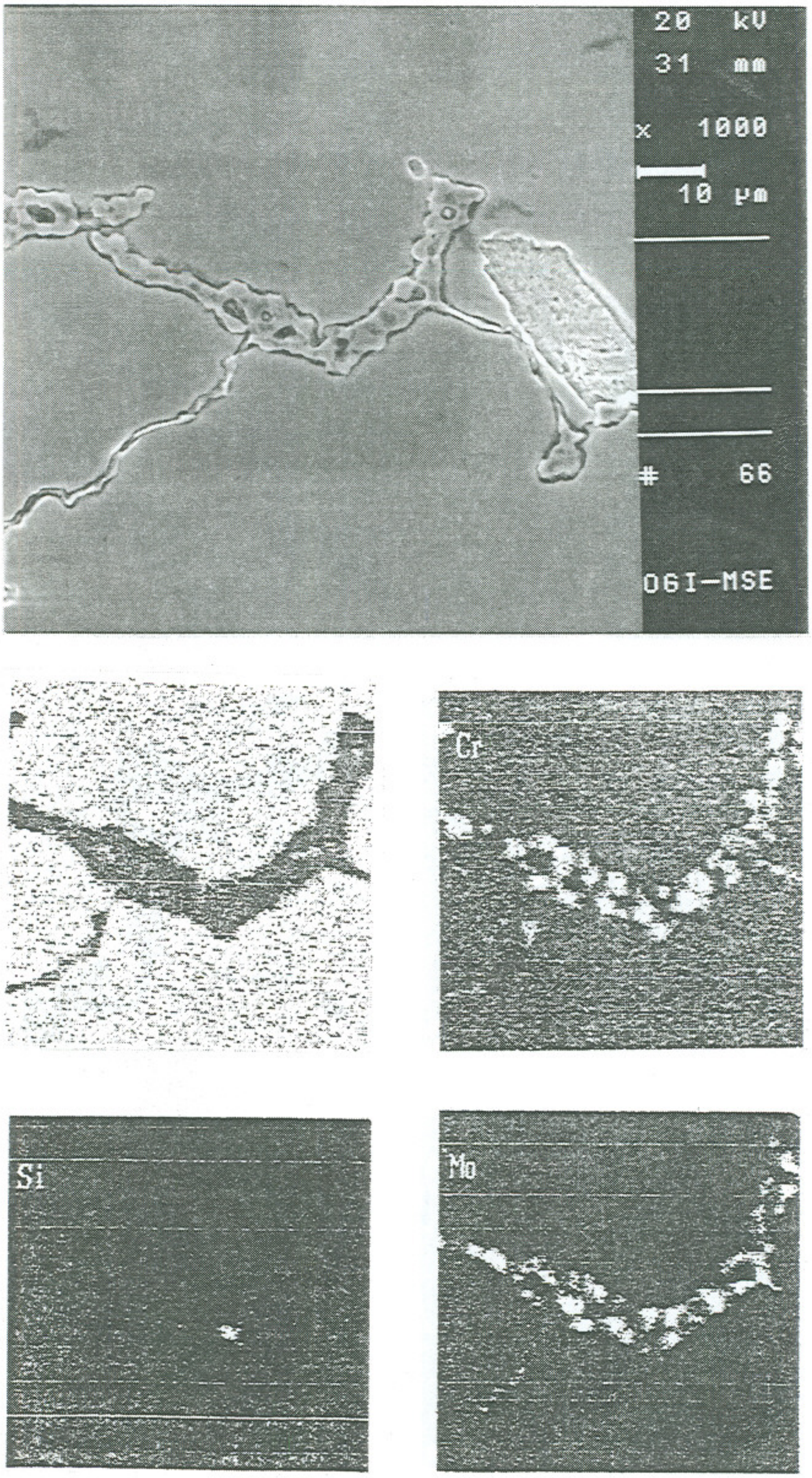

Figure 4-18: Secondary electron image and corresponding EDX maps for segregation in second phase material of a fine-grained specimen HIPed at 1220°C (2225°F) for 4 hours and then slow-cooled (1220). The images indicate heterogeneous segregation of the Cr and Mo within the second phase material, with very little Co in it.

Solutionized test bars

Microstructure

A variety of microstructures developed in the fine-grained test bars following the various heat treatments described in **Table 3-4** of the **Experimental Procedures** section. They ranged from heavy pearlitic precipitation as observed in **Figure 4-23** for sample 1220, to a retained fine grain size with minimal residual second phase, as shown in **Figure 4-24** for sample 1220/1190R. In general, the conventionally cooled specimens showed various degrees of precipitation at the grain boundaries, while the specimens with higher temperatures and longer times tended to have more large grains but less residual intergranular second phase. This is more readily observed in the results of quantitation of the microstructures of the test bars, as shown in **Table 4-5**. These microstructures were recorded for the mid-section of the hip-stems from which the test bars were excised, rather than from the gauge region of the test bars themselves. Thus, they may have a slightly inflated grain diameter over that of regions to which the mechanical properties are related.

Mechanical Properties

Shown in **Table 4-6** are the effects of the various solutionization processes on the mechanical properties of the fine-grained test bars taken from the cast hip-stems. It is apparent that, although there were processing variations, the strength values only varied by about 4 ksi, and the ductility by only 2-3%. Since these values represent only one test bar for each condition, they are subject to some statistical error. Thus, it is difficult to assess from the data whether or not a preferred processing method exists for solutionization of this material in this range.

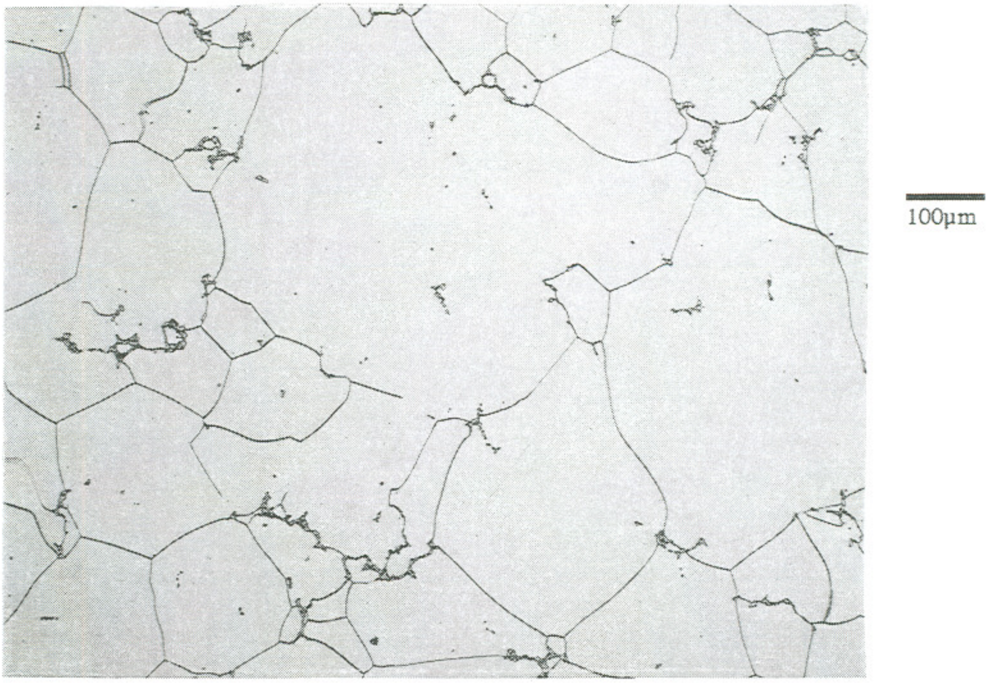

Figure 4-22: Fine-grained cast F75 B sample solutionized at 1220°C (2220°F) for 16 hours, followed by rapid cooling. Note the grain growth in reagions of less residual second phase; etched with 10% ammonium persulfate solution, 100x

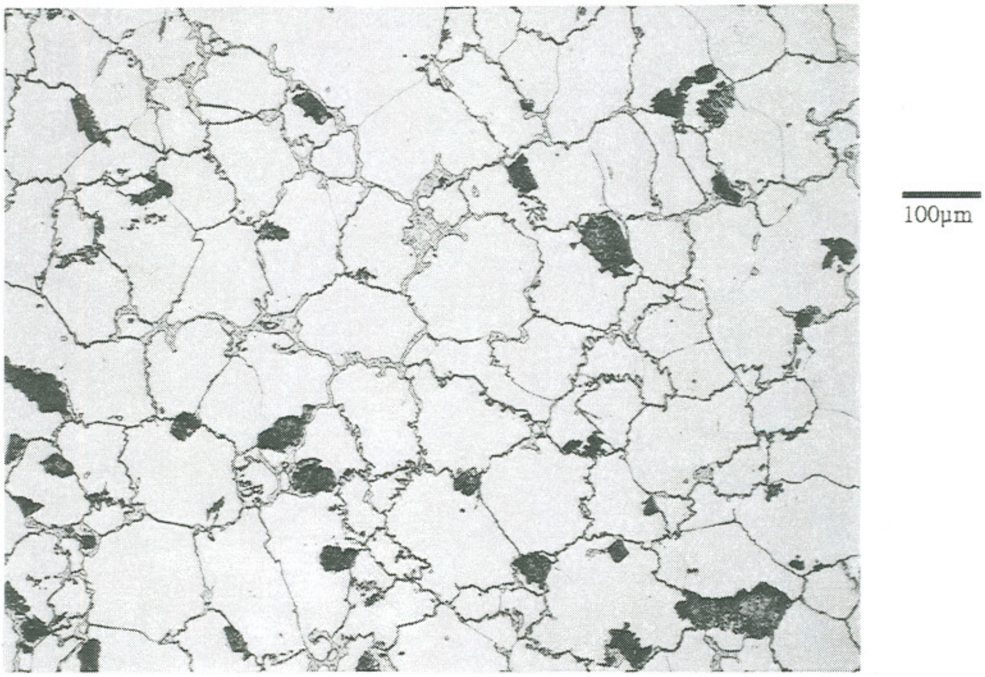

Figure 4-23: Fine-grained cast F75 B sample HIPed at 1220°C (2225°F) for 4 hours, followed by slow cooling. Note the heavy perlitic precipitation; etched with 10% ammonium persulfate solution, 100x

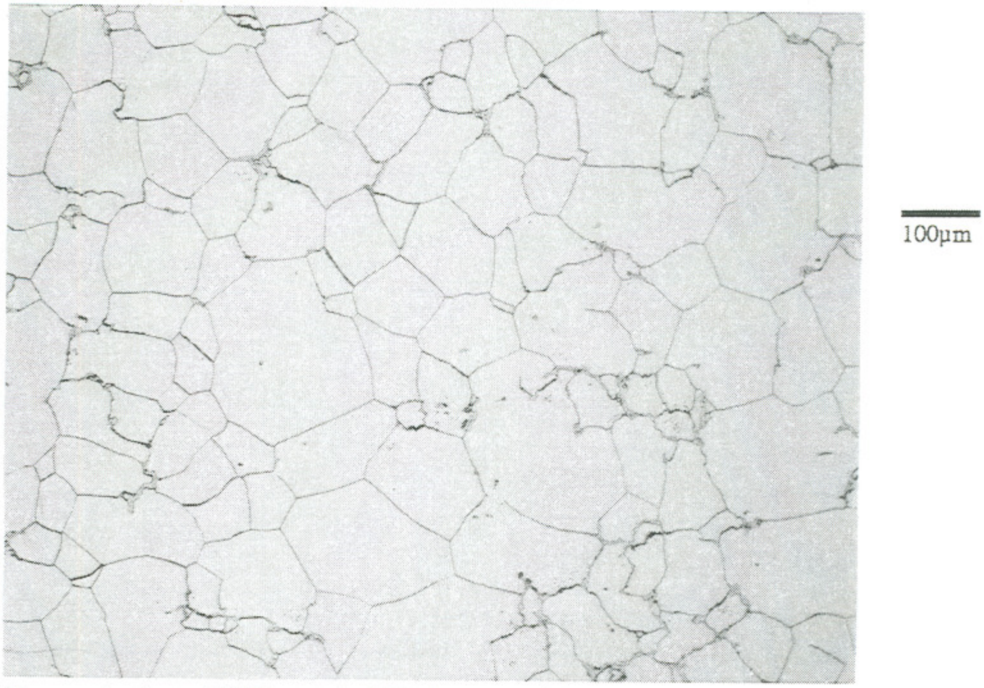

Figure 4-24: Fine-grained cast F75 B sample HIPed at 1220°C (2225°F) for 4 hours, slow cooled, then solutionized at 1190°C (2175°F) for 4 hours and rapidly cooled. Note the lack of precipitation; etched with 10% ammonium persulfate solution, 100x

Table 4-5: Quantification of microstructural features in fine-grained cast and solutionized samples F75

Sample ID	Average grain diameter (µm)	ASTM grain number	Second phase area%
1185R	64±11	4.7	3.5±0.8
1185/1190R	72±14	4.3	4.3±1.0
1185/1190	69±11	4.4	5.3±1.1
1185/1220R	80±16	4.0	3.2±0.8
1220/1190R	77±15	4.1	2.6±0.7
1220/1190	87±19	3.8	4.3±0.6
1220/1220R	93±18	3.6	2.5±0.8
1220/1220	138±44	2.4	6.2±1.6
1185	66±10	4.6	14.2±1.2
1220	79±14	4.0	16.3±1.0
1220R/1220R-B	306±105	0.1	1.5±0.5
1220R/1220R-T	220±136	1.1	1.0±0.5
pre aged-B	180±71	1.7	2.5±0.4
pre aged-T	164±40	1.9	2.8±0.8

Table 4-6: Mechanical properties of solutionized fine-grained cast test bars

Sample ID	Yield Strength; MPa (ksi)	Ultimate Tensile Strength; MPa (ksi)	Elong.; %	Red. in Area; %
1185R	582 (84.3)	756 (109.5)	4.1	5.0
1185/1190R	587 (85.1)	778 (112.8)	5.2	4.5
1185/1190	585 (84.8)	775 (112.3)	4.8	4.5
1185/1220R	573 (83.1)	784 (113.6)	5.2	4.7
1220/1190R	587 (85.1)	780 (113.1)	6.3	5.6
1220/1190	572 (82.9)	775 (112.3)	5.4	4.7
1220/1220R	565 (81.9)	783 (113.5)	7.2	6.6
1220/1220	562 (81.5)	783 (113.5)	6.6	4.9
1220R/1220R-B	553 (80.2)	887 (128.5)	14.1	13.5
1220R/1220R-T	558 (80.9)	762 (110.5)	8.5	8.3

B=bottom region, T=top region

Effect of aging on fine-grained material

Microstructure

Due to the lengthwise grain size variance previously observed in the cast bars, observations of the aged microstructure were made on samples taken from the ends of the test bars corresponding to the regions nearest the middle of the original 30 cm (12 in) cast bars.

The microstructures resulting from the aging cycles ranged from no noticeable change, as shown in **Figure 4-25** for the 650°C (1200°F), 16 hour specimen (B/650/16), to heavy grain boundary coverage and transgranular strings of fine precipitates, as shown in **Figure 4-26** for the 750°C (1380°F), 32 hour specimen (B/750/32). But, no other morphology was evident.

Mechanical Properties

The effect of the aging cycles on the mechanical properties of the fine-grained castings is shown in **Table 4-7**. Firstly, the solutionization was very good, reducing the yield strength of the "pre aged" sample by only about 50 MPa (7.4 ksi) in the bottom

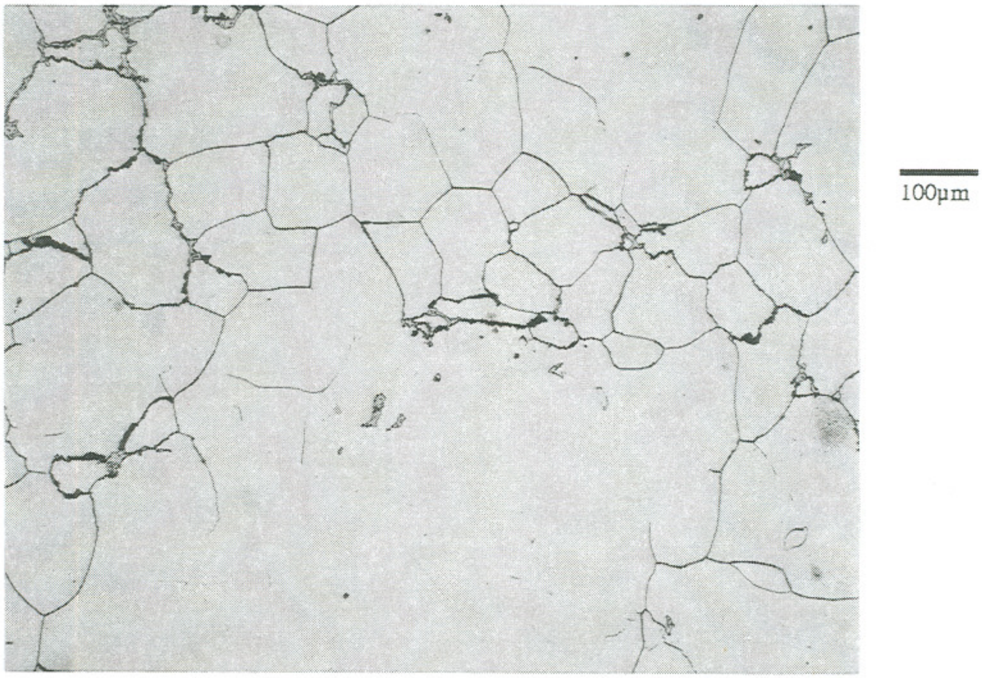

Figure 4-25: Fine-grained cast F75 B sample solutionized 16 hours at 1190°C (2175°F), then aged 16 hours at 650°C (1200°F) (specimen B/650/16). Note little microstructural change over solutionized condition; electrolytically etched with 10% ammonium persulfate, 100x

Figure 4-26: Fine-grained cast F75 B sample solutionized 16 hours at 1190°C (2175°F), then aged 32 hours at 750°C (1380°F) (specimen B/750/32). Note heavy grain boundary coverage and transgranular strings of fine precipitates; electrolytically etched with 10% ammonium persulfate, 100x

Table 4-7: Mechanical properties of aged fine-grained test bars

Sample ID	Yield Strength; MPa (ksi)	Ultimate Tensile Strength; MPa (ksi)	Elongation; %	Reduction in Area; %
as-cast-B	591 (85.7)	814 (118)	6.3	6.3
as-cast-M	558 (80.9)	745 (108)	5	4.7
as-cast-T	540 (78.2)	704 (102)	4.2	6.3
pre aged-B	542 (78.5)	904 (131)	18.6	20.5
pre aged-T	553 (80.2)	711 (103)	7.2	9.4
B/650/2-B	578 (83.7)	814 (118)	9.3	9.4
B/650/2-T	553 (80.1)	745 (108)	8.8	5.5
B/650/4-B	558 (80.8)	856 (124)	13	13.9
B/650/4-M	563 (81.6)	814 (118)	9.8	9.4
B/650/8-M	556 (80.6)	821 (119)	11.8	10.9
B/650/8-T	518 (75)	663 (96.1)	7.2	7.8
B/650/16-B	558 (80.9)	856 (124)	13.6	12.4
B/650/16-M	553 (80.1)	828 (120)	12.2	10.9
B/700/2-M	575 (83.4)	794 (115)	10	10.9
B/700/2-T	556 (80.6)	800 (116)	11.2	13.8
B/700/4-B	563 (81.6)	821 (119)	11.2	13.1
B/700/4-T	541 (78.4)	704 (102)	8.1	7.8
B/700/8-B	578 (83.7)	849 (123)	10.6	12.4
B/700/8-T	562 (81.4)	773 (112)	9.1	9.4
B/700/16-M	583 (84.5)	863 (125)	11.7	13.1
B/700/16-T	564 (81.8)	794 (115)	8.4	8.6
B/750/2-M	601 (87.1)	787 (114)	7.9	8.6
B/750/2-T	574 (83.2)	759 (110)	7.9	10.9
B/750/4-B	625 (90.6)	842 (122)	8.5	10.1
B/750/4-M	658 (95.3)	842 (122)	7.3	9.3
B/750/8-M	697 (101)	849 (123)	6.1	7.1
B/750/8-T	725 (105)	828 (120)	3.6	5.5
B/750/16-B	856 (124)	994 (144)	4	6.3
B/750/16-M	869 (126)	959 (139)	3.6	4.7
B/750/32-B	1042 (151)	1125 (163)	2.6	4.7
B/750/32-T	1000 (145)	1056 (153)	2.5	3.9

T=top, -M=middle, -B=bottom

region, while increasing the ductility three fold. Subsequent aging had very little effect on the yield strength in samples showing little precipitation , and the ductility may have been slightly reduced. Beginning with sample B/750/2, aged at 750°C (1380°F) for 2 hours, increasing time led to rapid increase in yield strength, but reduction in ductility. Nevertheless, a property balance was achieved in samples B/750/4 and B/750/8, in which ductilities were similar to or higher than the as-cast, but had a 12 to 25% higher yield strength. In general, the bottom, or finer region of the castings had slightly better properties.

4.2 Nitrogen-High Pressure Melted Stellite 21

The N-HPM materials were examined in both the as-cast form and the hot-rolled and heat-treated forms.

4.2.1 As-cast Material

Nitrogen Content

As shown in **Table 4-8**, the nitrogen content of the N-HPM ingots increased with melt over-pressure. The results confirm that the first melt done at 16 atm was not held for a long enough time to achieve an equilibrium of nitrogen in the melt, as shown by the higher nitrogen content of the second 16 atm melt. Nevertheless, as shown in **Table 4-8**, the melts gave a suitable range of nitrogen contents, which was the ultimate goal of the melting. Also evident in **Table 4-8** is the fact that there was a rather large discrepancy between the nitrogen content of the top and bottom of the 50 atm ingot. Subsequent nitrogen measurements from the mid-height region of the ingot yielded 0.86 wt% also, in agreement with the bottom measurement, showing that the nitrogen content was consistent in at least the lower half of the ingot. The high nitrogen measurement may have been the result of inflation due to gas bubbles which formed in the top region of the melt in the final stages of solidification, or else the upper region may more closely represent the equilibrium content, since it was closer to the nitrogen source. In the latter case, the lower region would not represent an equilibrium content though.

Sievert's law suggests that the amount of nitrogen dissolved in the melt should be proportional to the square root of the pressure. At high pressures, Sievert's law breaks down and then solubility is proportional to pressure to a power less than 0.5. **Figure 4-27** shows that Sievert's law was approximated in the case of nitrogen in Stellite 21, but not closely. It also shows that perhaps the equilibrium nitrogen content of the 50atm ingot lies somewhere between the low and high values measured, but perhaps closer to the lower value. Sources for deviation would most likely be due to variations in the actual melt kinetics such as stirring, diffusion, etc. It should be noted that the 0 atm nitrogen melt pressure is actually 10 atm of Ar, so that may not be an accurate assumption that the over-pressure is zero. Likely it is some number greater than that, since it did result in about 0.1 wt% N. The important thing is that a range of nitrogen contents was achieved in the materials through the N-HPM process.

Table 4-8: Weight percent nitrogen in N-HPM Stellite 21 ingots following casting

Melt ID (Melt #)	**10 atm Ar** #276	**1.4 atm** #265	**4 atm** #249	**16 atm A** #262	**16 atm B** #271	**50 atm** #259
Top	0.10	0.19	0.33	0.39	0.52	1.34
Bottom	0.10	0.19	0.35	0.39	0.52	0.86

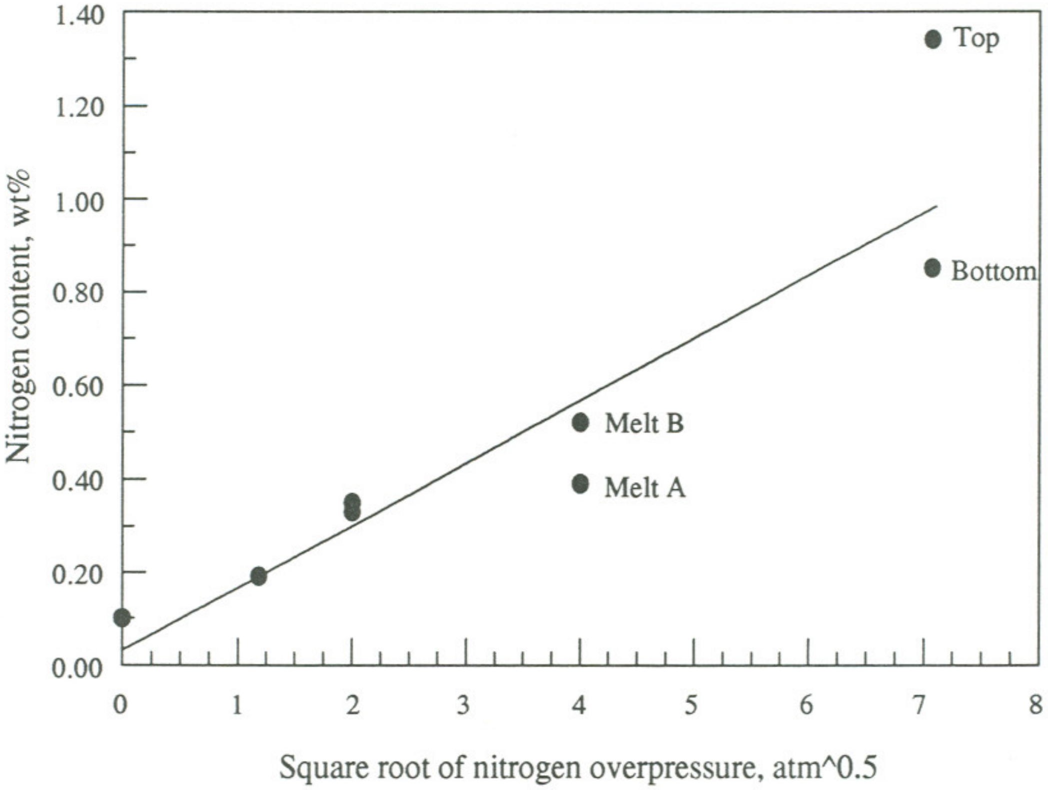

Figure 4-27: Nitrogen content as a function of melt pressure in N-HPM Stellite 21 ingots

Microstructure

Micrographs

The microstructure of the N-HPM ingots was characterized by large amounts of segregation. The macro structure of the 4 atm ingot is representative of the typical segregation structure (**Figures 4-28** to **4-30)** of all of the ingots. As depicted, the as-cast structure showed a cored dendritic structure in the bottom and edge regions, with heavily decorated grain boundaries present towards the mid-section and mid-radius regions, and finally a dense segregation network in the top and inner regions. Generally, as the nitrogen over-pressure was increased, the amount of second phase material also increased. This is evident in **Figure 4-31**, which shows the top, center region of the 50 atm as-cast ingot.

In the higher magnification micrographs shown in **Figures 4-32** to **4-36**, the second phase is observed to take on three basic morphologies. Near the edges and at the lower melt pressures, the second phase was generally interdendritic islands, as shown in **Figure 4-32**. As melt pressure was increased and as the middle of the ingot was approached, two changes were observed. Firstly, the interdendritic islands increased in size, and secondly, a lamellar morphology was observed (**Figures 4-33, 4-34**). These lamellar regions were often observed along grain boundaries, and tended to be associated with the interdendritic islands as shown at higher magnification in **Figure 4-35**. At the highest melt pressure, the fine lamellar morphology was not as evident as was a rosetting of the interdendritic islands, as shown in **Figure 4-36**. These are all artifacts of the solidification process, which had a slower cooling rate in the upper region.

SEM Examinations

Figures 4-37 and **4-38** show the two basic second phase morphologies observed in the ingots; the lamellar material, and the interdendritic islands. The resulting spectra from EDX analysis of the interdendritic material indicated that it was rich in Cr and Mo with respect to the matrix.

Figures 4-39 and **4-40** show the three-dimensional structure of the lamellar second phase as revealed by SEM following dissolution of the matrix. It is evident from these images that the lamellar material consisted of closely spaced plates which could be randomly oriented with respect to one another in a larger scale, but quite parallel on a fine scale.

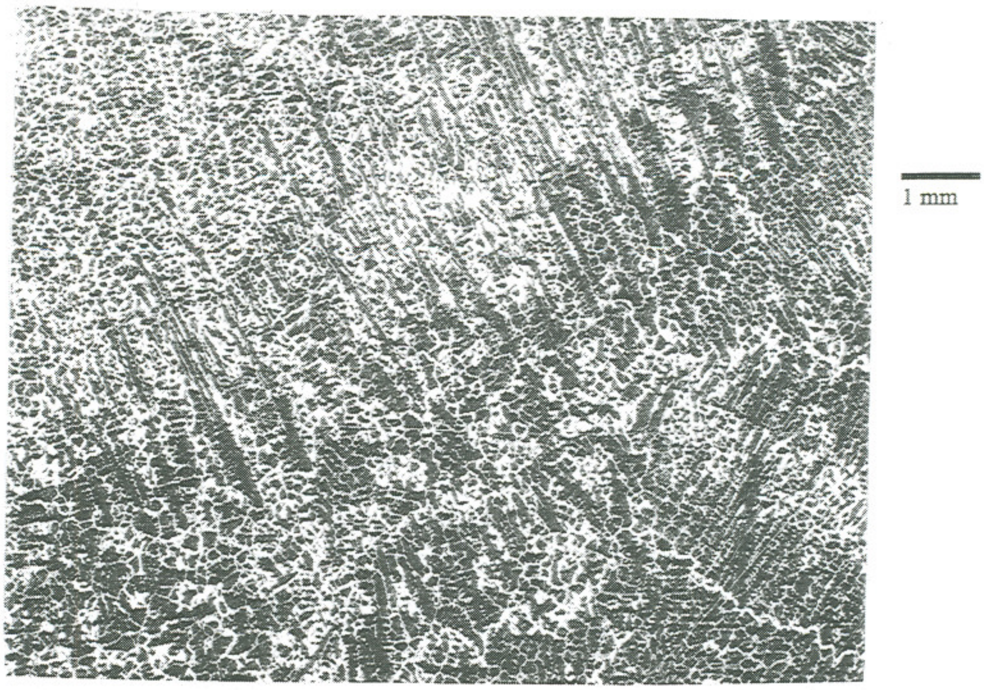

Figure 4-28: As-cast Stellite 21 ingot, N-HPM at 4 atm, upper region, longitudinal section, showing typical segregation; electrolytically etched with 10% ammonium persulfate, 10x

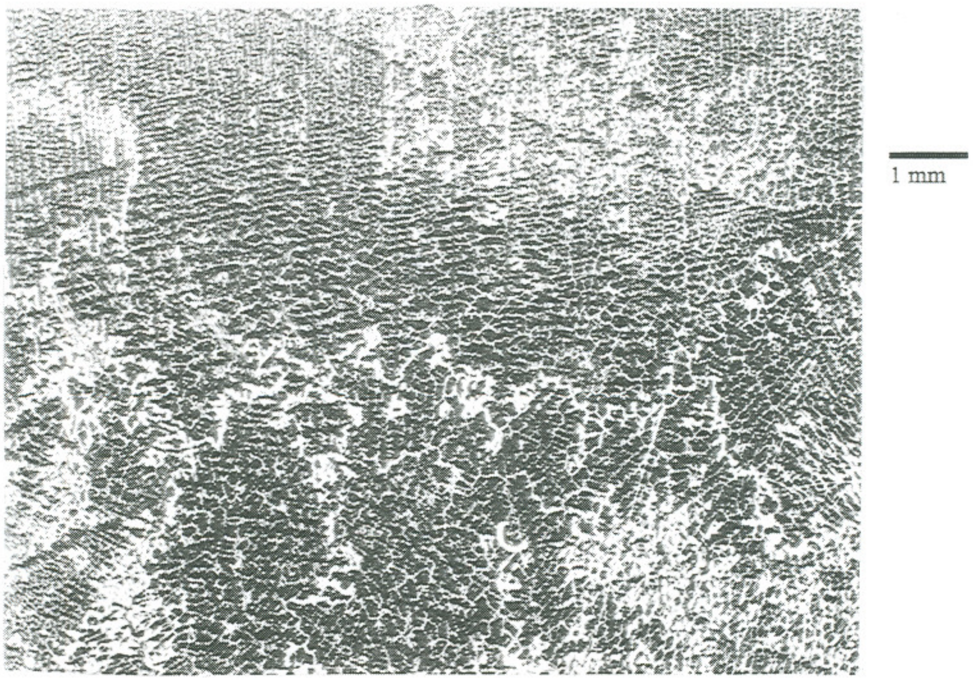

Figure 4-29: As-cast Stellite 21 ingot, N-HPM at 4 atm, lower region, longitudinal section, showing typical segregation; electrolytically etched with 10% ammonium persulfate, 10x

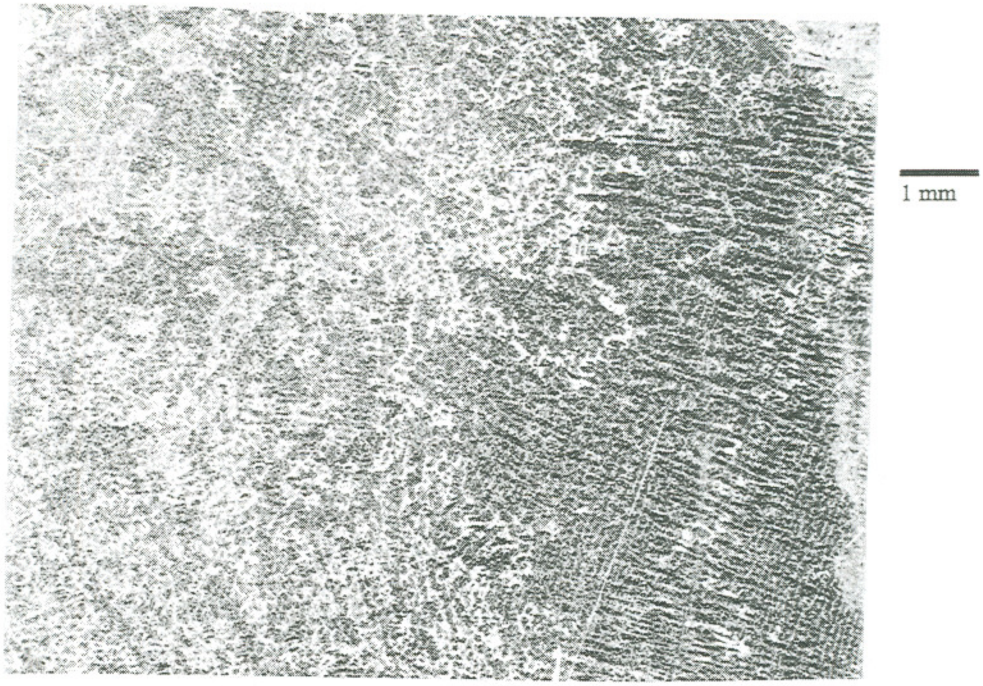

Figure 4-30: As-cast Stellite 21 ingot, N-HPM at 4 atm, upper region, cross section, showing typical segregation; electrolytically etched with 10% ammonium persulfate, 10x

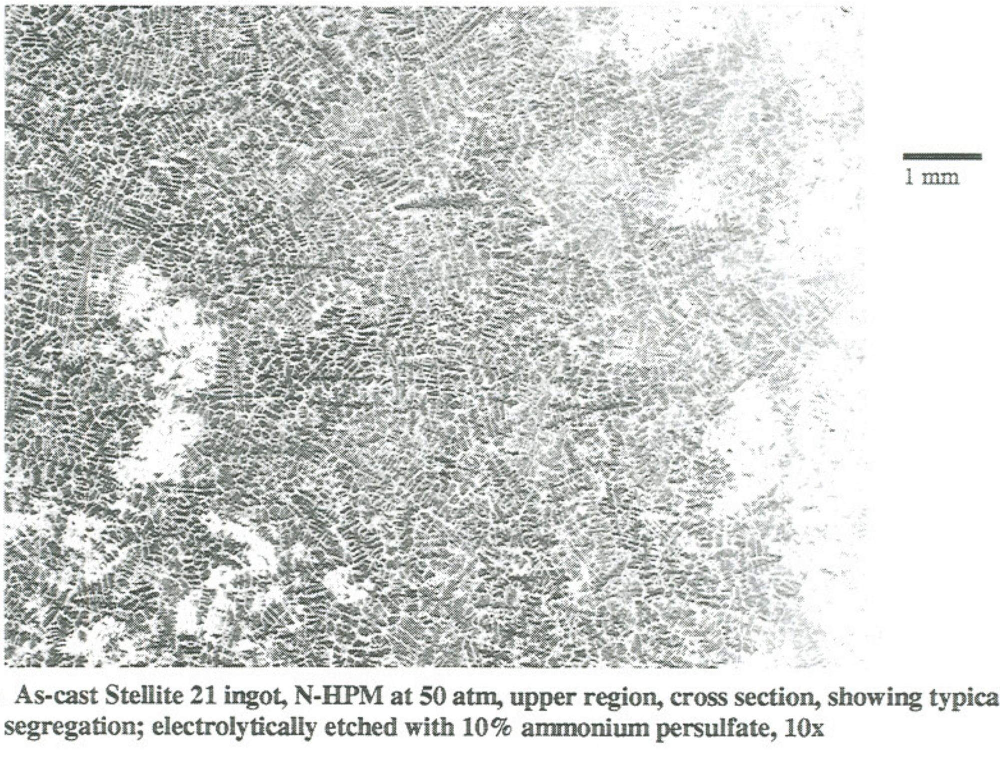

Figure 4-31: As-cast Stellite 21 ingot, N-HPM at 50 atm, upper region, cross section, showing typical segregation; electrolytically etched with 10% ammonium persulfate, 10x

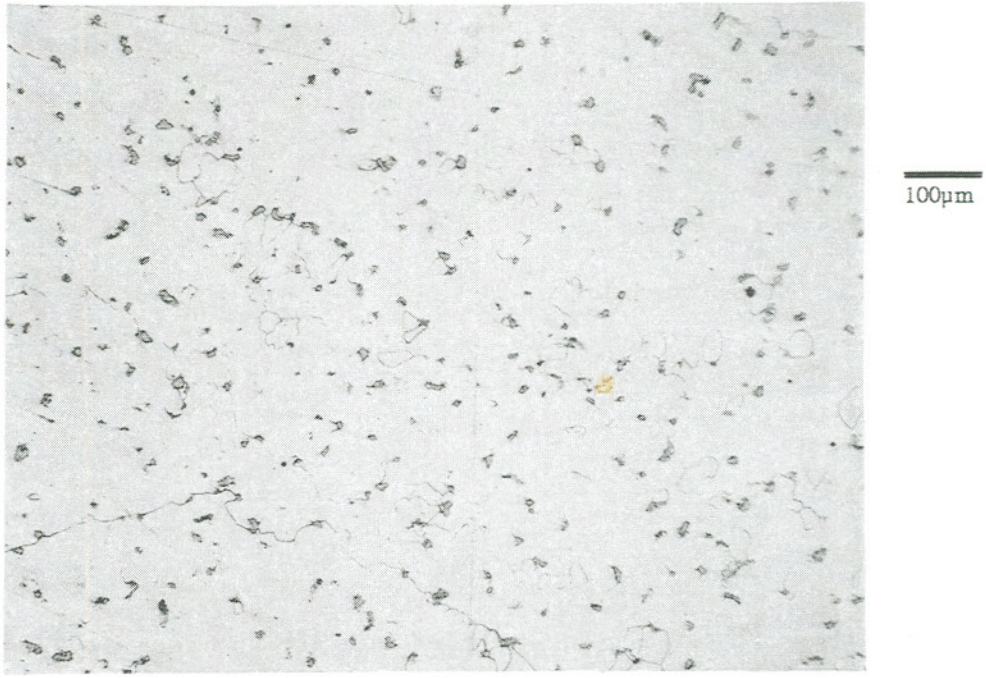

Figure 4-32: As-cast Stellite 21 ingot, N-HPM at 1.4 atm, ingot bottom, edge region, showing fine interdendritic material; electrolytically etched with 10% ammonium persulfate, 100x

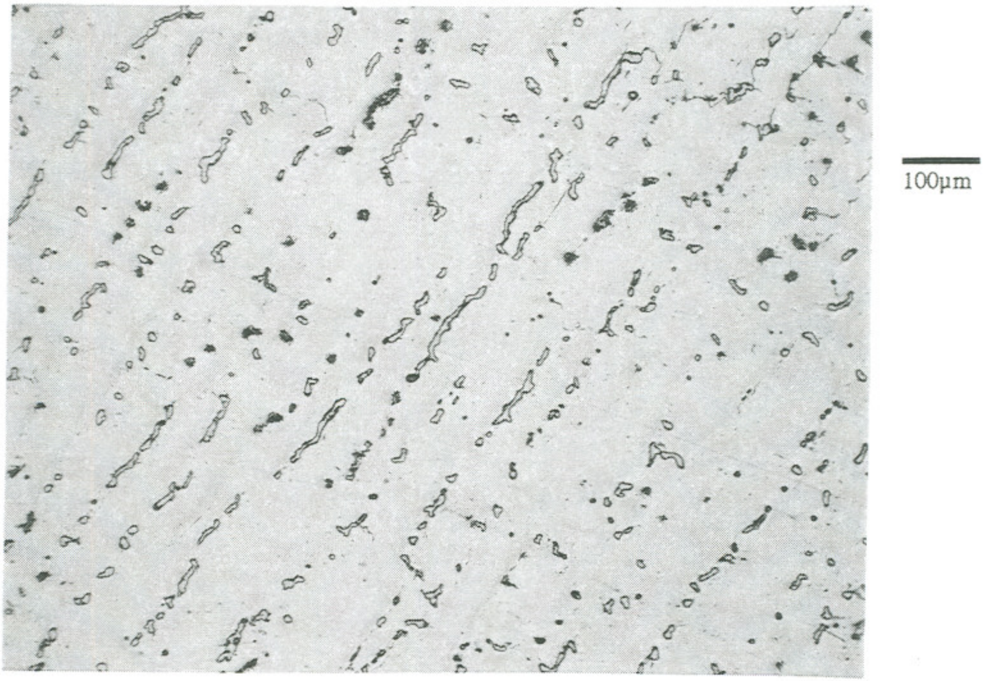

Figure 4-33: As-cast Stellite 21 ingot, N-HPM at 16 atm, ingot bottom, edge region, showing coarser interdendritic material; electrolytically etched with 10% ammonium persulfate, 100x

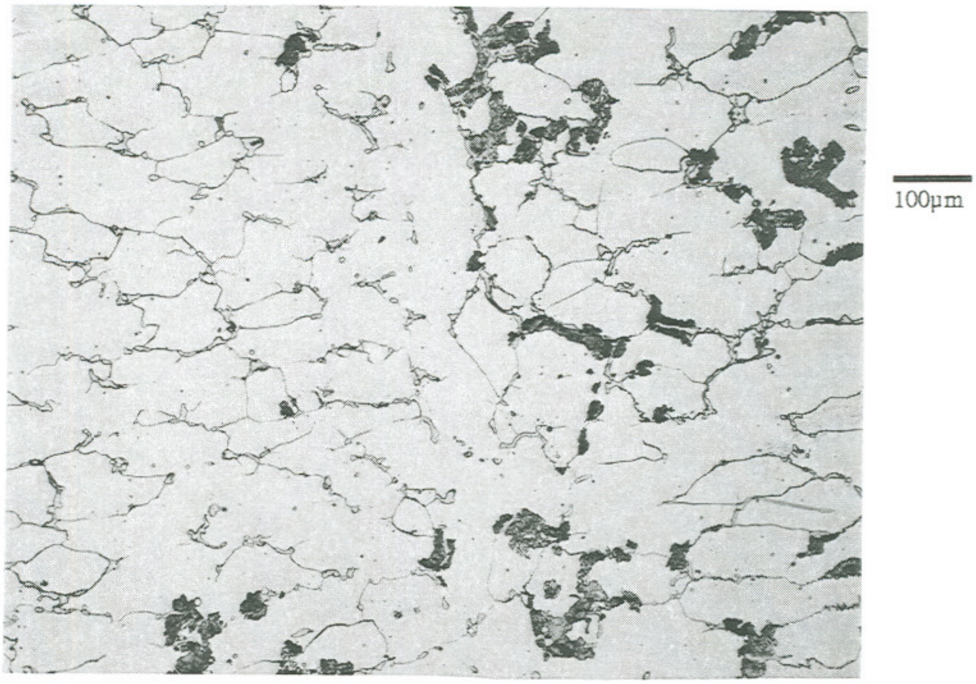

Figure 4-34: As-cast Stellite 21 ingot, N-HPM at 4 atm, ingot bottom, center region, showing emergence of lamellar second phase material; electrolytically etched with 10% ammonium persulfate, 100x

Figure 4-35: As-cast Stellite 21 ingot, N-HPM at 4 atm, ingot bottom, mid-radius region, showing lamellar second phase material associated with interdendritic islands; electrolytically etched with 10% ammonium persulfate, 400x

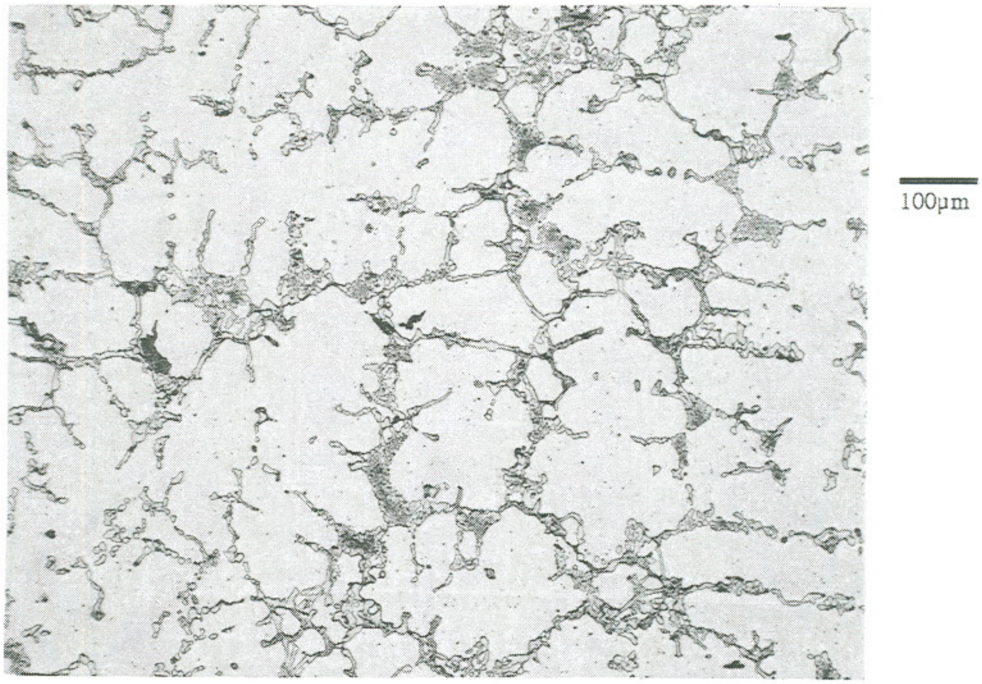

Figure 4-36: As-cast Stellite 21 ingot, N-HPM at 50 atm, ingot top, center region, showing coarse interdendritic material; electrolytically etched with 10% ammonium persulfate, 100x

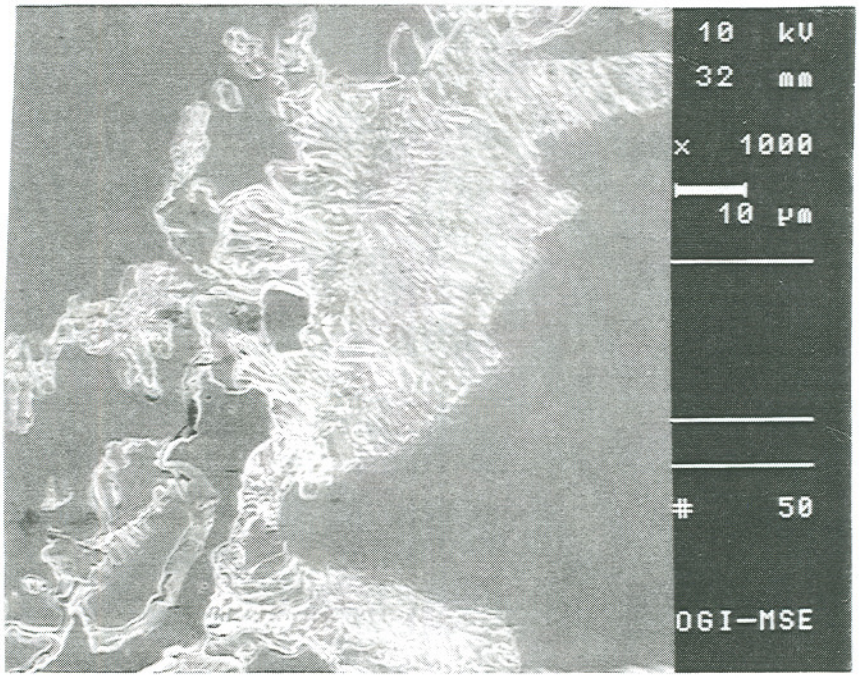

Figure 4-37: Secondary electron image of as-cast Stellite 21 ingot, N-HPM at 4 atm, ingot bottom, mid-radius region, showing lamellar second phase material

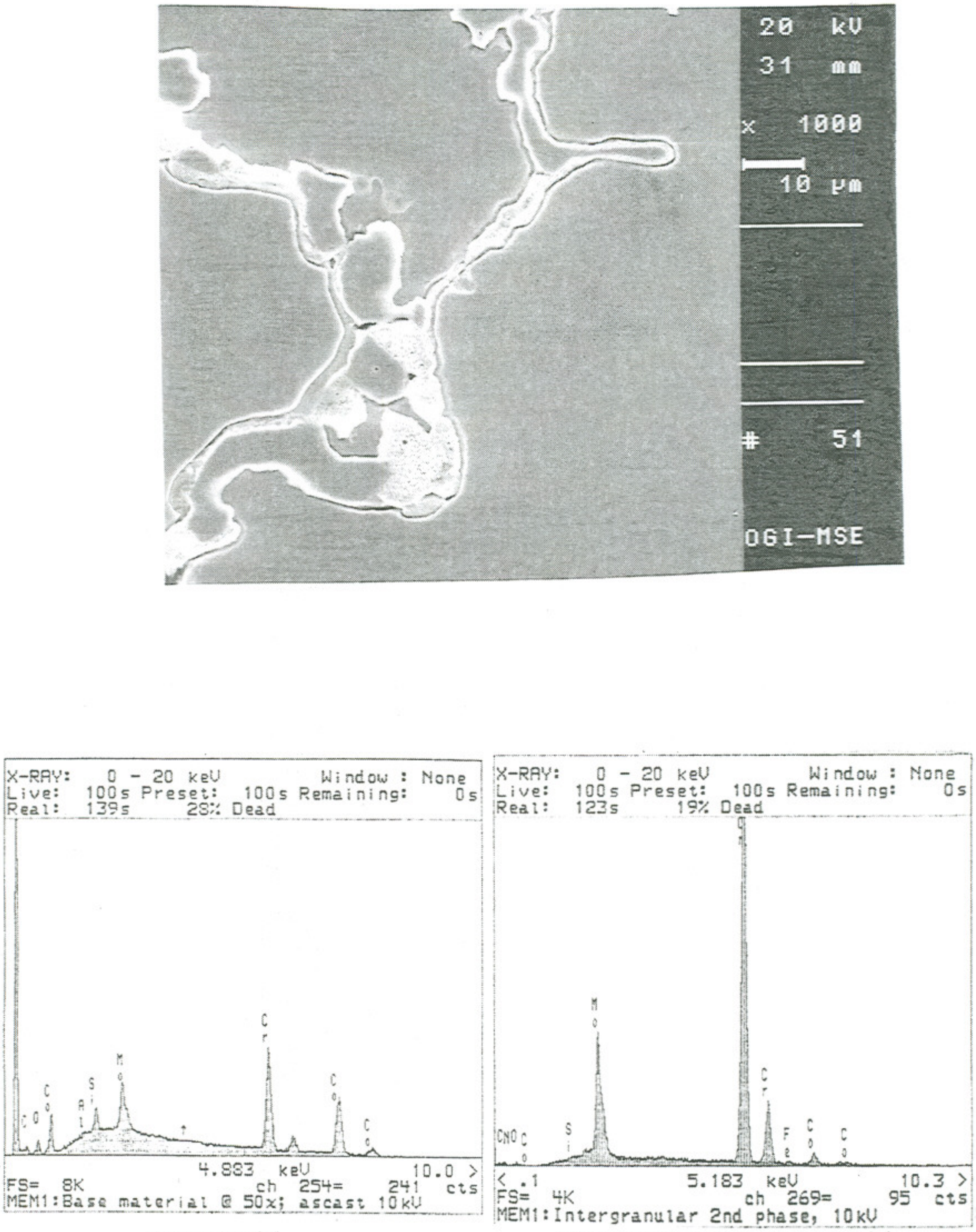

```
X-RAY:    0 - 20 keV            Window : None
Live:   100s Preset:   100s Remaining:     0s
Real:   139s       28% Dead

                       4.883  keV        10.0 >
FS=  8K                    ch  254=    241  cts
MEM1:Base material @ 50x; ascast 10kV
```

```
X-RAY:    0 - 20 keV            Window : None
Live:   100s Preset:   100s Remaining:     0s
Real:   123s       19% Dead

< .1                  5.183  keV         10.3 >
FS=  4K                    ch  269=     95  cts
MEM1:Intergranular 2nd phase, 10kV
```

Base Material

Intergranular second phase material

Figure 4-38: Secondary electron image of as-cast Stellite 21 ingot, N-HPM at 4 atm, ingot bottom, mid-radius region, showing lamellar second phase material, as well as EDX spectra associated with the second phase and the matrix

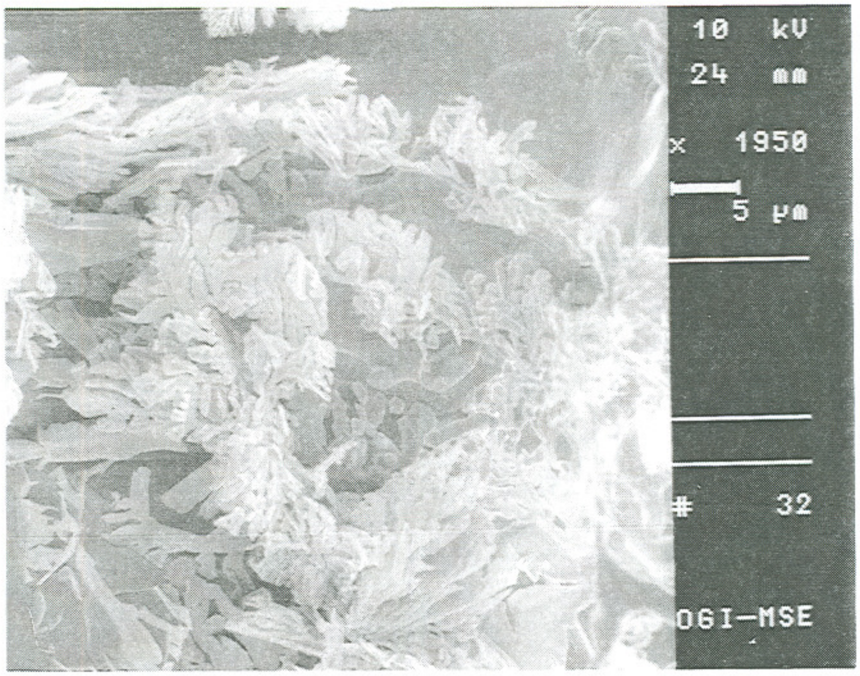

Figure 4-39: Secondary electron image of as-cast Stellite 21 ingot, N-HPM at 4 atm, showing 3-D lamellar second phase material; matrix removed with 10% bromine/methonal, 1950x.

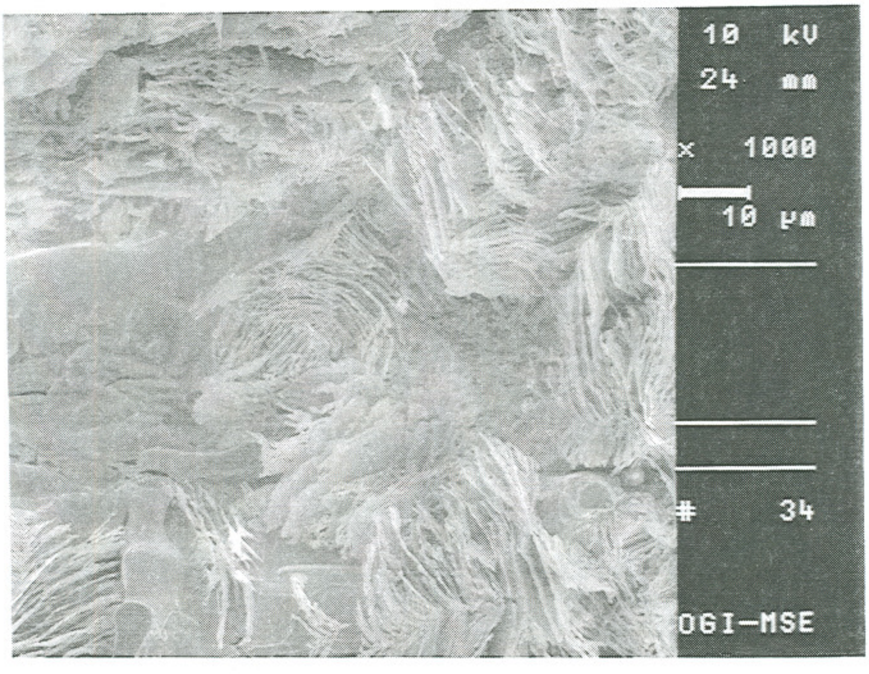

Figure 4-40: Secondary electron image of as-cast Stellite 21 ingot, N-HPM at 50 atm, showing 3-D lamellar second phase material; matrix removed with 10% bromine/methonal, 1000x.

Extracted Particles

Semi-quantitation of EDX spectra recorded for particles extracted from the as-cast 16 atm B material showed that very little Co matrix remained in the particles. It also showed very high Cr, with 75 to 89 wt%, and 8 to 23 wt% Mo. The Si, Al, O contents were quite low also, with from 0.0 to 0.1 wt%.

X-ray Diffraction Analysis

Results of XRD analyses on extracted residues from the as-cast ingots are tabulated in **Table 4-9**. Cobalt was present in most of the residues analyzed because of grain fallout during the electrolytic dissolution. In addition to the expected phases recorded in **Table 4-9**, some of the spectra contained peaks that were either unidentifiable, or were associated with compounds which were not consistent with what would be possible or expected in the alloy. Most significantly, the 1.4 atm as-cast ingot displayed the possible presence of a π carbide with a lattice parameter of 0.639-0.642 nm (6.39-6.42Å) and a stoichiometry of Fe_{29}-$Mn_{6.6}$-$Cr_{4.6}$-$MoAl_{1.8}$-C_3 (JCPDS-ICDD card # 37-1093). The stray peaks in other samples were not able to be related to any known compound in the JCPDS file. If the relative peak heights are taken as an indicator of the relative quantity of the phase, though, the source of these few other peaks may not be important with respect to the greater significance of the identified phases. Shown in **Figure 4-41** are samples of XRD spectra for the compounds of interest.

Table 4-9: XRD analysis of second phase extracted from as-cast N-HPM Stellite 21

Melt ID	FCC Co	$Cr_{23}C_6$	Cr_2N	CrN
10 atm Ar	X	x		
1.4 atm	x	x		
4 atm	x		x	
16 atm A	x		x	
16 atm B	x		X	
50 atm	x		X	x

X=primary phase, x=minor/secondary phase

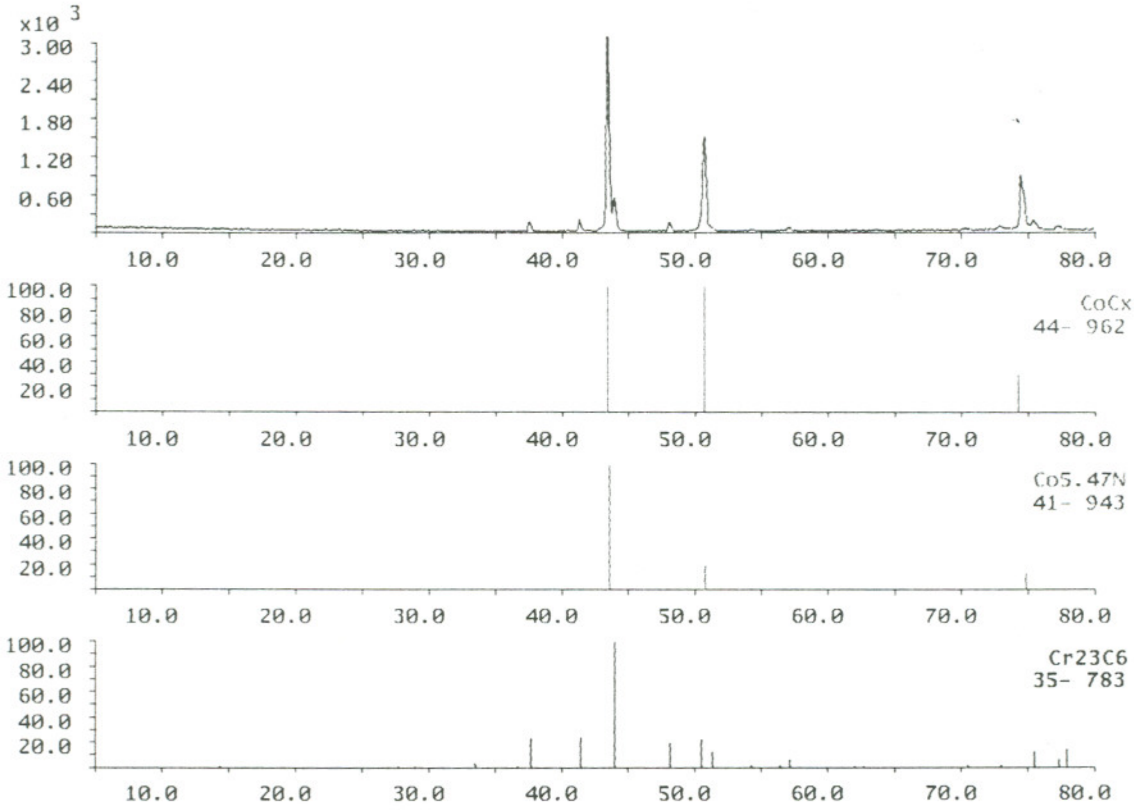

Figure 4-41: Sample XRD spectra and the corresponding peak patterns for the identified substances

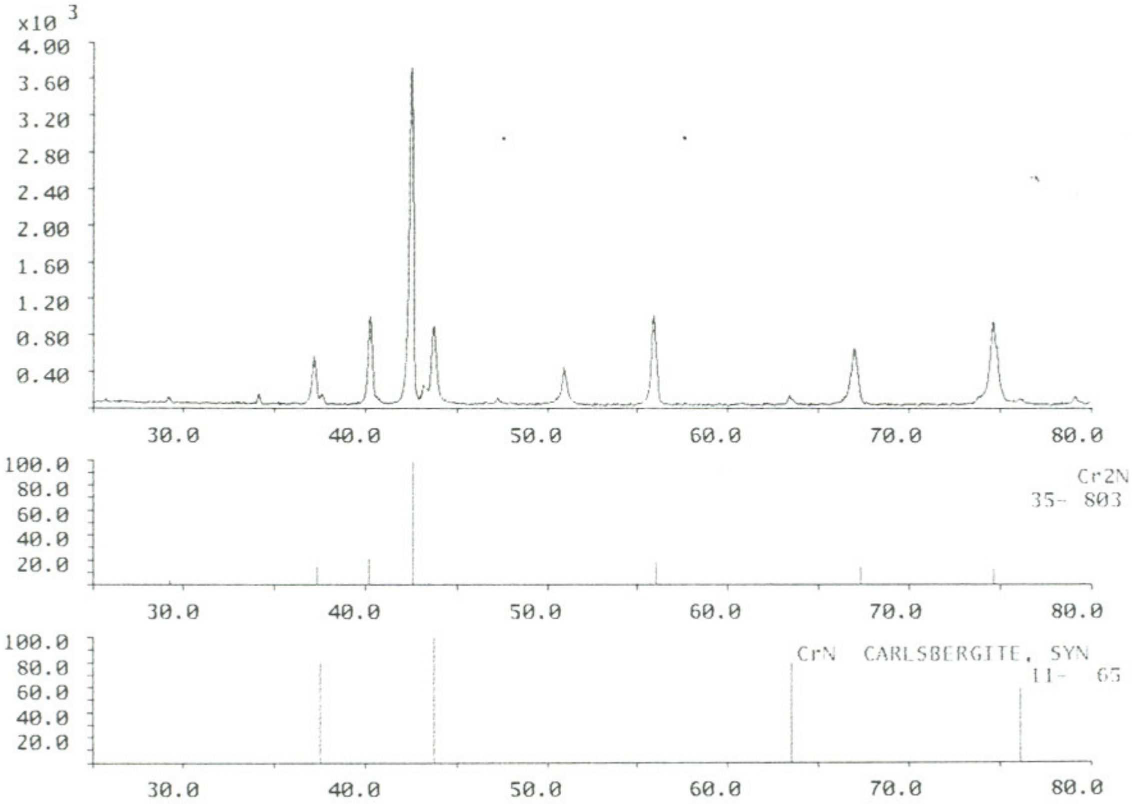

Figure 4-41: Sample XRD spectra and the corresponding peak patterns for the identified substances

4.2.2 Effects of Solutionization

Microstructure

Figure 4-42 shows the amount of second phase remaining after holding samples at 1220°C (2220°F) for 1 to 16 hours. It indicates that, even for fairly large average initial second phase contents, after 16 hours at 1220°C, substantial decreases in second phase content occurred. Several aspects of the curves in **Figure 4-42** are noteworthy. Firstly, the solutionization behavior does not appear as uniform as in the conventional or fine-grained cast F75 materials. This may be the result of the samples being taken from different regions of the initial ingot, which would contain different initial second phase contents. A better representation of the solutionization behavior may have been to measure the *change* in second phase content rather than only the final content. However, to achieve that, the *initial* phase content should have been measured for *each* sample. Yet, the samples were taken from the initial ingot such that the 1 hour specimen was taken from the bottom (region of lowest second phase content), the 2 hour specimen next, until finally the 16 hour specimen was taken from the top (region of highest second phase content). Thus, the fact that a relatively low second phase content was achieved after 16 hours even in the densely populated upper region of the ingot, is still significant.

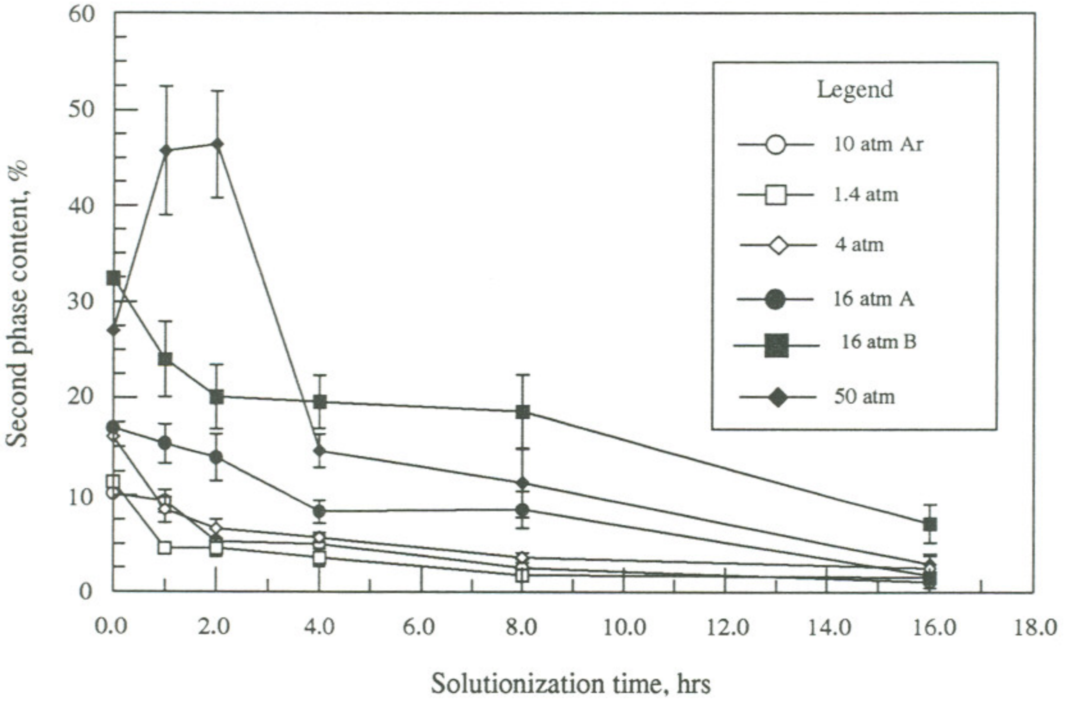

Figure 4-42: Second phase dissolution over time at 1220°C (2220°F) in as-cast N-HPM Stellite 21

Lastly, the solutionization behavior of the 50 atm sample requires additional consideration, as the behavior displayed was unexpected. As shown in **Figure 4-43**, there was an initial precipitation of second phase which *increased* the second phase content in the first two hours of the heat treatment (cp. **Figure 4-36**). The same observation was made upon performing the experiment a second time. As shown in **Figure 4-44**, this material had all been re-dissolved after 2 more hours, and further dissolution occurred to bring the second phase quantity down to less than 5%. However, the subsequent dissolution of the second phase material may have been partially aided by out-gassing of the nitrogen from the material, as this particular experiment used small samples and Ar as a shielding gas (which would reduce the nitrogen partial pressure outside the sample, increasing the susceptibility for out-gassing).

As indicated in **Table 3-5**, the nitrogen content of the 50 atm samples solutionized at 1220°C (2220°F) in an argon environment dropped to 0.74 wt% after 8 hours, then to 0.42 wt% after 16 hours. Still, as shown in **Table 4-10**, the nitrogen contents of the other samples tested was maintained after solutionization for 16 hours at 1220°C (2220°F) in the argon environment (although it was determined that subsequent heat treating should be done in air to avoid any further tendency for nitrogen loss).

Hardness

The results of Rockwell C (Rc) hardness testing of the as-cast and the solutionized materials are tabulated in **Table 4-11**. There was little change in the average hardness between the different melts, but, within each ingot, the hardness tended to randomly vary by several points. There was noticeable difference between the average hardness of the 10 atm Ar (Rc 25), and the 50 atm as-cast billets (Rc 32), but the hardness of the melts between them did not vary accordingly. Likewise, the solutionized billets did not show any consistent changes, although in all cases they were either the same or harder solutionized than in their as-cast condition. Again, the measurements varied to such a degree within each ingot that no strong statement can be made regarding the effect solutionization may have had on mechanical properties as indicated through hardness testing. What *can* be stated is that the average hardness of around 25-35 Rc is typical of Co-Cr-Mo alloys, and the variability in the measurements is a characteristic of cast versions of the alloys, and is attributed to the heterogeneity of the cored dendritic microstructure.

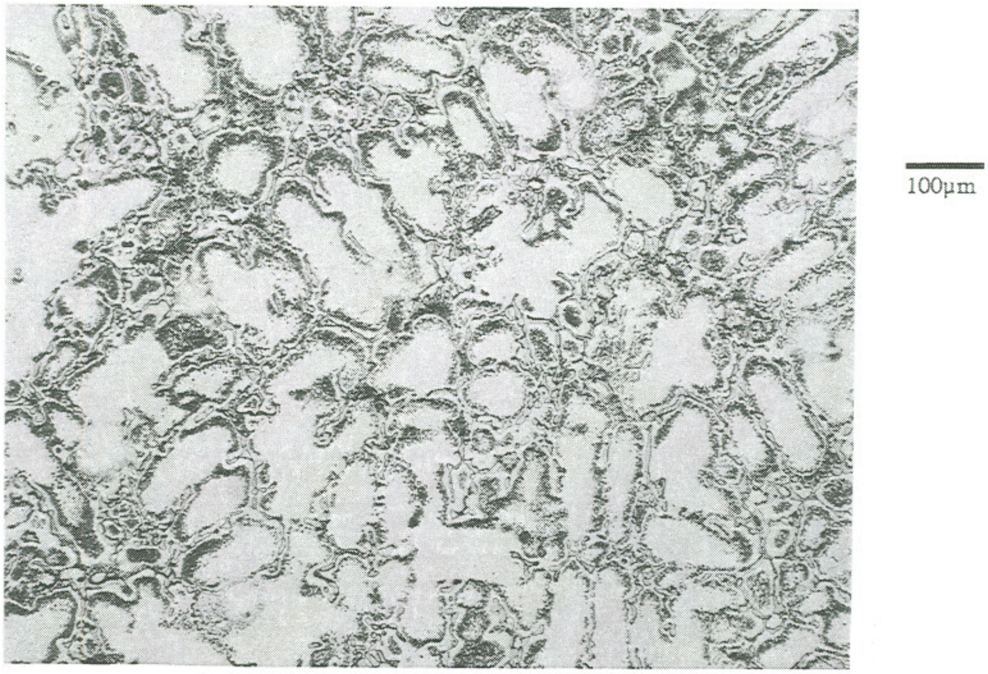

Figure 4-43: 50 atm N-HPM Stellite 21, soaked at 1220C (2220F) for 2 hours then water quenched, showing apparent precipitation around interdendritic islands; electrolytically etched with 10% ammonium persulfate, 100x

Figure 4-44: 50 atm N-HPM Stellite 21, soaked at 1220C (2220F) for 4 hours then water quenched, showing apparent dissolution of precipitation; electrolytically etched with 10% ammonium persulfate, 100x

Table 4-10: Nitrogen content of samples following solutionization in argon environment

Sample	Wt% nitrogen after 16 hrs @ 1220°C(222°F)
1.4 atm	0.18
4 atm	0.34
16 atm A	0.41
50 atm	0.42

Table 4-11: Hardness of as-cast and solutionized N-HPM Stellite 21 billets (Rc)

Sample ID	As-cast	Solutionized
10 atm Ar	25	31
1.4 atm	27	29
4 atm	30	31
16 atm A	29	30
16 atm B	28	35
50 atm	32	32

4.2.3 Effects of Hot-rolling

Nitrogen Content

In the previous section the concern was raised regarding potential for nitrogen loss during heat treatment of the cast N-HPM billets. The results of total nitrogen measurements of the hot-rolled plates are shown in **Table 4-12**. These results show that no significant nitrogen loss occurred in the specimens during the solutionization and the rolling of the billets into the plate materials.

Table 4-12: Nitrogen content of rolled/annealed N-HPM Stellite 21 plates

Sample ID	As-cast (wt%)	Annealed (wt%)
10 atm Ar	0.10	0.10
1.4 atm	0.19	0.19
4 atm	0.34	0.34
16 atm A	0.39	0.40
16 atm B	0.52	0.50
50 atm	0.85	0.84

Microstructure

Micrographs

Figures 4-45 to **4-47** show examples of the microstructures achieved following hot-rolling of the billets, and then annealing them for 15 minutes at 1200°C (2190°F). The as-hot-rolled materials displayed a very fine grain structure, with the second phase material broken up into stringers of particles oriented in the rolling direction. A fine dispersion of precipitates tended to obscure much of the microstructure in most of the samples. Immediately evident in the annealed samples were fine, uniform, equiaxed grains, and a significant reduction in the finely dispersed precipitates. The grains of the specimens of lower nitrogen tended to grow rapidly during annealing, especially in the 10 atm Ar specimen. Near the surface of the specimens there was a denuded zone that was free of second phase material, probably due to outgassing. This was especially noted in the higher nitrogen specimens, which still contained considerable second phase material in their cores. The second phase stringers appeared to be unchanged between the as-rolled and the annealed conditions, but they were certainly finer and more homogeneously distributed than in the as-cast condition.

Figure 4-45A: 10 atm Ar-HPM Stellite 21, in as-rolled condition; electrolytically etched with 10% ammonium persulfate, 100x

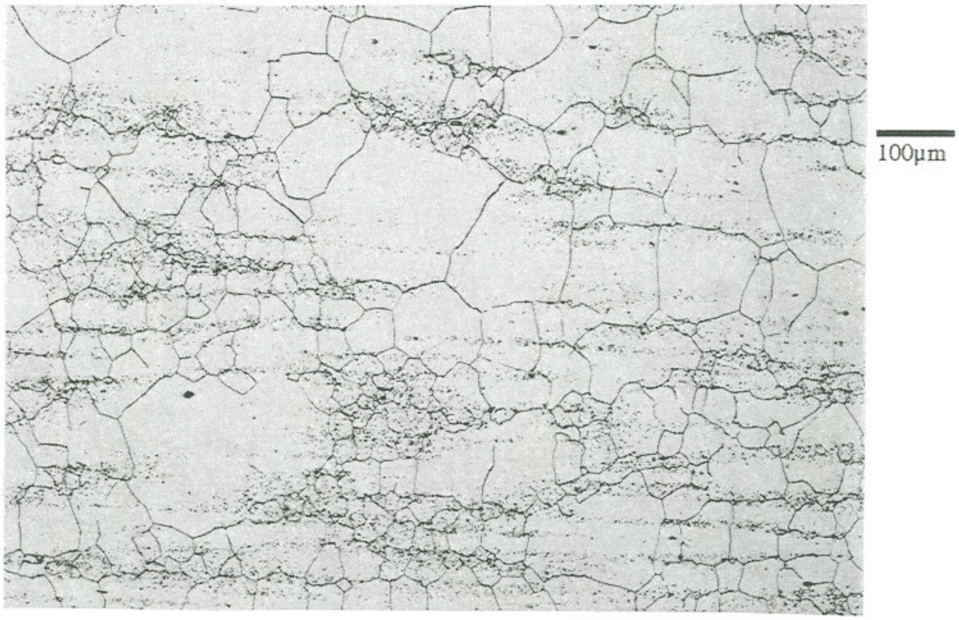

Figure 4-45B: 10 atm Ar-HPM Stellite 21, in rolled and annealed condition; electrolytically etched with 10% ammonium persulfate, 100x

Figure 4-46A: 4 atm N-HPM Stellite 21, in as-rolled condition; electrolytically etched with 10% ammonium persulfate, 100x

Figure 4-46B: 4 atm N-HPM Stellite 21, in rolled and annealed condition; electrolytically etched with 10% ammonium persulfate, 100x

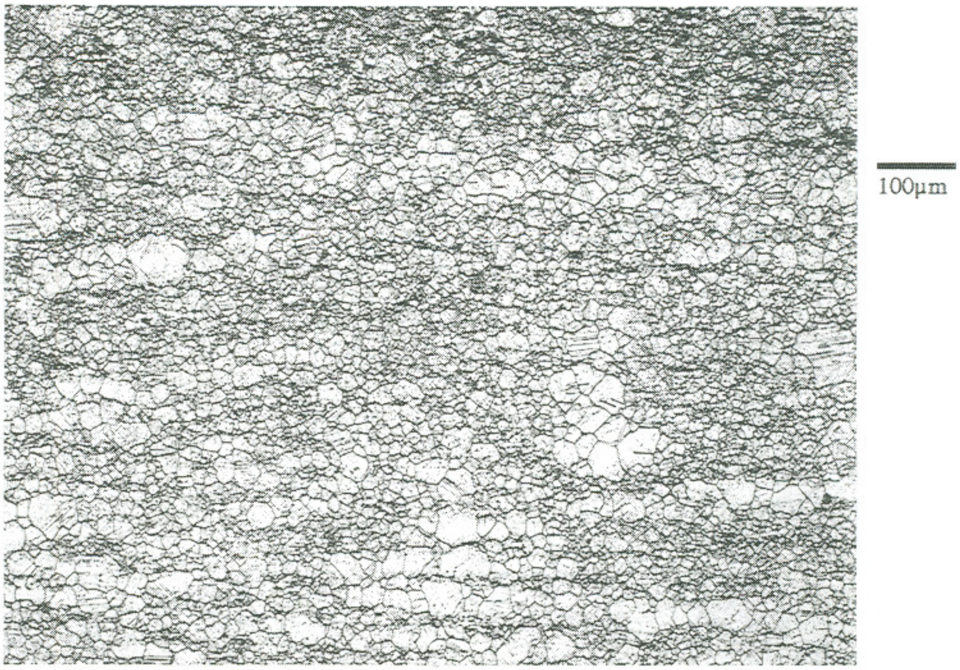

Figure 4-47A: 16 atm B N-HPM Stellite 21, in as-rolled condition; electrolytically etched with 10% ammonium persulfate, 100x

Figure 4-47B: 16 atm B N-HPM Stellite 21, in rolled and annealed condition; electrolytically etched with 10% ammonium persulfate, 100x

Quantification

Results of measurement of the grain size and the second phase content of the materials are tabulated in **Tables 4-13** and **4-14** respectively. The results for the *as-rolled* specimens are averages from samples taken directly from the plate material following cutting of the test bar blanks. The results for the *annealed* materials are averages from the microstructures of the grip regions following tensile testing of the test bars.

Quantification of the grain sizes of the specimens showed that grain growth occurred as a result of annealing in the samples, and that that growth was the most pronounced in the lower nitrogen samples. The grain size of the lower nitrogen annealed samples approached that of the fine-grained investment cast F75 samples observed previously. The grain size of the as-rolled 16 atm A sample was not measured because the grain boundaries were undelineable by etching, even after aging in an attempt to decorate them with precipitates. However, most likely the grain size was of a similar order as that observed in the other as-rolled specimens.

Table 4-14 shows that the trend towards higher second phase contents in the higher nitrogen materials was still observed in the rolled and annealed plates. This material appeared to have not dissolved in the 16 hour solutionization treatment given to the billets prior to rolling. The lower nitrogen samples all displayed second phase contents of around 2%.

Table 4-13: Grain size of hot-rolled, N-HPM, Stellite 21 plate

Sample	As-rolled		Annealed 1220°C (2220°F)/15 mins	
ID	Grain Diameter, μm	ASTM #	Grain Diameter, μm	ASTM #
10 atm Ar	10±3	10.1	68±28	4.7
1.4 atm	23±6	7.6	61±12	4.9
4 atm	17±3	8.5	62±28	5.0
16 atm A	NA	NA	37±11	6.4
16 atm B	14±2	9.0	27±1	7.2
50 atm	13±5	9.1	24±1	7.6

Table 4-14: Second phase content of rolled and annealed N-HPM Stellite 21 plate

Sample ID	Second Phase, %
10 atm Ar	2.3±0.6
1.4 atm	2.1±1.2
4 atm	2.0±0.9
16 atm A	4.6±1.0
16 atm B	7.7±1.0
50 atm	13.9±0.9

X-ray Diffraction Analysis

Results of XRD analyses on extracted residues from the annealed plates are tabulated in **Table 4-15**. Cobalt was again present in most of the residues analyzed because of grain fallout during the electrolytic dissolution. The results were very similar to those of the as-cast materials. However, in the rolled and annealed sample from the 50 atm ingot, CrN was not observed as it was in the as-cast material. The only other exception is that once again an unfamiliar and unexpected phase appeared to be present in the 1.4 atm sample. However, rather than the π-carbide suggested in the as-cast case, a FCC material with a lattice parameter of 1.098nm (10.98Å), referred to as ν, was indicated. This ν phase has a stoichiometry of $(Cr, Mo)_3(Co, Ni)_3C$ [72]. This is not entirely unreasonable for the Stellite 21 composition, but its presence was not predicted.

Hardness

Table 4-16 shows the Rockwell hardness of each of the nitrogen melts after hot-rolling and after annealing. The average of 10 measurements per sample resulted in a narrow distribution for the rolled plates as compared to the cast material. The as-rolled condition demonstrated no strong trend with respect to the material *composition*, but all of the samples showed a much higher hardness than the as-cast or solutionized N-HPM material. This was most likely a function of work hardening occurring in the plate due to rolling. A significant reduction in the hardness was observed following annealing of the plates. This was most notable in the lower nitrogen specimens. When the hardness data is plotted with respect to the nitrogen contents of the samples (**Figure 4-48**), a trend of increasing hardness with increasing nitrogen content is observed.

Table 4-15: XRD analysis of second phase of rolled and annealed N-HPM Stellite 21

Melt ID	FCC Co	$Cr_{23}C_6$	Cr_2N	CrN
10 atm Ar	X	x		
1.4 atm	X	x		
4 atm	x		x	
16 atm A	x		x	
16 atm B	x		X	
50 atm	x		X	

X=primary phase, x=minor/secondary phase

Mechanical Properties

The results of tensile testing of the materials annealed at 1220°C (2220°F) for 15 minutes are shown in **Table 4-17**. The yield strength (YS) values were calculated by the intersection of the 0.002 offset of the best fit linear regression line of the elastic region of the tensile curve. The ultimate tensile strength (UTS) was calculated from the highest recorded load. The elongation (%El) and the reduction in area (%RA) were measured from the specimens themselves.

The resulting properties show several things. Firstly, the samples show good consistency in most cases. Some negative influence on the properties may have resulted from difficulties encountered in machining the materials, which caused some non-uniformity to be introduced into the gauge regions of the bars. This could have led to reduced ductility results, which could also have influenced the UTS results. The yield strengths are less likely to have been influenced.

Table 4-16: Hardness of as-rolled and annealed N-HPM Stellite 21 plates (Rc)

Sample ID	As-rolled	Annealed
10 atm Ar	44±0.5	31±0.9
1.4 atm	38±1.0	31±2.0
4 atm	38±0.8	33±0.6
16 atm A	39±0.5	34±0.6
16 atm B	42±0.9	38±0.7
50 atm	41±0.8	39±0.9

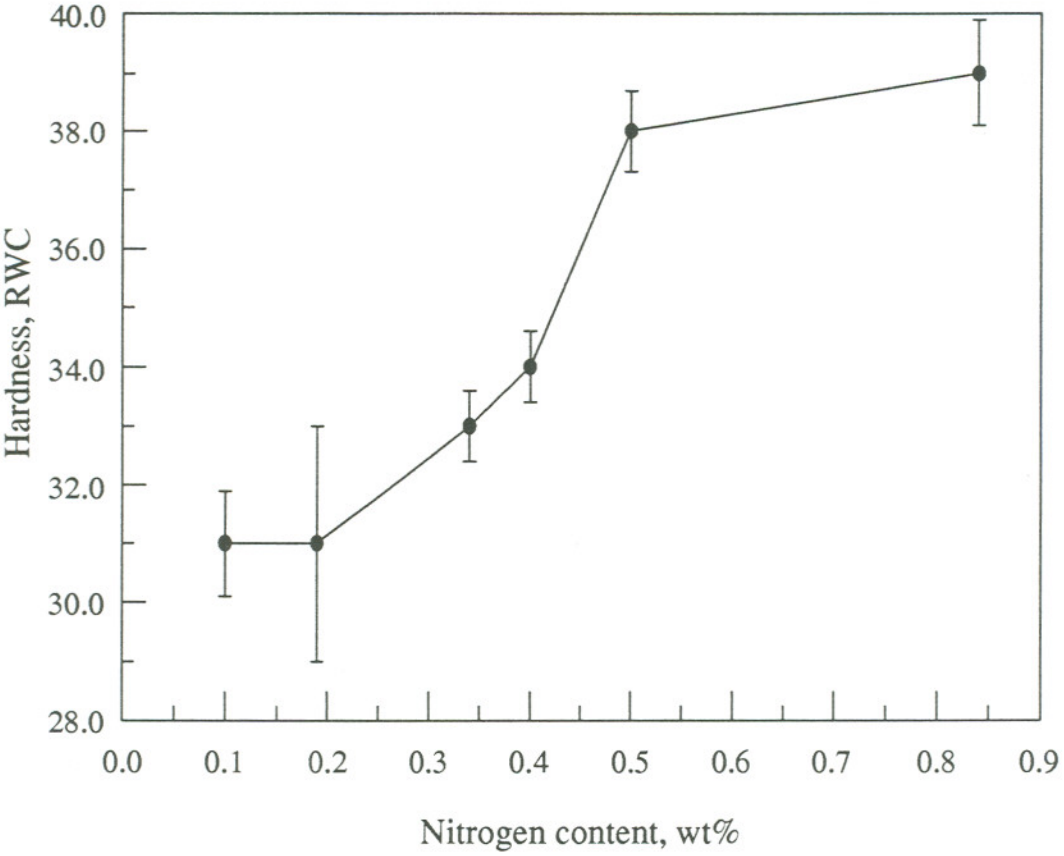

Figure 4-48: Relationship between hardness and nitrogen of rolled and annealed, N-HPM Stellite 21

In general, the rolled material showed high strength and high ductility with respect to either of the cast F75 materials. They demonstrated yield strengths from 634 to 863 MPa (91.9 to 125 ksi) in the 10 atm Ar and 50 atm groups respectively, with ductilities as high as 36.2% in the 4 atm group. This is expected, though, as the greater homogeneity and reduced porosity of wrought materials generally leads to increased strength and ductility. It is also apparent that the higher nitrogen samples displayed a higher yield strength than the lower ones, but that at 50 atm, the ductility was less than half that of the other specimens.

The mechanical property results are better depicted in **Figures 4-49** and **4-50**, where they are plotted with respect to their nitrogen contents. The plots indicate several things, but not clearly. Firstly, the yield strength increased with increasing nitrogen content, but not uniformly. The yield strength of the 0.34 wt% N samples (4 atm) were lower with respect to their neighboring samples, as were the 0.50 wt% N sample (16 atm B). In the region of the 0.40 wt% N samples (16 atm A), the UTS reached a maximum. This is likely related to the high ductility near this composition. The ductility increased with nitrogen up to the 0.40 wt% N sample (16 atm A), and then rapidly dropped off. There is an apparent transition in both the strength and ductility measurements observed in the regime of the 4 atm and the 16 atm A specimens, or around 0.34 to 0.4 wt% nitrogen.

4.2.4 Effects of Solutionization on Rolled and Annealed Coupons

Microstructure

Micrographs

Three important things occurred in the microstructure following solutionization of the rolled and annealed materials. Firstly, the second phase content was reduced with increasing time and temperature. Secondly, the grain size of the samples increased over that of the annealed samples. Finally (in the low nitrogen samples), *incipient melting* occurred in some of the remaining second phase regions at solution temperatures above 1220°C (2220°F).

Table 4-17: Mechanical properties of hot-rolled N-HPM Stellite 21 plate after annealing at 1220°C (2220°F) for 15 minutes

Sample ID	Bar #	YS, MPa (ksi)	UTS, MPa (ksi)	%El	%RA
10 atm Ar	1	641 (92.9)	1094 (158.6)	21.0	21.3
	2	634 (91.9)	1076 (156.0)	19.8	20.2
1.4 atm	1	718 (104.0)	1152 (167.0)	33.4	26.3
	2	676 (98.0)	1158 (167.8)	29.4	25.7
4 atm	1	678 (98.3)	1214 (175.9)	23.9	20.3
	2	633 (91.8)	1143 (165.6)	36.2	28.9
16 atm A	1	771 (111.8)	1181 (171.2)	18.4	15.0
	2	755 (109.4)	1208 (175.0)	29.0	21.2
16 atm B	1	733 (106.3)	1179 (170.9)	21.0	17.3
	2	742 (107.5)	1214 (175.9)	20.3	16.5
50 atm	1	863 (125.0)	1131 (163.9)	9.1	6.6
	2	847 (122.8)	1125 (163.0)	9.7	7.5
	3	834 (120.9)	1183 (171.4)	8.5	15.8

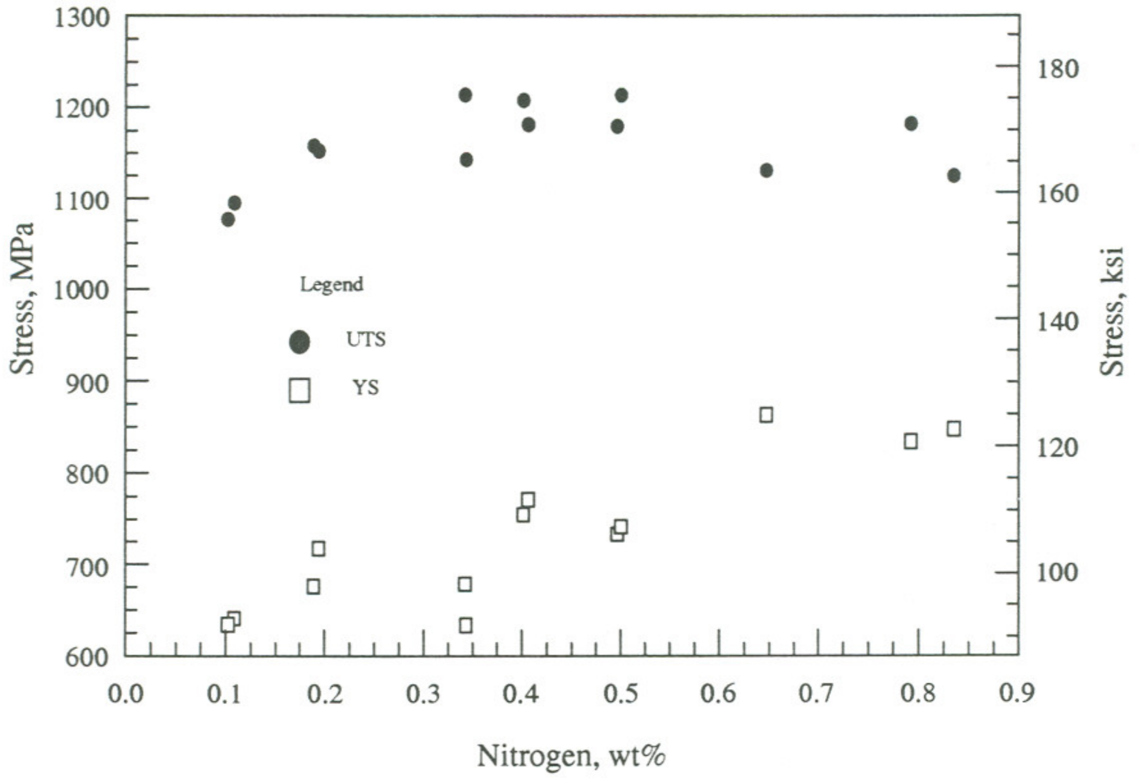

Figure 4-49: Strength of rolled and annealed, N-HPM Stellite 21 plate test bars

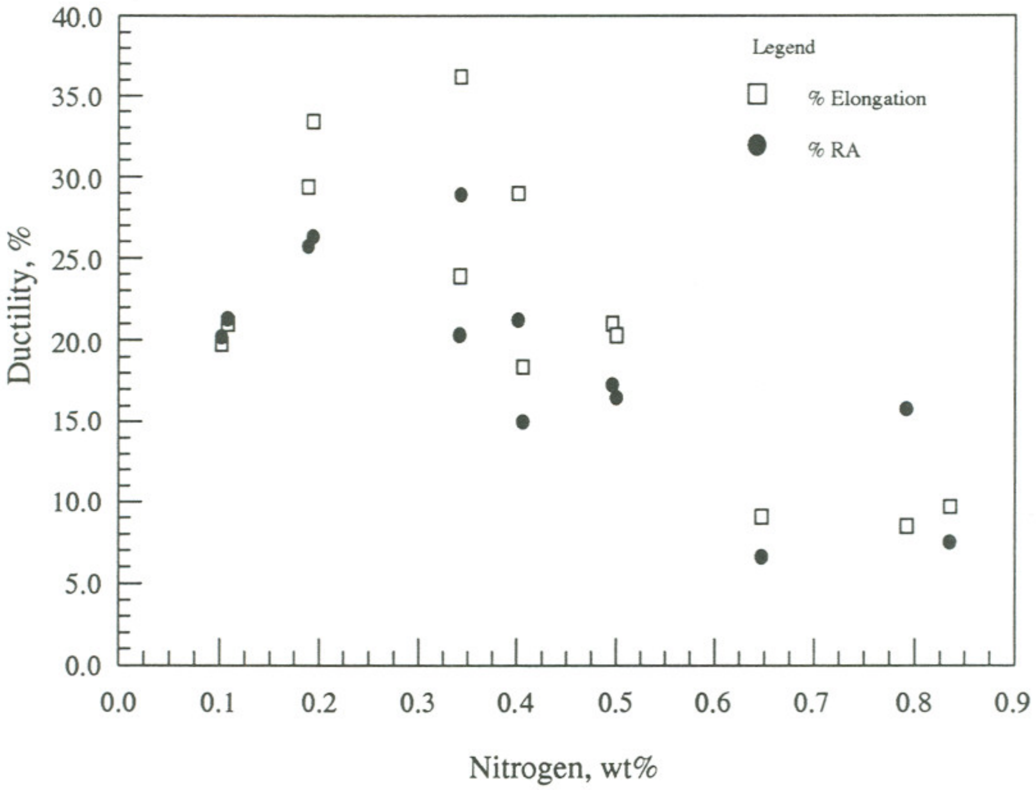

Figure 4-50: Ductility of rolled and annealed, N-HPM Stellite 21 plate test bars

Quantification

The second phase content measurements displayed in **Figure 4-51** show several things. Firstly, for melts with nitrogen contents of 0.10 wt% and 0.19 wt%, complete solutionization rapidly occurred even at the lowest temperatures. Then, for 0.34 wt% N (4 atm sample), the already low second phase content showed very little further solutionization, although a low 0.5% content was achieved. The samples with nitrogen contents of 0.40 wt% and above displayed reduced second phase with respect to the annealed condition with increasing temperature and time. They did not, however, achieve complete solutionization at any of the temperatures or times, and at most reduced their second phase content by only about 1/2. For the samples in the 4 atm and 50 atm groups which show an apparent *increase* in second phase content in some cases, without sign of precipitation, consideration must again be taken of the heterogeneity of the second phase distribution within the initial ingots before rolling.

The grain size calculations of **Figure 4-52** show that a dramatic increase in grain size was observed for all of the annealed samples following the additional solutionization treatment. As shown, longer times and higher temperatures generally led to larger average grain sizes, but comparisons between the various groups reveal that a finer grain size was retained in samples which had higher nitrogen contents. This was especially clear in the samples solutionized at 1260°C (2300°F) for 4 hours.

Incipient Melting

As shown in **Figure 4-53**, incipient melting occurred in some of the specimens. Incipient melting is characterized by serrated edges of the second phase caused by the cellular front of the liquid interface penetrating into the solid. This was observed in the second phase material of the 0.1 and 0.2 wt% N samples heat treated at 1240°C (2260°F) and 1260°C (2300°F).

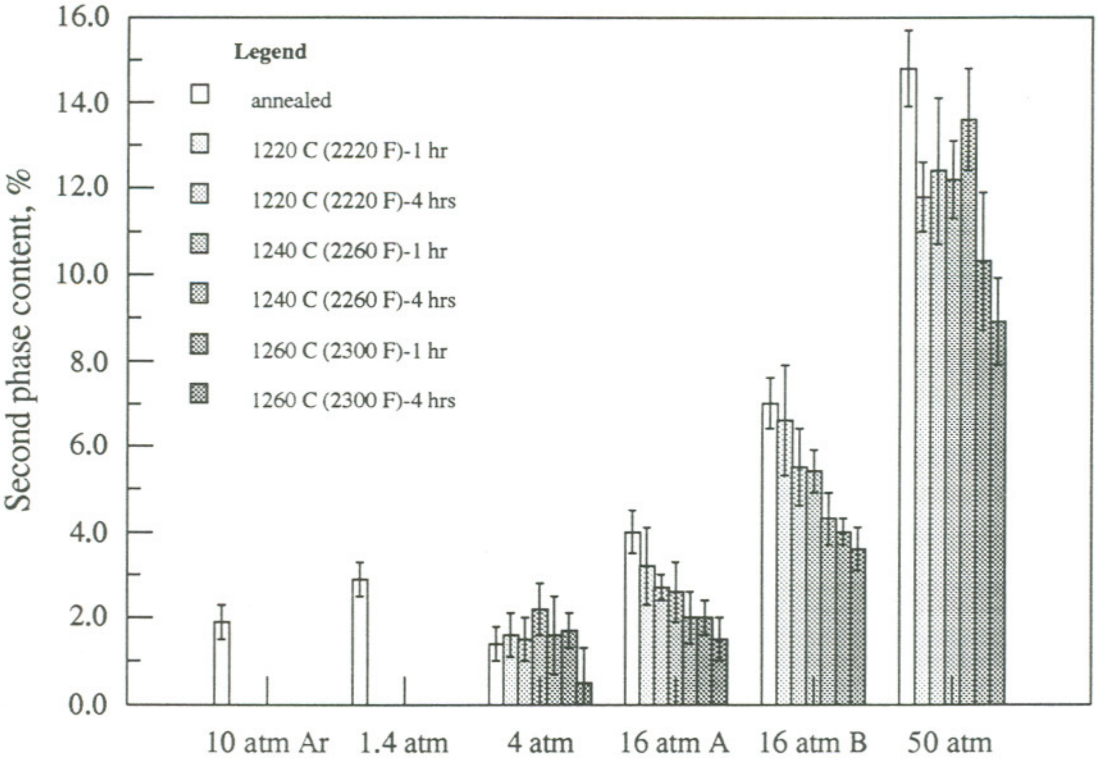

Figure 4-51: Second phase content after solutionization of rolled N-HPM Stellite 21 coupons

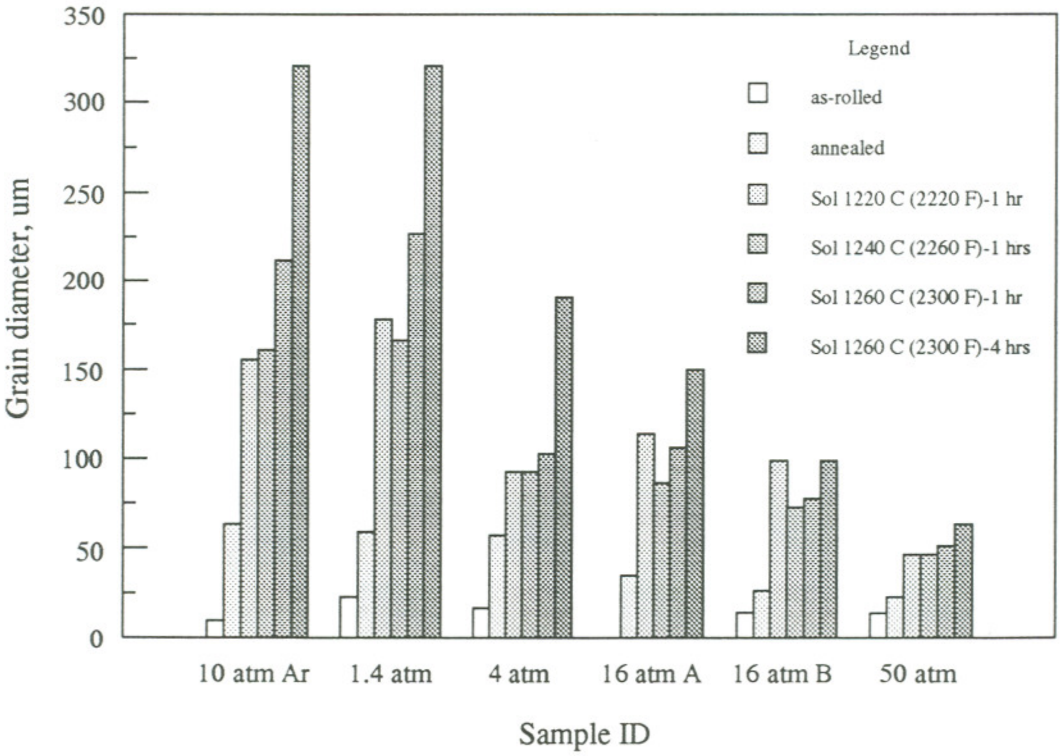

Figure 4-52: Grain size after solutionization of rolled N-HPM Stellite 21 coupons

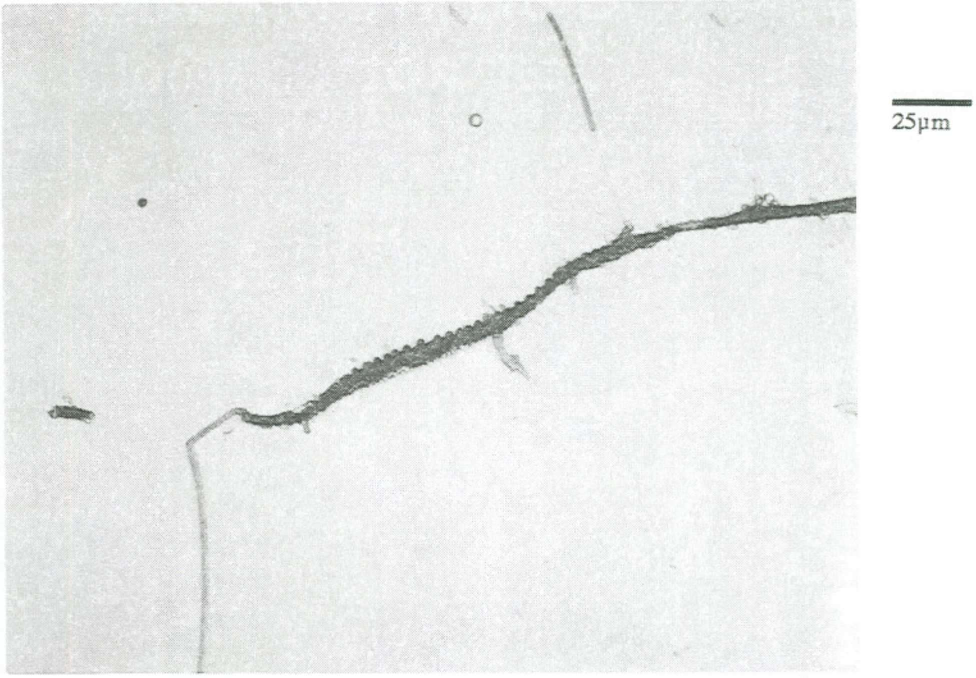

Figure 4-53: Example of evidence of incipient melting, as observed in 1.4 atm N-HPM Stellite 21 coupon following soaking at 1260°C (2300°F) for 1 hour and then water quenching; electrolytically etched with 10% ammonium persulfate, 400x

4.2.5 Solutionization of Rolled and Annealed Test bars

The solutionization study above was done to characterize the solutionization behavior of the N-HPM Stellite 21. To determine the mechanical properties, subsequent solutionization treatments were done on test bar blanks. The results of these mechanical properties, as well as their measured grain size and second phase content, are shown in **Table 4-18**. As a result of the solutionization processing of the bars, the yield strength in all cases was reduced, by as much as 23% (16 atm B). With the exception of the 50 atm bars, the yield strength of the bars was reduced to levels more typical of the cast materials. The ductility in many cases increased with some solutionization, but then decreased for samples heat treated for longer times. Most notable was the 16 atm A bars, whose ductility was increased by about 0.6 through solutionization. At the same time, the ductility of the 50 atm bars was increased while retaining a yield strength of about 110ksi. In most cases, the balance of yield strength and ductility was most desirable in the annealed condition.

Table 4-18: Microstructure and mechanical properties of solutionized, rolled, N-HPM Stellite 21 materials

Melt ID	Bar#	Processing	wt % N	Second phase	Grain diam.	YS, MPa (ksi)	UTS, MPa (ksi)	% El.	% RA
10 atm Ar	#1	Rolled/Annealed	0.108	2.7±0.5	48±20	641 (92.9)	1094 (158.6)	21.0	21.3
10 atm Ar	#2	Rolled/Annealed	0.102	1.9±0.4	87±20	634 (91.9)	1076 (156.0)	19.8	20.2
10 atm Ar	#1	R/A+1220-1hr	0.115	0.8±0.4	168±38	592 (85.8)	1043 (151.2)	25.1	23.4
10 atm Ar	#2	R/A+1220-1hr	0.113	1.4±0.4	146±36	621 (90.0)	1079 (156.5)	27.5	23.8
10 atm Ar	#1	R/A+1220-4hrs	0.129	0.5±0.2	176±55	571 (82.8)	914 (132.5)	20.0	19.5
10 atm Ar	#2	R/A+1220-4hrs	0.122	0.4±0.2	166±29	558 (80.9)	885 (128.4)	16.9	21.3
1.4 atm	#1	Rolled/Annealed	0.194	1.3±0.7	69±16	717 (104.0)	1152 (167.0)	33.4	26.3
1.4 atm	#2	Rolled/Annealed	0.189	2.9±0.4	52±13	676 (98.0)	1157 (167.8)	29.4	25.7
1.4 atm	#1	R/A+1220-1hr	0.202	0.6±0.2	132±32	601 (87.2)	1126 (163.3)	31.6	29.8
1.4 atm	#2	R/A+1220-1hr	0.203	0.5±0.4	115±26	636 (92.2)	1151 (166.9)	32.3	29.8
1.4 atm	#1	R/A+1220-4hrs	0.224	0.2±0.1	194±52	589 (85.5)	978 (141.8)	27.0	26.3
1.4 atm	#2	R/A+1220-4hrs	0.219	0.1±0.04	176±36	572 (82.9)	952 (138.0)	25.8	25.9
4 atm	#1	Rolled/Annealed	0.342	2.6±0.4	42±7	678 (98.3)	1213 (175.9)	23.9	20.3
4 atm	#2	Rolled/Annealed	0.343	1.4±0.4	81±18	633 (91.8)	1142 (165.6)	36.2	28.9
4 atm	#1	R/A+1260-4hrs	0.356	0.5±0.1	154±37	610 (88.5)	1091 (158.2)	29.0	19.4
4 atm	#2	R/A+1260-4hrs	0.354	0.5±0.1	136±31	660 (95.7)	1055 (152.9)	25.7	19.1
16 atm A	#1	Rolled/Annealed	0.406	5.3±1	44±8	771 (111.8)	1181 (171.2)	18.4	15.0
16 atm A	#2	Rolled/Annealed	0.401	4.0±0.5	29±8	754 (109.4)	1207 (175.0)	29	21.2
16 atm A	#1	R/A+1260-8hrs	0.447	1.2±0.3	144±33	620 (89.9)	1129 (163.7)	40.7	29.9
16 atm A	#2	R/A+1260-8hrs	0.464	1.3±0.3	136±31	596 (86.5)	1115 (161.6)	37.5	26.4
16 atm B	#1	Rolled/Annealed	0.496	8.4±0.9	26±7	733 (106.3)	1179 (170.9)	21.0	17.3
16 atm B	#3	Rolled/Annealed	0.5	7.0±0.6	27±5	741 (107.5)	1213 (175.9)	20.3	16.5
16 atm B	#1	R/A+1260-4hrs	0.497	2.4±0.5	99±23	691 (100.2)	999 (144.9)	17.7	19.6
16 atm B	#2	R/A+1260-4hrs	0.503	2.2±0.5	100±23	643 (93.3)	1039 (150.7)	12.0	13.7
16 atm B	#3	R/A+1260-4hrs	0.509	3.2±0.5	125±35	652 (94.6)	911 (132.1)	16.7	23.8
16 atm B	#1	R/A+1260-8hrs	0.541	2.0±0.4	115±23	541 (78.5)	1024 (148.5)	31.3	23.4
16 atm B	#2	R/A+1260-8hrs	0.567	2.1±0.6	110±24	609 (88.3)	1015 (147.2)	25.8	17.2
16 atm B	#3	R/A+1260-8hrs	0.526	3.4±0.5	102±29	626 (90.8)	991 (143.7)	21.8	20.1
16 atm B	#1	R/A+1260-16hrs	0.555	2.4±0.4	135±32	561 (81.4)	931 (135.0)	21.3	24.4
16 atm B	#2	R/A+1260-16hrs	0.572	1.9±0.5	131±36	577 (83.7)	926 (134.3)	21.2	21.8
50 atm	#1	Rolled/Annealed	0.647	13.2±1.4	23±5	862 (125.0)	1130 (163.9)	9.1	6.6
50 atm	#2	Rolled/Annealed	0.835	14.8±0.9	23±4	847 (122.8)	1124 (163.0)	9.7	7.5
50 atm	#3	Rolled/Annealed	0.792	13.6±1	25±5	834 (120.9)	1182 (171.4)	8.5	15.8
50 atm	#1	R/A+1260-8hrs	0.833	10.4±0.8	53±9	761 (110.4)	1121 (162.5)	16.8	12.9
50 atm	#2	R/A+1260-8hrs	0.909	10.8±1.2	60±13	744 (107.9)	1055 (152.9)	14.4	11.7
50 atm	#1	R/A+1260-16hrs	0.931	10.6±1.7	54±15	801 (116.2)	936 (135.7)	4.3	1.0
50 atm	#2	R/A+1260-16hrs	0.944	9.0±0.9	59±16	793 (115.0)	943 (136.8)	8.8	11.7
50 atm	#3	R/A+1260-16hrs	0.836	9.5±1.5	56±15	698 (101.3)	878 (127.3)	6.9	26.6

4.2.6 Abrasive Wear Resistance of Cast N-HPM Material

Tabulated in **Table 4-19** are the results of pin-on-drum abrasive wear testing of the cast N-HPM Stellite 21 materials. Immediately apparent is that the 600 grit SiC media was not very aggressive to any of the Stellite 21 materials, resulting in wear rates on the order of only 3 to 4e-3 mm^3/Nm. **Figure 4-54** shows the Dimensional Wear Rate results calculated for the tests on each alloy. It indicates a slight trend towards reduced wear rates with increasing nitrogen for the 150 grit garnet tests, but reduced wear rates for low and high nitrogen contents as compared to the medium contents in the 600 grit SiC tests. However, in the 150 grit garnet tests, the difference between the highest rate (10 atm Ar) and the lowest rate (50 atm) was only 2.0e-3 mm^3/Nm, with the compositions between yielding wear rates lying between those extremes. The results for the top versus the bottom regions of the ingots did not show a trend suggesting any obvious differences between them. None-the-less, as shown in **Table 4-20**, the N-HPM Stellite 21 materials were more wear resistant than other C and N alloyed materials tested on the same equipment at the DOE-ARC. This is quite likely attributable to the already excellent wear properties of cobalt alloys in general.

The most likely source for an increase in the abrasive wear resistance of the materials would be an increased quantity of hard particles in the Co matrix serving to block gouging of the material by the abrasive particles. But, as shown in **Figures 4-55** and **4-56**, even the softer (although coarser) garnet particles gouged the second phase particles in the N-HPM Stellite 21 materials. But yet the wear resistance was quite good, and the values of **Table 4-20** confirm that at least nitrogen alloying did not *harm* those properties, and may have even further improved them.

Table 4-19: Abrasive wear testing results of as-cast N-HPM material

				Avg. Mass Loss, mg		Specimen	Specific Wear Rate	
Sample ID	wt % N	Location	Grit Size/Type	average	S.D.	Density	(mm^3/Nm)	S. D.
10 atm Ar	0.100	Top	150 Garnet	85.81	0.29	8.37	1.200e-2	4.1e-5
10 atm Ar	0.100	Bottom	150 Garnet	85.02	0.26	8.37	1.189e-2	3.6e-5
10 atm Ar	0.100	Bottom	600 SiC	15.97	0.21	8.37	0.356e-2	4.7e-5
1.4 atm	0.193	Top	150 Garnet	71.03	0.74	8.337	0.997e-2	10.4e-5
1.4 atm	0.192	Bottom	150 Garnet	75.41	1.94	8.337	1.059e-2	27.2e-5
1.4 atm	0.192	Bottom	600 SiC	16.66	0.17	8.337	0.373e-2	3.8e-5
4 atm	0.332	Top	150 Garnet	79.49	0.78	8.303	1.121e-2	11.0e-5
4 atm	0.349	Bottom	150 Garnet	77.37	1.98	8.303	1.091e-2	27.9e-5
4 atm	0.349	Bottom	600 SiC	18.07	0.37	8.303	0.406e-2	8.3e-5
16 atm A	0.387	Top	150 Garnet	72.85	1.2	8.298	1.027e-2	16.9e-5
16 atm A	0.388	Bottom	150 Garnet	73.76	1.15	8.298	1.040e-2	16.2e-5
16 atm A	0.388	Bottom	600 SiC	16.89	0.33	8.298	0.380e-2	7.4e-5
16 atm B	0.540	Top	150 Garnet	77.04	0.34	8.332	1.082e-2	4.8e-5
16 atm B	0.540	Bottom	150 Garnet	75.12	1.09	8.332	1.055e-2	15.3e-5
16 atm B	0.540	Bottom	600 SiC	14.7	0.12	8.332	0.329e-2	2.7e-5
50 atm	1.340	Top	150 Garnet	71.3	0.98	8.257	1.011e-2	13.9e-5
50 atm	0.847	Bottom	150 Garnet	65.48	0.45	8.257	0.928e-2	6.4e-5
50 atm	0.847	Bottom	600 SiC	15.67	0.34	8.257	0.354e-2	7.7e-5

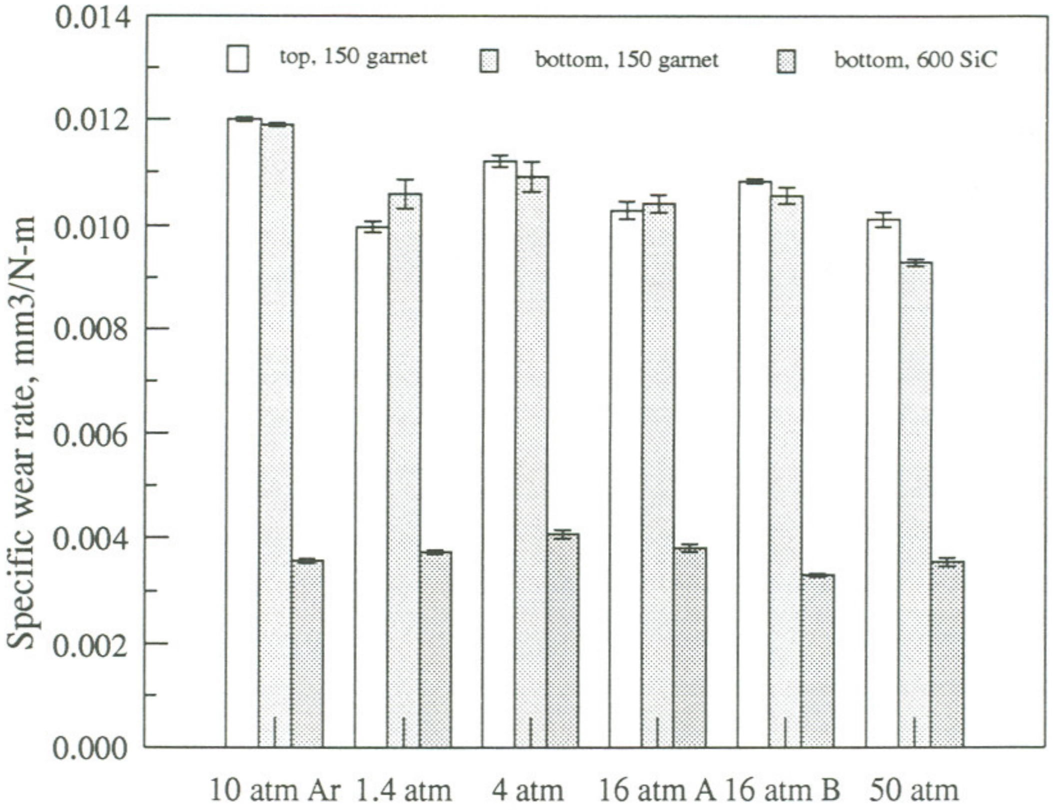

Figure 4-54: Pin-on-drum abrasive wear results for as-cast N-HPM materials

Table 4-20: Abrasive wear properties of cast N-HPM Stellite 21 and other materials

Alloy Designation	C-content wt %	N-content wt %	Dimensional Wear Rate (mm³/Nm)
10 atm Ar Stellite 21	0.25	0.10	1.200e-2
50 atm N Stellite 21	0.25	1.34	0.928e-2
21Cr-6Ni-9Mn	0.022	0.32	1.646e-2
Sea Fast (annealed)	0.023	0.37	1.466e-2
T304-HN	0.073	0.28	1.610e-2
18Cr-2Ni-12Mn	0.100	0.29	1.665e-2
22Cr-13Ni-5Mn	0.020	0.28	1.752e-2
Gall Tough	0.103	0.12	1.429e-2
15-15LC (unannealed)	0.033	0.41	1.662e-2
18-18 Plus (unannealed)	0.110	0.48	1.577e-2
Gall Tough Plus	0.104	0.20	1.757e-2
15-15LC Modified	0.047	0.46	1.563e-2

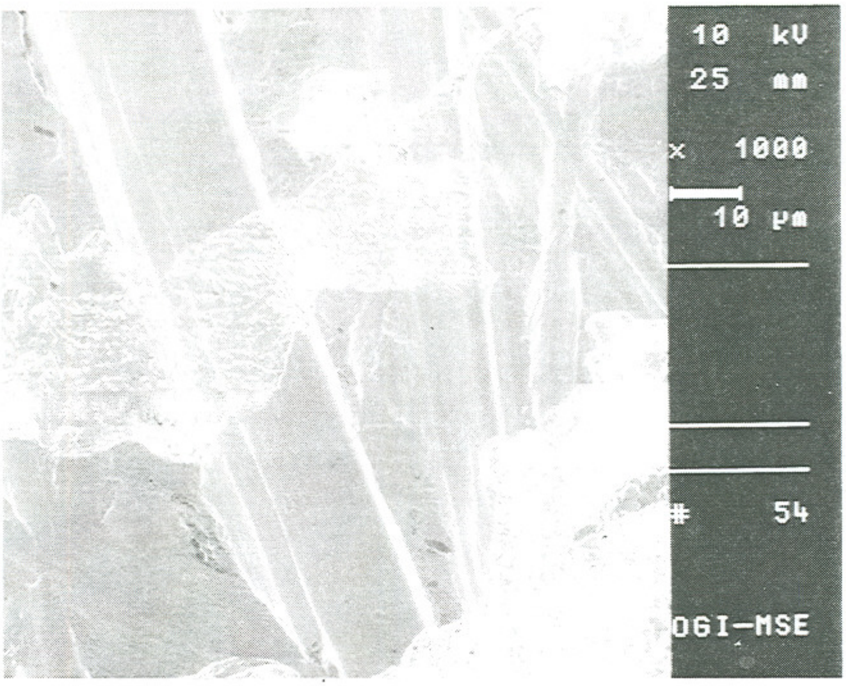

Figure 4-55: Secondary electron image of wear surface of as-cast 1.4 atm N-HPM pin following abrasion against 150 grit garnet; electrolytically etched with 10% ammonium persulfate to reveal grain structure, 1000x.

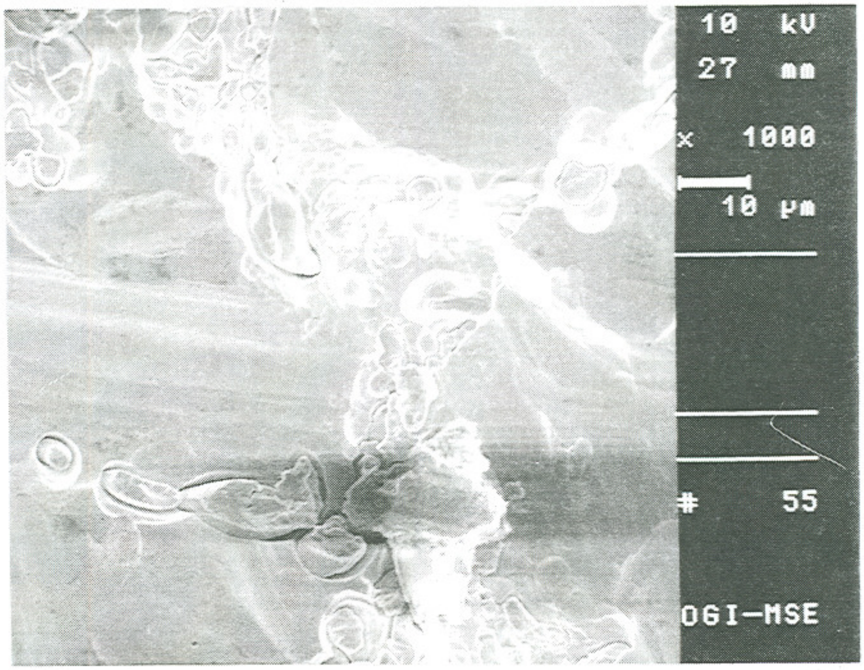

Figure 4-56: Secondary electron image of wear surface of as-cast 50 atm N-HPM pin following abrasion against 150 grit garnet; electrolytically etched with 10% ammonium persulfate to reveal grain structure, 1000x.

4.2.7 Corrosion Resistance of N-HPM Materials

The results of localized corrosion resistance testing are tabulated in **Table 4-21**.

Critical Pitting Potential Tests:

All of the samples tested behaved generally the same in the NaCl solution. None of the materials exhibited any pitting during the testing. Although the values were determined from only one test run, all of the samples had relatively similar values of E_{corr}, etc, as shown in **Table 4-22**. All of the samples exhibited passive and transpassive behavior, without pitting, as demonstrated in the sample polarization curves shown in **Figure 4-57**. Breakdown potentials were also similar for most of the samples.

Critical Crevice Temperature:

For stainless steels, it has been found that the CCT is generally about 20°C (35°F) lower than the Critical Pitting Temperature (CPT). Thus, the CCT test is more aggressive than the CPT. Therefore, only the CCT test was performed on these materials. All of the samples tested ran up to the upper limit of the test of ~96°C (205°F) without any crevice corrosion occurring. Thus, none of the materials were found to be susceptible to crevice corrosion under the test conditions used.

The results of the localized corrosion testing in conditions approaching biomedical ones, indicate that nitrogen alloying did not negatively alter the already excellent corrosion properties of the Stellite 21 material. Thus, the biocompatibility of the material was likely retained following nitrogen alloying and subsequent processing.

Table 4-21: Corrosion resistance results for rolled and annealed N-HPM materials

Sample ID	Materials Processing	N (wt%)	CPP(1)	CCT(2)
HIPed	Conventional cast and HIPed F75#1	~0.1	ND	ND
10 atm Ar	N-HPM 10 atm Ar, hot-rolled & annealed	0.102	ND	ND
1.4 atm	N-HPM 1.4 atm, hot-rolled & annealed	0.194	ND	ND
4 atm	N-HPM 4 atm, hot-rolled & annealed	0.342	ND	ND
16 atm A	N-HPM 16 atm A, hot-rolled & annealed	0.401	ND	ND
16 atm B	N-HPM 16 atm B, hot-rolled & annealed	0.496	ND	ND
50 atm	N-HPM 50 atm, hot-rolled & annealed	0.835	ND	ND

(1) Critical Pitting Potential [Potentiodynamic Anodic Polarization Scan (3.5% NaCl)]
(2) Critical Crevice Temperature Test (3.5% NaCl)
ND-No pitting/crevice corrosion detected

Table 4-22: Corrosion data for rolled and annealed N-HPM materials(1)

Sample ID	N (wt %)	B_a (anodic slope)	B_c (cathodic slope)	E_{corr} volt (SCE)	I_{corr} (amps/cm^2)
HIPed	~0.1	0.168	0.198	-0.405	5.68e-7
10 atm Ar	0.102	0.216	0.188	-0.383	1.00e-7
1.4 atm	0.194	0.205	0.216	-0.337	1.38e-7
4 atm	0.342	0.262	0.127	-0.350	1.92e-7
16 atm A	0.401	0.288	0.177	-0.374	2.83e-7
16 atm B	0.496	0.193	0.192	-0.351	7.11e-7
50 atm	0.835	0.210	0.196	-0.395	1.82e-7

(1) Data obtained from one Potentiodynamic Polarization Scan (3.5% NaCl) per sample

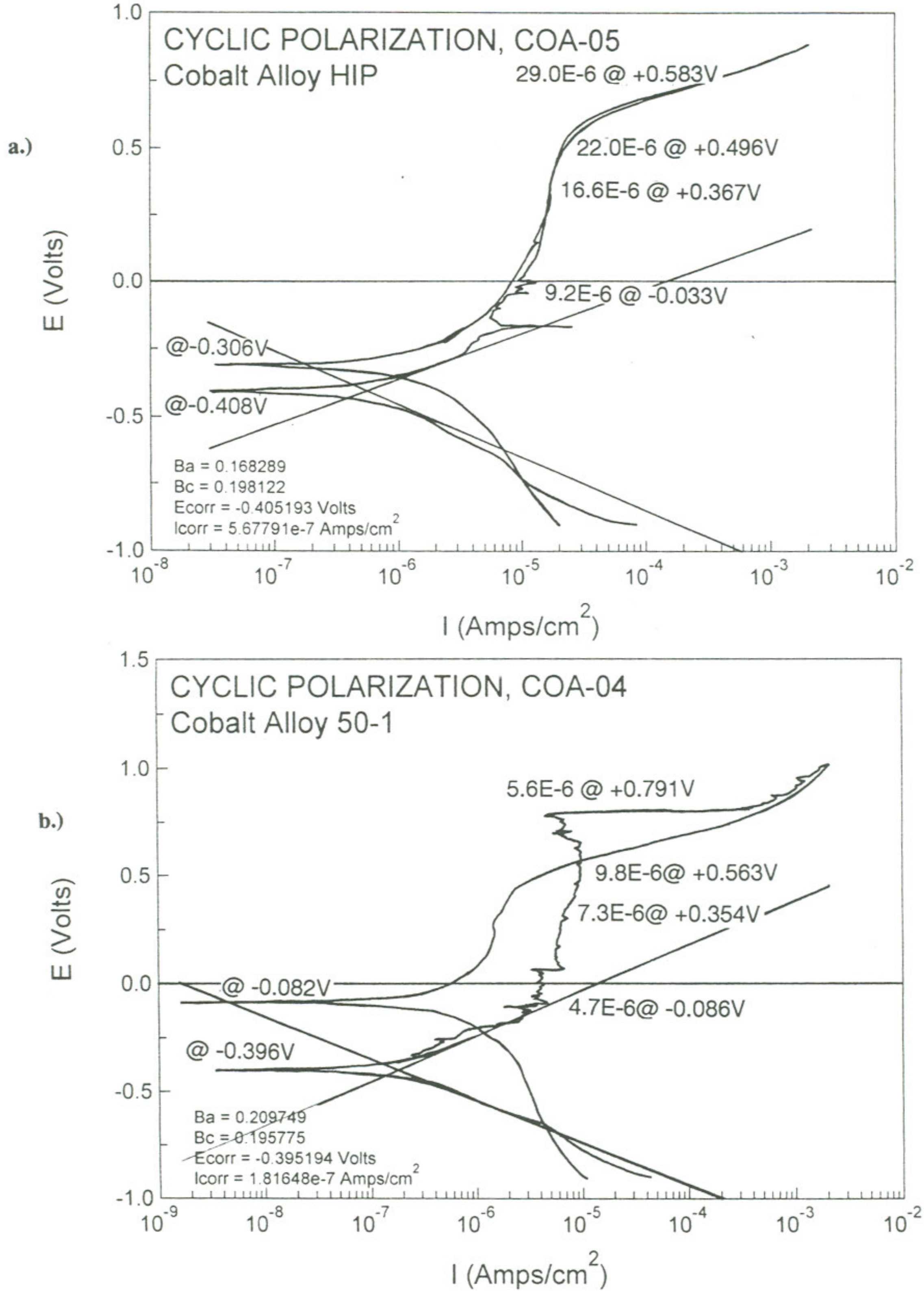

Figure 4-57: Sample polarization curves for a.) as cast and HIPed ASTM F75, and b.) rolled and annealed sample from 50 atm N-HPM Stellite 21.

5. DISCUSSION

Thermal and mechanical processing of the Co-Cr-Mo materials of this study altered the properties of the materials by changing certain microstructural features. The microstructural features considered in detail are the second phase material itself, its quantity and distribution, and the grain size distribution. The addition of nitrogen altered the microstructure, affecting the properties following thermal and mechanical processing.

5.1 Processing Effects on the Microstructure

5.1.1 Effects on the Second Phase Material

Initial second phase

Each of the initial cast structures showed a different distribution of second phase material. The second phase content was lowest in the F75 A conventionally cast materials, at about 6%. The conventionally cast and fine-grained cast F75 B yielded about 8 and 10% respectively, while the N-HPM materials ranged from 10% in the top of the lowest nitrogen ingots, to 30% in the top of the highest nitrogen ingots. While the basic casting processes in each case were different, the segregation differences were most likely attributable to compositional differences. This is shown by examination of the second phase material itself.

The interdendritically segregated material in the F75 A *conventional* castings was shown through TEM to have carbides of the type $M_{23}C_6$, with an occasional M_7C_3. These are the same carbide structures observed by other researchers in this material [23, 24, 26], and were expected to be present. Scanning electron microscopy energy dispersive x-ray spectroscopy (SEM-EDX) revealed that the composition of these carbides tended to be rich in Cr, as would be expected since their base structure is $Cr_{23}C_6$. They were also shown to be quite rich in Mo. Apparently, the Mo substituted for the Cr in the M of the

$M_{23}C_6$ structure. One other possibility is that the Mo_6C carbide was present in the interdendritic material. But since it was never observed in the TEM samples, that seems unlikely, especially considering that Mo was present in *all* of the SEM-EDX spectra for the segregated material.

The SEM-EDX spectra for the intergranular material in the *fine-grained* castings was similar to that of the interdendritic material in the conventional castings. However, for the same alloy F75 B, the second phase material in the fine-grained casting was richer in both Cr and Mo than in the conventional casting. It was also lower in Co. This same phenomenon was described by Zhuang and Langer in their work [36]. In their case, the difference was attributed to the fact that dendritic solidification in a conventionally cast alloy allowed solute composition gradients to be set up within the dendrite matrix, whereas in their fine-grained product this was not observed. Solute incorporation into the dendrite matrix would also explain why the second phase material could end up with less Cr fraction than the bulk material, as was observed in the F75 B alloy.

Comparison of the *distribution* of the second phase material shows that, although the grain structure was finer in the fine-grained castings, the average distance between the clusters of second phase was equal to the grain diameter, or on the order of 50 to 100 μm. This is significantly coarser than the 20 to 50 μm spacing of the interdendritic islands of the conventionally cast material.

As introduced above, there was a greater *quantity* of second phase segregation observed in alloy F75 B in both conventional and fine-grained morphologies, than in the conventionally cast F75 A. The bulk chemistries of the two investment cast F75 alloys showed that the F75 B material had 0.24 wt% carbon compared to the lower 0.21 wt% of the F75 A material. This could contribute to the additional second phase observed. More carbon available for the formation of carbides in the second phase material would encourage an increase in second phase material. Similar behavior was also observed in the N-HPM materials for nitrogen additions.

In the N-HPM materials, there was an increase in overall second phase content from 10% up to 30% with increasing nitrogen content, as shown in **Figure 5-1**. So, it becomes apparent that as, in the case of the carbon, as the nitrogen level increased in the starting material, so too the amount of nitrides increased in the subsequent casting.

Looking specifically at the changes in second phase structure that were observed in the N-HPM alloy, several important points are noted. Firstly, XRD on the residues showed that for 0.1 and 0.2 wt% N, $Cr_{23}C_6$ was the minority phase, with residual FCC cobalt being the majority phase. Then at 0.34 wt% N the Cr_2N replaced $Cr_{23}C_6$ as the minority phase, until at 0.52 wt% Cr_2N became the majority phase over the FCC Co.

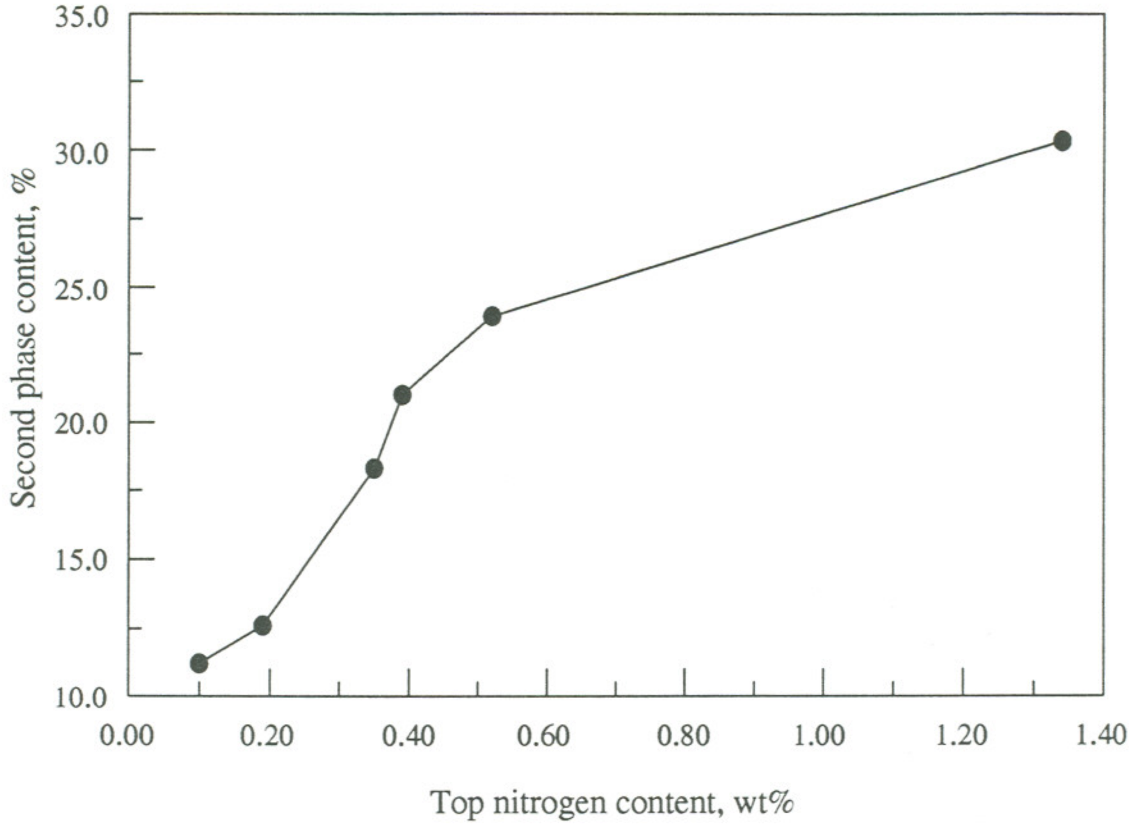

Figure 5-1: Second phase content v.s. nitrogen content in upper region of as-cast N-HPM Stellite 21

Finally, at 0.85 wt%, CrN also emerged in minor quantities. If N and C are taken as atoms competing to bond with Cr to form carbides, nitrides, or carbonitrides, the observed structure changes make sense. The ratio of Cr (or M) to the N or C (X) in each compound would be 3.8:1, 2:1, and 1:1 for $M_{23}X_6$, M_2X, and MX respectively. Thus, since the carbon content was uniform throughout the various ingots, as we enriched the alloy in nitrogen, we had a tendency to stabilize compounds of decreasing M:X ratios. The switch from a carbide structure to a nitride structure occurred between 0.20 and 0.34 wt% nitrogen, or the composition at which the nitrogen content exceeded the carbon content, which would explain why the Cr_2N structure becomes favored over the $Cr_{23}C_6$. The observation of the Cr nitrides described corresponds well to the observations made by Kilner et. al. in their solid-state work on Co-Cr-Mo [49]. As in their case, the carbon most likely substituted for some of the nitrogen atoms in the nitrides, and vice-versa in the carbides, with the composition determining the structure.

Having set the baseline for the second phase morphology as it resulted from casting, the effects of the subsequent processing steps are considered in turn. The two processing steps that had significant effects on the second phase materials were solutionization, and hot-working.

Hot-rolling effects

As introduced in the results, the effects of hot-working on the second phase material of the N-HPM billets were to mechanically break it down and redistribute it. This resulted in smaller second phase pieces that were more uniformly distributed, although they tended to form stringers of particles in the direction of the rolling. More importantly, the rolling broke apart the second phase such that it was no longer interconnected.

Solutionization effects

The solutionization success of the materials was found to be dependent not only on time and temperature, but also on the initial second phase type and morphology. The temperature and time response was typical of diffusion dependent predictions that higher temperatures and longer times lead to greater dissolution. Yet, for similar solutionization times and temperatures, the various materials of this study had different responses.

Firstly, the fine-grained castings tended to show less overall solutionization compared to the conventional castings. This was partly due to the higher initial second phase content, but it was also because the second phase material in the fine-grained castings was distributed in larger, coarser islands. Less interfacial area/volume through which diffusion could take place, would result in less diffusion, and thus more residual second phase material for a given temperature and time. This was observed to be true, even within a component displaying an initial microstructural gradient from fine to coarse along the length. In this latter case, more complete dissolution was observed in the fine regions compared to the coarse regions.

Considering the N-HPM materials, several more things are revealed. For the as-cast 0.1 and 0.2 wt% materials which contained *carbides* as the second phase, the solutionization behavior was very similar to that of the investment cast F75 alloys, showing a very rapid reduction in second phase after relatively short times at temperature. However, in the higher nitrogen materials containing *chromium nitrides*, the solutionization behavior was not as rapid. This was observed in the as-cast material, but as was noted previously, gradients in the second phase content existing in the original ingot may have obscured the solutionization response somewhat. The *rolled* N-HPM materials demonstrated the effects more clearly, as discussed next.

Before considering the solutionization response of the rolled material, it should be noted that the billets were all soaked for 16 hours at 1220°C (2220°F) prior to the rolling, which led to some preliminary solutionization. But, since incomplete solutionization occurred, consideration can be given to the results of solutionization subsequent to the rolling. These results showed rapid dissolution of the $Cr_{23}C_6$ in the low nitrogen samples, but then, beginning with the 4 atm specimen (0.34 wt% N), very little further dissolution of the nitrides was observed in the higher nitrogen samples, even after long times at 1260 °C (2300°F). This suggests that either the solubility of the nitrogen was already nearly exceeded in the matrix, the diffusion kinetics simply required more time, or that the chrome nitrides are quite stable at the elevated temperatures of the solutionization processes. As described next, these are all related to the composition.

Looking specifically at the 50 atm case, the first possibility is considered. In the solutionization study on the as-cast N-HPM material, the 50 atm sample displayed an initial precipitation of second phase material after 1 hour at 1220°C (2220°F). Although the material was subsequently re-dissolved, this observation suggests that at least some portions of the matrix (near the interdendritic islands) had exceeded the solid state nitrogen solubility at 1220°C (2220°F), and that the nitrogen content of the 50 atm material was approaching the solid solubility limit. However, this means that the specimens with lower nitrogen contents likely did not approach the solubility limit, especially since they did not show any signs of precipitation during the solutionization treatment.

Considering the diffusion kinetics, it is apparent that in most of the samples further dissolution occurred with increasing temperature and time. But, the amount of dissolution was much less for the samples containing nitrides rather than carbides. A good example is the 50 atm material, which showed a residual second phase content of 9-10% after 4, 8, *and* 16 hours of solutionization at 1260°C (2300°F), even after the original 16 hour pre-rolling solutionization treatment. By being near the solubility limit, the driving force for dissolution would be less, as would be lattice sites available for diffusion, effectively stabilizing the second phase.

In considering the phase stability, the 50 atm material is again a good example. The XRD results for the as-cast 50 atm sample showed the presence of CrN, but the rolled and annealed results did not. This indicates that perhaps the CrN was not stable at 1220°C (2220°F), because it disappeared somewhere between the cast condition and the rolled and annealed condition. Most likely the structure transformed and perhaps dissolved during the original 16 hour pre-rolling solutionization treatment. But, the fact that Cr_2N remained in the materials after both CrN and $Cr_{23}C_6$ dissolved, makes it likely that some quantity of the Cr_2N is stable in the material even at elevated temperatures. The stability is increased as the solubility limit is approached, so as more N was added, the Cr_2N was further stabilized. Thus, by increasing the nitrogen content to produce a more stable Cr_2N second phase material in greater quantities, full solutionization is not attained, as it was in the low nitrogen materials which contained $Cr_{23}C_6$ as the primary component of the second phase material.

Besides the dissolution rate already discussed, the solutionization treatments also led to some intermediate structural changes in the second phase. The first of these was just introduced, in which the CrN structure was found to have disappeared during the heat treatments following casting. A second case was the structural transformation of the M_7C_3 observed in the conventionally cast F75 material. The mechanism for this described by Kilner et. al. [26], involves the carbon atoms diffusing away from the M_7C_3 faster than the metal atoms (M), due to interstitial carbon's much greater diffusion rate [25]. In this way, the M:X ratio of the carbide increases from the 2.3:1 of M_7C_3, to the 3.8:1 of $M_{23}C_6$, encouraging a structural change. A similar mechanism could apply to transformation of the CrN to Cr_2N in the 50 atm samples. If the nitrogen atoms interstitially diffused away from the CrN, its 1:1 ratio would move towards the 2:1 ratio of the Cr_2N, preferentially stabilizing that phase. Thus, during the solutionization treatments of these alloys, the least stable compounds break down first, followed by dissolution of the more stable structure until the equilibrium distribution is approached. This two-stage solutionization concept has been described by other authors also [25].

The diffusion of the elements to the more stable *composition* of the compounds is similar to the intermediate transformation of compounds to a more stable phase during solutionization. This behavior was observed in the conventionally cast F75 A material by SEM-EDX measurements. As the carbide dissolved, the composition of the remaining material became richer in Cr than in Mo. This could be a result of the preference of the $M_{23}C_6$ to contain Cr rather than Mo. To approach the more stable composition, the Mo atoms could preferentially be released by the compound during dissolution. Thus, the most stable $Cr_{23}C_6$ structure would be approached in the material.

Incipient Melting:

An exceptional behavior related to the stability of the Cr_2N over the $M_{23}C_6$ in the alloy is that of the observed change in the incipient melting behavior of the interdendritic material. In the 0.10 and 0.20 wt% N samples which contained $M_{23}C_6$ as the primary segregating material, incipient melting was observed at 1240°C (2260°F) and at 1260°C (2300°F). However, incipient melting was *not* observed in any of the nitride containing alloys heat treated at these temperatures. Kilner [24] attributed incipient melting in the Co-Cr-Mo alloy to the presence of a low melting point eutectic containing $M_{23}C_6$ as a primary constituent. He measured the incipient melting temperature to be about 1235°C (2255°F) for an alloy of carbon content similar to that of this study. It is possible that replacement of the $M_{23}C_6$ with Cr_2N through nitrogen alloying was sufficient to raise the melting point of the interdendritic second phase to some temperature above 1260°C (2300°F). Such an improvement could contribute significantly to the retention of mechanical properties following sintered bead coating of biomedical implants made of this alloy, as was described by Farhangi [32].

Cooling Rate Effects:

In the study on the fine-grained investment cast F75, the materials conventionally cooled following solutionization or HIPing experienced precipitation of second phase material in a pearlitic morphology near regions of residual second phase islands. Cooling at a rate of 667°C/minute (1200°F/min) for the first 30 seconds was found to be sufficient to avoid this precipitation. The observation of precipitation upon cooling more slowly introduces the fact that, not far below the solutionization temperature rapid precipitation is possible. This leads to discussion of the effects of thermal treatments taking place *below* the solutionization temperature, or in the aging regime.

Aging effects

Conventionally cast materials

Since they give a basis for understanding the subsequent results, the results of the conventionally cast F75 A material are considered first. As described previously, pre-aging solutionization treatments resulted in the 1220°C (2220°F) treatment dissolving more second phase material than the 1190°C (2175°F) treatment, for the 8 hour solutionization time chosen. However, the 1070°C (1960°F) specimen showed almost as much interdendritic islands as the as-HIPed specimen of the heat treat series, suggesting that very little additional solutionization occurred in the 8 hours at this temperature. Also, as previously noted in **Table 4-2**, (**Results**), it contained many other second phase morphologies. In fact, the 1070°C (1960°F) appeared to contain most of the second phase morphologies observed in the aged specimens of the study. Thus, it is considered as a special case, and discussed before addressing the aged specimens proper.

Special case of 1070°C (1960°F):

Most likely, 1070°C (1960°F) lies in the region in which solutionization and precipitation occur simultaneously, as described by Levine [31]. Perhaps the activity taking place in this specimen was the diffusion of atoms away from the interdendritic and grain boundary carbides, into the lenticular precipitation nuclei. It could be theorized that the highly irregular surface of the interdendritic material led to a high total surface energy, so smoothing the surface by diffusing atoms to more suitable locations would result in lower total free energy, and lead to the spherical morphology observed in the residual interdendritic islands after the heat treatment. Coarsening of precipitates could also reduce the free energy, as in Oswald ripening. Whether the elements simply relocated along the interface or diffused to a whole new location was difficult to determine. The important point about the 1070°C (1960°F) "solutionization" temperature is that effective dissolution did not occur, and simultaneous random precipitation *did*.

TEM analyses of 1070°C (1960°F) material showed that the crystal structure of the precipitates was $M_{23}C_6$, and that their orientation relationship was of the $<111>_{Carbide}//<111>_{FCC}$ type. This $M_{23}C_6$ crystal structure has been documented in the literature to be the expected type; however, the orientation relationship with the FCC matrix is one of controversy [17]. Some authors have maintained that the precipitation only occurs in the HCP phase, but Robertson [23] identified precipitation in the FCC grains of a 0.25%C F75 alloy. The susceptibility of precipitation *has* been shown to be partial to the HCP phase, especially at low carbon, but with increasing carbon content, precipitation in FCC grains is also observed. With about 0.2%C in the alloy of this study, precipitation in the FCC phase is not unreasonable. The orientation relationship observed is attractive from a strengthening standpoint, because it indicates potential for blocking dislocations on the specific planes in which slip would be taking place (the octahedral planes). Taking $M_{23}C_6$ as the crystal structure of the precipitates, the *morphology* of the precipitates becomes the main subject as the aged samples are discussed.

Aging Cycles:

The results of the *aging* cycles of this study appear to be similar to the results reported by Robertson [23]. Robertson described the typical morphology of the precipitates in his 0.25%C specimen as rhombic. He also found aging at 700°C (1290°F) to produce lenticular-type plates near grain boundaries, and then precipitation at grain boundaries. Aging at 800°C (1470°F) reportedly showed a tendency to precipitate in parallel rows across the grains, with some plates and perhaps grain boundary precipitates. Aging at 900°C (1650°F) led to profuse precipitation across the grains in 1 hour. Robertson also noted that at higher temperatures, rod shapes and needle morphologies were present, even in very low carbon alloys. These are all morphologies observed in the aged materials of this study.

Specimen A/1070/700/3 had a microstructure very similar to the 1070°C (1960°F) specimen. In TEM, facetted (rhombic) precipitates were observed, although these were also found in the 1070°C (1960°F) specimen. There appeared to be more lenticular precipitates in the 700°C (1290°F) aged specimen than the specimen that wasn't intentionally aged, but due to the substantial heterogeneity of the microstructure, it is difficult to conclude if the difference is significant. There is also a possibility that the portion of the heat treat cycle intended as a solutionization treatment, since it has been shown to actually be in the aging regime, led to nucleation and growth of all of the precipitates in the microstructure, and then the aging step merely led to a continued growth of the existing precipitates, if anything at all.

Moving to the specimen solutionized at 1190°C (2175°F), examination of the results of the 700°C (1290°F) aging treatment is easier. The specimen from A/1190/700/6 indicated very little except residual interdendritic islands, a microstructure that was the same as the 1190°C (2175°F) solutionized specimen, even after the 6 hour aging time. The residual grain boundary precipitates from the HIP cycle were dissolved, and no subsequent grain boundary precipitation was evident. This suggests two things: that the grain boundary precipitates readily re-dissolve before the interdendritic islands finish dissolving, and that these precipitates do not occur at temperatures as low as 700°C (1290°F) for the short times investigated. TEM of the A/1190/700/6 specimen revealed very fine strings of second phase particles, although the analysis was very cursory. The optical microscope analysis *also* showed faint precipitate strings in highly polished regions, but with those exceptions, the 700°C (1290°F) aging temperature did not show any of the other morphologies.

Moving up in solutionization temperature once again to the specimen that underwent the maximum solutionization at 1220°C (2220°F), as well as the longest aging time, the effects of the 700°C (1290°F) aging treatment are further clarified. With the maximum solutionization cycle, the microstructure of the group A/1220/700/12 sample was quite uniform and clean. There were, however, faint transgranular strings of precipitates, confirming that this morphology is the only one which reaches down to the 700°C (1290°F) temperature regime, at least in the 12 hours spent at this temperature. This is confirmed by the TEM analysis, which revealed very fine, facetted precipitates present within the grains, in a cube-cube orientation that would be conducive to the uniform distribution of the precipitates within the matrix, as observed.

Considering the 900°C (1650°F) aged specimens, the specimen from group A/1220/900/3 also showed clean grains, but there was very heavy precipitation on the grain boundaries. The 900°C (1650°F) temperature seems to be one at which grain boundary precipitation is dominant. In sample A/1220/900/3, though, there was even more carbide material present than in any of the other 900°C (1650°F) specimens, even though it was aged for only 3 hours. This may be attributed to the fact that greater solutionization occurred at 1220°C (2220°F), so more material was in solution, serving as a heightened driving force for subsequent precipitation.

The results of the 6 hour 900°C (1650°F) aging cycle of the A/1070/900/6 specimen, also appear to be the same as the 1070°C (1960°F) heat treated specimen, and may be residual from that step in the cycle.

The specimens from groups A/1190/900/12 showed thin, continuous, grain boundary precipitates, indicating that the 900°C (1650°F) aging temperature following the 1190°C (2175°F) solution treatment appears to favor a grain boundary precipitate over the lenticular morphology, in the 12 hours spent at temperature. This confirms that the other precipitate morphologies observed in A/1070/900/6 are most likely a result of the 1070°C (1960°F) heat treatment prior to the aging treatment.

The microstructure of the specimen from group A/1190/1050/3 showed abundant transgranular strings of precipitation after only 3 hours at the highest aging temperature, with nodes forming at the intersections of these strings. This suggests that the transgranular precipitation morphology occurred readily at 1050°C (1920°F). This specimen also displayed continuous grain boundary precipitation, confirming that this morphology is a high temperature one.

In specimen A/1220/1050/6, aged at 1050°C (1920°F) for 6 hours, the grain boundary carbides were once again present, but were thin and well defined. The transgranular strings, although present, were not very continuous. They were very similar in morphology to those of the 1070°C (1960°F) specimen, supporting the earlier remarks that the transgranular strings seen in groups A/1070/700/3, and A/1070/900/6 were probably due to the higher temperature portion of their heat treatment cycle. One carbide morphology present in A/1220/1050/6, and shared by the 1070°C (1960°F) specimen, had a pearlitic appearance. This morphology is similar to the morphology of the precipitation observed in fine-grained samples that had been cooled too slowly after the solutionization treatments. This indicates that perhaps this is a high-temperature morphology. Another type of precipitate morphology present in A/1220/1050/6 in great quantities, was a stipple morphology. It consisted of small precipitates widely distributed in the microstructure. Specimens A/1220/1050/6 and A/1190/1050/3 showed the greatest quantity of this morphology, but it was also present in appreciable amounts in the specimens aged at 1050 °C (1920°F), and less so in those aged at 900°C (1650°F). The stipple morphology was not present in the specimens aged at 700°C (1290°F).

It appears from the results that the 1050°C (1920°F) cycle of group A/1070/1050/12 was near the regime of maximum grain boundary and lenticular precipitates. The 1050°C (1920°F) aging temperature also led to further dissolution of the interdendritic islands in the 12 hours that the specimen spent at this temperature, which is not unexpected, since it lies so near the 1070°C (1960°F) heat treatment temperature. Some things noted were that no strings of transgranular precipitates were present in this specimen, and that the lenticular carbides tended to precipitate near and among the interdendritic islands. The likely reason for not observing transgranular strings is that the low initial heat treatment temperature of A/1070/1050/12 did not allow enough solute transport deep into the grains for these transgranular strings of precipitates, so the material preferentially precipitated near the residual second phase islands. The temperatures of the initial and final heat treatments are so similar, that this sample can be considered in a similar manner as the 1070°C (1960°F) sample, in which simultaneous dissolution and re-precipitation occurred.

Fine-grained cast material:

The previous analysis was for aged specimens which had been *conventionally* cast. If comparison is made to the aging response of samples which began with a fine-grained microstructure, and were aged only at low temperatures, some similarities and differences are observed. Firstly, the precipitates in the fine-grained material were about the same size as the stipple-type morphology observed in the conventional material, but as they emerged in the matrix, they did so oriented in transgranular strings.

Simultaneously, precipitates advanced into the grains from the grain boundaries in a morphology similar to the pearlitic morphology described previously, but on a much finer scale. This was most pronounced in the specimens aged at 750°C (1380°F). Not until after about 8 hours did the fine-grained specimens heat treated at 700°C (1290°F) demonstrate much precipitation visible under the light microscope, and then the only morphology was some fine, transgranular strings in parallel rows. Thus, the transgranular strings of fine precipitates seem to be the preferred morphology in the 700°C (1290°F) temperature range for both casting types. However, the pearlitic precipitation associated with the grain boundary also occurred at longer times, at 750°C (1380°F) in the fine-grained material. This may have been due to the fact that the fine-grained material was shown to have much greater segregation at the grain boundaries, so the solute elements would be richer near the grain boundaries following solutionization, and subsequently would encourage re-precipitation near the grain boundaries. If greater homogenization were achieved, this may not occur as readily.

To summarize the carbide morphologies present to differing degrees at different temperatures and times as reflected by the aging results, a rough sketch of pseudo T-T-T curves for each morphology is shown in **Figure 5-2**. The important point is that aging at 900°C (1650°F) results in coating of the grain boundaries by precipitates. Aging above that temperature results in a wide array of morphologies precipitating in an uncontrolled fashion. Near 700°C to 750°C (1290°F-1380°F), the precipitation occurs in a more controlled fashion. This is most likely a function of the competing nucleation and growth kinetics of the precipitates. At the lower temperature, the diffusion rate of the solute elements would be slow, but the driving force to precipitate would be large, resulting in a high nucleation rate but slow growth rate. At the higher temperature, the driving force to precipitate may not be as large, but the diffusion rate of the solute elements would be rapid, and thus a low nucleation rate would be coupled with a high growth rate. Since the aging study was done from a processing and mechanical properties perspective, analysis of the precipitate kinetics is incomplete.

5.1.2 Effects on the Grain Structure

As introduced in the Results section, the conventional and N-HPM castings demonstrated a very large-grained dendritic structure. But, by design, the fine-grained cast material showed comparatively small, equiaxed grains that ranged from about 50μm in the bottom region, to about 120μm in the top region. This is on the same order as the size developed in the material of Zhuang and Langer [36].

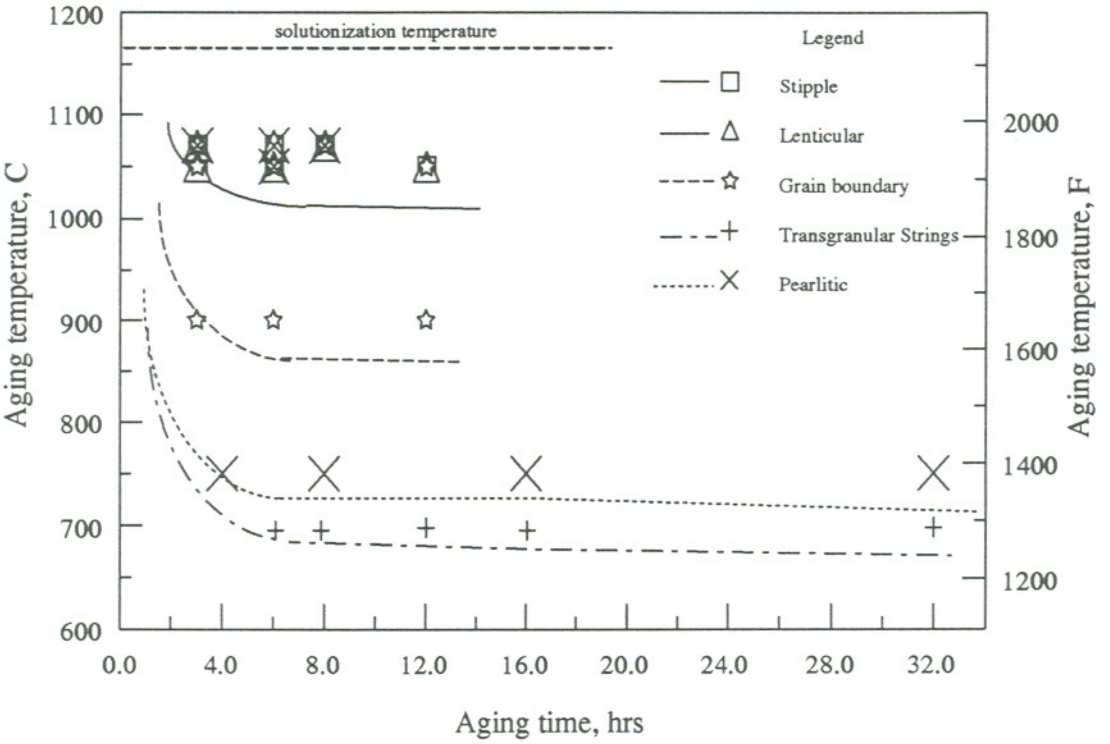

Figure 5-2: Sketch of preferred precipitation morphology regimes for cast Co-Cr-Mo material

Hot-rolling effects

Following hot-rolling of the N-HPM castings, a fine, equiaxed grain structure was produced in the material which showed an average grain size that ranged from 1/5 to 1/10 the grain diameter of the fine-grained investment cast material of this study. This grain structure was the result of recrystallization, in which the deformed grain structure of a worked material reduces its residual stress by essentially sweeping the dislocations out of the grain matrix, forming into new grain boundaries. The empirical equation describing this behavior shows a dependence upon time and temperature, but the subsequent grain size is also a function of the deformation prior to annealing. It is difficult to assess the amount of deformation that each of the N-HPM plates experienced, since multiple passes were taken to roll each billet. This is reflected in the apparently random grain size measured for the "as-rolled" plates which underwent a final 15 minute heat at 1100°C (2010°F) prior to cooling following rolling.

However, upon subsequent "annealing" of the plates at 1200°C (2190°F) for 15 minutes, the grain size of the hot-rolled materials grew to 2 to 6 times their original diameter. The subsequent grain size distribution showed a uniform trend of decreasing grain sizes with increasing nitrogen content. After the annealing, the grain size of the rolled N-HPM material approached that of the fine-grained investment cast material. Further high temperature processing led to grain growth in both the rolled N-HPM materials, and the fine-grained investment cast material.

Grain growth

Both the rolled N-HPM materials and the fine-grained investment cast materials experienced an increase in grain size following high temperature heat treatments. The subsequent grain size generally increased with increasing time and temperature in samples from the same group.

In the classical models, grain growth has been shown to be driven by the reduction in free energy attained by reducing the surface to volume ratio. The rate of growth has been shown to be a function of the square-root of time and of an activation constant. The activation constant is an exponential function of the inverse of the temperature. Although experimental data rarely follows the equation very closely, the grain growth does generally increase with increasing time and temperature. The increase in grain size over time was shown particularly well in **Figure 4-21** of the **Results** section, in which the grain size of the fine-grained cast material is shown to increase over time at 1220°C (2220°F), but change little at 1190°C (2175°F).

Effect of second phase on grain size

It is known that second phase material within the matrix of a metal can reduce grain growth. It does so by "pinning" the grain boundaries, thereby slowing their advance during grain growth. The mechanism is analogous to dislocations being blocked by precipitates. Second phase pinning of the grain boundaries was observed in the fine-grained materials of this study in two capacities. The first was in the retention of finer grains following hot-rolling and annealing of the N-HPM materials from different sample groups, and the second was in the retardation of grain growth during solutionization of samples within the *same* group.

Figure 5-3 shows the relationship between the second phase content of the material and the grain size following annealing of the hot-rolled N-HPM material. It demonstrates that although the *same* thermal treatment was experienced by each of the samples, those with higher second phase content were able to retain a finer grain size following annealing. This is most likely attributable to pinning of the grain boundaries by the second phase.

A similar relationship was observed following solutionization in the fine-grained materials. The second phase contents and corresponding grain sizes of the solutionized fine-grained investment cast materials are shown in **Figure 5-4**, and for the solutionized rolled N-HPM materials in **Figure 5-5**. As the plots indicate, as the second phase content was reduced by solutionization, a simultaneous increase in grain size was observed. This was because, with dissolution of the second phase, there was less residual second phase to serve as pins at the grain boundaries. As they became unpinned, some boundaries were able to accelerate their motion, leading to expansion of the grains. In both materials, the *range* of grain sizes measured within a sample was broad. This is a natural function of grain growth, as larger grains expand to gradually consume the smaller ones, a range of large and small grains results.

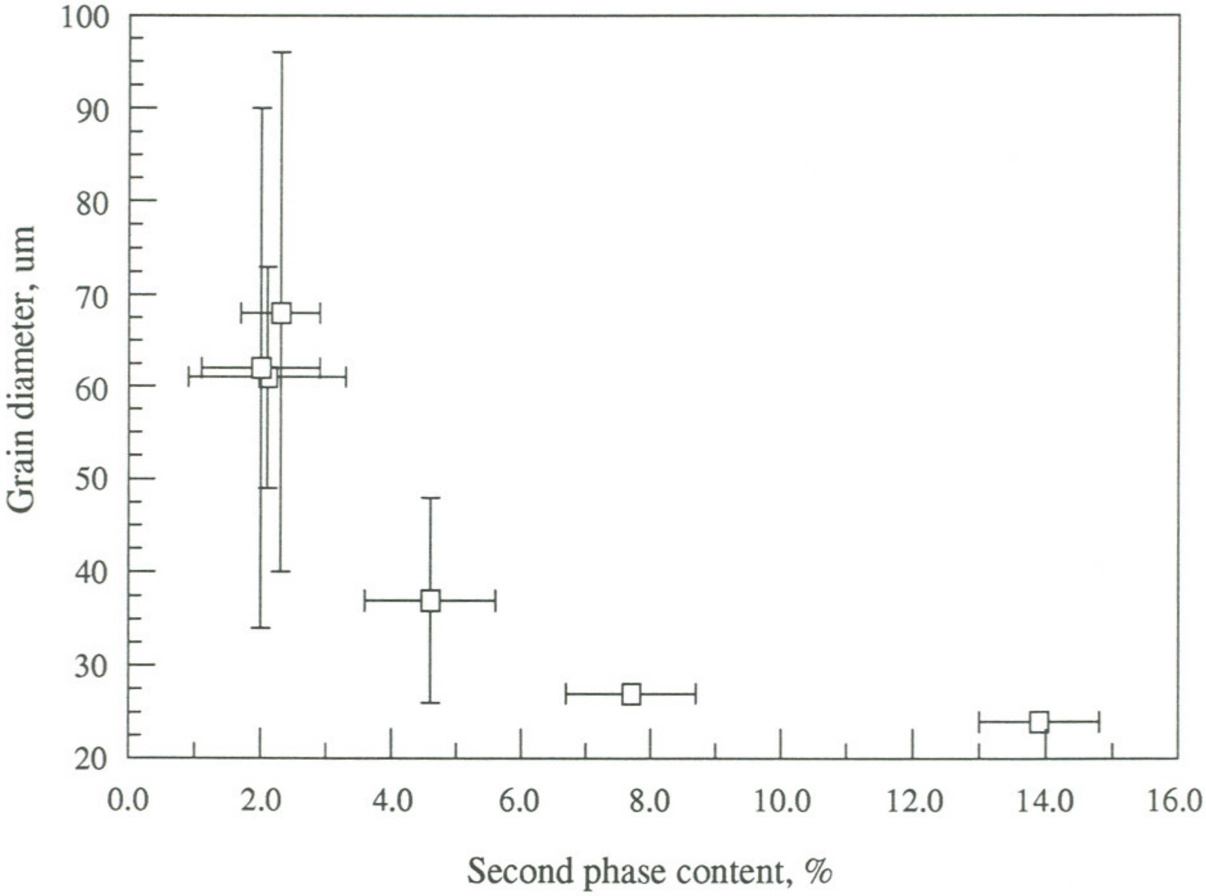

Figure 5-3: Relationship between the second phase content and the grain size of N-HPM material rolled and then annealed at 1200°C (2190°F) for 15 minutes

It is apparent that about 3-4% second phase material was required for retention of <100μm diameter grains in the rolled N-HPM material. On the other hand, the same size was retained in the investment cast materials with only about 1% second phase. While the increased grain growth in the rolled N-HPM materials may be partially due to the higher solutionization temperatures experienced by many of the specimens, if the pinned microstructures in **Figure 5-6** are compared, a contributing factor is revealed. The microstructures show that more effective pinning in the cast materials at lower second phase contents could be due to the fact that the second phase content is originally distributed at the grain boundaries, so in a morphology conducive to grain boundary pinning. On the other hand, the rolled N-HPM materials have a second phase distribution developed by hot-rolling that is independent of the equiaxed grain structure. In this case, the interaction between grain boundaries and second phase particles is somewhat more random, leading to more second phase being required for effective pinning.

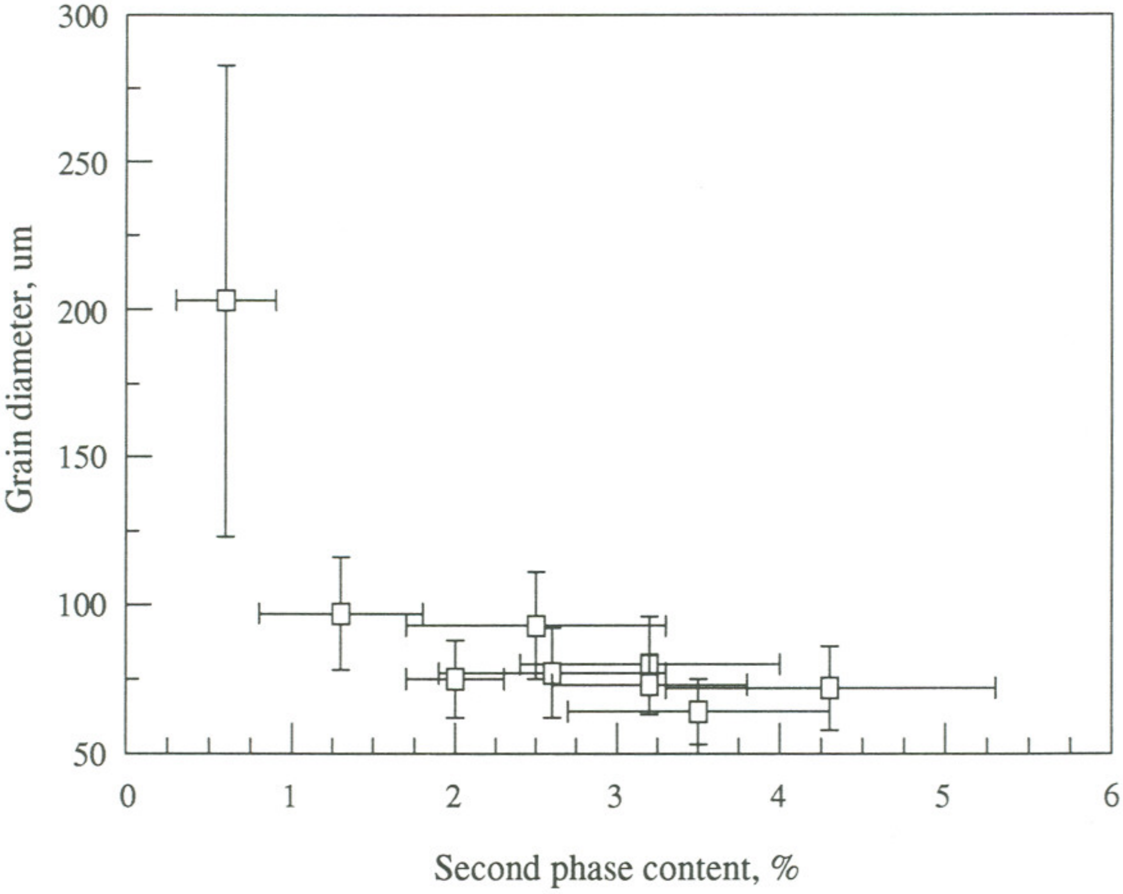

Figure 5-4: Relationship between the second phase content and the grain size in fine-grained cast material

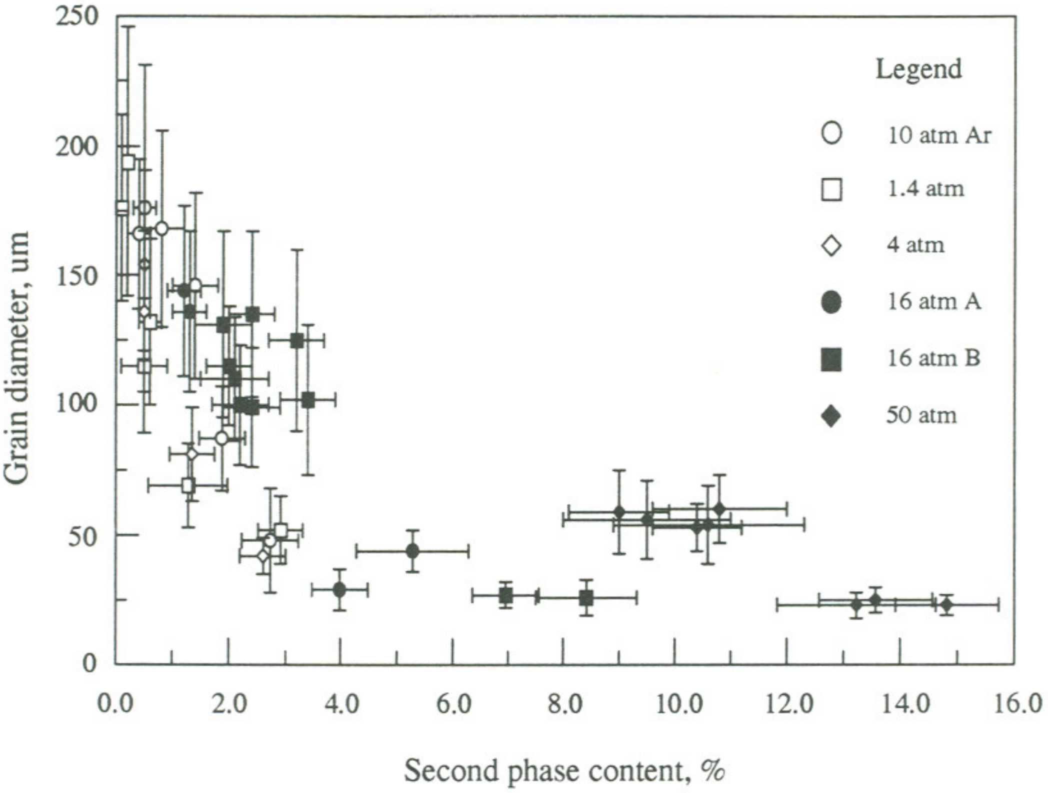

Figure 5-5: Relationship between the second phase content and the grain size in solutionized, rolled N-HPM Stellite 21 material

The above discussion has focused on how the initial cast structure, and then subsequent processing by rolling and by both high and low temperature thermal treatments, can result in a variety of microstructures being developed in the Co-Cr-Mo material. The effect that these microstructural features play on the properties is discussed next, with the ultimate intention of discovering what effects nitrogen alloying may have had on the mechanical properties of the Co-Cr-Mo alloy.

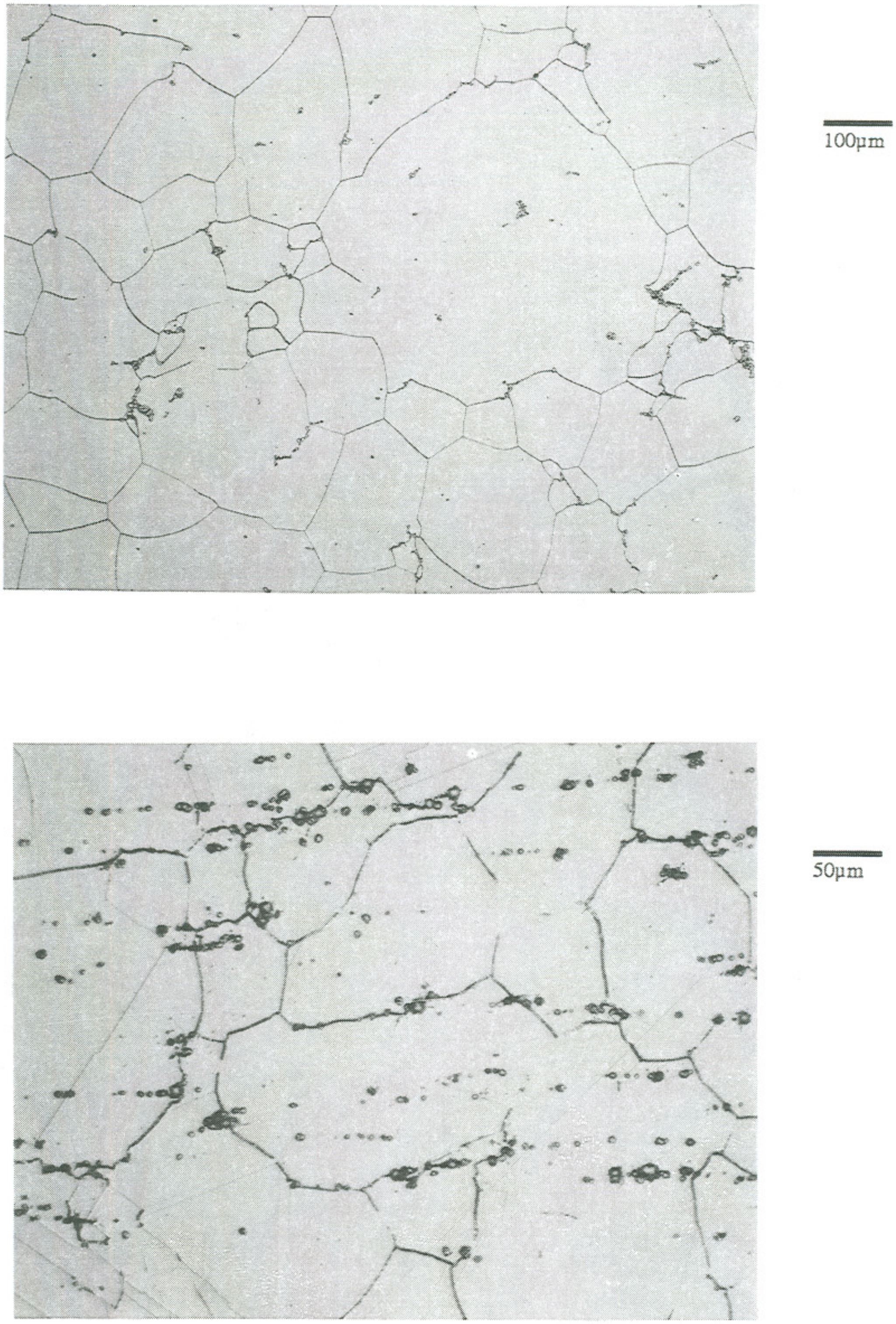

Figure 5-6: Examples of the second phase pinning of grain boundaries in a.) fine-grained cast and solutionized ASTM F75, 100x, and b.) rolled, annealed, and solutionized samples 10 atm Ar-HPM Stellite 21 200x; electrolytically etched with 10% ammonium persulfate

5.2 Microstructural Effects on the Properties

5.2.1 Effects of Second Phase

Effects on the hardness

Hardness is a measure of the resistance of a material to deformation upon loading. It is often taken as an indicator of potential changes in yield strength.

Considering that the second phase material is quite hard, one may expect increasing quantities in the Co-Cr-Mo alloy to result in increased hardness, and consequently a reduction in hardness following solutionization. But, when averaged over many measurements in a given sample, the *conventionally* cast F75 materials showed no significant change. The already moderately hard matrix remained at about Rockwell C (Rc) 30±2 whether the alloying elements were present as carbides, or were dissolved into the matrix.

The much greater second phase content of the *cast* N-HPM material would be expected to show much more significant differences. Indeed, as shown in **Table 4-11** (**Results**), the difference between the lowest nitrogen and highest nitrogen ingots was Rc 7, which could represent differences due to increased amounts of second phase material. The solutionized billets showed higher hardness than their as-cast counterparts. This would indicate that perhaps the alloying elements served to harden more effectively as solid solution strengtheners rather than as coarse second phase particles. On the other hand, coarseness of microstructure tends to negate the hardness values to some degree, since they are a local measurement only. Thus, no definitive statement can be made regarding any apparent changes in hardness with changes in the second phase content in the cast N-HPM material.

As stated earlier, rolling the N-HPM material led to a more homogeneous distribution of second phase material. **Figure 5-7** shows how the hardness apparently increased with increasing second phase content in the rolled and annealed N-HPM material. The trend is most significant above about 3% second phase content, suggesting a minimum content for effective strengthening.

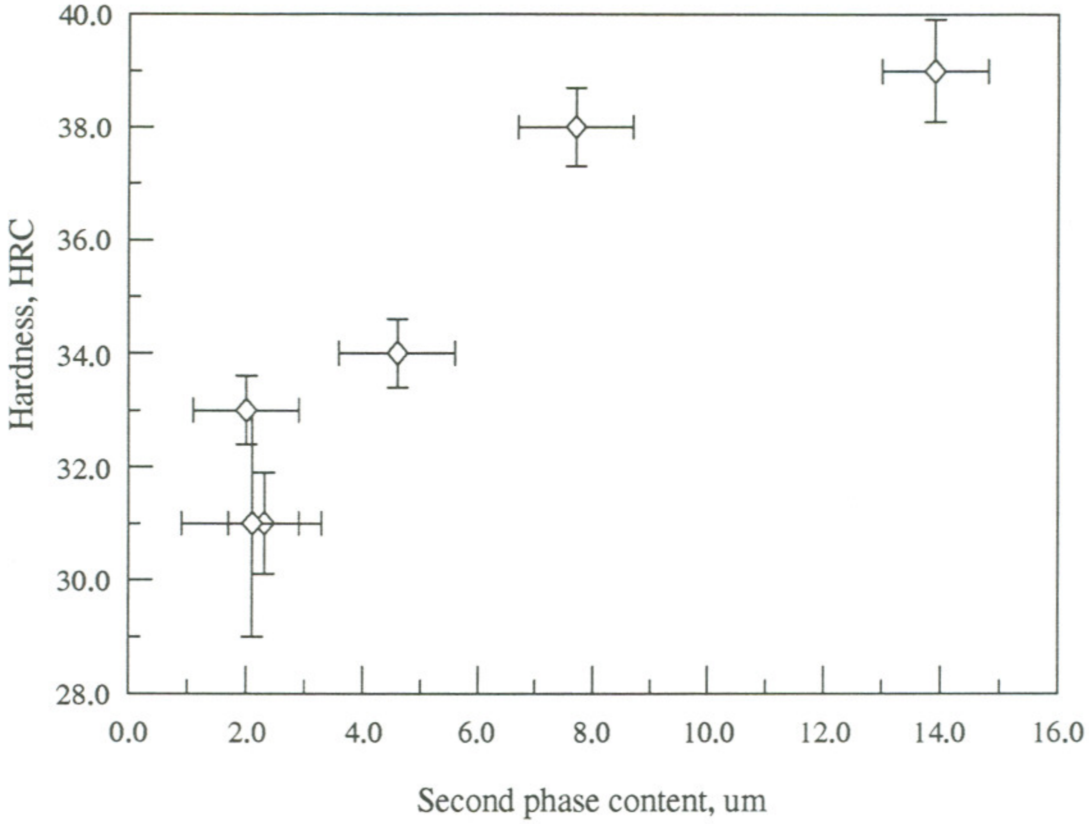

Figure 5-7: Relationship between the second phase content and the hardness in rolled and annealed N-HPM Stellite 21 material

Effects on the yield strength

In the conventionally cast materials, the interdendritic islands formed during casting serve to strengthen the material. This interdendritic second phase has traditionally served as an important strengthening mechanism [25, 26, 31]. As interdendritic islands, the second phase serves as a coarse dispersoid type of strengthener in which it does not interact intimately with dislocations in the classical pinning and looping sense. Rather, it blocks the dislocations so that they must pile up, or climb around. The strengthening is a function of the quantity of second phase content. As the second phase is dissolved, the strength decreases. As the second phase was dissolved in the investment cast F75 materials following solutionization processing, there was a decline in strength of 15 MPa (2 ksi).

This type of strengthening was displayed more strongly in the N-HPM materials, as demonstrated by **Figure 5-8**, where the yield strength is shown to increase with increasing second phase content. Most of the samples with 2% or less second phase had a yield strength (YS) of less than 650 MPa, whereas the samples with over 13% second phase had a YS of about 850 MPa, an increase of 30%. As indicated in the figure, this tendency was most pronounced above about 3-4% second phase, as below this amount the results are clustered in a seemingly random fashion at YS levels below 700 MPa.

Effects on the ductility

One consequence of strengthening through a dispersion of second phase material, is that the ductility suffers. According to the literature [72], the ductility of a material can be reduced by particles in the matrix because their interface with the matrix can serve as a point for free surface growth by ductile cutting. For this reason, conventionally investment cast Co-Cr-Mo medical implants generally undergo some partial solutionization treatment to increase the ductility of the material. As the second phase content is reduced, the ductility increases. For the conventionally cast F75A of this study, the ductility increased from about 10% up to about 18% upon partial solutionization.

This relationship between the second phase content and ductility was also observed in the N-HPM materials to some degree, as shown in **Figure 5-9**. Here, the samples with less than 2% second phase showed ductilities of at least 16%, and as high as 42%. On the other hand, with 13% second phase, the ductility was only about 10%. Again, 3-4% and above appears to be the quantity of second phase which shows the most influence.

Effects of second phase in fine-grained cast material

Up to this point the discussion of the effects of the second phase on the mechanical properties has not included the fine-grained investment cast materials, because of the additional contribution to the properties of grain size. **Figures 5-10** and **5-11** are plots of the second phase content effects on the yield strength and ductility, respectively, for the samples of the solutionized fine-grained investment cast materials. Although a weak correlation is observed with respect to the yield strength, a stronger effect is observed in the reduction in ductility for second phase contents above ~3%. Over the range of 1 to 6% second phase content, the yield strength changed by a maximum of 60 MPa (9 ksi), although the samples with the lowest and highest second phase contents differed by less than 10MPa. However, an apparent change of about 3 times that amount was observed for the yield strength of the N-HPM materials over the same range of second phase content. Thus, the second phase content of the fine-grained *castings* does not show a significanly strong effect on the yield strength. This is not true for the ductility though.

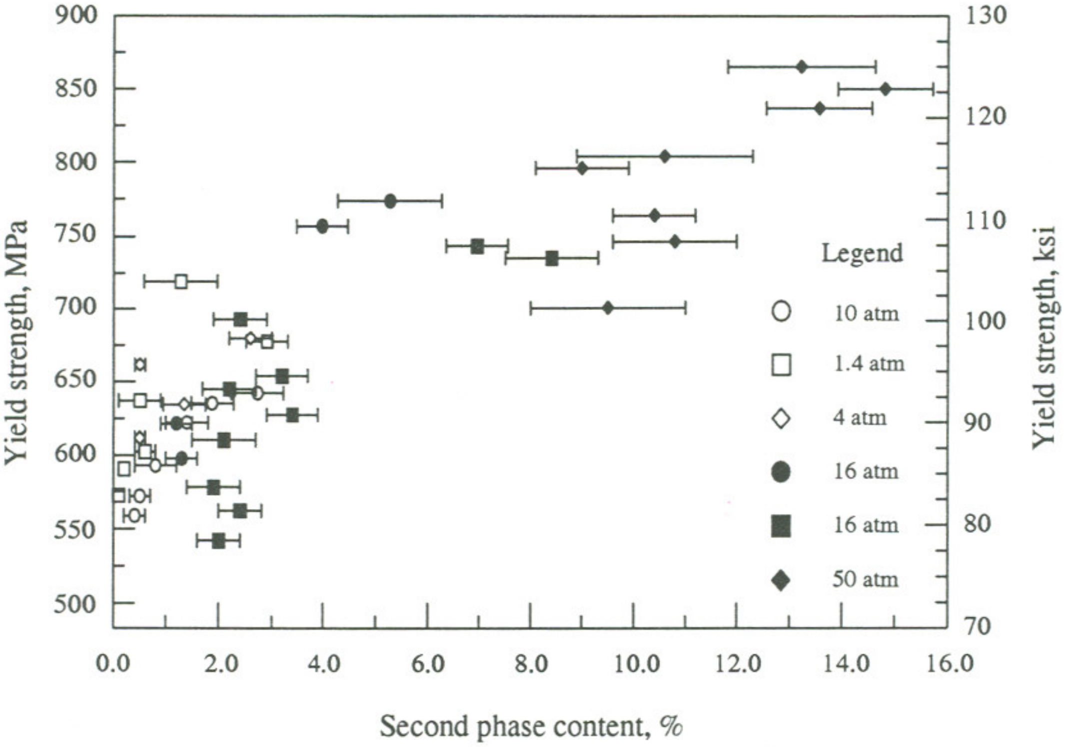

Figure 5-8: Relationship between the second phase content and the yield strength of solutionized, rolled N-HPM materials

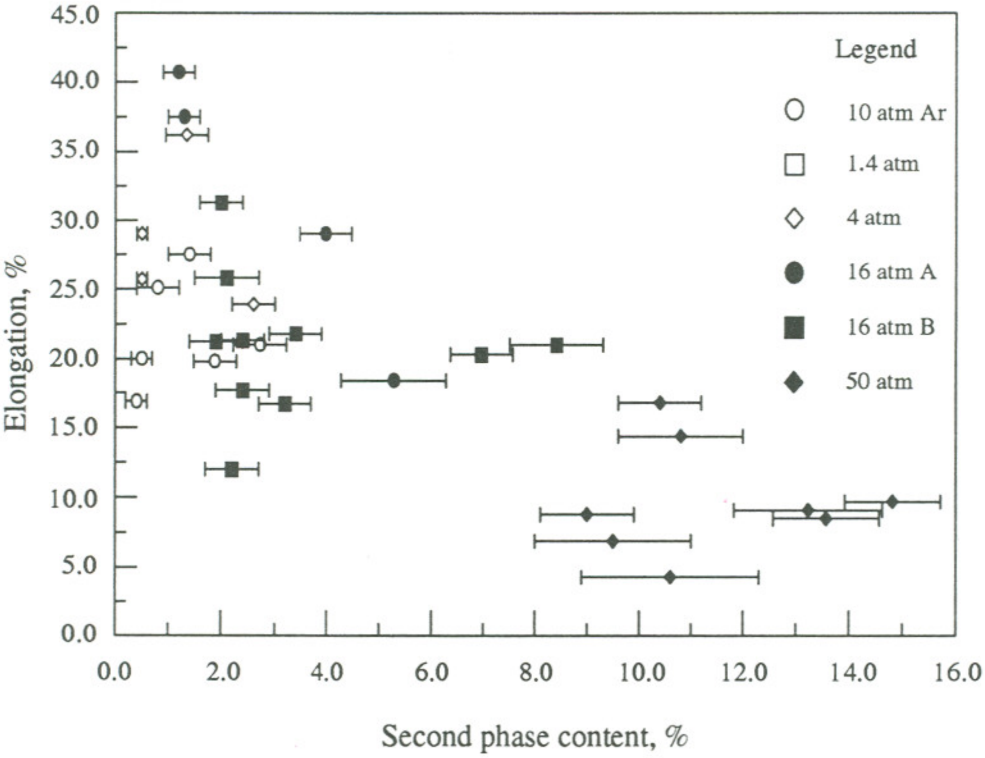

Figure 5-9: Relationship between the second phase content and the elongation of solutionized, rolled, N-HPM materials

As stated in the literature [71], ". . . when a processing step changes the precipitate make-up . . . mechanical properties may undergo drastic alterations." In the fine-grained casting case, the microstructure with fine, equiaxed grains with heavy second phase decoration at the grain boundaries, experienced significant ductility alterations. **Figure 5-11** shows the relationship between the second phase content and the ductility of the fine-grained cast material. As shown, above 3% second phase the ductility was dramatically reduced. In **Figure 5-11**, the bars showing the highest ductility were taken from the bottom region of the castings, where the distribution of second phase was finer due to the finer grain structure, exaggerating the effect of the content alone. This is due to the location of the second phase material at the grain boundaries. The effect of the second phase *morphology* is further addressed in consideration of the results of aging.

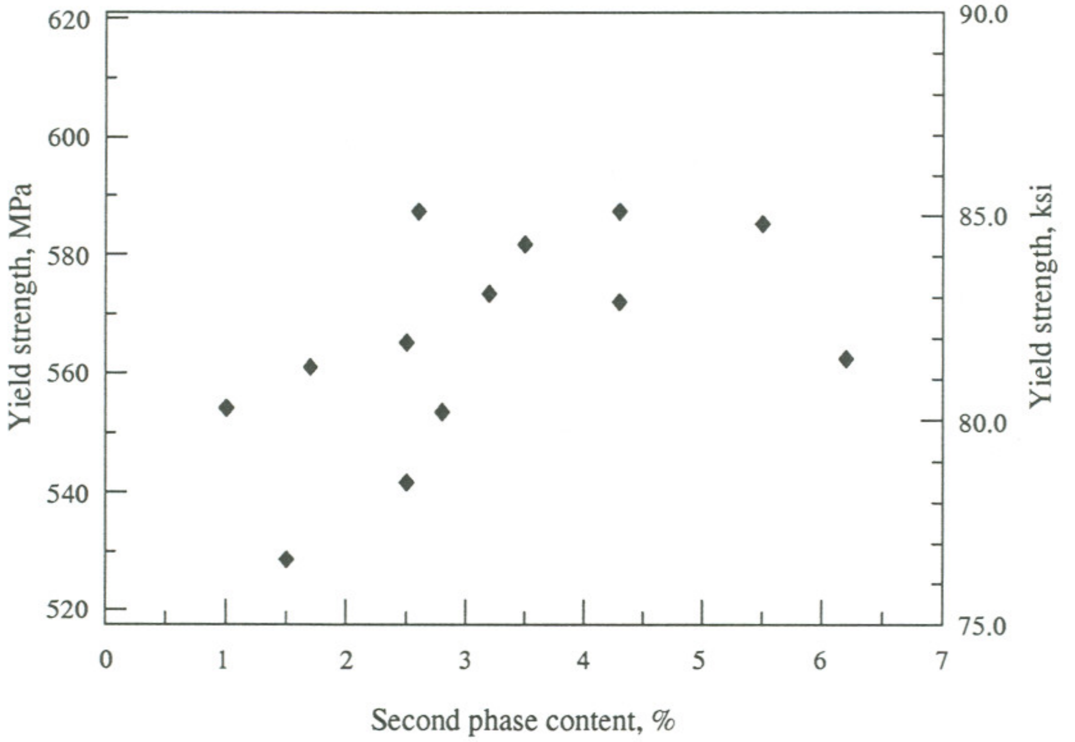

Figure 5-10: Relationship between the second phase content and the yield strength of fine-grained cast material

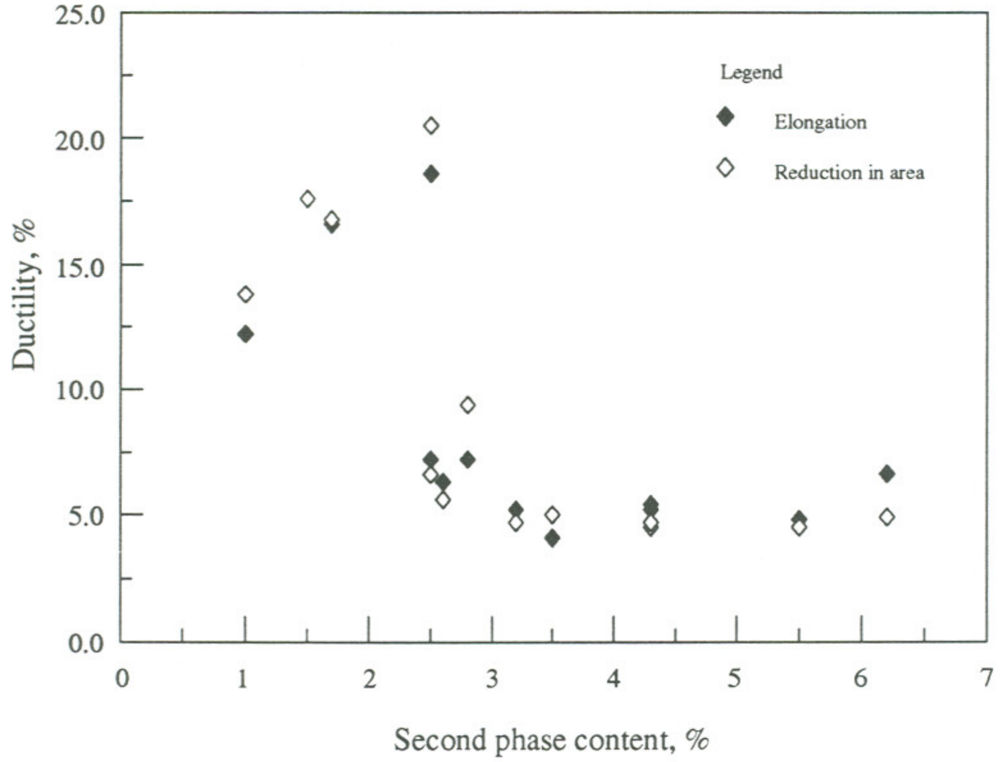

Figure 5-11: Relationship between the second phase content and the ductility of fine-grained cast material

Effect of precipitates on mechanical properties

To further consider the effect of the second phase material on the properties, the microstructures and mechanical property results of the aged investment cast materials are revisited. Those specimens which were aged at 700°C (1290°F), and which yielded a clean microstructure by light microscope, showed the highest ductility. In both the conventional and fine-grained cases, the yield strength was increased by aging, so the microstructural changes responsible for the improvement likely occurred on a level finer than that resolved in the light microscope. The TEM micrographs for conventionally cast A/1220/700/12 and A/1190/700/6 both showed very small precipitates. As would be expected, with the longer aging time of specimen A/1220/700/12, the precipitates were larger than in specimen A/1190/700/6. They also appeared to have formed rod shapes residing on specific planes.

It would be a logical extension from that process that with further aging, strings of precipitates, either continuous or discontinuous, could grow across the grains. As the strings became more densely populated, they would have a greater effect on the matrix to resist deformation, serving as effective blocks for free dislocation travel. However, since they were so coarse, the classical dislocation looping would not occur, but rather, the ductility would decline with increased precipitation in the manner observed.

Looking at the TEM micrographs of specimen A/1220/900/3, aged at 900°C (1650°F) rather than 700°C (1290°F), the precipitates were considerably larger, and there was also the massive lamellar region mentioned previously. Specimen A/1220/900/3 showed a very high yield strength, but very little ductility. As the light micrographs pointed out, there were also continuous, heavy grain boundary carbides present. The most likely case, therefore, is that the $M_{23}C_6$ carbides increased the yield strength substantially by forming a partially covalently bonded network of grain boundary carbides which supported some of the load, but as is the nature of covalent bonding, the network did not allow strain to be easily manifested in the material through dislocation motion. This would be an extreme version of the as-cast fine-grained investment cast material, which also showed higher strength but lower ductility than the conventionally cast material.

Most of the precipitation leading to embrittlement in the conventionally cast specimens occurred at the higher aging temperatures. However, the fine-grained investment cast material was aged in the lower regime, and led to a yield strength increased to levels achieved by casting alone, while retaining much of the ductility introduced by the solutionization. The largest yield strength increase was observed in those samples which showed not only precipitation in transgranular strings, but also in the grain boundaries. However, the grain boundary precipitates led to a rapid reduction in the ductility. At the low aging temperatures used, the increase in strength and parallel reduction in ductility occurred in a much more controlled fashion. Additionally, both the yield strength and ductility were generally higher in those bars taken from regions of the casting with a finer grain size, due to the contribution of a finer initial second phase distribution.

The small, facetted carbides observed in the conventional castings are better for increasing the yield strength without substantially compromising the ductility. In this case, they would act more like a strengthening precipitate would be expected to, by blocking the path of dislocations gliding along slip planes, perhaps even leading to dislocation looping. This would be more desirable than a continuous network of carbides at the grain boundaries or in the matrix leading to deformation behavior more like that of a brittle composite. Thus, by aging at temperatures around 700-750°C (1290-1380°F), controlled precipitation in discontinuous transgranular strings and sparingly at grain boundaries can increase the strength while reducing the ductility only moderately.

5.2.2 Effects of Grain Size

While the previous discussion has focused on the contribution to the properties by the second phase, as was introduced in discussing the fine-grained cast materials, there are effects exerted by the grain boundaries also. The grain size can play a role both indirectly via the homogeneity associated with a finer structure (as was observed in the aged material), and directly by grain boundary interaction with dislocations.

Effects on the hardness

As indicated by **Figure 5-12**, there may be a strong dependence of the hardness upon the grain size of the N-HPM material. This suggests that by decreasing the grain size greater resistance to deformation is achieved. Yet, revisiting **Figure 5-7** recalls that the second phase content of these same samples also showed a strong effect on hardness, especially above about 3% second phase content. Thus, the parallel contribution by the second phase content must be taken into consideration in analyzing the mechanical properties.

Effects on the yield strength

Hall and Petch pointed out that the yield stress of polycrystalline α-iron is proportional to $d^{-1/2}$, where d is the grain diameter. As stated in [76], this form of the relationship also describes quite generally the grain size dependence of flow stress and fracture stress in many materials. The mechanism envisioned involves a pile-up of dislocations at the grain boundaries such that yielding or flow occurs when the pile-up exerts sufficient stress at the boundary to propagate plastic deformation from one grain to another. However, L. E. Murr [77] states that the Hall-Petch relation is generally inappropriate for describing yielding phenomena in alloys, but does concede that an effective hardening can be observed at the grain boundaries due to the dislocation entanglement during pile-up. Thus, although attempting to fit the data of this study to a Hall-Petch type of relation may be inappropriate, some effect of grain size on the yield strength of the material would be expected.

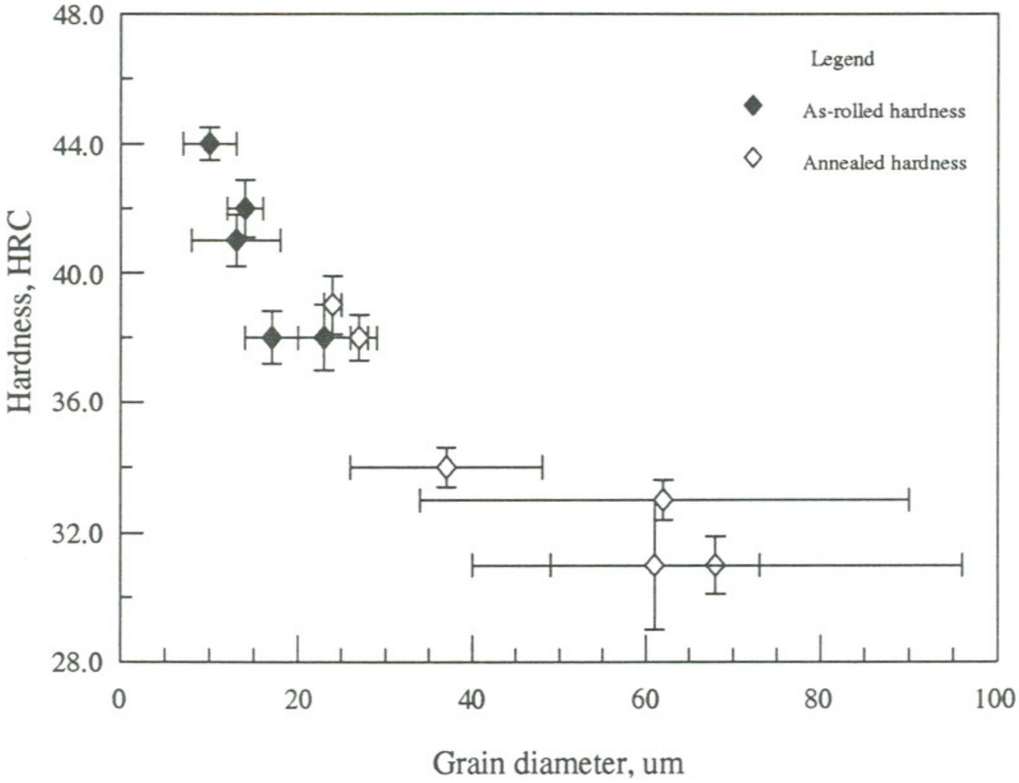

Figure 5-12: Relationship between the grain size and the hardness for as-rolled and annealed N-HPM materials.

Looking at the results for fine-grained investment cast materials, **Figure 5-13** demonstrates a much stronger influence of grain size on the yield strength than the second phase content had (**Figure 5-9**). The yield strength generally increased with decreasing grain size, with a four-fold decrease in grain size showing up to 12% better yield strength. Also, the finest grained material had the highest yield strength, while the largest grained material had the lowest yield strength. In their study, Zhuang and Langer [36] reported a similar yield strength of 578 MPa (83.8 ksi) for their as-cast fine-grained material of similar grain size, and also concluded that a finer grain size in the material is definitely desirable. This statement is further supported by Zhuang and Langer's data showing a 55 MPa (8 ksi) lower yield strength in their conventional castings, and the 68 MPa (10 ksi) lower yield strength in the conventional castings of this study. However, part of the contribution to the higher yield strength of the materials in this study, is that the fine-grained castings had slightly higher second phase content than the conventional castings (which does have *some* effect).

A similar grain size relationship is indicated for the rolled N-HPM bar materials following annealing and solutionization treatments (**Figure 5-14**). In this figure, the low-

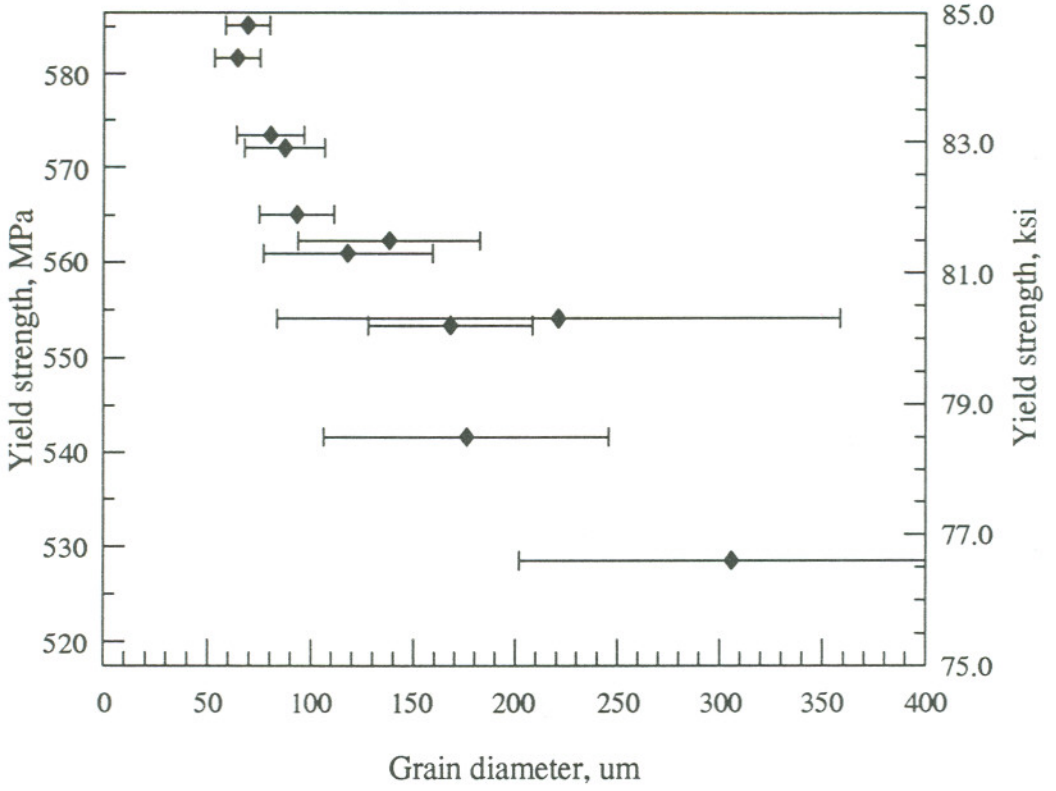

Figure 5-13: Relationship between the grain size and the yield strength of fine-grained cast material

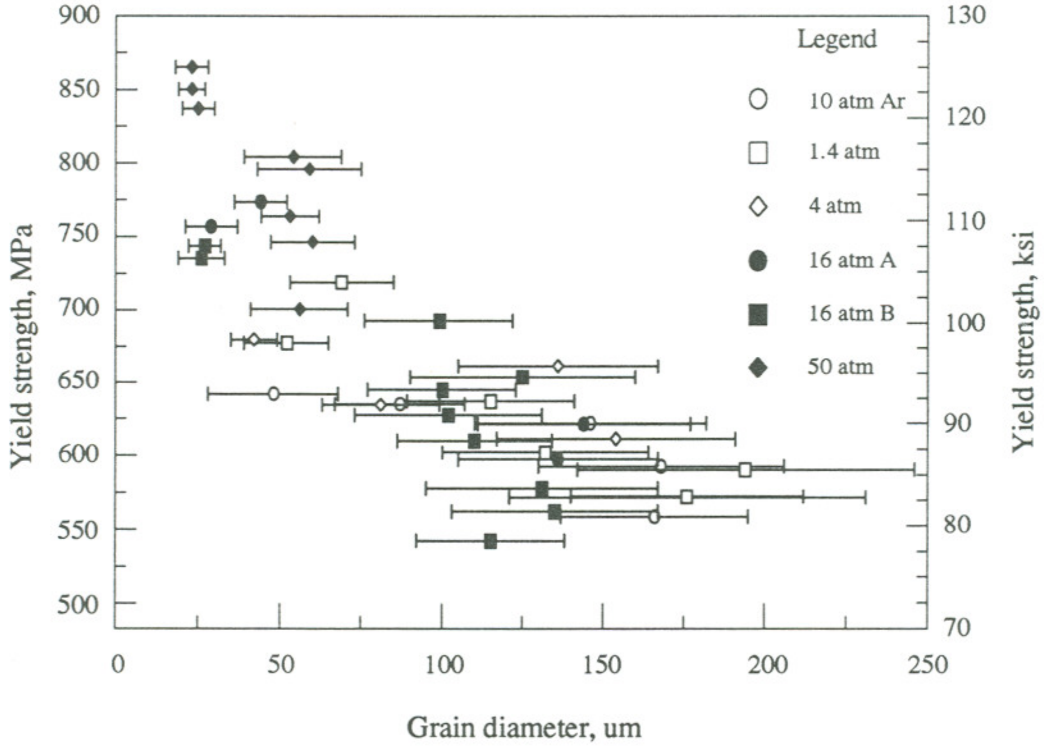

Figure 5-14: Apparent effect of grain size on yield strength of rolled N-HPM materials

nitrogen group samples that were bunched in **Figure 5-8**, are now spread out, whereas the high-nitrogen group samples are bunched together. So, the lower nitrogen samples experienced more influence by the grain size than the second phase content, and vice-versa for the high-nitrogen group samples. In general, with larger grain sizes, the samples displayed lower yield strength. However, neither the trend in **Figure5-8** nor in **Figure 5-14** is very uniform.

There is apparently a synergistic contribution by the grain size *and* the second phase material. The best way to represent the combined effects of second phase material and grain size on the yield strength, is three dimensionally as shown in **Figure 5-15**. In **Figure 5-15**, the projection of the second phase content versus the grain size is **Figure 5-5**, the second phase content versus yield strength is **Figure 5-8**, and the grain size versus yield strength is **Figure 5-14**.

This figure shows that at the lower second phase contents, the yield strength was largely a function of the grain size. However, above about 3-4% second phase content, there was an increased influence exerted by the second phase content. If there were equal contributions by the grain size and the second phase at all contents, a straight line relationship along the cube diagonal would be adhered to. Instead, for low second phase contents the grain diameter exerted a strong influence, or conversely, at high second phase contents the second phase exerted a strong influence. The underlying reason for this lies in the role that the second phase plays in retaining a finer grain size through grain boundary pinning.

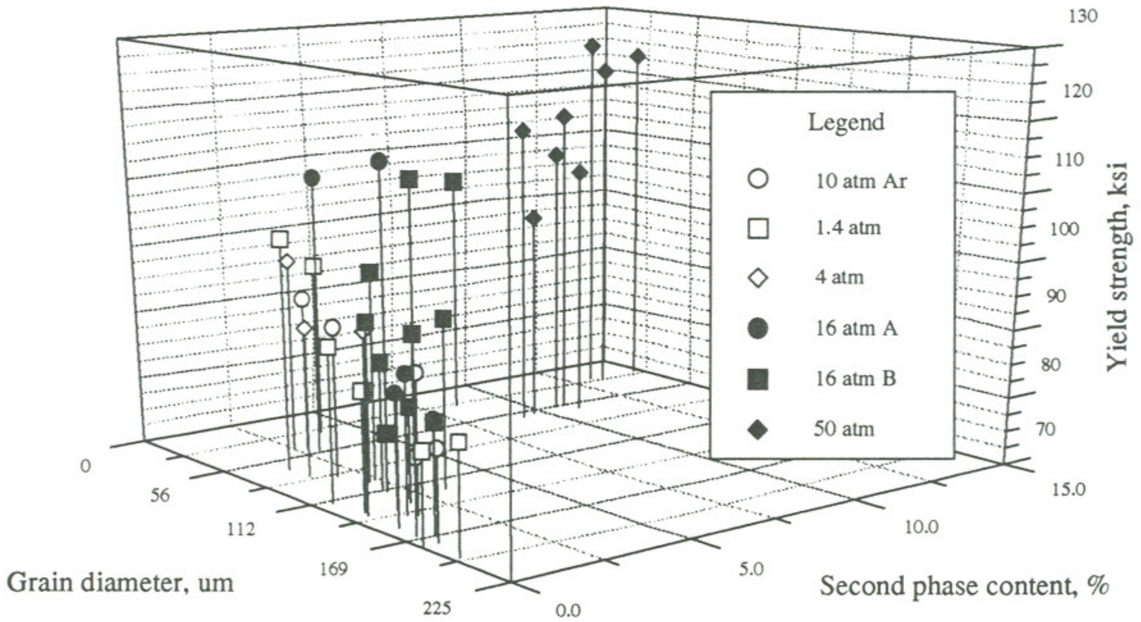

Figure 5-15: Relationship of second phase content and grain size with the yield strength in solutionized, rolled, N-HPM materials

Effects on the ductility

According to literature [72], in most instances the ductility of a material increases with decreasing grain size. This is said to be related to the small increase in strain-hardening rate with reduced grain size. But, the same text notes that microsegregation can have a deleterious effect on ductility, so may overshadow the grain size effects.

For the as-cast fine-grained investment cast material, greater ductility was observed with decreasing grain size. In the as-cast case, the second phase content was fairly uniform with respect to the regions of different grain sizes, at 8 to 12 ± 2 % (**Figures 4-16** and **4-17**, **Results**), so the detraction due to it would be somewhat uniform, allowing comparison of grain size effects. Indeed, as predicted, the already low ductility tended to decrease with increasing grain size in the as-cast condition, with 6.3% elongation in the fine grained bottom region going down to 4.2% elongation in the coarser top region. However, with solutionization treatments, this correlation was no longer observed.

The effects of the grain size on ductility of the *solutionized* fine-grained investment cast material are shown in **Figure 5-16**. The plot indicates an apparent increase in ductility with *increasing* grain size, although the trend is very weakly correlated. If the figure is compared to the similar plot for the rolled N-HPM shown in **Figure 5-17**, no trend is observed. Most likely the reason for a slight trend in the fine-grained cast material but not in the N-HPM bars, is the contribution to the properties by the second phase *distribution*. As described previously, the second phase of the investment cast material is distributed at the grain boundaries, where it strongly influenced the ductility. Since it has been shown that grain growth occurred more readily when the second phase was dissolved from the boundaries, the increased ductility reflected in **Figure 5-16** associated with the larger grains is most likely a function of the lower second phase content, with the larger grains an artifact of simultaneous grain growth. Similarly, in the case of the N-HPM materials, the potential effect of a finer grain size on the ductility was overshadowed by the large quantities of second phase material present in the finer grain sized materials, which reduced the ductility markedly (**Figure 5-9**).

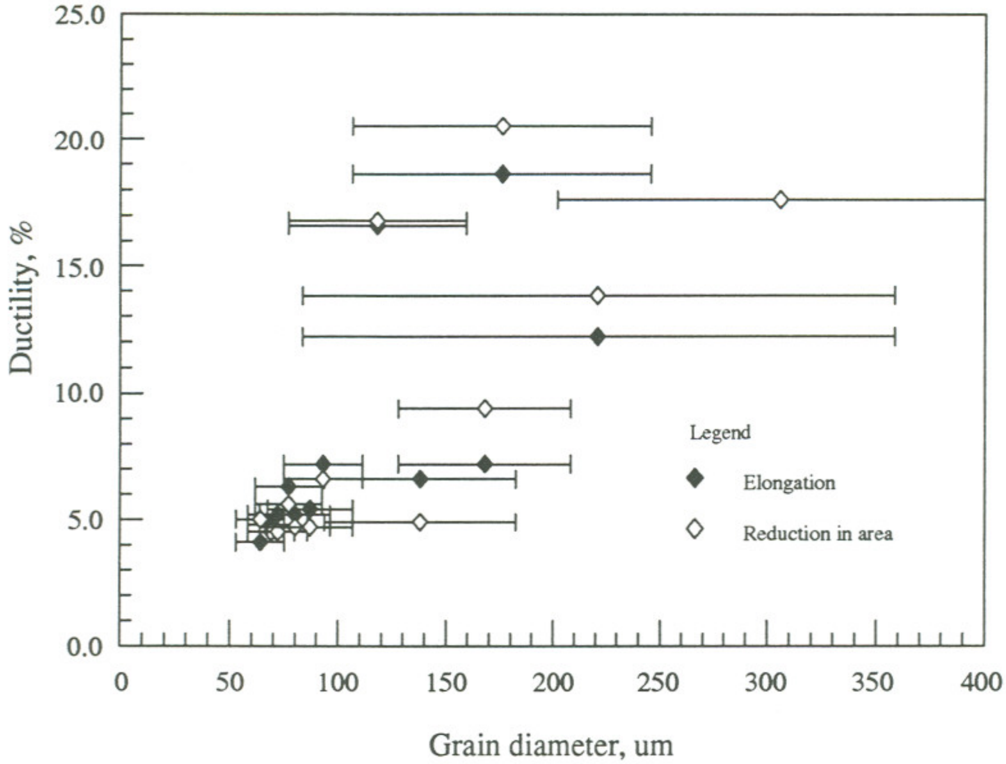

Figure 5-16: Relationship between the grain size and the ductility of fine-grained cast material

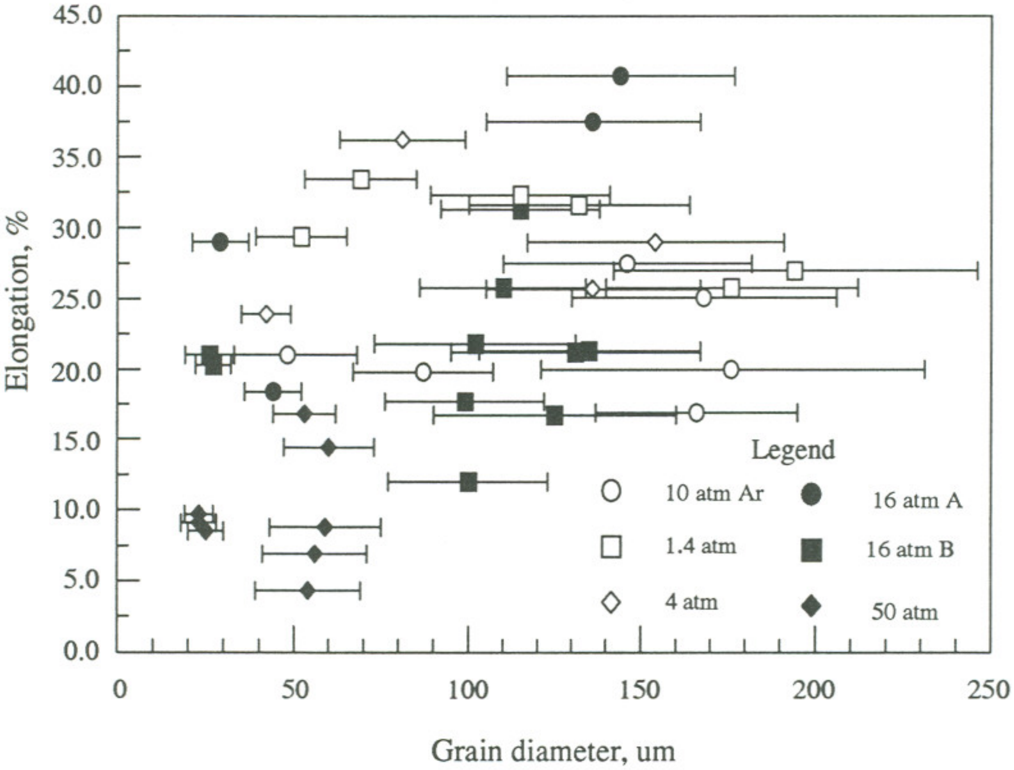

Figure 5-17: Relationship between the grain size and the elongation of solutionized, rolled, N-HPM materials

5.2.3 Special Considerations

Up to this point, the microstructural effects on the N-HPM material properties have been discussed as generalities. In general, at quantities above 3-4% the second phase strengthened the material but reduced the ductility. At second phase quantities less than 3-4%, a finer grain size strengthened the material, but had little additional effect on the ductility. However, if the tensile results of solutionized bars for *individual* melt groups are considered, many of them show an initial increase in ductility with solutionization, followed by a decrease in ductility at longer solutionization times. There are two possible contributing factors to this observation, both related to the solutionization heat treatment.

Firstly, there is the factor of *specimen geometry.* It is said [72] that ductility measurements are affected by the ratio of the cross sectional area to the gauge length of test bars as $\sqrt{A}/l$. When a material can deform in a linearly viscous fashion, the tendency for necking is greatly reduced. Suppression of necking leads to larger elongations. Now, in the heat treatment of the N-HPM plate materials, longer heat treatment times at higher temperatures led to increased oxidation and pitting of the surface. In the fabrication of the test bars, this pitted layer was ground down to produce a uniform surface, and then the gauge was machined to produce a region of uniform length and width. But those bars which experienced greater solutionization times and temperatures required their thickness to be reduced by a greater amount to result in a uniform surface. In this way the ductility of the samples were not measured on bars having equal $\sqrt{A}/l$ ratios, so technically are not directly comparable. The cross sectional areas of this study ranged from 21mm^2 (0.033in^2) for the 10 atm Ar annealed bar, to 12mm^2 (0.018in^2) for the 50 atm bar solutionized at 1260°C (2300°F) for 16 hours. Thus, the cross sectional area of the test bar specimens varied by as much as 2 times. Combining this factor with the already sub-sized 2.5 cm (1 in) gauge length suggests effects which should be taken into consideration. Data recorded in source [72] for copper and for tool steel for a change in cross sectional area over a range corresponding to that of the current study, show a change by a factor of 0.25 for elongations of less than 10%, but of only 0.10 for elongations of around 40%. Thus, the bars of groups 16 atm B and 50 atm which were the thinnest due to their long, high temperature solutionization treatments, which also showed low ductilities already due to high second phase contents, would be most affected by the bar geometry. Indeed, the bars of those groups showed the greatest loss of measured ductility with increased solution time (**Table 4-18, Results**).

The second important factor is that of microstructural defects. As described by Reed-Hill and Abbaschian in their textbook [18], diffusion by a vacancy mechanism can lead to void development. Furthermore, the presence of voids in a matrix can serve as initiation points for cracks, leading to premature fracture [72]. Thus, a contributing factor to the reduction in measured ductility observed in bars experiencing longer solutionization times could be premature fracture at voids resulting from solutionization. It is unclear whether voids were present, due to second phase pullout and etching pits that occurred during metallographic preparation. However, HIPing has been shown to increase properties by closing voids. These bars were not HIPed, and in many cases were solutionized for longer times at higher temperatures than the conventional materials of this study. Combining the effect of these voids with the smaller cross-sectional areas of the bars just described could certainly lead to the reduction in the ductility measurements observed. Since the results of the ductility measurements for the samples solutionized for long times and temperatures are not of particular importance to any of the other arguments made in the discussion of the results of N-HPM materials, further investigation of the contributing factors is not worthwhile.

Another aspect revealed in considering the results of specific melt groups is that, with increasing nitrogen content, there appears to be consistently higher ductility in samples processed under similar conditions. This leads to consideration of the effect of nitrogen on the material.

5.3 Effects of Nitrogen Alloying on Material

5.3.1 Effects on Mechanical Properties

Effects on the ductility

It has been shown that grain size did not strongly influence the ductility of the N-HPM material, but that the second phase did. Thus, to examine the potential influence of nitrogen on the ductility of the material, samples with similar second phase contents were plotted. The grain size of the samples ranged from 69μm in the 0.2 wt% N sample, to 146μm in the 0.1 wt% N sample. **Figure 5-18** is a plot of the ductility of samples of varying nitrogen contents, which all had an average second phase content of 1.2-1.4%.

As indicated by the graph, there is a definite positive influence of nitrogen on enhancing the ductility of the Co-Cr-Mo alloy. In fact, a four-fold increase in nitrogen from 0.12 to 0.45 wt% led to a factor of 0.3 increase in the elongation. Beyond the 0.45

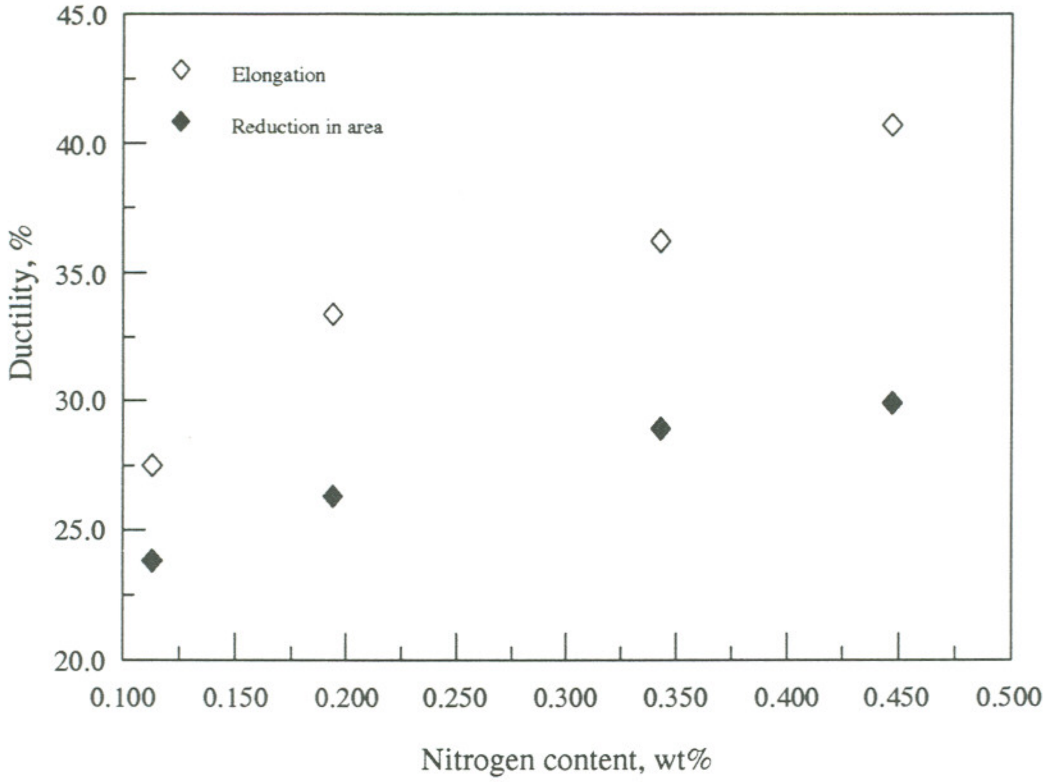

Figure 5-18: Effect of nitrogen on ductility for solutionized, rolled, N-HPM samples of 1.2-1.4% second phase content

wt% specimen, the greater residual second phase began to exert a negative influence on the ductility, as has already been shown.

The manner in which the nitrogen increases the ductility is most likely through alteration of the stacking fault energy (SFE) of the matrix as an interstitial solid solution element. In an FCC metal, adding elements in solid solution usually *lowers* the SFE relative to that of the pure metal. Thus, the separation of the partial dislocations increases, requiring greater load to be applied to contract them, which makes it more difficult to initiate cross-slip [72]. The SFE of an already alloyed material can be *increased* by addition of high stacking fault alloying elements. Zhuang and Langer [73] showed that additions of Ni increased the stacking fault energy of a Co-Cr-Mo alloy . The result of the increased SFE was an increase in the ductility of the alloy. The reasoning is that formation of a stacking fault on every other $<111>_{FCC}$ plane results in the $<0001>_{HCP}$ stacking sequence, increasing the SFE essentially increases the stability of the FCC crystal structure, reducing the formation of strain induced FCC to HCP martensitic transformation during deformation (i.e. stacking faults on every other plane) [74]. In this way deformation in the material would tend to be through cross-slip of dislocations as characteristic of the FCC phase, rather than through formation of dissociated dislocations, stacking faults, and twins as is characteristic of the HCP phase.

A similar increase in SFE as just described is likely the mechanism through which the nitrogen additions increased the ductility of the Stellite 21. While in stainless steels the SFE is said to be lowered with increasing nitrogen contents [20, 75], the statement is made in association with an observation of increased planarity in the fracture surface. Planarity in a fracture surface is generally associated with a brittle fracture mode, as was described by Zhuang and Langer [73]. In their study, Zhuang and Langer saw an increase in ductility with increasing Ni content in Co-Cr-Mo, and an associated reduction in the planarity of the fracture surface. The observed reduction in planarity led to their statements alleging a reduction in the SFE due to the increased Ni content. Thus, the increase in the ductility observed with increasing nitrogen content in samples which had similar second phase contents and in which the grain size was shown to not have an effect, is likely due to an increase in the SFE of the material. To fully determine whether there is an increase in the SFE of the Stellite 21 due to nitrogen alloying, SEM observation of the fracture surface of the bars, and TEM analysis of stacking fault densities in the materials should be performed.

Effects on the strength

Besides the effect on ductility just described, the nitrogen does not appear to have any other direct influence on the mechanical properties of the N-HPM Stellite 21. Dempsey et. al. [51] claimed to have observed an increased yield strength due to interstitial nitrogen additions to Co-Cr-Mo alloys, but this was not directly observed in this study. While the effect of nitrogen on the yield strength of stainless steels is substantial, the increase observed in the Co-Cr-Mo alloys by Dempsey et. al. was not. Besides not being very consistent, at the greatest, their material only showed an improvement of 135 MPa (20 ksi) over their poorest baseline condition (0.14% C cast bar with simulated porous coating thermal treatment). Comparatively, the magnitude of increase in yield strength observed in the current study (annealed 50 atm bar) was 228 MPa (33 ksi) over the baseline (annealed 10 atm Ar bar). The baseline yield strength in turn was 111 MPa (16 ksi) over the typical conventionally cast material. However, as has already been shown, these yield strength results were generally a function of the grain size at lower nitrogen contents, and upon the second phase content at higher nitrogen contents. Thus, it cannot be said that the observed increased strengths are directly a function of the interstitial nitrogen content of the alloy.

5.3.2 Effects on Metallurgy of Co-Cr-Mo

Interstitial nitrogen content

Dempsey et. al. [51] claimed to have observed an increased yield strength due to interstitial nitrogen additions to Co-Cr-Mo alloys. But, the study was done on samples of four different carbon contents, 0.14, 0.19, 0.21, and 0.33 wt%. The yield strength of the material in the baseline condition (simulated porous coating thermal treatment) increased with increasing carbon content. Consequently, the effect of additional interstitial nitrogen was minimized with increasing carbon content. The data in that study indicated that lower initial carbon contents may allow the potential effects on the yield strength of subsequent nitrogen alloying to be better manifested. That may be why, with 0.25wt% carbon in the Stellite 21 starting material of the current study, interstitial strengthening by nitrogen was not readily observed. Instead, the already high interstitial carbon content encouraged the formation of more second phase material with increased nitrogen additions.

In their solid state work, Kilner et. al. [49] suggested a solubility limit of 0.35wt% N in Co-Cr-Mo. This was based upon the measured nitrogen contents at points of increasing depth within their nitrided bars. The solubility limit was taken as the nitrogen content of the material at the point at which nitrides ceased to be formed. Indeed, in the 0.35wt% samples (4 atm) of the current study, rapid solutionization of the second phase material was achieved, with only 0.5% second phase remaining after 4 hours at 1260°C (2300°F). Above that nitrogen content, full solutionization was not achieved in samples, even after 16 hours at 1260°C (2300°F). However, in the 0.4 wt% and 0.5 wt% N samples (16 atm A and B), more solutionization was occurring with increasing time. Since equilibrium was not yet achieved, it cannot be said that the solubility limit had been reached. As addressed earlier, the 0.85 wt% N samples (50 atm) *did* appear to be close to the solubility limit, since they experienced initial re-precipitation at early solutionization times, and showed very little solutionization even at long times at a high temperature. Based on these observations, the best approximation is that the nitrogen solubility at high temperatures within solid Co-Cr-Mo material is at least 0.35 wt%, but probably not much more than 0.85 wt%.

The nitrogen measurements for individual bars also varied. However, they varied in a consistent manner. The graph in **Figure 5-19** shows the effect of solutionization on the nitrogen content of the samples. It indicates that greater nitrogen contents were achieved in the bars with increased solutionization. However, whatever the cause, the magnitude of the change in nitrogen content within the same nitrogen group is less than the difference between the average nitrogen contents of the adjacent groups, so should not negate the discussion regarding the role that nitrogen played in this material.

Effects on the second phase and incipient melting behavior

As was discussed in Section **5.1**, nitrogen alloying served to alter the type of second phase that was preferentially formed upon solidification. Rather than the $Cr_{23}C_6$ that is typically observed in the Co-Cr-Mo alloys, the Cr_2N material was stabilized with increased nitrogen content. It is supposed that if a lower carbon content were present in the alloy, the Cr_2N would still be preferred. At high nitrogen contents, the stoichiometry could be reduced to CrN, but the quantities of second phase would be quite high, as they were in this study.

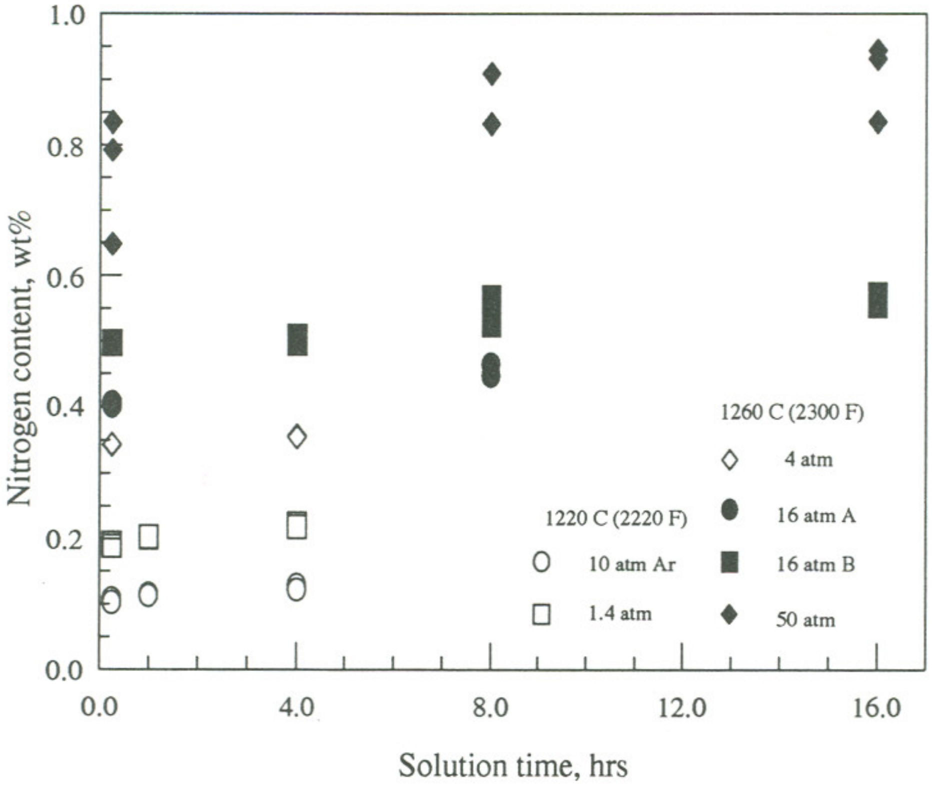

Figure 5-19: Measured nitrogen contents for solutionized, rolled, N-HPM test bars

The change in second phase type due to nitrogen additions was shown in Section **5.1** to have important implications in terms of the incipient melting behavior of the Co-Cr-Mo alloys. The Cr_2N material did not show signs of incipient melting even at temperatures as high as 1260°C (2300°F), when the samples containing $Cr_{23}C_6$ showed incipient melting already at 1240°C (2260°F). As was described in the Background chapter, avoidance of incipient melting is very desirable for applications in biomedical implants expected to undergo sintered bead processing.

5.3.3 Other Effects of Nitrogen

For application of the high-nitrogen material in a biomedical capacity, it is desirable that neither the localized corrosion nor abrasive wear properties of the Co-Cr-Mo material showed a negative impact by the addition of nitrogen. Thus, the results of this research supports the potential application of nitrogen as a useful alloying element in the Co-Cr-Mo biomedical implant alloy, the determination of which was the ultimate goal of this project.

6. CONCLUSIONS

Through melting with high over-pressures of nitrogen, and subsequent thermal mechanical processing, this study determined some basic roles played by nitrogen both metallurgically and mechanically as an alloying element in Co-Cr-Mo. Through experiments done on conventional and fine-grained investment cast materials, further insight was gained on aspects of the microstructural features that contributed to the mechanical properties, and how the processing steps affected them. Several specific findings related to these aspects are summarized below:

1. It was found that N-HPM processing achieved total nitrogen contents as high as 1.2 wt% in Stellite 21 Co-Cr-Mo.

2. It was shown that at least 0.35 wt% N could be dissolved completely in solid Stellite 21 Co-Cr-Mo.

3. Excess nitrogen was found to form second phase chrome nitrides.

4. Grain growth was slowed during high temperature solution treatments by the pinning action of the second phase material.

5. Whereas the typical Co-Cr-Mo castings were shown to contain $Cr_{23}C_6$ with an occasional Cr_7C_3 carbide, with increasing nitrogen additions from 0.1 wt% to over 0.85 wt %, the preferred second phase type in the as-cast form of the Stellite 21 alloy was shown to change from $Cr_{23}C_6$, to Cr_2N, and finally to CrN.

6. Replacement of the $Cr_{23}C_6$ with Cr_2N through nitrogen alloying was sufficient to raise the melting point of the interdendritic second phase to a temperature above 1260°C (2300°F).

7. A finer second phase structure, achieved either by dendritic solidification or mechanical break-down and redistribution through rolling, led to better response to solutionization and homogenization treatments.

8. The preferential segregation of second phase at the grain boundaries and consequent coarseness of the second phase structure of the fine-grained cast material led to longer solutionization time requirements.

9. In the low nitrogen materials which contained $Cr_{23}C_6$ as the primary component of the second phase material, full solutionization was achieved. The greater stability of the Cr_2N second phase material produced with increasing nitrogen content did not allow full solutionization to be achieved.

10. Interstitial nitrogen was shown to increase the ductility of the material, likely by increasing the SFE.

11. In the fine-grained investment castings, it was shown that the finer the *as-cast* grain structure was, the greater the yield strength and ductility were.

12. In the fine-grained cast materials, the location of the carbides at the grain boundaries was determined to be harmful to the ductility of the material.

13. The second phase was found to serve as a coarse dispersoid type of strengthener, in which the yield strength increased with the quantity of second phase content.

14. In general, at quantities above 3-4%, the second phase in the N-HPM alloys was shown to strengthen the material but to reduce the ductility.

15. It was found that there was a decline in strength but increase in ductility as the second phase was dissolved following the solutionization processing.

16. The fine, equiaxed grains developed through hot-rolling and annealing were found to increase the yield strength of the lower nitrogen N-HPM materials having a low second phase content.

17. Grain size strengthening combined with an already high 0.25 wt% C content prevented discernment of the contribution of interstitial nitrogen to the strength.

18. Cooling the investment cast materials slowly to below the solutionization temperature resulted in rapid precipitation at the grain boundaries. Cooling at a rate of 667°C/minute (1200°F/min) for the first 30 seconds was found to be sufficient to avoid this precipitation.

19. Thermal treatment at 1070°C (1960°F) was shown to result in poor second phase dissolution, and simultaneous random and uncontrollable precipitation.

20. The crystal structure of the precipitates in the non-nitrogen alloys was shown to be $M_{23}C_6$, but the *morphology* of the precipitates was found to vary widely.

21. Transgranular strings of fine precipitates was shown to be the preferred morphology in the 700-750°C (1290-1380°F) temperature range for both non-nitrogen casting types, and to occur in a controlled fashion

22. Precipitation in discontinuous transgranular strings and sparingly at grain boundaries increased the strength while only moderately reducing the ductility of the non-nitrogen materials.

23. It was found that at 900°C (1650°F) the precipitation occurred preferentially at grain boundaries, resulting in rapid embrittlement in the non-nitrogen materials.

24. At 1050°C (1920°F), precipitation was found to occur along grain boundaries, lamellarly into grains from grain boundaries, in a lenticular form near areas of prior segregation, and as fine, stippled precipitates within grains. In all cases, embrittlement resulted, and the particular morphologies apparently precipitated in concert.

7. FUTURE WORK

The work completed thus far introduced the behavior of nitrogen in this alloy over a wide range of compositions, and revealed several areas of potential further examination.

Firstly, the mechanical properties were characterized in general, but evaluation of the properties over a more precise range of nitrogen distributions would be beneficial, especially in the 3 to 5 wt% range. To better characterize the effects of interstitial nitrogen on the mechanical properties, better control of the grain size and second phase distribution and content would be desirable. Because these microstructural characteristics are largely determined at solidification in N-HPM materials, a more controllable process would be desirable for more accurate evaluation of interstitial nitrogen effects.

The use of low carbon starting materials would better allow the effects of interstitial nitrogen to be evaluated, because there would be reduced competition for interstitial sites. Lower carbon could also yield less second phase in the initial solidification microstructure. This could be especially desirable in the fine-grained castings, which would then require less solutionization, and thus may experience less grain-growth. This could also result in better response to aging, which could bring the yield strength up to levels beyond that lost due to the reduction in carbon.

Solid state nitrogen additions through nitriding of powders could enable specimens to be produced with more accurate control of the grain size. Additionally, the rapid solidification rate of powders generally yields a much more homogeneous second phase distribution. With a low carbon material the second phase content most likely would also be substantially lower. Thus, the effects of interstitial nitrogen on the mechanical properties could be more clearly discerned.

Further investigation of the mechanism by which nitrogen alloying increases the ductility would also be of interest. This would most likely involve analysis of stacking fault energies (SFE). Due to its close relationship to the SFE, the role of the HCP phase, and the potential for the strain-induced transformation thereof, would also be of interest. Extension of this work would point to fatigue property analysis, in which the strain induced transformation to HCP has been shown to play a role. This type of work would likely follow mastery of making controlled, uniform nitrogen additions to the material.

Work other than that directly involving the mechanical properties of the nitrogen alloyed materials would also be of interest. For example, the precipitation behavior and aging response of the materials may be significant. Nitrogen additions introduce the possibility of nitride precipitate formation, which has been found to be more desirable than carbide precipitation in many stainless steel cases.

The current work indicated that nitrogen alloying increases the temperature at which incipient melting occurs in the material, possibly through the replacement of $Cr_{23}C_6$ with Cr_2C. However, further examination to determine the new incipient melting temperature, and to determine the mechanism whereby the temperature in increased, would be useful.

Finally, it was noticed that the materials with higher nitrogen content were more difficult to etch to reveal the grain boundaries, indicating a change in corrosion properties. More severe corrosion testing in order to distinguish the effects of nitrogen on the corrosion resistance of the materials would be of interest for future work.

8. REFERENCES

[1] H. S. Dobbs and J. L. M. Robertson, "Alloys for orthopaedic implant use," *Engineering in Medicine*, vol. 11, no. 2, 1982, pgs. 175-182.

[2] W. Bonfield, "Materials for the replacement of osteoarthritic hip joints", *Metals and Materials*, vol. 3, no. 12, December 1987, pgs. 712-716.

[3] A. I. Aziz, "Corrosion of cobalt-base alloys", *ASM Metals Handbook*, 9th Ed., vol. 13: Corrosion; Metals Park, OH: ASM International, 1978, pgs. 658-668.

[4] D. Dowson, "Friction and wear of medical implants and prosthetic devices", *ASM Metals Handbook*, 10th Ed., vol. 18: Friction, Lubrication, and Wear Technology; Metals Park, OH: ASM International, 1992, pgs. 656-664.

[5] P. Crook, A. V. Levy, "Friction and wear of cobalt-base wrought alloys", *ASM Metals Handbook*, 10th Ed., vol. 18: Friction, Lubrication, and Wear Technology; Metals Park, OH: ASM International, 1992, pgs. 766-771.

[6] A. C. Fraker, "Corrosion of metallic implants and prosthetic devices", *ASM Metals Handbook*, 9th Ed., vol. 13: Corrosion; Metals Park, OH: ASM International, 1978, pgs. 1324-1335.

[7] "Standard specification for cast cobalt-chrome-molybdenum alloy for surgical implant applications", *ASTM F75-92*, American Society for Testing Materials, 1992.

[8] "Standard specification for wrought cobalt-chrome-molybdenum alloy for surgical implant applications", *ASTM F799-96*, American Society for Testing Materials, 1996.

[9] T. M. Devine & J. Wulff, "Wrought Co-Cr surgical implant alloys", *Journal of Biomedical Materials Research*, vol. 7, no. 1, January 1972, pgs. 151-167.

[10] H. A. Luckey & L. J. Barnard "Improved properties of Co-Cr-Mo alloy by hot isostatic pressing of powder", *Transactions of the 4th Annual Meeting, April 29-May 2, 1978, San Antonio, TX, USA*, Society for Biomaterials, 1978, pgs. 71-72.

[11] K. K. Wang, L. J. Gustavson & J. H. Dumbleton, "The development of a new dispersion strengthened Vitallium alloy for medical implants", *Proceedings of the 1988 International Powder Metallugy Conference, Orlando, FL, USA, June 5-10, 1988*; Metal Powder Industries Federation, American Powder Metallurgy Institute, 1988, pgs. 361-375.

[12] P. Crook, "Cobalt and cobalt alloys", *ASM Metals Handbook*, 10th Ed., vol. 2: Properties and selection of nonferrous alloys and special-purpose materials; Metals Park, OH: ASM International, 1992, pgs. 446-454.

[13] P. Villars & L.D. Calvert, *Pearson's Handbook of Crystallographic Data for Intermetallic Phases*, 3rd. Ed., Metals Park, OH: ASM International, 1989.

[14] A. E. Ray, S. R. Smith, & J. D. Scofield "Study of the phase transformation of cobalt", *Journal of Phase Equilibria*, vol. 12, No. 6, 1991, pgs. 644-647.

[15] G. L. Erickson, "Polycrystalline cast superalloys", *ASM Metals Handbook*, 10th Ed., vol 1: Properties and selection: iron, steels, and high performance alloys, Metals Park, OH: ASM International, 1992, pgs. 981-987.

[16] C. T. Sims, "A contemporary view of cobalt base alloys", *Journal of Metals*, vol. 21, no. 12, Dec. 1969, pgs. 27-42.

[17] K. Rajan, "Phase transformations in a wrought Co-Cr-Mo-C alloy", *Metallurgical Transactions A*, vol. 13A, no. 7, July 1982, pgs. 1161-1166.

[18] R. E. Reed-Hill & R. Abbaschian, *Physical Metallurgy Principles*, 3rd Ed., Boston: PWS-KENT, 1992.

[19] R. P. Reed, "Nitrogen in austenitic stainless steel", *JOM*, vol. 41, no.3, March 1989, pgs. 16-21.

[20] R. E. Stoltz and J. D. Vander Sande, "The effect of nitrogen on stacking fault energy in Fe-Ni-Cr-Mn steels", *Metallurgical Transactions A*, volume 11A, no. 6, June 1980, pgs. 1033-1037.

[21] C. Brooks, *Heat treatment, structure, and properties of non-ferrous alloys*, Metals Park, OH: ASM International, 1982.

[22] L. Z. Zhuang, & E. W. Langer, "Effects of alloy additions on the fatigue properties of cast Co-Cr-Mo alloy used for surgical implants", *Journal of Materials Science*, vol. 25, no. 1B, 1990, pgs. 683-689.

[23] S. R. Robertson, *The Effect of Thermal and Thermomechanical Treatments on Low Carbon ASTM F75 Alloys for Possible Use in Prosthetic Applications*, doctoral dissertation, The University of California at Los Angeles, 1982.

[24] T. Kilner, *The Relationship of Microstructure to the Mechanical Properties of a Cobalt-Chromium-Molybdenum Alloy Used for Prosthetic Devices*, doctoral dissertation, The University of Toronto, 1984.

[25] A. J. T. Clemow & B. L. Daniell, "Solution treatment behavior of Co-Cr-Mo alloy", *Journal of Biomedical Materials Research*, vol. 13, no. 6, 1979, pgs. 265-279.

[26] T. Kilner, R. M. Pilliar, G. C. Weatherly & C. Allibert, "Phase identification and incipient melting in a cast Co-Cr surgical implant alloy", *Journal of Biomedical Materials Research*, vol. 16, no. 1, 1982, pgs. 63-79.

[27] D. A. DeAntonio, D. Duhl, T. Howson, M. F. Rothman, "Heat treating of superalloys", *ASM Metals Handbook*, 10th Ed., vol. 4: Heat treating, Metals Park, OH: ASM International, 1992.

[28] W. D. Kingery, H. K. Bowen & D. R. Uhlmann, *Introduction to Ceramics*, New York, NY: John Wiley & Sons, Inc., 1976.

[29] T. B. Massalski, (Ed.) *Binary Alloy Phase Diagrams*, 2nd Ed., Materials Park, OH: ASM International, 1990.

[30] P. Villars, A. Prince, and H. Okamoto, *Handbook of Ternary Alloy Phase Diagrams,* vol. 6, Metals Park, OH: ASM International, 1995, pgs. 8120-8125.

[31] D. J. Levine, "Metallurgical relationships of porous-coated ASTM F75 alloys", Reprint from: *ASTM Special Technical Publication # 953*, American Society for Testing and Materials, Philadelphia, 1987, pgs. 60-73.

[32] H. Farhangi, *Fatigue Cracking of Hot Isostatically Pressed, Porous Coated F75 Prosthetic Device Material*, doctoral dissertation, The University of Maryland, 1989.

[33] E. P. DeGarmo, J. T. Black & R. A. Kohser, R.A., *Materials and Processes in Manufacturing,* 7th Ed., New York: Macmillan Publishing Company, 1988.

[34] M. C. Flemings, *Solidification Processing*. New York: McGraw-Hill, 1974.

[35] C. Beckermann, "Modeling segregation and grain structure development in equiaxed solidification with convection", *JOM*, vol. 49, no. 3, March 1997, pgs. 13-17.

[36] L. Z. Zhuang & E. W. Langer, "Effects of cooling rate control during the solidification process on the microstructure and mechanical properties of cast Co-Cr-Mo alloy used for surgical implant", *Journal of Materials Science*, vol. 24, no. 2, 1989, pgs. 381-388.

[37] J. B. Vander Sande, J. R. Coke & J. Wulff, "A transmission electron microscopy study of the mechanisms of strengthening in heat-treated Co-Cr-Mo-C alloys", *Metallurgical Transactions A*, vol. 7A, no. 3, March 1976, pgs. 389-397.

[38] F. G. Hodge, T. S. Lee, III, "Effects of processing on performance of cast prosthesis alloys", *Corrosion*, vol. 31, No. 3, March 1975, pgs. 111-112.

[39] F. S. Georgette & J. A. Davidson, "The effect of HIPing on the fatigue and tensile strength of a cast, porous-coated Co-Cr-Mo alloy", *Transactions of the Eleventh Annual Meeting of the Society for Biomaterials in Conjunction with the Seventeenth International Biomaterials Symposium*, San Diego, CA, vol. 8, 1985.

[40] H. S. Dobbs & J. L. M. Robertson, "Heat treatment of cast Co-Cr-Mo for orthopaedic implant use", *Journal of Materials Science*, vol. 18, no. 2, 1983, pgs. 391-401.

[41] J. Rawers, J. S. Dunning, G. Asai, R. P. Reed, "Characterization of stainless steels melted under high nitrogen pressure", *Metallurgical Transactions A*, vol. 23A, no. 5, July 1992, pgs. 2061-2068.

[42] J. C. Tsai, J. B. Duh, S. C. Chueh, "The evaluation of hot-working characteristics of cobalt-based implant alloys", *Journal of Materials Science*, vol. 29, no. 15, 1994, pgs. 4086-4092.

[43] L. Shi, D. O. Northwood, Z. Cao, "The properties of a wrought biomedical cobalt-chromium alloy", *Journal of Materials Science*, vol. 29, no. 5, 1994, pgs. 1233-1238.

[44] "Bio-Dur Carpenter CCM alloy", *Alloy Digest*, vol. CO-96, no. 3, March 1995, pgs 2.

[45] J. P. Immargeon, K. Rajan, W. Wallace, "Microstructural changes during isothermal forging of a Co-Cr-Mo alloy", *Metallurgical Transactions A*, vol. 15A, no. 2, Feb. 1984, pgs 339-345.

[46] J. C. Tsai, J. B. Duh, "Hot-working behaviors of cast cobalt-based superalloy", *Scripta Metallurgica et Materialia*, vol. 27, no. 5, 1992, pgs. 561-564.

[47] J. C. Tsai, J. B. Duh, S. C. Chueh, "Flow stress behavior of cast Co-Cr-Mo alloy evaluated by high strain rate of compression tests", *Materials Science and Engineering*, vol. A168, no.1, 1993, pgs. 1-3.

[48] "High-pressure-nitrogen alloying of steels", *Advanced Materials & Processes*, vol. 138, no. 2, Aug. 1990, pgs. 50-51.

[49] T. Kilner, A. J. Dempsey, R. M. Pilliar, G. C. Weatherly, "The effects of nitrogen additions to a cobalt-chromium surgical implant alloy, Part 1: Processing and microstructure", *Journal of Materials Science*, vol. 22, no. 2, Feb. 1987, pgs. 565-574.

[50] M. C. Monteiro Dias, N. Shohoji, "Stability of hydrogen and nitrogen in group VIa metals (Cr, Mo, W) and iron-group metals (Fe, Co, Ni) evaluated by statistical thermodynamics", *Journal of Materials Science*, vol. 27, no. 19, 1992, pgs. 5154-5158.

[51] A. J. Dempsey, R. M. Pilliar, G. C. Weatherly, T. Kilner, "The effects of nitrogen additions to a cobalt-chromium surgical implant alloy, Part 2: Mechanical properties", *Journal of Materials Science*, vol. 22, no. 2, 1987, pgs. 575-581.

[52] J. Rawers, G. Asai, R. Doan, and J. Dunning, "Mechanical and microstructural properties of nitrogen-high pressure melted Fe-Cr-Ni alloys", *Journal of Materials Research*, vol. 7, no. 5, May 1992, pgs 1083-1092.

[53] G. R. Blossey and R. D. Pehlke, "Solubility of nitrogen in liquid cobalt alloys", *Transactions of the AIME*, vol. 236, No. 1, Jan. 1966, pgs. 28-32.

[54] J. C. Rawers, N. A. Gokcen, and R. D. Pehlke, "High nitrogen concentration in Fe-Cr-Ni alloys", *Metallurgical Transactions A*, vol. 24A, no. 1, Jan. 1993, pgs. 73-82.

[55] J. Rawers, J. Bennet, R. Doan and J. Siple, "Nitrogen solubility and nitride formation in Fe-Cr-Ni alloys", *Acta Metallurgica et Materialia*, vol. 40, no. 6, June 1992, pgs. 1195-1199.

[56] K. H. Jack, "Heat Treatment '73", *Proceedings of Conference, London*, Dec. 1973 London: The Metals Society, 1975, pg. 39.

[57] J. Aghazadeh-Mohondesi and R. Priestner, "Effects of nitriding at low nitrogen partial pressures on yield and fatigue in some stainless steels", *Metals Technology*, March 1983, vol. 10, no. pt 3, pgs 89-95.

[58] American Academy of Orthopaedic Surgeons, Brochure, "Total joint replacement" [1993?].

[59] D. L. Bartel, "Polyethylene components for hip and knee replacements", *Cornell Engineering Quarterly*, vol. 26, no. 4, Summer 1992, pgs. 26-31.

[60] D. Taylor & B. McCormack, "The durability of materials used in orthopaedic implants", *Proceedings of the 5th. Irish Durability and Fracture Conference, Cork RTC, Cork*, October 1-2, 1987, pgs. 35-44.

[61] W. Krause & R. S. Mathis, "Fatigue properties of acrylic bone cements: Review of the literature", *Journal of Biomedical Materials Research: Applied Biomaterials*, vol. 22, no. A1, suppl. 1988, pgs. 35-44.

[62] V. Saikko, "Wear and friction properties of prosthetic joint materials evaluated on a reciprocating pin-on-flat apparatus", *Wear*, vol. 166, no. 2, July 1993, pgs. 169-178

[63] G. Heimke, "Orthopedic reconstruction: Taking the right approach", *Advanced Materials*, vol. 4, No. 10, 1992, pgs. 676-679.

[64] C. D. Peterson, B. M. Hillberry & D. A. Heck, "Component wear of total knee prostheses using Ti-6Al-4V, titanium nitride coated Ti-6Al-4V, and cobalt-chromium-molybdenum femoral components", *Journal of Biomedical Materials Research Research*, vol. 22, no. 10, Oct. 1988, pgs. 887-903.

[65] H. A. Luckey, E. G. Lamprecht & M. J. Walt, "Bone apposition to plasma-sprayed cobalt-chromium alloy", *Journal of Biomedical Materials Research*, vol. 26, no. 5, 1992, pgs. 557-575.

[66] G. C. Carter & W. L. Hoke, "Vacuum heat treating of medical implants", *Industrial Heating*, vol. 57, no. 3, March 1990, pgs. 28-31.

[67] K. Nielsen, "Corrosion of metallic implants", *British Corrosion Journal*, vol. 22, No. 4, 1987, pg 272.

[68] W. J. Bratina & S. Yue, "Fatigue crack growth-A metallurgist's point of view", *Conference-Time Dependent Fracture: Proceedings of the Eleventh Canadian Fracture Conference, Ottowa, Canada, June 1984*, The Netherlands: Martinus Nijhoff Publishers, 1985, pgs. 27-42.

[69] R. Blickensderfer & G. Laird II, "Pin-on-drum abrasive wear test and comparison with other pin tests", *Journal of Testing and Evaluation*, vol. 16, no. 6, 1988, pgs. 516-526.

[70] R. Blickensderfer, B. W. Madsen, & J. H. Tylczak, "Comparison of several types of abrasive wear tests", *Proceedings of International Conference on Wear of Materials 1985, Vancouver, BC, Canada*, ASME, New York, NY, USA, pgs. 313-323

[71] C. P. Sullivan, M. J. Donachie, Jr, & F. R. Morral, *Cobalt-base superalloys-1970*, Brussels: Center D'Information du Cobalt, 1970.

[72] H. W. Paxton, *Ductility*, Materials Park, OH: ASM International, 1968.

[73] L. Z. Zhuang and E. W. Langer, "Observations on the faceted fatigue fracture of cast Co-Cr-Mo alloy used for surgical implants", *Metallurgical Transactions A*, vol. 20A, no. 1, January 1989, pg. 99.

[74] L. Z. Zhuang and E. W. Langer, "Strain-induced martensitic transformation in fatigued cast Co-Cr-Mo alloy used for surgical implants" *Proceedings of Conference on the Martensitic Transformation in Science and Technology, 9 March 1989*, Bochum, F. R. Germany, 1989, pg. 343.

[75] V. G. Gavriljuk, "Nitrogen in iron and steel", *ISIJ International*, vol. 36, No. 7, 1996, pgs. 738-745

[76] J. P. Hirth and J. Lothe, *Theory of Dislocations*, Reading, MA: McGraw-Hill, Inc., 1968.

[77] L. E. Murr, *Interfacial Phenomena in Metals and Alloys*, New York, NY: Addison Wesley Publishing Company, Inc., 1975.

[78] T. C. Tisone, "The concentration and temperature dependence of the stacking fault energy in face-centered cubic Co-Fe alloys", *Acta Metallurgica*, vol. 21, no. 3, 1973, pg. 229.

[79] L. Z. Zhuang and E. W. Langer, "Effects of alloy additions on the microstructures and tensile properties of cast Co-Cr-Mo alloy used for surgical implants", *Journal of Materials Science*, vol. 24, no. 12, 1989, pg. 4324.

[80] M. Kühlmeyer, "Relation between statistical grainsize and yield strength", *Strength of Metals and Alloys, Fifth International Conference, Aachen, Federal Republic of Germany, August 27-31, 1979*, vol. II, P. Haasen, V. Gerold, G. Kostorz, Bochum, Germany, 1979, pgs 855-860.

9. APPENDIX A: Background on biomedical implants

9.1 Introduction

The American Academy of Orthopedic Surgeons (AAOS) writes that "total joint replacement is one of the great orthopedic surgical advances of this century." This now common surgical procedure resulted from the pioneering efforts of Sir John Charnley, an orthopedist who worked with engineers to develop the techniques and materials used in total joint replacement [58]. When the bones that articulate in hips and knees are damaged through injury, disease, or normal wear and tear, they are replaced with joints made of metals, ceramics, and plastics. The most frequent reason for performing a total joint replacement is to relieve the pain and disability caused by severe arthritis, and in general, these artificial joints perform remarkably well, providing an excellent range of motion that permits the recipients to engage in most everyday activities with little or no pain associated with damaged joints [59]. Joint replacements can be expected to perform well for ten to fifteen years [59], but with more than 150,000 total joint replacements performed each year by orthopedists [58], and younger, more active recipients of them, there is a continuous effort towards improvement. **Figure 9-1** shows schematically the configuration for an artificial hip joint.

The materials used in a total joint replacement are designed to enable the new joint to move in the same way as the normal joint. The artificial components are generally composed of a metal piece fitting closely into a matching sturdy, plastic element. More recently, ceramics and varied composites are also being considered. The metals are varied and include stainless steel, alloys of cobalt, chrome, and titanium, and some pure elements such as tantalum, titanium, or precious metals. The plastic material is most commonly a extremely durable and wear-resistant high density polyethylene. Often, a bone cement such as (poly)methylemethacrylate (PMMA) is used to anchor the bone to the new, artificial component [60]. However, cementless joint replacements are being reconsidered, and are intended to allow bone to grow into and around the device to avoid loosening.

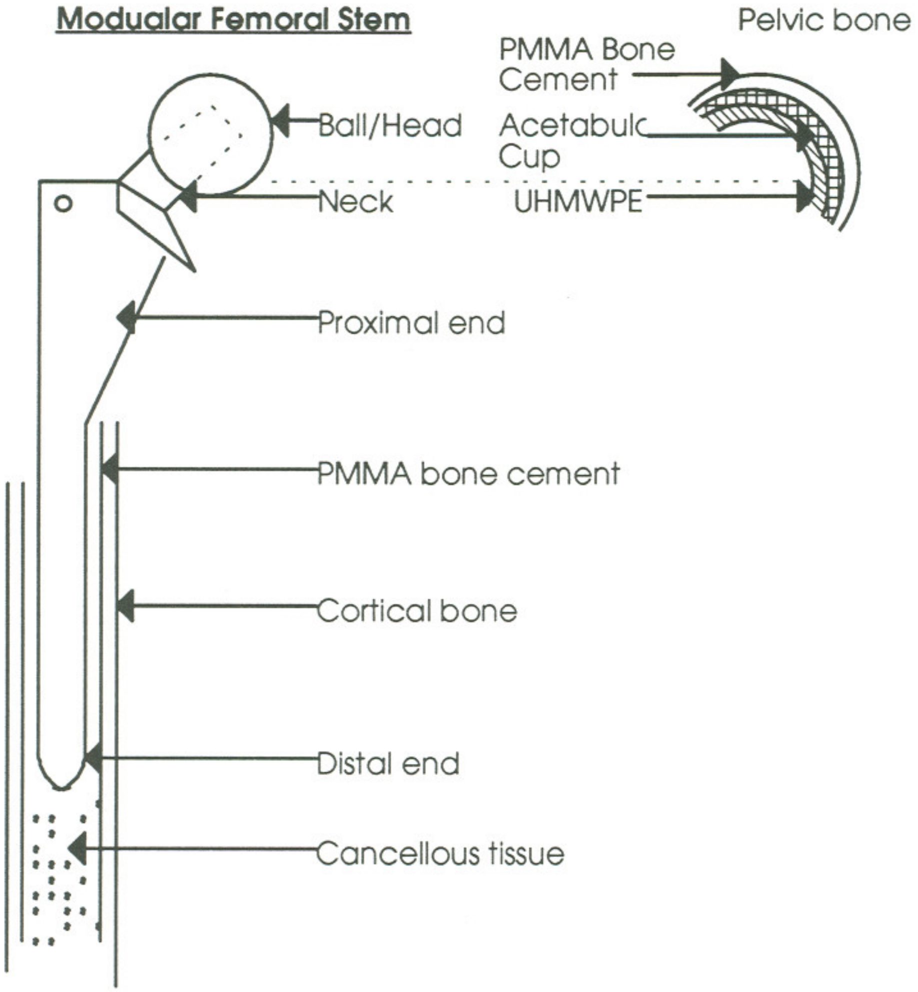

Figure 9-1: Schematic of a typical cemented biomedical hip implant

9.2 Reasons for Implant Failure

Complications that are directly related to the implanted prosthesis are breakage, wear, and loosening [58].

Breakage of an implanted joint is rare, but is a painful experience requiring a second operation to remove the fractured device, and then replacement with a new one. Although it is rare for a prosthesis to break by a single overload, the repeated cyclic loading as a person walks, climbs stairs, etc., can lead to fatigue failure of the implanted joint. This is especially important considering that it is estimated [61] that a person takes about 10^6 steps per year, and that the loads can be 3 to 4 times ones body weight [59]. Breakage, is intimately related to the properties of the materials chosen for the prosthetic device.

Wear is a problem because over time, debris is generated by the motion of the components under loads transferred across the joint. It is felt that *granulomatosis*, which can lead to loosening by gradually destroying bone around the implant, is a biological response to wear products in the implant [62]. This debris, which is mostly polyethylene, migrates to the surrounding soft tissue where it eventually triggers a biological reaction. When the body deals with the debris it also releases agents that attack the bone (osteolysis), generally near its interface with the implant. As a result, the joint becomes more susceptible to infection and bone resorption, which loosens the prosthetic components [59].

Loosening causes pain, and increases the likelihood of premature fracture of an implant. One study [63] found that 40% of the studied cases showed significant loosening after 5 years of service. If loosening is significant, a second total joint replacement may need to be performed. Besides wear, a source of this problem is in the method of fixing the prosthesis to the bone [58], and in the fact that bone is capable of remodeling such that areas of bone which are relatively unstressed tend to dissolve away, whereas highly-stressed regions build up thicker bone deposits [64]. Attempts to alleviate the problem of loosening have lead to a number of different approaches. These include better fixation through cements, cementless porous coated prostheses, and cementless plasma spray coated prostheses, as well as better materials selection and processing to reduce the wear taking place in the joint.

The current commonly used PMMA bone cement has some unsuitable characteristics that are being examined. These include poor tissue response owing to release of the monomer, an exothermic curing reaction which can cause a temperature rise above 70^{o}C (160^{o}F) in the bone, poor adhesion to bone, and low toughness leading to fatigue cracking in use [60].

The alternative approach to using bone cement are the cementless prostheses, which are intended to allow bone to grow into and around the device, thereby holding it in without a third party. Recently, work has being done with plasma sprayed coatings, especially using *apatite* [65], a major component of bone. But the more common method is the use of a sintered bead porous coating.

In fabricating porous coated implants, two or three layers of bead coatings are placed onto the core using an organic binder, and then a sintering process is carried out at 80 to 95 percent of the melting point of the substrate, to facilitate localized fusion at bead-bead and bead-substrate junctions[32]. Concerns about porous bead coatings include long-term effects of metal ion release, potential coating loss, and most importantly, decreased substrate fatigue strength [66].

So, although cementless prostheses may have adequate fixation properties, the conventional processing methods may lead to compromised mechanical performance. Thus, attempts to alleviate the loosening problem in total joint replacements leads back to potential breakage problems. For that reason, continued efforts towards improving the properties of the substrate materials is important.

9.3 Biomedical Implant Materials

For a material to be considered acceptable for biomedical implant applications, there is a rigorous criteria that must be fulfilled. Good static compressive properties are important to guard against breakage due to an overload, and excellent fatigue performance is required for at least 10 million cycles to allow a component life of at least 10 years. Also, the surface hardness and polishability is important from a wear standpoint, so that only a minimal quantity of debris will result. Besides the above qualities, a material used in a prosthetic device requires adequate corrosion resistance for both the slightly saline environment of the body, and the potentially highly acidic fluids that congregate in the locale of injuries. A certain biocompatibility is required such that the body does not reject the device material, and such that metal ions do not escape and render harm to other parts of the body. The combination of cyclic loading and the corrosive environment also requires of the material a resistance to corrosion-fatigue.

There are many different *novel* materials and processing approaches that target various problems associated with total joint replacement components. However, few if any have gained wide-spread acceptance, largely due to the fact that the novel materials and methods are generally not as economically viable.

As a method for increasing the corrosion resistance and the biocompatibility of implant devices, unalloyed materials have been chosen such as pure titanium or pure tantalum in a wrought state. For their relative inertness, precious metals and alloys have also been used [67].

Novel approaches to fixation include the exploration of a range of ceramics, glasses and glass-ceramics which are bioactive, i.e. bone growth (apposition) is promoted around the implant. These include such materials as glass ceramics containing apatite (notably hydroxyapatite, the major constituent of cortical bone), and the calcium phosphate ceramics such as tricalcium phosphate. However, these materials are brittle and could not be used as a bulk stem, so would have to be applied to the surface of another implant material [65].

Since wear is of importance, the ball of hip stems is being targeted for development of a greater wear resistant surface. In Germany and France there has been considerable progress in the use of alumina (Al_2O_3) both for stems and cups. The advantage of alumina is relative inertness in the body combined with superior wear resistance. However, the Young's modulus of alumina is even higher than that of the cobalt chromium alloy, and a potential for catastrophic brittle fracture if overloaded is not to be overlooked [65]. An alternative ceramic considered for the same femoral heads is zirconia (ZrO_2), which can have twice the bend strength of alumina's 400 MPa (58 ksi). However, depending on their geological origin, the zirconia raw materials contain different radioactive impurities. The dangers resulting from this nuclear radiation have been discussed for several years, and although the radioactive impurities can be removed, to do so is expensive [63].

The most common materials used for prostheses are 316L stainless steel, Ti-6Al-4V titanium alloy, and F75 cobalt chromium molybdenum alloys.

316L, an austenitic steel, is generally used in the wrought form [67] as pins and plates for bone fracture repair.. More than 90% of implants of 316 L stainless steel show corrosion attack when removed from the body. In the case of specimens exposed to extremely high loads in surgical applications, failure due to corrosion fatigue may be seen, though it is seen in only a low percentage of failed devices [68]. 316L an economical advantage in situations in which a long life is not required of the component.

The titanium alloy Ti-6Al-4V is used extensively as an implant material (in the extra low interstitial, ELI, condition) because of good mechanical and corrosion resistance properties. It provides a modulus of elasticity that is more closely matched to that of natural bone than other alloys [67], and has been thought to encourage bone fusion by a crystal stacking sequence that is similar to that of bone. The primary importance of this alloy is, however, in aerospace because of its favorable strength to weight ratio. The alloy is two phase even at cryogenic temperatures; however, at room temperature the alloy is predominantly α with only a few percent β. Control of microstructure depends on processing history and heat treatment, and the overall effects can be very complex [69]. As shown in **Table 9-1**, the fatigue strength of Ti-6Al-4V is good, and it can be processed to achieve very high static properties. Due to the excellent corrosion resistance of titanium alloys, good biocompatibility is observed. Ti-6Al-4V is also found to be more resistant to corrosion fatigue than F75 or 316L stainless steel. However, Peterson et. al. [64] found one significant drawback of the titanium alloy in prosthetic applications. When wear tests were conducted against ultrahigh molecular weight polyethylene (UHMWPE), against acrylics, and with acrylic chips present, the metal received light scratches and other signs of abrasion, when Co-Cr-Mo did not. This, added to the high processing cost of Ti-6Al-4V, and the fact that its properties have essentially been maximized, has lead to some people predicting that Ti-6Al-4V will decline in use for prosthetics in the future.

The ASM Metals Handbook [3] states that the good corrosion and wear resistance, and fatigue strength of cobalt-base alloys prompt their use as orthopedic implants. The chapter goes on to extensively address the orthopedic aspect of cobalt alloys. An additional entire chapter in the ASM Metals Handbook [6] is subsequently devoted to biomedical implants. In this chapter, the cobalt alloys discussed included, predominately, Stellite 21.

The Co-Cr-Mo alloy now used in prostheses as either forgings or castings, began under the trade name of Vitallium. It was originally used for dental work but eventually also was applied as a heat resistance alloy for jet engine applications [67]. The version specifically designated for use in cast implant devices falls under the ASTM F75 specification [7]. The structure of most commercial alloys is complex, and ASTM F75 Co-Cr-Mo alloy is no different in this respect. Significant variations in microstructure can be achieved by various heat treatments, but it remains basically an FCC structure. The fatigue strength of F75 was down to around 200-250 MPa (29-36 ksi), but now is up to 400-600 MPa (58-87 ksi) [63]. The corrosion resistance of Co-Cr-Mo alloys depends upon a Cr_2O_3 passive film [3], but it is reported that small changes in alloying additions of some elements can result in significant changes in the corrosion behavior [6]. Even though the cobalt alloys do not passivate as well as titanium alloys, good resistance against pitting corrosion and crevice corrosion has been confirmed for the cobalt alloys containing molybdenum [68]. However, results [40] suggest that corrosion fatigue failures of cast cobalt-chromium alloys do occasionally cause *in situ* implant breakdown, and are a weakness of F75. The ASM Metals Handbook points out that corrosion fatigue properties can be improved by producing a microstructure for resisting mechanical damage in the material. Because it's overall corrosion resistance is very good, F75's biocompatibility is also good. In Peterson's study, the wear of total joint replacements using F75 for the metal component resulted in no wear on the metal, but scratches were observed in the polymer cup the prosthesis was riding in [64]. The ASM Metals Handbook [3] also confirms that retrieved Co-Cr-Mo implants generally show very low amounts of wear on the metal surface.

Table 9-1: Mechanical properties of typical biomedical implant alloys

Material	Elastic Modulus GPa (ksi)	YS MPa, (ksi)	UTS MPa, (ksi)	%Elong	10^7 Fatigue MPa, (ksi)	Hardness (Rockwell)
Ti-6Al-4V	106 (15,400)					
annealed		897 (130)	966 (140)	17	414 (60)	
aged		1104 (160)	1173 (170)	12	345 (50)	
316L Stainless	207 (30,000)					
annealed		207 (30)	538 (78)	55		B-80
1/2 hard		621 (90)	862 (125)	25	290 (42)	C-25
full hard		876 (127)	1139 (165)	12		
forged		518 (75)	897 (130)	12		C-25
Co-Cr-Mo						
cast	207 (30,000)	552 (80)	690 (100)	8	414 (60)	C-30
cast/solutionized		511 (74)	842 (122)	15	511 (74)	
forged		828 (120)	1173 (170)	12		
forged/HT		690 (100)	1642 (238)	26	656 (95)	C-35

10. APPENDIX B: Hot-Working Study on F75

10.1 Introduction

An alternative method to casting biomedical implants, is forging them. There have been several studies involving hot-working of Co-Cr-Mo alloys. Typically the forged alloys have a lower carbon content than the cast version, to lower its interstitial hardening effect. However, the alloys of this study had high carbon contents, and quite likely some amounts of interstitial nitrogen. Thus, hot-working was expected to be difficult.

The most important considerations in hot-working of alloys are the temperature at which the working occurs, and the rate at which the material is deformed. **Table 2-2** of the **Background** summarized various hot-working parameters for Co-Cr-Mo materials, as recorded in various studies. The data indicated that hot-working done by preheating at 1220°C (2230°F), then hot-rolling at or below 1200°C (2190°F) would be most desirable. The temperature of 900°C (1650°F) was reported to be the lower range of hot-workability. Although Carpenter Technology Corp. claimed [44] that greater ductility during hot-working of their Co-Cr-Mo-N alloy could be obtained by not solutionizing first, J-P Immarigeon et. al. [45] found that pre-solutionization avoided carbide stringers and eliminated banding during forging. Immarigeon et. al. also found that pre-solutionizing and then reheating to a lower hot-working temperature could produce carbides that pinned the grain-boundaries after hot-working reduced the grain size.

10.2 Hot-Rolling Temperature Determination

Superalloys such as the Co-Cr-Mo alloy are quite sensitive to hot-working, and care is needed to successfully deform them. In order to determine the appropriate parameters for hot-rolling of the N-HPM ingots, the test matrix in **Table 10-1** was set up. Round, 0.5" diameter investment cast bars of ASTM F75 were used as the test material. Since the Ni added to Stellite 21 would contribute to enhanced workability, the use of

Table 10-1: Exploratory hot-working parameters for F75 materials

Rolling Temperature	Deformation		
1000°C (1830°F)	20%	40%	20% x 2
1100°C (2010°F)	20%	40%	20% x 2
1200°C (2190°F)	20%	40%	20% x 2

F75 was expected to give conservative results. The bars were first solutionized for 16 hours at 1220°C (2220°F) under continuously flowing argon (~400*l*h or ~15cfh). The thermomechanical matrix was then carried out at the DOE-ARC. All subsequent heating was done in air, with 15 minute reheats between passes.

Following hot-rolling, the samples were water quenched, and then examined for signs of cracking or other defects. Additionally, metallography of the resultant microstructure was used to determine what degree of dynamic recrystallization had occurred, and whether uniform deformation had been achieved without formation of internal defects such as cracks.

Immediately evident in the rolled bars, is that at 1200°C (2190°) for 20% reduction, and at all temperatures for 40% reduction, the ends of the bars displayed centerbursting. In the polished and etched cross sections the samples show a hyperbolic pattern of dense distortion that is likely due to the non-uniform deformation experienced in flattening a round section. The centerbursting was generally observed at the apex of the hyperbolae (**Figure 10-1**). Close examination shows that at the high and low temperatures following the 40% reduction passes, cracking was present along the hyperbolic distortion paths, as shown in **Figures 10-2** and **10-3**. As displayed by **Figures 10-4** and **10-5**, for 20% reduction, the 1000°C (1830°F) and 1100°C (2010°F) samples displayed grains filled with cross-hatched slip planes, but overall no cracks were present. Although some cracking was observed, the 1200°C (2190°) 20% reduction samples also showed evidence of recrystallization, as shown in **Figure 10-6**. Following two passes of 20% reduction, cracking was observed in the 1000°C (1830°F) bars. Ultimately, repeated deformations of 20% at a temperature of 1100°C (2010°F) were found to lead to an acceptable microstructure in the F75 material, as shown in **Figure 10-7**.

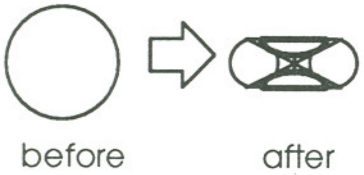

Figure 10-1: Deformation structure in rolled round bar.

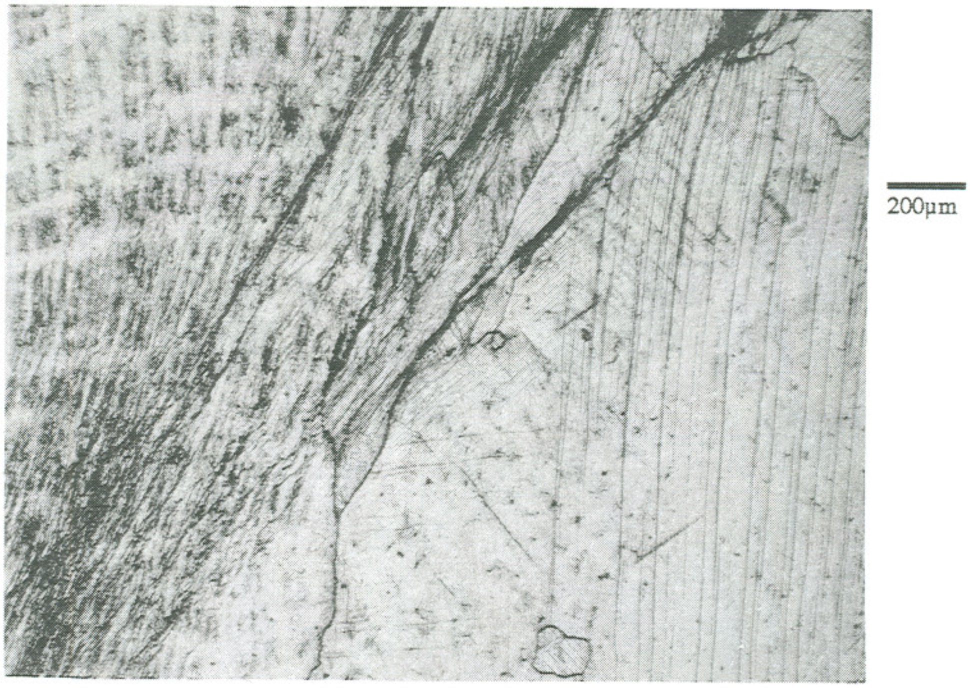

Figure 10-2: ASTM F75 hot-rolled at 1000°C (1830°F) with 40% reduction; electrolytically etched with 10% ammonium persulfate, 50x

Figure 10-3: ASTM F75 hot-rolled at 1200°C (2190°F) with 40% reduction; electrolytically etched with 10% ammonium persulfate, 50x

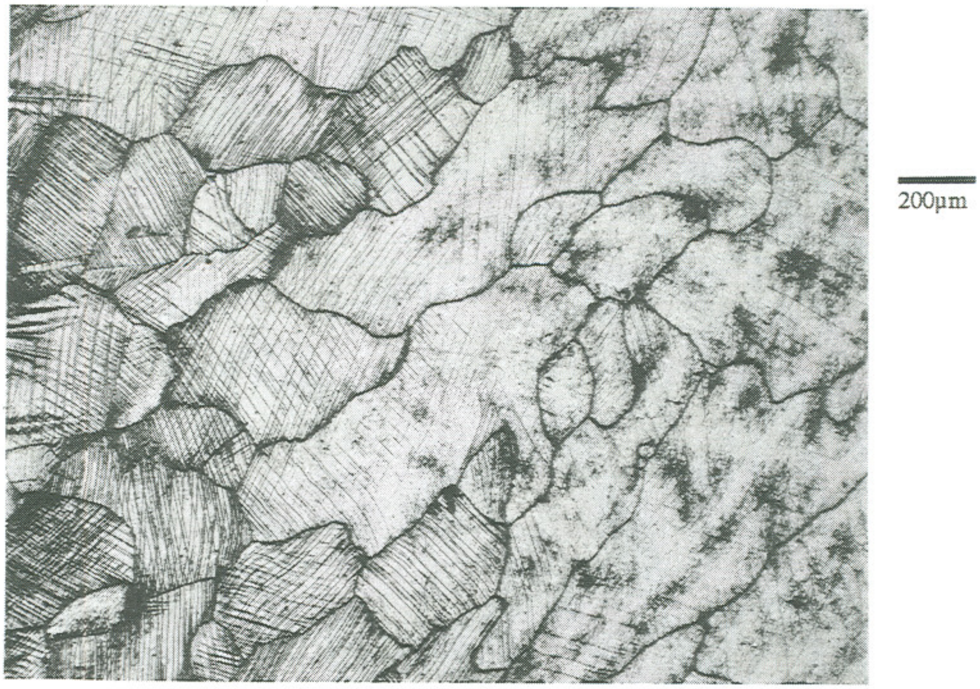

Figure 10-4: ASTM F75 hot-rolled at 1000°C (1830°F) with 20% reduction; electrolytically etched with 10% ammonium persulfate, 50x

Figure 10-5: ASTM F75 hot-rolled at 1100°C (2010°F) with 20% reduction; electrolytically etched with 10% ammonium persulfate, 50x

Figure 10-6: ASTM F75 hot-rolled at 1200°C (2190°F) with 20% reduction; electrolytically etched with 10% ammonium persulfate, 50x

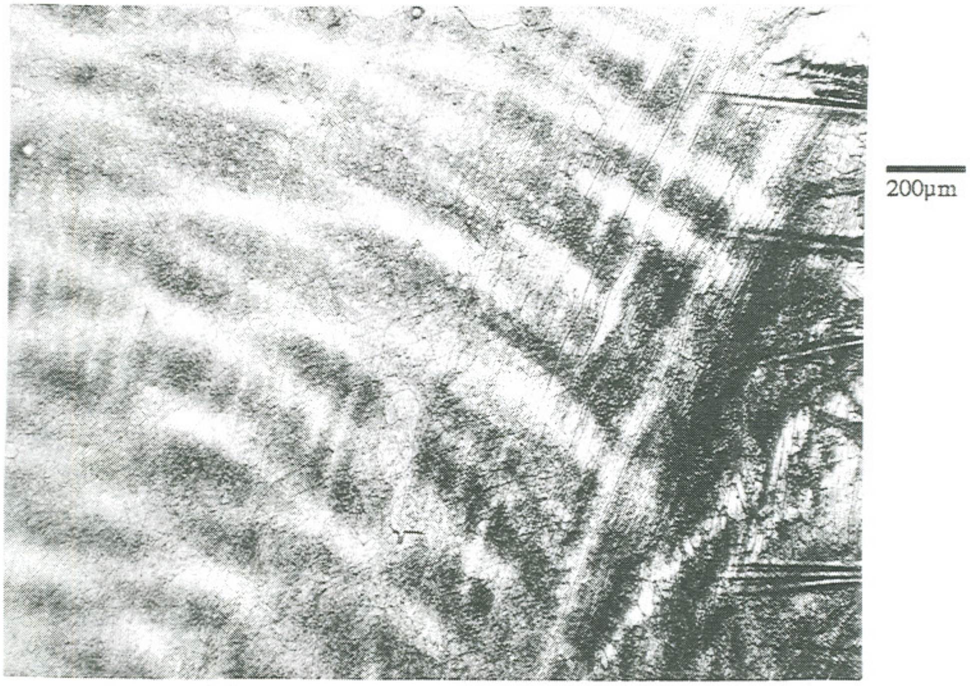

Figure 10-7: ASTM F75 hot-rolled at 1100°C (2010°F) with 3 passes of 20% reduction; electrolytically etched with 10% ammonium persulfate, 50x

While an acceptable microstructure was achieved following repeated deformations of 20% at 1100°C (2010°F), the use of round bars as the initial material most likely led to additional difficulty in minimizing cracking in the material. If the rolling process is visualized mid-pass, it seems that the use of round rolls perpendicularly on round bars could set up a severe flow localization along intense shear bands, which could lead to the hyperbolic distortion structure observed. As the rolls first contacted the tangents to the diameter of the bar, the load would have to be distributed over the infinitely small area of the tangent point, which could lead to drastic work hardening, and banding at the center of the bar along the vertical line between the tangent points on opposite sides of the bar. As the bar continued into the rolls, the contact area would widen, but the deformation would be preferentially distributed over the area that has not already been work hardened, thus leading to a hyperbolic distribution across the cross section of the bars. However complete description and proof of this fact would require more intense analysis.

As described by Jong-Chen Tsai et. al. [47], at 1200°C (2190°) incipient melting could occur in the Co-Cr-Mo alloy when deformed at a high strain rate, because the temperature increase due to deformation and interface friction may raise the temperature of the alloy to near the melting point of the eutectic, 1235°C (2255°F). This, combined with the intense, undistributed residual stresses in the lower temperature bars, appears to by the most likely reason for the cracking and centerbursting observed in the hyperbolic distortion bands in so many of the deformed round bars samples. The fact that this was *not* observed in the bars rolled repeated at 1100°C (2010°F) in 20% reduction passes, suggests that these conditions achieved a safe balance between distortion rates that do not lead to high localized temperature increases, a temperature high enough to reduce residual stress structures, and a temperature low enough to avoid incipient melting. Application of these temperature conditions combined with even lower reductions per pass, would be expected to be suitable for the N-HPM Stellite 21 billets.

10.3 Effect of Annealing on Plate Softening

Leaving hot-rolled material in a condition of potentially high residual stress may lead to widely scattered mechanical property results, as well as to machining difficulties. The effects of the hot-working on the N-HPM plates could also disguise the strengthening effects of the interstitial nitrogen. Thus, annealing of the material would be desirable.

In order to evaluate the appropriate annealing temperature and time, a round, investment cast, ASTM F75 bar which had been hot-rolled at 1100°C (2010°F) for 5 passes of 20% reduction each, was cut into several pieces which were then annealed in different manners. The pieces were about 1 cm x 2 cm x 3 mm (3/8"x3/4"x1/8"). Annealing was done in air at 1100°C (2010°F) for times of 1/4, 1/2, 1, 2, and 4 hours, at 1150°C (2100°F) for 1/4, 1/2, 1, and 2 hours, and at 1150°C (2100°F) for 2 hours followed by 1200°C (2190°F) for 1 hour.

Rockwell hardness testing of the samples showed initial softening followed by constant or slightly increasing hardness over time in the samples annealed at 1100 and 1150°C (2010 and 2100°F). Only the specimen which included the 1200°C (2190°F) soak softened effectively. Metallography showed that at 1100 and 1150°C (2010 and 2100°F), some precipitation may have occurred **(Figure 10-8)**. J. P. Immarigeon et. al. [45] also observed this phenomenon, suggesting that it was beneficial to pinning the grainboundaries to retain a fine-grained wrought product. This precipitation could have led to the slight increase in hardness over time that followed the initial softening.

At 1200°C (2190°F) there were signs of solutionization of the precipitates, as shown in **Figure 10-9**. It was concluded that short times even at 1100°C (2010°F) were sufficient to soften the hot-worked material, but that 1200°C (2190°F) countered the precipitation, as well as contributed further softening.

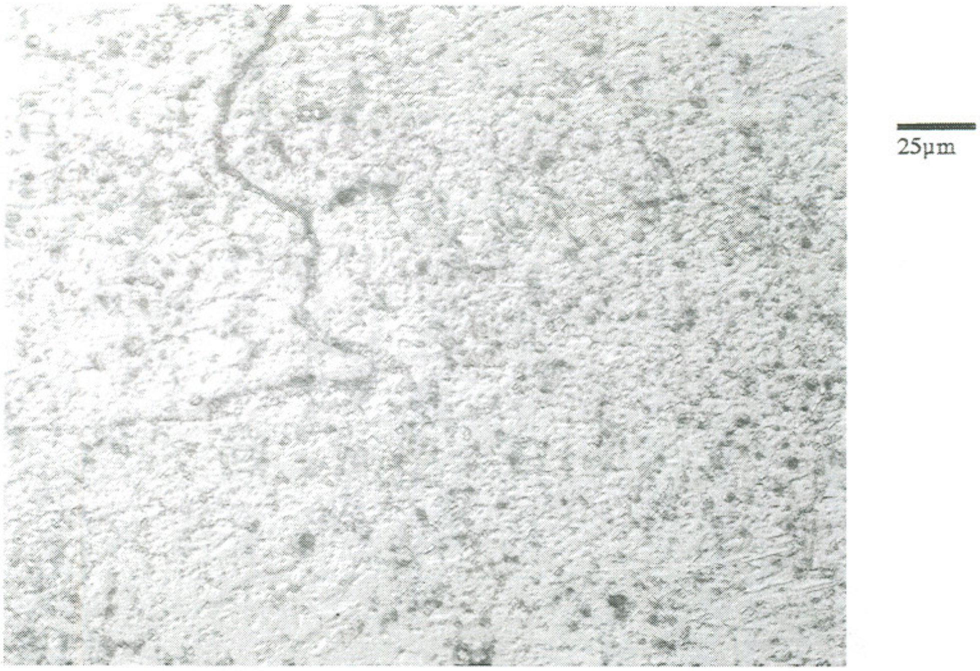

Figure 10-8: ASTM F75 hot-rolled at 1100°C (2010°F) with 20% reductions, then held at 1150°C (2100°F) for 4 hours. Note apparent precipitation; unetched, DIC, 400x

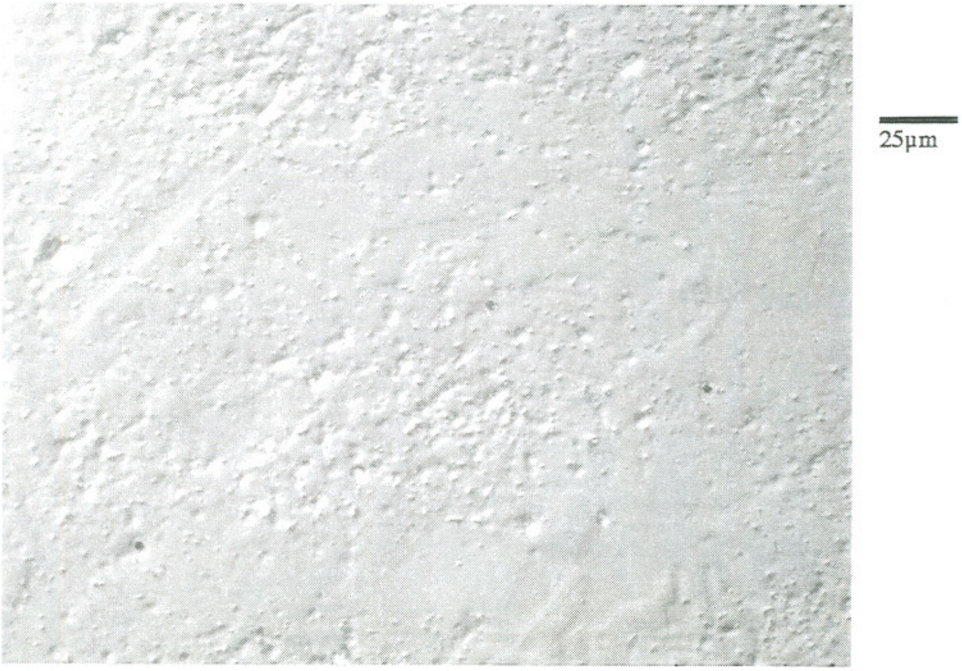

Figure 10-9: ASTM F75 hot-rolled at 1100°C (2010°F) with 20% reductions, then held at 1150°C (2100°F) for 4 hours followed by 15 minutes at 1200°C (2190°F). Note dissolution of precipitates; unetched, DIC, 400x

BIOGRAPHICAL SKETCH

Wade Lewis Karlsen was born in Vancouver, Washington, USA, on August 8th, 1971, and grew up in the nearby rural town of Hockinson, Washington. Following graduation from his hometown high school of Prairie High School in 1989, he entered the University of Washington (UW), in Seattle, Washington. In June of 1993, he graduated from the University of Washington's Materials Science & Engineering department with a Bachelor of Science in Metallurgical Engineering. Later that summer, he entered the Oregon Graduate Institute of Science & Technology (OGI) in Beaverton, Oregon. The next four years were spent in OGI's Materials Science & Engineering department performing the research work for his Ph. D. thesis, and contract research on biomedical implant alloys for PED Manufacturing, Ltd. and Precision Castparts Corporation. In August of 1997, he accepted a position as a Research Scientist in the Laboratory of Engineering Materials at Helsinki University of Technology, in Espoo, Finland, to explore nitrogen alloying of Co-Cr-Mo metal powders for biomedical implant applications.

During his university career to date, he has been actively involved in the American Society for Materials (ASM) and The Metals, Minerals, and Materials Society (TMS), serving as Chairman of the ASM/TMS joint student chapters at both the UW and OGI for a total of 4 years. In his final year at the UW, he received an ASM Scholar award, as well as the Louis and Katherine Marsh scholarship. While at OGI, he was twice consecutively awarded the ASM Oregon student scholarship.